Titre: Title:	Micro-mechanical damage accumulation in airframe materials and structural components
Auteur: Author:	Sanjay Tiku
Date:	1997
Type:	Mémoire ou thèse / Dissertation or Thesis
Référence: Citation:	Tiku, S. (1997). Micro-mechanical damage accumulation in airframe materials and structural components [Thèse de doctorat, École Polytechnique de Montréal]. PolyPublie. https://publications.polymtl.ca/6839/

UNIVERSITÉ DE MONTRÉAL

MICRO-MECHANICAL DAMAGE ACCUMULATION IN AIRFRAME MATERIALS AND STRUCTURAL COMPONENTS

SANJAY TIKU

DÉPARTEMENT DE MÉTALLURGIE ET DE GÉNIE DES MATÉRIAUX

ÉCOLE POLYTECHNIQUE DE MONTRÉAL

THÈSE PRÉSENTÉE EN VUE DE L'OBTENTION

DU DIPLÔME DE PHILOSOPHIAE DOCTOR (Ph.D.)

(GÉNIE MÉTALLURGIQUE)

MARS 1997

National Library
of Canada

Acquisitions and
Bibliographic Services

395 Wellington Street
Ottawa ON K1A 0N4
Canada

Bibliothèque nationale
du Canada

Acquisitions et
services bibliographiques

395, rue Wellington
Ottawa ON K1A 0N4
Canada

Your file Votre référence

Our file Notre référence

0-612-33033-8

Canada

UNIVERSITÉ DE MONTRÉAL

ÉCOLE POLYTECHNIQUE DE MONTREAL

Cette thèse intitulée:

MICRO-MECHANICAL DAMAGE ACCUMULATION IN AIRFRAME MATERIALS AND STRUCTURAL COMPONENTS

présentée par: TIKU Sanjay

en vue de l' obtention du diplôme de: Philosophiae Doctor

a été dûment acceptée par le jury d' examen constitué de:

M. Verreman, Yves, Ph.D., président

M. MARCHAND Norman J., Sc. D., membre et directeur de recherche

M. DICKSON J.I., Ph.D., membre

M. HONGOH, M., Ph.D., membre

To my Parents, "Jiji & Papa"

&

my brother Bobby

ACKNOWLEDGEMENTS

It gives me immense pleasure to acknowledge Dr. Norman Marchand, for providing me with an excellent opportunity to work on this project. I have enjoyed working with him and his infectious optimism always made the problems appear less difficult.

Dr. Bikhu Unvala's help and guidance albeit at times over long distance phone calls and faxes has been a key to the success of this project. I have benefitted greatly with our association.

Words are not enough to thank Dr. Ashok Koul for the help and guidance provided at all times during the course of this work. He has been an inspiration and an infinite source of knowledge. I have benefitted immensely, professionally and otherwise from him.

I am thankful to Prof. J.P. Bailon, Head of the Department, for providing all the needful facilities and Prof. J.J. Dickson for his help in the fractography.

Many thanks to my colleagues and friends for their help and assistance with special mention to Leslie, for developing all the softwares that were needed within the course of this work and Jamal, for technical discussions and the great time we had together.

I would like to thank Dr. M. Hongoh, Prof. J.J. Dickson and Prof. Y. Verreman for painstakingly going through the manuscript and making helpful suggestions.

I would like to acknowledge Major N. Landry and Capt. S. Dubois for their help during the course of this work and Department of National Defense for the funding of this project.

A special thanks to my aunt, Anju for all the support and encouragement (and great meals too). I never felt that I was away from my home.

I would like to thank Shalini for her patience in listening to whatever I had to say about my work. It was a great pleasure to be in her company.

Finally I would like to thank my parents for their love and support through out my life.

RÉSUMÉ

On décrit en détails la méthodologie de design de nouveaux types de capteurs de contraintes /déformations et de fissures basés sur la technologie de chute de potential en courant alternatif (ACPD). Ces capteurs. qui utilisent la technique de focalisation du courant (current focusing technique). permettent la mesure en continu et/ou de manière discrète. des contraintes (déformations) et des fissures en environnements de laboratoire et en milieux industriels (moteurs. structures. avions. etc). Les performances de la technique de focalisation du courant et le confinement tri-dimensionnel de la densité de courant qui en résulte. ont été vérifiés. La technologie ACPD a été utilisée sur un alliage Al-7075 pour obtenir des courbes de calibration reliant la profondeur des fissures. l'amplitude des déformations. et/ou l'amplitude des contraintes résiduelles. en fonction de la variation de potentiel ACPD. Des fissures. ayant au plus 140 μm de profondeur. ont été mesurées avec plus de 99% de certitude (confidence level) en utilisant des courants de 5 Amp.. 120 kHz de fréquence. et un gain de 3000. On démontre que la relation entre la profondeur des fissures et la différence de potentiel est une fonction quadratique.

Les nouveaux capteurs développés ont été installés sur un avion F18-A soumis à des chargements aérodynamiques simulés (essai à grande échelle - Canadair/DND). On montre que les capteurs sont capables de mesurer avec précision les déformations qui

résultent des chargements aérodynamiques imposés. Les capteurs ACPD ont détecté, avec une certitude supérieure à 99.9%, la présence de fissures après 3400 spectres de vol simulé (SVS). Plus de 2500 SVS supplémentaires ont été nécessaires pour que la fissure devienne suffisamment longue pour qu'elle soit détectable par les autres techniques d'essai non-destructif utilisées par Canadair/DND (courant de Foucault, liquides pénétrants, émission acoustique etc).

La technique ACPD a aussi été utilisée en laboratoire pour caractériser le comportement des fissures courtes (>40 μm) initiées de façon naturelle. Les fissures étudiées étaient semi-elliptiques avec des taux de croissance latérale (en surface) supérieurs aux taux de croissance transversale (en profondeur). Le comportement des fissures courtes en fonction de l'orientation des grains (par rapport à l'entaille) a été étudié en détails. On montre que l'interaction des joints de grains avec le fond des fissures courtes contrôle le taux de propagation, et cela, à des niveaux de contraintes égaux ou même supérieurs à la limite d'écoulement du matériau. Les taux de propagation de fissures courtes ont été corrélés avec le facteur d'intensité de contraintes (FIC). Les formules empiriques, obtenues à partir des résultats numériques de Newman pour les fissures semi-elliptiques, ont été utilisées pour calculer les FICs. La corrélation ainsi obtenue est très mauvaise avec une dispersion considérable des résultats. Finalement, on montre que l'utilisation de facteurs d'intensité de contraintes modifiés, tels ($\Delta K^2/\sigma$ et $\Delta K/C$, permet une meilleure corrélation des résultats expérimentaux.

ABSTRACT

A simple and flexible ACPD probe design methodology incorporating current focusing technique was developed for on-line as well as off-line measurements in laboratory and industrial scale test environments. The effectiveness of the current focusing technique and the resulting three-dimensional control of the current density distribution was demonstrated. The ACPD technique was successfully used to obtain strain calibration and crack calibration curves in 7075 Al alloys. This also included quantifying the effect of residual stresses on ACPD signal. The smallest crack depth detected was 140 μm at 120 kHz. 5 amp. and 3000 gain. A quadratic relation was found to correlate crack depth with potential change. The ACPD sensors were installed on a F-18 aircraft undergoing full scale test at Canadair. The sensors were able to measure the response of the structure to spectrum loading. A crack was detected by the ACPD sensors only after 3400 SFH and it was established that ACPD probes were able to detect the crack long before (~2500 SFH) any other established techniques utilized by DND/Canadair was able to detect the crack.

The technique was sucessfully used to characterize short crack growth behaviour of naturally initiated fatigue cracks in Al alloys from 40μm crack depth onwards.The cracks were semi-elliptical in shape and crack growth along the notch root was faster than crack growth into the specimen. The effect of various grain orientations on short

crack growth behaviour was studied. The crack tip interactions with grain boundaries were shown to control the SCG behaviour of Al alloys even at notch root peak stresses close to yield stress of the material. This effect was less prominent at notch root peak stresses considerably higher than yield stresses. The fatigue crack growth rates were correlated with the SIF (K) calculated using Newman's model for thumb nail cracks. This correlation resulted in a very large scatter in the data. The fatigue crack growth rate data were better correlated using modified parameters. $\Delta K^2/\sigma$ and $\Delta K/C$.

CONDENSÉ EN FRANÇAIS

Plus que jamais auparavant, il est devenu impératif de pouvoir prédire la durée de vie en service des structures aéronautiques existantes. Par exemple, la philosophie 'safe-life' utilisée pour le design de ces structures prévoyait leur remplacement lorsque celle-ci avaient atteintes leurs durées de vie calculées. Cependant, à cause des facteurs de sécurité utilisés lors du design, il s'en suit qu'une pièce sur 1000 a réellement atteint sa durée de vie lorsque celle-ci est retirée du service (999 pièces encore bonnes sont remplacées!). Pour pallier aux inconvénients économiques causés par la philosophie 'safe-life', une nouvelle philosophie de design et d'utilisation, appellée 'Damage Tolerant Design' ou DTD, a été dévelopée. Avec la philosophie 'DTD', la présence de défauts doit être prise en compte dès le départ et le constructeur 'designer' doit démontrer que la structure ne peut pas se briser catastrophiquement en-dedans d'une période de temps bien définie. Cependant, l'application de cette philosophie de design (et de suivi de structures) repose sur certaines prémisses. Entre autres, il doit être possible de détecter, avec fiabilité et confiance, l'initiation et la croissance de microfissures dans des pièces de structures en environnements industriels. De plus, la croissance des fissures sous chargements réels doit pouvoir être calculée de façon précise et celà implique que le comportement en service des fissures courtes soit connu. Les objectifs de ce programme de doctorat s'inscrivent dans cette ligne de pensée, c.à.d. (1) développer un nouveau type de capteur non-destructif capable de détecter l'initiation

et la croissance de microfissures dans des pièces de structures d'avions sous chargemements aérodynamiques, (2) calibrer ces capteurs. c.à.d. associer une dimension (profondeur) de fissure aux signaux électriques produits par ces capteurs. et (3) mesurer et analyser le comportement en services des fissures courtes incluant les effets des contraintes résiduelles sur les taux de croissance. Les résultats et conclusions qui découlent de ces travaux se résument ainsi:

Un nouveau type de capteur de mesure de contraintes/déformations et de profondeur de fissures. basés sur la technologie ACPD. ainsi que la méthodologie de design de ces capteurs. ont été développés. Ces capteurs. qui utilisent la technique de focalisation du courant (current focusing technique). permettent la mesure en continu et/ou de manière discrète (off-line). des contraintes et des fissures en environnements de laboratoire et ou en milieux industriels (moteurs. structures. avions. etc).

Les performances de la technique de focalisation du courant et le confinement tri-dimensionnel de la densité de courant qui en résultent. ont été vérifiés. Les avantages et les désavantages de la focalisation du courant (FC) ont été étudiés. La technique a été optimisée et incorporée dans le design des capteurs. Ceci a été validé expérimentalement sur un grand nombre de géométries.

La technologie de soudage ultrasonique (ultrasonic welding procedure) a été modifiée significativement de manière à permettre l'installation de capteurs sur des échantillons de laboratoire et des pièces utilisées en service (sur un avion). On a démontré que cette procédure d'attache des sondes ACPD n'influence aucunement le comportement en service ou la durée de vie des pièces, et celà, quel que soit le type de chargement thermo-mécanique appliqué sur la structure (pièce) .

La technologie ACPD a été utilisée sur un alliage Al-7075 pour obtenir des courbes de calibration reliant la profondeur des fissures en fonction de la variation de potentiel ACPD. Les courbes de calibration ont été obtenues à trois fréquences différentes (30, 90 et 120 kHz). Des fissures de 140 μm de profondeur, ont été mesurées avec plus de 99% de certitude (confidence level) en utilisant des courants de 5 ampères, 120 kHz de fréquence, et un gain de 3000. On a montré que la relation entre la profondeur des fissures et la différence de potentiel est toujours une fonction quadratique. Les résultats expérimentaux sont en accord avec les résultats de simulations numériques (calculs par la méthode des élements finis) montrant une relation quadratique entre le potentiel et la profondeur des fissures.

La variation de potentiel ACPD a été correlée en fonction de la surface (aire) fissurée. Une relation quadratique a aussi été obtenue entre le potentiel et l'aire fissurée (avec

99% de confiance). Ce résultat démontre que la technique ACPD/FC peut-être utilisée pour analyser les problèmes de fissuration multiples (Multiple Site Damage - MSD).

On a mesuré la réponse en contrainte/déformation sur un alliage Al-7075 soumis à des chargements mécaniques avec la méthode ACPD/FC. Les courbes de calibration contrainte/déformation en fonction du potentiel ACPD ont été obtenues sur des éprouvettes de flexion quatre-points. Ces éprouvettes étaient instrumentées avec des jauges de contraintes. Une relation linéaire entre les signaux ACPD et la déformation/contrainte mesurée par les jauges a été obtenue. L'intervalle de confiance pour cette courbe de calibration est de 97% (confidence level).

La relaxation des contraintes résiduelles, a pu être mesurée avec la technique ACPD/FC. Cette relaxation a été mesurée sur des échantillons soumis à des chargements cycliques. Les niveaux de contraintes résiduelles avant et après chargement cycliques (et/ou thermiques) ont été vérifiés par diffraction des rayons-X. L'accord entre les résultats obtenus par rayon-X et la méthode ACPD/FC est excellent. Ce résultat constitu l'une des plus grandes retombées de ce programme de recherche.

On a démontré que l'interruption des essais de fatigue lors de mesure en continu (on-line measurement) n'affectait pas la sensibilité et/ou la précision des résultats ACPD/FC. De plus, la variation de potentiel associée à la présence d'une fissure de

dimension donnée, demeure inchangée quel que soit l'état de chargement. Ceci prouve que la fissure peut être détectée et quantifiée même si celle-ci est fermée. Ce résultat démontre aussi que la technique ACPD/FC peut être utilisée comme outil de maintenance préventive (détection des fissures ou suivi des fissures à intervalle régulier 'off-line measurement') et servir comme à l' inspection non-destructive des structures (Non-destructive Inspection - NDI).

Les nouveaux capteurs développés ont été installés sur un avion F18-A soumis à des chargements aérodynamiques simulés (essai à grande échelle - Canadair/DND). On a montré que les capteurs sont capables de mesurer avec précision les déformations qui résultent des chargements aérodynamiques imposés. Les capteurs ACPD ont détecté, avec une certitude supérieure à 99.9%, la présence de fissures après 3400 heures de vols simulés (SVS). Plus de 2500 SVS supplémentaires ont été nécessaires afin que la fissure devienne suffisamment longue pour qu'elle soit détectable par les autres techniques d'essai non-destructif utilisées par Canadair/DND (c.à.d. courants de Foucault, liquides pénétrants, émission acoustique, etc). L'utilisation des courbes de calibration (profondeur/ACPD) produites en laboratoire a permis d'estimer avec précision la profondeur et la longueur initiale de la fissure.

La technique ACPD/FC a été utilisée en laboratoire pour caractériser le comportement en fatigue des fissures courtes (>40 μm) initiées de façon naturelle. Les fissures

étudiées étaient toutes semi-elliptiques avec des taux de croissance latérale (en surface) supérieurs aux taux de croissance transversale (en profondeur) de façon à maintenir le rapport longueur sur profondeur (c/a) quasi-constant à 1.3. On montre qu'il est préférable de tracer l'évolution de la profondeur (a) en fonction de la longueur surfacique (c) des fissures plutôt que de tracer l'évolution du rapport c/a en fonction de a (ou c). Ceci provient du fait que l'évolution du rapport c/a est faussée lorsque que la fissure devient débouchante.

On démontre que la procédure d'analyse des résultats bruts. c.à.d. la procédure pour convertir les signaux ACPD/Cycles de fatigue en termes de longueur de fissures/Cycles de fatigue. peut introduire des artefacts dans la courbe da/dN vs a. On montre que cette conclusion s'applique quelque soit la méthode utilisée pour mesurer la longueur de la fissure (ou des fissures).

Les résultats de fatigue obtenus sur l'alliage Al 7075 en conditions T651 et T7351 montrent que la résistance à l'initiation des fissures dépend du niveau de contraintes. A faibles niveaux de contraintes ($\sigma \leq$ contrainte d'écolement) la résistance à l'initiation de fissures est supérieure en condition T651. À niveaux de contraintes élevés ($\sigma \geq$ contrainte d'écolement) la condition T7351 est plus résistante à l'initiation des fissures que la condition T651. Dans tous les cas, les zones d'initiation sont associées à une rupture en mode I qui est de nature transgranulaire crystallographique .

Le comportement en fatigue des fissures courtes a été étudié en détail en fonction de l'orientation des grains. On montre que l'interaction des joints de grains avec le fond des fissures courtes contrôle le taux de propagation, et celà, à des niveaux de contraintes égaux ou même supérieurs à la limite d'écoulement du matériau. L'effet de l'orientation des grains disparait lorsque le niveau de contrainte devient largement supérieur à la limite d'écoulement plastique (~ 795 MPa).

Les taux de propagation de fissures courtes obtenus à R = 0 (avec $R = \sigma_{min} / \sigma_{max}$) ont été corrélés avec le facteur d'intensité de contraintes cyclique (ΔK). Les formules empiriques, obtenues à partir des résultats numériques de Newman pour les fissures semi-elliptiques, ont été utilisées pour calculer les ΔK's. On montre que la corrélation obtenue est très mauvaise. Ainsi, des fissures de longueurs variées mais ayant le même ΔK, présentent des vitesses de fissuration qui augmentent avec une augmentation de la contrainte maximale (σ_{max}). Ceci démontre clairement que ΔK n'est pas le paramètre approprié pour caractériser la force motrice pour la propagation des fissures courtes de fatigue dans l'alliages Al 7075. Ceci est en accord avec les résultats expérimentaux de Dubonski [114] sur l'alliage 7075 T6, ainsi qu'avec les résultats de Newman obtenus sur un alliage 2024 T3 [57].

Finalement, on montre que l'utilisation de facteurs d'intensité de contraintes modifiés (énergie par unité de surface), tels $\Delta K^2/\sigma$ et $\Delta K/C$, permet une meilleure corrélation des résultats expérimentaux.

TABLE OF CONTENTS

LIST OF TABLES

LIST OF FIGURES

LIST OF ABBREVIATIONS AND SYMBOLS

δ	skin depth
δV	change in ACPD
ΔK	stress intensity factor range
ΔK_{th}	long crack threshold stress intensity factor
ρ	electrical resistivity
σ_e	fatigue limit
σ_{max}	peak stress
σ_{min}	minimum stress
μ_r	relative permeability
μ_o	absolute permeability of vacuum
a	crack depth
a_i	minimum detectable crack size
A	crack area
ACPD	alternating current potential difference
c	half surface crack length
C	notch root peak stress/flow stress
CGM	crack growth monitor
D	notch depth
DCPD	direct current potential difference

DND	Department of National Defence
DTD	damage tolerant design
DVM	digital voltmeter
emf	electro magnetic field
f	frequency
IFOSTP	international follow on structural test program
IAR	Institute for Aerospace Research
K	stress intensity factor
K_{eff}	effective stress intensity factor
K_f	fatigue concentration factor
K_{th}	threshold stress intensity factor
LCF	low cycle fatigue
LEFM	linear elastic fracture mechanics
N	number of cycles
N_i	number of cycles for crack initiation
NDI	nondestructive inspection
NDT	non destructive testing
NRC	National Research Council
PD	potential difference
PLC	power line cycles
PSB	persistent slip band

PSD	phase sensitive detection
PWC	Pratt & Whitney Canada
r	notch radius
R	stress ratio
RFC	retirement for cause
S	far-field remote stress
SCG	short crack growth
SEN	single edge notch
SFH	spectrum flight hour
SG	strain gauge

LIST OF APPENDICES

1.0 INTRODUCTION

The safe life philosophy for the design and life cycle management of aerospace structures subjected to fatigue loading conditions incorporated "large" safety factors to guard against fatigue failures during service [1]. In this design approach, the structures or structural components are retired after a finite service life based on a statistical crack initiation criterion. This approach is costly because there can be a significant amount of service life remaining in retired components. The conservativeness of this approach can truly be appreciated when considering the case of gas turbine discs. The service life of discs is based on statistical analysis of the low cycle fatigue (LCF) data obtained on laboratory specimens. Using this design criterion, only one in every one thousand retired components is expected to contain a LCF crack. Obviously a major disadvantage of this approach is that 999 components out of one thousand are retired in a crack free condition. The results of a theoretical analysis, as shown in fig. 1.1 indicate that majority of the components have over 10 life times to crack initiation remaining in them [2].

Safe life approach therefore leads to an inefficient use of component lives and results in severe cost penalties from a user's point of view. The limitation of safe life design led to the development of alternative design approaches which considered the performance of structures and structural components in the presence of cracks. Fracture mechanics provided a better understanding of fatigue crack growth characteristics of materials and

enabled the prediction of the crack growth behaviour of components. The application of fracture mechanics principles to design. form the basis of the damage tolerant design (DTD) methodology. The DTD approach was initiated by the United States Air Force (USAF) in 1970 [1]. The basic difference between the DTD methodology and the original safe life approach is that. in DTD philosophy, it is assumed that cracks already exist in the structure. but the components should be able to tolerate the propagation of cracks without causing structural failure. The size of the crack assumed to pre-exist in a structure is taken as the minimum detectable crack size. (a_i) that can be resolved by the non destructive inspection (NDI) technique employed in the field. Using the fatigue crack growth rate data for the material under simulated service conditions. a critical crack length (a_c). that can lead to the failure of the component is determined. A suitable safety factor is then applied to a_c to determine a safe crack length. (a_s). The number of cycles required to grow these inherent cracks to a_s is then divided by safe inspection intervals (S_i) to monitor the health of the component in the field.

While damage tolerant design approach was being considered for the airframe structures in the 70's, the consequences of a crack propagation in primary structural members of the airframe were also being evaluated and this led to the development of the fail safe design approach. The fail safe design approach requires designing for adequate service life of the overall structure in the presence of damage in the primary members of the structure. The structure is designed in such a way that the presence of cracks in the

primary load bearing part will not lead to catastrophic failure because the secondary members of the structure are capable of bearing the additional load. However, a prime requisite for this approach is that it needs to be shown that the damage can be easily detected during routine inspection in fracture critical locations. Fail safe philosophy was first applied to civil transport aircraft [1].

With the accumulation of over two decades of field experience with DTD, two important factors which are considered critical for the cost effectiveness of a DTD include the reliability of a minimum detectable crack size, a_i, of the NDI technique used in the field and the knowledge of the short crack growth (SCG) behaviour of the structural material. If the size of a_i can be reliably reduced by using sensitive NDI techniques, then S_i can be increased, thus significantly reducing the down times for inspections and improving the cost effectiveness of DTD methodology.

With the advent of sensitive NDI techniques, the detectable crack size may fall within the realm of short, as opposed to long crack regime of the material. Therefore, the second important requirement for the DTD philosophy to be successful would be to have the ability to accurately predict the short crack growth behaviour of the material in order to improve the accuracy of S_i. This would enable the designers to have better capabilities in life prediction of fracture critical components and help in establishing more economic safety inspection intervals.

In meeting the afore-mentioned objectives, there is an ever increasing demand for developing a sensitive NDI technique such that the size of a_i can be significantly reduced. In addition, in certain applications in military aircraft a need for an NDI technique for on-line detection of crack initiation and monitoring of crack growth has always existed for optimising the cost effectiveness of expensive structural repair schemes. Furthermore, with the development of sophisticated modeling approaches to life prediction, there is also a need for NDT techniques that can be used for on-line monitoring of stress/strain history prior to crack initiation in structures, either during service or under simulated service conditions. This will allow the designers to (i) acquire a better understanding of the crack initiation and growth mechanisms under service conditions, (ii) help in obtaining useful data for accurate life prediction and design, (iii) provide insights in designing experiments and modeling approaches that duplicate the real life situations.

Presently, the techniques most commonly employed for studying the short crack behaviour of materials include (a) plastic replica, (b) in-situ scanning electron microscopy, (c) Direct Current Potential Difference (DCPD) and (d) Alternating Current Potential Difference (ACPD) methods. Owing to the laborious and cumbersome nature of the replication technique and the sensitivity limitations of the DCPD technique, the ACPD technique appears more promising. However, a number of glitches need to be worked out in terms of probe design and instrumentation prior to using the technique for

short crack growth work. Some attempts have been made to conduct short crack work with Ti and Ni-base superalloys [3,4] and steels [5] but not on Al alloys because of their low electrical resistivity. On the other hand, the techniques most frequently used for NDI applications in the aerospace industry include (a) visual inspection, (b) eddy current and (c) liquid penetrant methods. None of these NDT techniques are capable of on-line detection and monitoring of cracks on real structures. Attempts have been made to use acoustic emission technique for on-line monitoring of cracks in real structures as well as in specimens in a laboratory environment but with limited success. The ACPD technique has been used as an NDI technique in off-shore steel structures [6] but never in aircraft structures, again because of the low resistivity of the aluminium alloys.

The ACPD technique, therefore appears to be most promising in terms of fulfilling the DTD requirements, provided that the science of probe design can be perfected to obtain repeatable results and the electronics can be made flexible enough to study a wide range of material systems.

1.1 Statement of Work

The importance of the ACPD technique as an NDI method and for generating short crack growth rate data for DTD design methodology prompted the present study. The objectives of the present study are to :

1. Design and develop the ACPD technique such that it can be effectively used for fracture mechanics studies in Al alloys.
2. Obtain crack calibration curves for selected Al-alloys.
3. Evaluate the possibility of measuring strains with the ACPD technique and obtain strain calibration curves.
4. Study the short crack growth behaviour of Al alloys.
5. Install the ACPD sensors on an F/18 aircraft for on-line monitoring of strains and cracks during a full scale test which was being carried out under the aegis of International Follow on Structural Test Program (IFOSTP).
6. Evaluate the possibility of using ACPD as an off-line preventive maintenance scheduling tool for measuring stresses, strains and cracks in fracture critical location of components and structures.

2.0 LITERATURE REVIEW:

2.1 Short Crack Growth

Since the early observations of Pearson [7] about the apparent inconsistent behaviour of fatigue microcracks, a significant amount of effort has been invested in studying the short crack behaviour. Pearson [7], while working on Al alloys found that short crack growth (SCG) rates were abnormally high as compared to long cracks, when the correlating parameter was ΔK. A common conclusion reached by researchers studying SCG is that the short cracks grow differently than long cracks [8-11]. Several reviews and conferences have been dedicated to understand this behaviour [10, 12-17]. The following summarizes the findings and observations found in the literature.

2.1.1 Classification of Short Cracks

Ritchie and Lankford [18] classified short cracks according to the following criteria :

- Microstructurally Short cracks: Cracks that are short compared to the microstructural features, e.g. grain size.
- Mechanically Short cracks: Cracks that are short in comparison with the plastic zone size.

- Physically short cracks: Cracks which are of size less than 0.5-1mm.

2.1.2 Characteristics of Short Cracks

The main characteristics associated with short cracks and observed by various researchers [8-11, 19-27] are schematically summarized by Lankford in fig., 2.1 [28]. These include the following :

- They propagate at stress intensity factor range below the threshold value of long cracks ($\Delta K < \Delta K_{th}$) and the endurance limit.
- They grow faster and more irregularly than long cracks when the correlating parameter is ΔK.
- The above two effects are more pronounced when the fatigue cycling includes compression (stress ratio, $R < 0$).

One of the great advantages of LEFM is its potential for extrapolating from a limited amount of data to predict the structural behaviour under service conditions. Based on the above features of short cracks, long crack threshold (ΔK_{th}) data cannot be used in the analysis of early stages of crack growth, because this leads to an infinite fatigue life at ΔK values below the threshold. Moreover, the LEFM cannot explain the higher crack

growth rate at lower ΔK, the decrease of crack growth rate with increasing ΔK and crack arrest.

Suresh et al [10] and Tanaka [12] provide some explanations for these differences between long and short cracks which are summarized below:

- Break down of continuum mechanics: The basic assumption in LEFM is that the material is isotropic and a continuum. When the crack is within a grain or is comparable to the size of second phase particles, etc., continuum mechanics is no longer applicable.
- Small scale yielding: The LEFM requirement of confined crack tip plasticity is violated. In LEFM, it is assumed that the crack tip plastic zone is much smaller than the crack length. When the crack length is comparable to the plastic zone size, the LEFM is no longer valid.
- Differences in crack extension mechanisms.
- Differences in crack closure effects.
- Differences in local crack tip environment.

In an effort to understand the SCG behaviour and rationalize the anomalies. researchers have concentrated their effort in three different directions as described by Lankford et al.[19].

- LEFM is assumed to be applicable to both LCG and SCG. The small crack data can be fixed by sliding it over to the large crack curve through the adjustment of the crack length. This gives a larger effective length which accounts for the higher fatigue crack growth rates.
- The second line of thinking also assumes LEFM to be applicable. However. crack closure is taken as the source of discrepancy. Here ΔK_{eff} is used as the correlation parameter.
- Short crack behaviour is truly different from the long cracks. LEFM is not applicable. thus requiring other methods to rationalize the SCG behaviour.

2.1.3 Short Crack Dimensions

The main problem encountered by researchers has been to associate the short crack behaviour to a particular crack length range. The transition from short to long crack growth was assumed to be the point at which the LEFM parameter ΔK_{th} is applicable [29]. Kitagawa and Takahashi [29] determined this "transition crack length", as shown in fig. 2.2. to be

$$l \cong 1 / \pi \, [\Delta K_{th} / Y * 0.66 \, \Delta \sigma_{cy}]^2 \qquad (2.1)$$

where ΔK_{th} is the long crack threshold stress intensity factor (SIF), $\Delta \sigma_{cy}$ is the cyclic yield stress at R = -1 and Y is the shape factor for a given specimen and crack geometry. Crack lengths below l are within the SCG regime. However crack growth beyond this length may still exhibit an anomalous fatigue crack growth behaviour indicating that the short crack regime can extend beyond this length [30].

Taylor [31], reported that for LEFM to be applicable to short cracks, the crack length must be greater than ten times the characteristic microstructural dimension (d), such as grain size.

$$l \sim 10 \, d \qquad (2.2)$$

Lankford [32] reviewed many published data and concluded that short cracks behave as long cracks, or the merger of the short cracks and long cracks coincided when the crack tip plastic zone size was equal to the relevant microstructural dimension as shown in fig. 2.3.

Miller et al [30] made the observation that, based on Kitagawa Takahashi diagram in fig. 2.2, it is the long crack data which is a special case in fracture mechanics analysis rather than assuming that short cracks show an anomalous behaviour relative to long cracks.

2.1.4 Factors Affecting Short Crack Growth

2.1.4.1 Microstructure

A number of studies [7, 8, 10, 28, 32-36] conducted on the initiation and growth of short cracks in a wide range of materials have revealed that, when the crack size is comparable to the dominant microstructural feature, the SCG is anomalous, often with a higher and a more irregular FCG as compared to long cracks. The difficulty arises due to the lack of material continuity with respect to the crack. This results in a continuum mechanics limitation since the surrounding material no longer resembles a continuum, but consists of discrete microstructural features. In addition, the LEFM is typically invalid because the requirement for the crack to be much larger than the plastic zone is not fulfilled [10].

The anomalous behaviour associated with the deceleration of the growth rates has been rationalized as a result of crack interaction with the microstructural features, particularly the grain boundaries [10, 37-42]. After crossing the grain boundary, the growth rate increases until the crack front reaches the next grain boundary and the process is repeated [21,43,44]. Retardations in the growth rates have also been observed within the grains and these are explained in terms of the interaction between the crack front and the

submicrostructural features [25], and by crack deflections within the grain caused by variations in slip band orientations [36].

Propagation of a crack occurs when a PSB is formed in the adjacent grain which allows the crack to extend into the grain [9, 21, 45-47]. Since there is an incoherency in the lattice structure across the grain boundary, the activated slip system will have a different orientation thus causing a deflection of the crack [47]. Navarro analytically determined that the activation of the slip system in the neighbouring grain occurs when the stress concentration due to piling up of the dislocations, reaches the critical shear stress in the next grain [48]. The propagation into the neighbouring grain depends upon the orientation of that grain. If it is not favourably oriented, it will be difficult for the slip band to extend. However, if it is favourably oriented, the grain boundary will not significantly inhibit crack extension [19]. The combination of crack arrest and deflection at the grain boundary results in irregular growth and faceted fracture surface which is often associated with the stage I SCG [9,21,45,47,49,50]. As the crack advances, scatter in the data usually decreases indicating that the influence of the microstructural features becomes less pronounced due to large crack tip deformation. Several authors have made this observation and recognized that the first few grain boundaries encountered has the most significant retarding effect on crack propagation [11,49,50].

Zhang et al [45] carried out an interesting study on the evolution of the plastic zone size and shape associated with short cracks and their subsequent effect on further crack growth rates. They observed that the plasticity associated with short cracks has three stages. First, when the crack is small with respect to the grain size, little constraint is provided from the surrounding grains and the crack essentially sees a single crystal environment and therefore the crack has a large portion of stage I growth. This results in a slender plastic zone shape as shown in fig. 2.4a. At this stage, the cracks are predominantly crystallographic in nature. Secondly, after passing through one or two grains, the crack growth changes from stage I to stage II, and the deformation field ahead of the crack tip is governed by a combination of mode I and mode II stress states, causing the plastic zone to be roughly semicircular in shape. Finally, as the crack grows further so that more grains are encountered, the deformation within the plastic zone is constrained by the need to maintain compatibility among the randomly oriented grains, and the crack tip finally acquires a mode I deformation behaviour. This induces the typical plastic zone shape found in long fatigue cracks loaded in mode I as shown in fig. 2.4b. Zhang et al further related the SCG behaviour to the interaction of the plastic zone with the grain boundaries rather than the crack tip. They concluded that the initiation of plasticity in the neighbouring grains is the controlling factor for crack growth. Crack retardation or arrest will only cease when the stress concentration associated with the accumulated strain in the blocked plastic zone is of sufficient magnitude to overcome

the barrier caused by the misorientation of grains and thus activate slip sources in the neighbouring grain.

Decreasing the grain size increases the yield strength and decreases the SCG because of the resulting increase in shear strength [47,48]. A decrease in grain size also causes an increase in the number of grain boundaries per unit volume which results in retarding the stage I SCG. In addition, decreasing the grain size entails that the crack tip plastic zone becomes equal to the grain size sooner, thereby decreasing the amount of stage I growth [47]. There is, however, a trade off with a small grain size because smaller grains have a higher long crack growth (LCG) and creep crack growth (CCG) [51]. The increase in the LCG rates occurs due to a decrease in the closure effects (see section 2.1.4.2 for more details) caused by the higher yield strength. A higher yield strength will reduce the amount of plastic deformation at the crack tip, thereby reducing the residual plastic wake. This results in an increase in the ΔK_{eff}, thus increasing the LCG [20,47]. The increase in the CCG is due to the large amount of grain boundary area associated with a smaller grain size.

2.1.4.2 Crack Closure Effect

Ever since Elber's observations [52], fatigue crack closure has been recognized as an important factor in controlling the long crack growth behaviour. Crack closure is caused

by the crack faces contacting before the crack opening load drops to zero. Henceforth, there is a minimum stress required for the crack to be opened, σ_{op}. This entails that crack growth is driven by an effective alternating SIF, ΔK_{eff} given by,

$$\Delta K_{eff} = K_{max} - K_{op} \tag{2.3}$$

where K_{max} is the SIF corresponding to the maximum stress and K_{op} is the SIF corresponding to the stress required to open the crack.

Three principal mechanisms have been proposed to explain the crack closure phenomenon namely (i) plasticity induced closure, (ii) oxide induced closure and (iii) roughness induced closure. In plasticity induced closure, crack closure is caused by the plastic wake created by the plasticity at the crack tip [52]. The deformation at the crack tip causes a permanent expansion of the material within the crack tip plastic zone. As the crack grows through this region there is mating of the expanded material on both faces left behind the crack tip. Thus a contact between the two opposite faces of the crack takes place under a tensile load.

Oxide induced closure is caused by the presence of corrosion debris in the wake of the crack [10]. Finally, roughness induced closure [10] is caused by the faceted fracture surfaces contacting at discrete points. All three mechanisms are illustrated in fig. 2.5 In all cases the contact of the fracture surfaces in the crack wake is responsible for crack closure.

Crack closure has been one of the most commonly used arguments for rationalizing the anomalously high SCG rates [10, 53-55]. Short cracks are considered to have short wakes compared to long cracks and as a result the amount of crack closure is expected to be smaller for short cracks. This results in a higher ΔK_{eff} for short cracks and thus higher FCG rates [10.12]. A newly initiated crack is not expected to experience plasticity induced closure because it has not grown into its residual plastic wake. Blom et al [21] found that closure effects did not prevail until the crack length reaches a size just under the transition length from stage I to stage II. The slender plastic zone shape, as observed by Zhang et al [45] during stage I growth, shows that only a small amount of material at the crack tip experiences plastic deformation thereby producing only a very small plastic wake. Therefore, compensating for the crack closure, as is usually carried-out with LCG, may account for the anomalously high crack growth rates associated with short cracks [9.10].

Evidence showing that the extent of crack closure varies as a function of crack size has been reported by James and Morris [56] for the growth of short cracks in titanium alloys. They monitored the crack tip opening displacement (CTOD) at zero load for cracks ranging in length from 50 to 500 μm and concluded that in cracks less than approximately 160 μm, the extent of crack closure (particularly that induced by roughness) decreased with decreasing crack length. Newman [57] analytically examined crack initiation at defects and observed that, initially, the low opening stresses give rise

to high effective stress ranges and consequently high crack growth rates. However, as the cracks grow longer, the crack opening stress rises much more rapidly than the SIF, thus causing a reduction in the effective stress range. Eventually, the crack opening stress levels-off with increasing crack length. This provides an additional explanation (besides interaction with microstructural features), that the SCG may decrease to a minimum and then accelerate again or even arrest.

Newman also observed that closure varies with the plastic deformation at the crack tip [57]. As the closure effect increases, ΔK_{eff} decreases, thus decreasing the cyclic plastic zone size (ω). The fully reversed plastic zone corrected for closure effects, is given by,

$$\omega = (1 - \sigma_{op} / \sigma_{max})^2 \rho/4 \qquad (2.4)$$

where ρ is the monotonic plastic zone size calculated using the maximum applied stress, σ_{op} is the stress at which the crack is open and σ_{max} is the stress at maximum load. Equation 2.4 shows that as the closure effects increase, σ_{op} increases, thus resulting in a reduction in the crack tip plastic zone size.

Although closure effects provide one important explanation for the anomalous short crack behaviour, it is not the only factor affecting short crack growth. Lankford et al [19] observed in Al 7075 T6 alloy that compensating for closure effects still did not result in a good agreement between the SCG and the LCG. They found that the opening

load was a constant fraction of the maximum load and hence independent of crack length, at least for crack lengths between 35 to 200 μm.

2.1.4.3 Stress Intensity Range and Stress Ratio Effect

Newman et al [27] observed that the growth of short cracks is strongly dependent on the loading path and stress level. They found that the growth rate differences between short and long cracks at the same stress intensity factor range were more pronounced for loading paths which include compressive loading. On the other hand, the short crack growth behaviour in tests with only positive loads was nearly the same as for long cracks. Lee et al [58] observed that short cracks grow faster than long cracks for negative R ratios and grow slower for R = 0.5. At R = 0, both short and long cracks are found to grow at about the same rates. This is consistent with the observations of Obabueiki et al [59] who reported that dips in SCG rate faded with increasing stress range and virtually faded completely at higher stress range values. At the root of the notches, the SCG behaviour was found to display the similar trends as the microstructurally short cracks when either R or ΔK was varied with the scatter of results being less [60-64]. In addition, the short cracks initiating from notches and exhibiting a well (dip) in their crack growth rates, did not show this characteristic when either the R ratio or the stress range was increased [60-64].

2.1.4.4 Environmental Effects

The magnitude of the environmental effect depends upon the severity of the environmental interaction at the crack tip. Corrosion and oxidation can introduce crack closure and thus may introduce a wide range of effects on the short and long cracks [10. 64-67]. When the faces are in contact (touching). interaction with the external environment is reduced. thus reducing its effect on the FCG. In general. environmental effects are higher for short cracks due to lesser closure effects compared to long cracks [10]. Chemical and electrochemical effects are also known to increase the growth rates of short cracks [68]. This interaction is affected by the distance from the crack tip to the external environment. i.e. the crack depth [68]. Crack tip interactions with the environment decrease as the crack tip moves away from the surface of the specimen. since it is usually more difficult for the environment to reach the crack tip [10].

2.1.4.5 Notch Root Effects

The notch root plasticity has been found to increase the SCG. Frost [69] observed. in mild steel V notched specimens at R = -1. that cracks could initiate below the fatigue limit and afterwards stop permanently if the notch root radii was small enough. Broek [70] reported faster crack propagation rates with increasing notch root radii when compared to the same ΔK or crack length. Smith and Miller [71] also concluded that the

localized plastic deformation at the root of the notch can be significant enough to initiate a crack. However, the crack will only continue to grow after leaving the notch plastic zone if the crack tip plastic field is large enough to drive the crack [71]. Therefore a crack can initiate at the root of a sharp notch under far-field stress, although it may probably not be able to grow after leaving the stress field of the notch due to insufficient crack tip plastic deformation. The minimum alternating stress range required for crack initiation at a notch is given by [71].

$$\sigma_{min} = \sigma_e / K_f \qquad (2.5)$$

where σ_e is the fatigue limit (R = -1) and K_f is the fatigue concentration factor given by

$$K_f = [\, 1 + 7.69\, (D/\rho)^{0.5}]^{0.5} \qquad (2.6)$$

where D is the notch depth and ρ is the notch root radius [71].

Dai [72] observed abnormally high growth rates during stage II growth and concluded that the effects were due to the notch stress field. The higher growth rates within the notch plastic field is due to the large plastic strain range within this region. This strain range rapidly drops off as the crack passes through the notch plastic zone and this results in a rapid decrease of the SCG rates. After having passed through the stress field of the notch, further propagation of the crack is dependent upon the crack tip plasticity [71]. Smith and Miller [71] defined the minimum nominal stress required for a crack to initiate and propagate until failure at small notches under fully reversed loading as.

$$\Delta\sigma = 0.5\, \Delta K_{th} / \sqrt{D} \qquad (2.7)$$

where ΔK_{th} is the long crack threshold stress intensity factor and D is the depth of the notch.

2.2 Short Crack Measurement Techniques

The commonly used short crack measurement techniques are.

1. Plastic replication
2. In-situ scanning electron microscopy
3. Electrical Potential difference techniques
    - Direct Current Potential Difference (DCPD)
    - Alternating Current Potential Difference (ACPD)

2.2.1 Replication Techniques

Replication techniques are widely used for studying short crack growth characteristics of the materials during fatigue testing [27,73]. Among the available replication techniques the plastic replica is most widely used. It involves softening of a plastic film in a solvent, application of this soft film on to the surface, and then allowing it to harden as the solvent evaporates. After careful removal of the replica from the surface, the resulting plastic film contains a negative image (or replica) of the surface that can be examined using an optical microscope, a scanning electron microscope (SEM) or a

transmission electron microscope (TEM) depending on the resolution required. For improved resolution, the back side of the replica can be painted with any fast drying black paint or ink prior to removal, or an evaporated coating of carbon or Au-Pd can be applied after the removal. The details of the replication technique can be found in the Metals HandBook [74]. The plastic replica technique has a high resolution, but it is very labour intensive and the testing needs to be interrupted each time a measurement (replica) is required.

2.2.2 In-situ Microscopy

In-situ analyses of fatigue crack propagation in a scanning electron microscope enables a detailed observation of the fatigue process. With the in situ microscopy, the specimen and its loading attachments are fit inside the SEM chamber such that the fatigue testing is carried-out inside the SEM. In-situ SEM investigations enable a cycle by cycle observation of the crack propagation. An example of the type of investigation that can be carried-out with in-situ microscopy can be found in the work carried out by Zhang et al [45.]. The technique has been used to study the effect of variable amplitude loading on the acceleration and deceleration of cracks, crack closure etc. [75].

In situ SEM is restrictive because the specimen size and loading attachments must be small enough to fit inside an SEM. The tests are always performed in vacuum and this

may not be representative of the real life conditions. Furthermore, the technique can only monitor the near surface cracks.

2.2.3 Electrical Potential Difference Techniques

Electrical potential difference techniques have been used effectively for measurement of short crack growth. In its simplest form, it involves passing a constant current through the test piece and measuring the potential across two points where potential probes are attached. Due to the presence of a crack, there is an increase in the path length of the current flow. This, in turn, results in an increase in the electrical resistivity (ρ) and therefore an increase in potential difference. The potential difference techniques have many advantages, most notable among them are (i) continuous monitoring of the crack length without interruptions and (ii) no requirement for visual accessibility.

2.2.3.1 DCPD Technique

In DCPD, a direct current is injected into the specimen. The current is distributed uniformly in the specimen (volume). Since the current flows uniformly throughout the specimen volume, the amount of current required depends on the size and resistivity of the specimen. Currents up to 100 amperes have been used [76]. High DC currents can result in specimen heating. High currents require high capacity power amplifiers and

therefore heavy equipment. Additionally, DCPD also suffers from the problems of thermo-electric emf which can be of the same magnitude as of the DC signals [77]. On the other hand, the technique is simple to use and the electronics is also fairly simple. The many disadvantages of DCPD have been recently eliminated in part by using the pulsed DC measurement method [77].

DCPD has been used for monitoring short crack growth in steels and superalloys [78-81]. Donald et al [82] have illustrated the magnitude of voltages measured on a standard specimen type (CT) samples having a width of 50 mm, thickness of 7.67 mm and a crack length of 11 mm for a direct current of 10 amperes. For Al alloys, the potential difference measured was 0.1 mV, where as for steel and titanium the potential difference was 0.6 mV and 3.5 mV respectively. It was also shown that 0.1 μV change was observed for a crack extension of 0.66 mm in Al alloys, 0.11 mm for steel and 0.022 mm for titanium. Burgers et al [83] observed that the sensitivity of DCPD to crack extension also depends on the initial crack length. For a crack 1 mm in length, a crack extension of 0.4 mm may be resolved, whereas for a crack of 30 mm, a crack extension of 0.013 mm may be resolved.

In the case of the DCPD, the specimen volume is very important. This is one of the governing factors in determining the sensitivity of the system. Therefore, the DCPD

technique is mostly used on pre-cracked (EDM) small specimens and the problem is in fact reduced to measuring crack growth rates as accurately as possible.

2.2.3.2 ACPD Technique

ACPD has generated considerable interest since the DTD methodology came into existence. With the ACPD, an alternating current (AC) is injected into the specimen and the resulting potential difference is measured across two points on the surface. The current distributes uniformly at the surface, but is confined to a narrow region in the thickness direction [84]. This effect is known as skin effect which will be discussed later in section 3.1. This effect results in an increased sensitivity in detecting surface cracks because of the presence of higher current densities compared to DCPD. The sensitivity can be increased by increasing the current frequency since this results in an enhanced skin effect. In ACPD, small currents, from 200 mA to 1 amperes are usually sufficient. Therefore, the ACPD has two distinct advantages over DCPD. First, the specimen thickness is not important and therefore large coupons can be used. Secondly, small amounts of currents are injected, therefore specimen heating is not a problem. Moreover, ACPD is not affected by the thermal emf as in the case of DCPD.

Since the current is concentrated near the surface of the material when passing the high frequency AC, the measurements are more sensitive to surface cracks. As a result, the

technique can be used to study naturally initiated fatigue cracks. This removes the requirements of pre cracking the specimen and the knowledge of the origin of the crack need not be known in advance. Comparative schematics of the current configuration around a crack (short and long) for the DCPD and the ACPD techniques are shown in fig. 2.6 [5].

Increasing the frequency, leads to an increase in sensitivity, but there is a drawback in increasing the frequency. Since, AC currents are used, there is a magnetic field associated with them. The probes used for the measurement of the potentials can be affected by the induced magnetic field caused by the high frequency AC. Thus, the probes are measuring both the surface voltage and an induced voltage. Veropest et al [5] used a 40 kHz current frequency and reported the detection of surface micro-cracks of 0.0066 mm^2 area in steel wires, but recommended the use of 10 kHz frequency for accurate and reproducible crack growth measurements. They showed that by increasing the frequency, the induction effect becomes stronger. In another publication, Veropest et al [85] recommended the use of 5 kHz current frequency for obtaining reproducible results. They demonstrated the effect of the probe configuration (loop) on the signal as shown in the fig. 2.7.

Charlesworth et al [86] reported that the pick up voltage is directly proportional to the AC frequency, whereas the ACPD readings are proportional to the square root of the

frequency. They also reported that the percentage error due to a pick-up loop made by the potential sensing wires is much higher in the case of non magnetic materials than in ferromagnetic materials. They suggested that to reduce the pick-up. the pick-up loop should be minimized by twisting the cables tightly. Charlesworth et al [86] also showed all the possible arrangements of injecting current into the specimen as shown in fig. 2.8. They considered the arrangement shown in fig. 2.8 c to be ideal one but not practically possible. As a result. the arrangement shown in fig 2.8 d was suggested to be the best practical arrangement physically possible. They concluded that the two most important sources of errors are probe design and the AC field uniformity. Dover et al [87] reported that a frequency of 5 kHz and a current of 2 amperes produced good reproducible results in a wide range of materials.

Watt [88] used the ACPD technique in a wide range of titanium alloys. He applied the technique to monitor crack propagation in single edge notch (SEN) and CT specimens. He also applied the technique for crack detection in small SEN specimens and during fatigue testing of T butt welds. He used his ACPD system up to 8 kHz frequency and reported that lead interaction problems were exacerbated at higher frequencies (10 kHz and above).

Phase sensitive detection (PSD) is a common feature in many ACPD systems [5]. PSD allows the tracking and detection of one particular frequency embedded in a signal

composed of different frequencies. The ACPD signal is at 45° to the phase of the current [86]. A PSD circuitry can detect and measure a very small ACPD signal which is embedded in a lot of unwanted induced signals. It is the PSD that has made the ACPD technique a powerful tool for crack detection and crack growth measurement.

Another important advantage of ACPD over DCPD. has been the "claimed" enhanced linearity of the ACPD signal with crack depth. Charlesworth and Dover [86]. Dai et al [89]. Jablonski [90] and Watt [88] have reported a linear relationship with crack depth. On the other hand. Hwang and Ballinger [3] and Lu et al [91] reported a second order polynomial and power law relation ship respectively as a function of crack depth.

Hwang and Ballinger [3] used an ACPD system which was capable of generating a current at a frequency of up to 230 kHz. However. their experiments were conducted at a frequency of up to 203 kHz. They reported a sensitivity of 50 μm for multiple crack initiation using a probe spacing of 10 mm in a Ni base superalloy. For single crack initiation. they observed a decrease in sensitivity. To achieve the same sensitivity of 50 μm crack depth. the probe spacing was reduced to 1.2 mm. They also observed that long term signal stability is achieved if (i) rigid probe attachments are used. (ii) the signal is pre-amplified close to the specimen and (iii) adequate lead grounding and shielding are employed. They concluded that ACPD is more suitable for constant load than for

dynamic loading. They observed that the problem of induced signal in the probe wires becomes more important above 100 kHz current frequency.

Marchand et al [92] used an ACPD system to study thermal fatigue crack initiation and growth in Ni base superalloy in the temperature range of 400 - 1000° C. They reported the detection of microcracks of the order of about 10-20 μm in length and the measurement of crack growth rates lower than 1μm / cycle. They used 30 kHz current frequency and 1.2 amperes current. Dai et al [4,89] used the ACPD technique effectively for on-line monitoring of crack initiation and growth during thermal mechanical fatigue testing. The resolution for crack detection at the root of the notch of a single-edge notch (SEN) specimen test geometry was reported to be 50 μm with 95% confidence, while the resolution for crack growth was reported as being 2 μm / mV change of ACPD. They also reported the ACPD signal changing during load cycling as a result of straining and crack opening / closing. They used a one ampere current at a frequency of 30 kHz.

Gendron et al [93,94] used the technique successfully for on-line crack initiation and crack growth measurements in coated and uncoated blades of Ni-based superalloys during thermal fatigue experiments carried out in a high velocity burner rig. The maximum temperature of the flame was around 1323° C and gas velocity was around Mach 0.4. The resolution of the ACPD technique to crack detection (at the leading and

trailing edges) was reported to be 125 μm under the harsh testing conditions of the experiments.

Fuleki [95] used the technique to detect naturally initiated fatigue cracks in double edge notch specimen in Ni based superalloys. The maximum temperature used was 480° C. He reported the capability of detecting and sizing cracks in the range of 200 μm in depth. He also utilized the current focusing technique (which will be discussed later) to focus the current at the notch root.

Jablonski [90] used the ACPD system for the measurement of multiple site cracking in simulated aircraft panels (Alclad 2024). He determined the relationships of current frequencies (3, 10 and 30 kHz) with the crack lengths. He observed that the sensitivity to crack length increased with increasing frequencies. He also used the current focusing technique which allowed him to concentrate the current at the area of interest thereby increasing sensitivity to crack detection. He reported that, an increase in potential was always observed long before the cracks were visually detected.

Charlesworth and Dover [86] used their system for crack measurement under water with no modifications. The testing was carried-out on a tubular welded T-joint in which a fatigue crack was introduced. The measurements were carried-out both in air and water. They reported a negligible difference in the measurements in both cases. Hwang and

Ballinger [3] also performed measurements in water at high temperatures up to 350° C under both static and dynamic loading. The AC currents used ranged between 1 to 1.4 amperes with frequencies between 17 to 203 kHz. They found the ACPD technique to be compatible with aggressive environments.

Watt [88] also compared the ACPD and DCPD techniques and summarized their advantages and disadvantages as follows:

Advantages of ACPD technique

- Ease of calibration for differing specimen geometries.
- Inherently linear response.
- Lack of coupon size dependence of the method.
- Ease of amplification of input signal.
- Multiple P.D. probe systems can be used.

Disadvantages of ACPD technique

- Reliance on advanced electronics.
- Lead interaction.
- Requirement for high stability in electronics.

Advantages of DCPD

- Simple technique does not rely on advanced electronics.
- Well established techniques for certain specimen sizes and geometries.

Disadvantages of DCPD

- Complex relationship between P.D. and crack length.
- Thermal emf effects.

Dover et al [6] were the first to use the ACPD as a NDI tool on off-shore structural components. The equipment used was limited to a maximum frequency of 6 kHz and 1 ampere current. They reported that the system was capable of measuring cracks of any size. However, no data or results were presented. They also described another low frequency (50 Hz), instrument for NDI application of off-shore structures. The smallest crack size that could be detected with the unit was reported to be 25 mm in length. Watt [88] has also reported using the ACPD as a NDI tool for a wide range of items of various complexities including large structural items. However, no results pertaining to its performance were reported.

2.3 NDI Techniques used for Airframe Structures

The commonly used NDI techniques for airframe structures are

(a) Eddy current

(b) Liquid penetration

(c) Visual inspection

(d) Acoustic emission

2.3.1 Eddy Current Inspection Technique

Eddy current is the most popular and common NDI technique utilized by the aerospace industry. It is based on the principle of electromagnetic induction. The part (or component) to be inspected is placed within or adjacent to an electrical coil in which an alternating current is passed. The current flowing in the coil is called an exciting current. This current generates a magnetic field which causes eddy currents to flow in the part as a result of the electromagnetic induction. The electromagnetic field in the region depends on both the exciting current from the coil and the resulting magnetic field due to the eddy current flowing in the part. The flow of eddy currents in the part is disturbed due to the presence of a crack. This, in turn, changes the corresponding magnetic field (the one produced by the eddy currents) which is monitored by observing the induced voltages in the pick-up coil placed within the field. The inspection frequencies used in

eddy currents range from 200 Hz to 6 MHz [96]. By varying the frequency, the depth at which eddy currents flow in the material can be varied. This effect is also known as the skin effect. The details of the technique and the instruments utilized for eddy current measurements can be obtained from the reference [96].

Hagemaier [97] has carried-out an extensive study on the application of eddy current to crack detection in airframe structures. He reported that the 90% probability of detection (POD) was achieved at 1.78 mm and 3.55 mm crack length with two different types of eddy current instruments used in the program. The cracks were artificially introduced EDM notches on Al specimens.

Bellinger et al [98] carried-out a study to characterize the sensitivity and reliability of several NDI techniques in detecting low cycle fatigue (LCF) cracks in bolt holes of J85-Can 40 fifth stage compressor discs. The crack lengths detected by eddy current at 90% Probability of Detection (POD) and 95% confidence limit were 1.65 mm and 4.1 mm respectively.

2.3.2 Liquid Penetrant Inspection Technique (LPI)

Liquid penetration inspection is a method for revealing discontinuities that are open to the surfaces of solid and essentially non porous materials. LPI depends mainly on a

penetrant's effective wetting of the specimen surface. flowing over that surface to form a continuous and reasonably uniform coating and then migrating into cavities that are open to the surface. The process is well suited to the detection of all types of surface cracks [99]. In practice. the process is simple to utilize and control. This technique essentially requires five steps. The surface is thoroughly cleaned and dried. The penetrant. which is usually fluorescent or visible is then applied to the specimen. After the application of the penetrant. the excess penetrant is removed. Uniform removal of the excess penetrant is necessary for effective inspection. A developer is then applied over the surface. This forms a film and acts as a blotter to assist the natural seepage of the penetrant out of the surface openings (spread out at the edges of the cracks) as to enhance the penetrant inspection. The surface is then visually examined for indications of penetrant bleed back from the surface openings. Visible penetrant is examined using the white light while the fluorescence penetrant is examined in dark area using ultraviolet light.

The technique is simple and it can be used to inspect a wide variety of materials and varying geometries. The main disadvantages of the technique are that it cannot be used for subsurface flaws. It requires extensive surface preparation and is time consuming. Haigemair [97] compared the results for both the eddy current and the LPI. The results are shown in the fig. 2.9. LPI technique is used extensively in aircraft maintenance for

crack detection and more often to confirm the presence of a crack detected by other techniques.

2.3.3 Visual Inspection

Visual inspection is still the most widely and frequently used NDI technique in the aerospace industry. The inspection is simple and easy and no surface preparations are required. The main disadvantages are that the subsurface flaws cannot be detected. the resolution is very poor and is manpower dependent.

2.3.4 Acoustic Emission Inspection Technique

The acoustic emission technique relies on stress waves produced by sudden changes or movements in stressed materials. Sudden changes or movements such as crack growth or plastic deformation. act as stress wave sources. The stress waves radiate out into the structure and can be sensed by a sensitive piezo-electric transducer. The piezo-electric transducer delivers an electric signal proportional to the stress wave to a nearby pre-amplifier and then to the main signal processing unit. The common range of operation is 100 kHz to 2 MHz [100]. As the stress imposed on the material increases. many sources of stress waves (emissions) are activated. The signals captured by one or more sensors are amplified and measured. The source of the acoustic energy is a disturbance in the

elastic stress field and hence without stress there will be no emission. An acoustic emission inspection can therefore be only carried out when the specimen or the structure is under load. As such. the acoustic emission technique can be used for on-line measurement.

The main differences between the acoustic emission and the other NDI methods are (i) the signal has its origin in the material itself and not in an external source: (ii) the acoustic emission detects movements while other techniques detect existing geometrical discontinuities [101.102]. A major benefit of the acoustic emission method is that it allows the whole volume of the structure to be inspected in a single loading operation: the only requirement being that a suitable number of fixed sensors. typically placed four to twenty feet apart. must be used. The main disadvantages of the technique are (i) the technique is very sensitive to noise. Many external sources of acoustic emissions with no relation to cracking or plastic deformation (e.g. rivets) can mask the overall signal measured by the transducers: (ii) the structure/specimen must be under stress.

3. ALTERNATING CURRENT POTENTIAL DIFFERENCE (ACPD) TECHNIQUE : PROBE DESIGN AND DEVELOPMENT

3.1 Introduction

The potential difference (PD) technique makes use of an increase in electrical resistance in conducting materials due to stress/strain and cracking. Typically an AC current injected in the solid flows as shown in fig. 3.1a. The current distributes itself in the shape of a balloon in the XY plane and is confined to a narrow layer in the XZ plane [87]. The potential readings taken across AA' are of the same magnitude because they are measured between two equipotential lines as shown in fig. 3.1a. In the XZ plane, the narrow region (or the depth) where the current is confined is called the skin depth, δ, and is governed by the following equation [84]:

$$\delta = \sqrt{\rho / \pi \mu_r \mu_o f} \qquad (3.1)$$

where

ρ = resistivity (ohm-meter),

μ_r = relative permeability,

μ_o = permeability of vacuum ($4.\pi.10^{-7}$ H/meter),

f = frequency of AC current (Hz).

Equation (1) indicates that, for a given material, the skin depth is inversely proportional to the square root of the frequency of the applied current. Therefore, if we increase the frequency of the applied current, the skin depth decreases. This in turn means that the current density distribution near the surface increases, leading to a higher sensitivity to surface breaking cracks and strain or stress (applied or residual). In the case of 7075 Al alloy in T651 condition, the skin depth, δ is estimated to be around 3.6 mm for a 1 kHz current frequency and about 0.235 mm for a 240 kHz current frequency. That is why there is always a need for high frequency electronics to maximize the advantages of ACPD.

The theoretical distribution of current density below the surface in the YZ plane is shown in fig. 3.1b. The current density distribution within the skin depth, δ and beyond is not uniform but decreases exponentially and approaches an asymptotic value of 0.0025 of the surface value (J_0) at a distance of 6 δ [84]. In fact, the skin depth refers to the distance from the surface where the current density has reduced to 36.86% [96] of the surface value. It is due to this skin effect that the sensitivity to crack sizing is not affected by the material thickness, so long as the material or component is thicker than 6 times the δ value.

Figure 3.2 shows the change in the flow of the current when the crack is present in the solid [87]. As is evident, the current has to follow the crack faces, which results in an

increase in the path length of current traveling from point I to point O. The increase in path length results in an increase in the resistance and hence in an increase in the potential difference measured across points AA'. This difference in the potential occurs due to the presence of a crack and therefore, the change in potential can be related to the crack depth. As a result, ACPD can be used to quantify cracks.

Since the current is confined to a narrow region (skin effect), much smaller amounts of currents are required, as compared to DCPD methods, in order to have the same current density distribution (J_0) near the surface. In order to have the same current density at the surface for the ACPD or DCPD the following relationship must be observed.

$$I_{AC} / \delta = I_{DC} / T \qquad (3.2)$$

where I_{AC} = amplitude of the AC current,

δ = skin depth,

I_{DC} = amplitude of the DC current, and

T = thickness of the material

For a 10 mm thick Al alloy specimen, to achieve the same current density as that produced by 30 kHz current frequency and 1 amp. AC current, a DC current of 15 amps has to be supplied. If the frequency is increased to 240 kHz, a DC current of 43 amperes must be supplied, to achieve the same current density distribution as 1 amp. AC. Therefore, one advantage of ACPD technique is that, by simply increasing the frequency

of current injected in the solid a much higher current density distribution can easily be achieved.

Now, if the specimen thickness is increased from 10 mm to 30 mm, and in order to have the same surface current density as that achieved by injecting an AC current of 1 amps. at 240 kHz frequency in 10 mm thick specimen, the AC current to be supplied does not change because the skin depth is the same. However, a DC current of 127 amperes has to be injected to achieve the same current density as that produced by 1 amp., 240 kHz AC current. This results in another significant advantage of the ACPD technique, i.e., the sensitivity of the ACPD in detecting surface cracks or other near surface phenomenon is not affected by the thickness of the specimen so long as the specimen or the component is thicker than 6 δ.

The DCPD technique on the other hand requires much higher currents [76]. Such high currents are difficult to handle, the current cables are difficult to attach to the components and can create serious specimen heating problems. Thus, it is very difficult to measure strain and short cracks with the DCPD technique in low resistivity materials such as Al alloys. The resistivity of the Al alloys (7000 series) is in the range of 50 nano-ohm meter [103]. In the ACPD technique, however, depending upon the requirements, very small currents ranging from 500 mA to 5 amperes can be

successfully used to measure short cracks, stresses and strains in steels, superalloys and low resistive materials.

3.2 Current Focusing and its Relevance to Probe Design

Although the sensitivity of the ACPD technique is not affected by the thickness of the specimen or component, the distribution of the AC current in the XY plane (see fig. 3.1a) indicates that it is affected by the surface area of the material. The higher the surface area of the plane XY, the lower will be the current density distribution, since the same amount of current is flowing in a larger area. This results in a lower sensitivity to the detection of cracks and stresses (strains). A novel technology, named current focusing has been developed to overcome this problem [104]. With the help of this technique, the current distribution can be confined to a narrow region rather than being spread over the entire surface area.

Current focusing technique is based on the premise that when a conductor carrying an AC current is placed near the return conductor (e.g., a specimen surface), then the distribution of the AC current in the return conductor is confined and tends to be a mirror image of the current flowing in the upper conductor. This phenomenon can be explained by the fact that a high frequency AC flowing in a conductor generates an electro magnetic field (emf) and this emf impinges on the specimen surface, (which acts

as a return conductor, placed directly below the conductor carrying the AC) and making the electrons in the specimen surface to flow backward and forward [104]. This motion of electrons results in induced circulating currents in the specimen. The resulting emf generated by the induced currents tends to block the emf (created by the AC conductor) from penetrating inside the specimen and from spreading laterally. The act of blocking the penetration inside the specimen results in skin depth control.

The prevention of the lateral spread of the emf created by the AC conductor due to the emf created by the induced currents results in a confined magnetic field. Thus, the magnetic field is confined between the conductor carrying the AC and the specimen, acting as a return conductor. This results in a strong magnetic field between the conductor and the part of the specimen below the conductor. The current injected in the specimen therefore flows where the magnetic field is stronger. This prevents the uniform lateral spread (balloon shape shown in fig. 3.1a) of the injected current in the specimen and results in the current focusing effect.

The current can therefore, be constrained or focused in a region of the specimen near the conductor, and the effect can be maximized by bringing the conductor (which from now on will be called the current focusing device) as close to the surface as possible. This implies that the potential measurements across AA' as shown in fig. 3.1a are no longer the same. This occurs due to the modified current distribution which, instead of being

spread out as a balloon shape, is now focused below the current focusing device leading to an increased sensitivity to cracks, straining etc.

The modified current distribution in the return conductor (the specimen) is shown in fig. 3.3a. A cross sectional view of the current focusing effect is shown in the fig. 3.3b. An experiment was carried out to quantify the current focusing effect in 7075 T651 material. A current focusing device was installed on the Al alloy specimen as shown in fig 3.4a. The current focusing device consisted of a copper tape 3.175 mm in width and 0.05 mm in thickness. The copper tape was electrically insulated from the specimen and glued as close to the surface as possible ($\leq$ 0.1mm). Measurements of the potential at various current frequencies (30, 60, 90, 120, 150, 180, 210 and 240 kHz) were carried out near one of the edges (AA' in fig. 3.4a) of the current focusing device and away from the device in one mm steps. The results are shown in fig. 3.4b. Note that the potential drops when the measurements are taken farther away from the focusing device. The potential would have been the same at all points without the current focusing device. (see fig. 3.1a). Thus, the frequency control of the AC current combined with the current focusing technique allows one to have a three dimensional control of the current density distribution in a solid.

The current focusing principle indicates that stronger the magnetic field, stronger is the current focusing effect. However, the potential drops to one third of the maximum value

(measured near the edge, AA' of the focusing device) around ten mm away from the edge of the Cu tape at all the frequencies investigated, i.e. between 30 kHz to 240 kHz. The only logical explanation for this effect lies in the fact that the optimum advantages of the focusing effect are governed by the way the current focusing device and the ACPD probes are laid on the specimen.

The current focusing effect also depends on the height of the device from the return conductor, which is the specimen in this case. A set of experiments was conducted in which the height of the focusing device was altered. The previous results were obtained for conditions where the current focusing device was kept as close to the specimen surface as was physically possible ($\leq$ 0.1mm). Figures 3.5a-3.5c show the results of this set of experiments where the height of the focusing device was changed to 0.9, 3, and 9.3 mm from the surface of the specimen. There was no significant difference in the focusing effect when the device was kept at a height of 0.9 mm. This suggests that even when the focusing device is 0.9 mm away from the specimen surface the magnetic field was strong enough to obtain the optimum focusing effect. When the focusing device was located 3 mm above the specimen surface, the focusing effect started to decay, but was still significant. When the focusing device was placed 9.3 mm above the surface of the specimen, the values had dropped to one half at 10 mm away with respect to the potential difference measurements obtained near the edge of the focusing device. Note that in the previous two cases, i.e. close to the surface and at 0.9 mm height from the

specimen surface, the readings had dropped to one third of the edge values at 10 mm away (see fig. 3.4b. fig. 3.5a).

The ACPD values were observed to increase with an increase in the height of the focusing device from the specimen surface. This may be attributed to the fact that the magnetic field between the device and the specimen surface is not confined to the same extent as in the case where the focusing device lies close to the specimen surface. However, the confinement of the magnetic field was sufficient to have led to same focusing effect even when the conductor lies 0.9 mm away from the specimen surface. The radiated magnetic field is picked up by the potential probes which leads to an increase in the ACPD values. These results do nevertheless indicate that the magnetic field remains confined between the focusing device and the specimen when they are held close to one another.

From the experiments involving the variation of the height of the focusing device from the specimen surface, the following conclusions can be drawn for 7075 Al alloy in T651 condition. Firstly, the current focusing effect remains the same (for the above mentioned setup) when the height of the focusing device varies from close to the surface of the specimen to at least up to 0.9 mm from the specimen surface. Secondly, a higher ACPD signal does not necessarily mean that the probe layout is any better. Thirdly, and perhaps most importantly, the difference in potential due to the presence of a crack should

always be expressed in absolute values rather than in percentages relative to the base values. This is because a crack (e.g. 0.5 mm) will induce the same change in ACPD. when the focusing device is close to the specimen or at a height of 0.9 mm. since the focusing effect is similar in both cases (see figs. 3.4b and 3.5b). However. the initial value. observed was relatively lower in the first case when the current focusing device was held close to the specimen surface (fig. 3.4b) than at a height of 0.9 mm (fig. 3.5b). Therefore. the percentage change due to the same crack will be much lower when the current focusing device lies at a height of 0.9 mm from the specimen surface. Thus. if the data is analyzed or reported in terms of percentage changes. the results become dependent on the probe design or the conditions of the probe lay out.

The optimum design in terms of current focusing also implies. that scanning the current frequencies does not change the current focusing effect (see fig. 3.4b). which is an added advantage of the focusing device. Since. scanning the current frequencies does not change the current focusing effect. the calibration curves are not affected. A change in the amplitude of the signal would only occur due to the variation in the skin effect caused by the change in frequency. This change can be easily quantified and taken into account through equation 3.1.

The above results so far provide reasonable evidence that a complete three dimensional control of the current density distribution can be achieved. The skin effect and the

current focusing technique allow one to make the ACPD technique completely independent of the specimen thickness (so long as the thickness is greater than 6 δ) and specimen area. As a result, the current can be focused at critical areas in a specimen or in a structure without losing the sensitivity. Since the current can be forced to flow through smaller areas as desired, the probe design is greatly simplified and made flexible. Taking into account the complicated geometries encountered in real life structures, e.g. holes, notches, sharp or smooth bends etc., the current can be focused exactly in the area of interest without sacrificing the sensitivity of the technique.

3.3 ACPD Electronics

The ACPD electronic equipment used in this program are (i) CGM-5 (Crack Growth Monitor -5, a Trade mark of Matelect Ltd in U.K.), (ii) CGM-6 (a prototype developed for the IFOST Program of DND, Canada) and (iii) CGM 6-3 (final version of CGM-6). The CGM 6-3 is an advanced two channel ACPD system. A simplified block diagram of the ACPD system is shown in fig. 3.6. The electronics can mainly be divided into six parts i.e. oscillator, current source, pre-amplifier, de modulator, filters and multiplexing unit. A brief description of the electronics is provided in the following sub-sections.

3.3.1 Oscillator

Oscillator design should ensure a high stability of frequency and amplitude. very low distortion and capable of providing continuously variable frequency. The voltage controlled oscillator (V.C.O.) in the CGM 6-3 generates a sinusoidal wave form of variable frequency i.e. in the range of 500 Hz to 240 kHz. with a high stability of frequency and amplitude (0.1%) and very low distortion (< 0.2%).

3.3.2 Current source

The current source is a power amplifier which delivers a constant current of up to 5 A regardless of the variations in the load impedance (resistance of the specimen and impedance of the cable). This has been accomplished by Matelect by introducing a large amount of negative feedback voltage proportional to the output current derived from a highly stable and low inductance resistor (8 nano henry and 0.1 ohm). in the path of the output current. This requires that the amplifier must maintain a large open loop gain at high values of frequencies and currents used.

3.3.3 Pre-amplifier

The main requirements of a pre-amplifier are (i) low noise, (ii) high common mode rejection ratio and (iii) maintaining the phase of the signal. This is achieved by a specially designed transformer with a turns ratio of ten. The transformer has the unique advantages of low noise, high common mode rejection ratio and complete isolation. This is followed by a series of integrated circuit amplifiers which can be selectively switched in to give gains of 1000, 3000, 10 000 and 30 000. The pre-amplification and final amplification is carried-out in a separate shielded enclosure which is mounted near the specimen with the main instrument several feet away. The reason for keeping the pre-amplifier near the specimen is that the ACPD signal picked up by the probes is very small (especially in case of aluminium alloys, due to their low resistivity), in the range of sub micro volts. Therefore, it is necessary to amplify the signal as near its source as possible. The input impedance of the pre-amplifier is 1000 ohms, therefore the resistivity of the signal cables is not really an issue. Assuming resistivity of the signal wires to be 1 ohm, (which is very pessimistic) the percentage loss of signal due to resistivity of cable will be only 0.1%.

3.3.4 Demodulation

The presence of a crack or strain changes the amplitude of the signal and hence modulates it. Therefore, the purpose of demodulation is to recover that change in the signal which occurs due to the presence of a crack or stress. Demodulation is the process of obtaining accurate information about the amplitude and phase of the voltage across the probes on the specimen.

The voltage picked-up by the probes from the test specimen is in an AC mode. The signal is of the same frequency as that of the current passing through the specimen. However, the phase of the signal will be different from that of the current passing through the specimen, because of the inductance of the specimen and the leads and the skin effect. This phase difference will depend upon the ratio of the resistive and the inductive parts of the total impedance. In addition, the probes will also be picking up electro-magnetic radiation generated by the current flowing through the current cable and the specimen. This pick up will also be affecting the phase of the signal. Thus, the phase of the voltage picked up by the probes will vary considerably from the phase of the current passing through the specimen, which is the same as that of sine wave generated by the oscillator.

Once the current and potential leads are fixed, then the emf pick up should remain constant and the increase in the signal would primarily occur due to the presence of a crack or stress (strain) applied to the material. However, the conditions imposed in keeping the current and potential leads the same all the time are somewhat stringent and may not always be possible to achieve (unless working with a fixed probe assembly). If the above two conditions are not satisfied, then the emf picked-up will vary and the overall signal will also change and these changes may not necessarily represent a crack or a stress (strain) field.

In this case the technique of phase sensitive detection (PSD) is used to demodulate the signal and obtain the amplitude and phase of the signal. Its overwhelming advantage is the rejection of noise.

Figure 3.7 shows a schematic of the phase of the ACPD component with respect to the phase of the current and its inductive component. In this figure, OC component is the in-phase with the current, OD is the inductive component. Note that the ACPD component (theoretical) lies at 45^{o} to the phase of the current [86]. By utilizing the PSD, the OA component, which is maximum in amplitude (i.e. $\sqrt{OC^2 + OD^2}$), can be picked up and thus the effect of emf is removed. However, this procedure is not completely error free. At higher frequencies, the inductive pick up becomes higher and the inductive component will be OD' rather than OD. The maximum output, thus will be OB (i.e.

$\sqrt{OD'^2 + OC^2}$) instead of OA as in the previous case. As a result, the value of ACPD is changing which will not truly represent the changes associated with the specimen/material state under consideration. However, in both cases there is one component of the phase, OC, that remains unchanged. It is the component of the signal which is in-phase with the current component. In PSD, if the reference phase is of the same phase as that of the current then PS detector will measure OC component which remains unaffected by the electromagnetic pick up.

In CGM-6, 0^{o} component is always measured and referred to as the ACPD signal. Moreover, CGM-6 possesses the capability of measuring the 90^{o} component as well. In CGM-6, the switching wave form generator involves the generation of two square waves, one in phase with the sine wave and the other at 90^{o} with respect to the sine wave. Figure 3.8 shows the principle of PSD circuitry. There is a square wave which is in-phase (C in fig. 3.8) with the current injected into the specimen. Also shown is a sine wave corresponding to the phase of the signal picked up by the probes (marked as A). At position 1 of the switch, only the first part of the sine wave which is in-phase with the square wave appears at output of the switch as shown in B of fig. 3.8. When the switch has changes to position 2, the second part of the sine wave in phase with the corresponding square wave will appear at B. The second part of the sine wave is however inverted, because it goes through an inverting amplifier. The process repeats itself over the next cycles. Thus, a DC signal corresponding to the AC signal of same

phase as that of current is produced. Taking another case, when the signal wave form is at 90°, to the switching wave form the output DC component will be zero as shown in fig. 3.9 and thus the inductive component is reduced to zero.

As mentioned earlier, besides the ACPD signal, electro-magnetic noise is also present. Fig. 3.10 shows a typical signal along with random noise. Besides the AC component of the signal the noise at position 1 of the switch will come out as is, whereas, at position 2 it will get inverted. The noise appears at C as an AC output. The output will be a DC component of the signal and the noise appears as an AC, which will be filtered out later. Thus, the PSD effectively removes noise. However, a limitation of the technique is that the odd harmonics of the frequencies of the current will not be rejected. As shown in fig. 3.11, one third of the third harmonics has come through. Similarly, one fifth of the fifth harmonics will come through. Since the odd harmonics are not eliminated, they will have some effect on noise rejection. However, as they are progressively smaller in amplitude, this limitation does not significantly affect the noise rejection. CGM-6 has the capabilities of performing PSD in real time over a range of frequencies varying between 500 Hz to 240 kHz.

3.3.5 Filters

The purpose of the filter is to block the AC noise and allow the DC voltage to pass through. or more correctly the DC component of the signal and low frequencies to pass through. The CGM-6 possesses a bank of 4^{th} order active filters through which the signal is processed. The filters can be selected from one of the preset values of 1 Hz. 80 Hz. 1 kHz and 20 kHz or can be switched out completely.

3.3.6 Multiplexing

There are two multiplexing units. one for the current and the other for the voltage. The current multiplexer has three channels and the voltage multiplexer has eight channels. The purpose of multiplexing units is to allow the monitoring of various locations in one specimen or different specimens at the same time. Extra care was taken to ensure that during scanning. the voltage multiplexer does not pick up more noise and that there is no phase shift while scanning the currents. The multiplexing units were enclosed in separate shielded enclosures and were mounted as close to the specimen as possible.

3.4 Specific Probe Design Requirements

As discussed in section 3.3 (electronics/signal processing). all necessary precautions were taken either to minimize or to negate the effect of emf on potential readings. Moreover. only the resistive component (0^{o}) of the signal was measured all the time. and the inductive component does not interfere with the signal. Under such circumstances. the probe design should not be a critical factor in the implementation of the technique. However. during the course of this project. it was found that probe design was very critical for the successful application of the ACPD technique. The lay out of the current and potential leads. the shielding of both these cables. the movement of the wires. grounding of cables etc. do play a significant role in controlling the sensitivity and reliability of the technique. The reason being. that some of the noise. or the inductive component still appears and adds on the real signal.

The current cable which injects the current in the solid. forms a loop with the specimen. and is known as the transmitter loop as shown in fig. 3.12. The inductive component due to this loop is at 90^{o} to the phase of the current as well as to the resistive component of the signal. The emf radiated from the current flowing through the specimen is influenced by the skin effect and the geometry of the specimen. Once the current is injected into the solid, it will take some time for the skin effect to build up and again some time for it to die out. The diffusion of the current due to the skin effect will possess a lagging

component. The inductive component of the lagging current is at 90° to it. which in turn be lagging with respect to the inductive component of the current transmitted through the current loop. The interaction of both inductive components results in an over all lag of the 90° component, OE. The electronics. therefore measures OC' instead of OC as shown in fig. 3.13. Therefore. an error of CC' results in the measurement of the resistive component [105].

At high frequencies. the magnetic field is strong for both the transmitted current loop and the one radiated from the specimen. but the skin effect building up and dying out remains constant. As a result. there are more problems associated with the erroneous pick ups and the error becomes larger at higher frequencies. The diffusion of the current in the specimen also varies with the geometry of the specimen e.g. the presence of a notch. This can also affect the inductive component and therefore the overall signal. The primary purpose of a good probe design is to minimize the pick up by the potential probes as much as possible. The major factors that have a substantial impact are as follows:

3.4.1 Current cable

The important requirement for the current cable is to have a resistance as low as possible because of the limited voltage compliance available from the power amplifier. The

flexibility of the cable also plays an important role especially when the ACPD sensors have to be installed on real life components. The current cable is one of the prime sources of emf radiations. therefore proper shielding of the cable must be achieved. This is why a co-axial current cable is used. The current is passed through the inner conductor and the shield of the co-axial cable acts as the return conductor as shown in fig. 3.14a. The purpose of this arrangement is to ensure that the current in the conductor and the shield flow in the opposite direction and therefore the emf generated by both cancel each other out. The ideal arrangement. however. will be to have a tri-axial cable as shown in 3.14b. The outer shield of the tri axial cable will then be connected to earth so that whatever emf is radiated out is blocked by the outer shield.

The other problem concerns the precise point at which the current is injected in the solid. fig. 3.12. The hatched area represents the current loop which transmits the emf. Since the voltage probes are placed very close to this area. this area must be minimized to reduce the pick-up by the probes. The inner conductor. must be kept very close to the surface. This has two advantages. First. the loop area is minimized and secondly. the current focusing effect is maximized. As shown earlier in the current focusing results (see fig. 3.4b. 3.5a-c). when the current focusing device is moved higher from the surface of the specimen. the ACPD signal (which is always the 0° component in the present study) becomes stronger. However. the resistive component should not have changed. The difference in the ACPD values arises from an increase in the emf picked-

up by the potential probes as the current carrying conductor is placed at a greater height from the specimen surface which in turn leads to an expansion of the transmitted loop.

3.4.2 Potential Leads

The potential leads also form a loop in the proximity where they are in contact with the specimen as shown in the fig. 3.15. The loop area must be minimized. otherwise it acts as a pick up area (antenna) for the emf radiated from the current flowing in the conductor as well as in the specimen [5]. This has been achieved by twisting the two conductors of the potential cable as tightly as possible so that they are separated just enough at the ends to make the contact with the specimen. The probe wires are placed at an angle of 90^{o} relative to the position of the focusing device such that a minimum length of the potential leads is exposed to the emf generated by the current. The twisted pair is connected to the input of the pre amplifier and the drain (shield) is connected to the ground on the CGM instrument.

The probe set up is shown in fig. 3.16. The conductor of the current is attached to a copper strip which is glued to the surface of the specimen. The other end of the copper strip is connected to the specimen at point 2. The return conductor. i.e. the shield. is connected at point 3. The copper strip acts as a current focusing device and is used because of ease of handling. The ease of handling results in better reproducibility and

consistency from one specimen to another. The height of the focusing device from the surface of the specimen is controlled and is equal to the thickness of the glue. A twisted pair of potential leads is attached at points 4 and 5 with the loop being minimized as much as physically possible.

The designed probe discussed above was built manually and care must be exercised at all times in the placement of various leads to achieve reproducibility. However, in a fixed probe assembly, manual error will not be substantial and hence better reproducibility in the results can be achieved. A configuration of a fixed probe assembly, designed during the course of this work and encompassing the above probe design features is shown in fig. 3.17. As can be seen, the focusing device is laid along the surface of the specimen and connected to pin 1. The shield of the current cable is connected to pin 2. Pins 3 and 4 are connected to the twisted pair of potential cable and all four pins can be spring loaded. When the pins are pressed against the specimen surface, the current will flow in the focusing device and then jump in to pin 1. From pin 1 it will pass onto the specimen and the circuit will be completed through pin 2. Pins 3 and 4 will measure the ACPD signal.

3.4.3 Probe Attachment Procedure

As part of the test program, the ACPD sensors were to be attached to CF-18 aircraft structure undergoing full scale fatigue test. Therefore, a probe attachment procedure had to be devised which did not affect the fatigue behaviour of the base material or act as a crack initiation site. Ultrasonic welding was selected for the attachment of the probes [106]. The ultrasonic welding procedure along with the detailed investigation of its effect on the material is described in the following sub-sections.

3.4.3.1 Ultrasonic Welding

The ultrasonic welding equipment used was Stapla Mini Albatros. A photograph of the original system (assembled and disassembled) is shown in fig. 3.18(a-b). The unit consists of a power supply, welding horn, converter, booster and polar mount assembly. The horn is used to transmit the acoustical vibrations to the workpiece. In addition, the horn maintains the pressure necessary to form a weld. The horn and the welding tip form one solid piece made out of tool steel. The 35 kHz electrical energy from the main unit is supplied to the converter which then transforms the high frequency electrical oscillations into high frequency mechanical vibrations at a certain amplitude, in a longitudinal direction. The heart of a converter is a piezo electric crystal which expands and contracts when subjected to an alternating voltage. The booster is located between

the converter assembly and the horn. Besides acting as a mechanical interface and amplitude adjuster, it also reduces the heat transfer back into the converter. The booster also allows acoustical tolerances to be less critical, thus promoting more efficient operation of the unit. The polar mount assembly supports the converter whereas the booster and horn assemblies are used for the transmission of ultrasonic vibration energy.

3.4.3.1.1 Modifications to the Welding Equipment

The existing set up could not be used for welding in the middle of the specimen (~ 20 mm from the edge of the specimen) because of the shape of the horn. To be able to weld in the middle of the specimen, the horn had to be tilted (~ 5-10°) because it was not otherwise possible with the original set up. In addition, the original set up could not be used to weld wires on large immovable items. In order to weld on components, the mounting assembly was taken out of the polar mount and the welding was tried by holding the assembly by hand. This arrangement posed some problems due to the sliding of the welding head since it was not mechanically fixed in the original assembly. To overcome this problem, the booster was removed. Although, the booster doubles the wave amplitude and helps to reduce the heat transfer back to the converter, the removal of the booster did not introduce any system limitations because only thin aluminium wires (0.5, 0.25 or 0.1 mm in diameter) were to be welded which did not require much power. The unit was only required to perform a small number of minute welds where

heat transfer was not an issue. Therefore. removal of the booster did not really lead to any work limitations. A photograph of the modified system is shown in fig. 3.18c.

Three slots equal in diameter to the wires (0.5. 0.25 and 0.1 mm) were machined on the edges of the welding head where as. the fourth edge was kept unchanged as shown in fig. 3.19. This was done to position the wires firmly in place on an area where they had to be welded and also to overcome the problem of the weld head sliding. However. this technique did not function properly because the Al wires would tightly fit in the weld head edges slot leaving little wire area for welding. However. when the Al wire was held under a slot of smaller dimension. e.g. 0.25 mm diameter slot was positioned on top of the 0.5 mm diameter wire. the desired results were achieved and the problem of weld head sliding was also overcome.

To achieve good results. it is imperative that the welding head be kept parallel to the work piece. As mentioned earlier. this was not possible to achieve with the shape of the original weld head configuration because of the shape of the horn and therefore tilting of the horn was necessary. To overcome this problem. a completely different design of the weld head was worked out. The schematic and the photograph of the new welding horn are shown in fig. 3.20(a-c). The area of the welding tips is 1.5×1.5 mm^2 with the length of the protruding tip around 3 mm. With the new horn design the aluminium wires could be easily welded anywhere on the specimen or the structure. The modified weld head

design also focuses the mechanical vibrations on the tips where it is most required. Therefore, the power required to weld was found to be even smaller than the original configuration. Sliding of the weld head was also found not to be a problem. Smaller wires 0.1 mm to 0.25 mm in diameter were easily weldable which was not possible with the old horn design. These changes to the setup made the ultrasonic welding procedure simple, flexible and efficient.

3.4.3.1.2 Effect of Welding on the Material

A rectangular piece of Al 7075 T651 was cut and 0.5 mm diameter wires were welded on two sides as shown in the fig. 3.21. Optical microscopy was carried out to observe the effect of welding on the microstructure of the base material. The observations were first carried out away from the welding zone and then by removing the material by polishing, the microstructure near the welds and directly under the welds was observed. Figure 3.22(a-c) shows the microstructure away from the weld, near the weld and under the weld respectively. No change in the microstructure was observed due to the welding process. These results were further confirmed by taking microhardness measurements, far away from the weld, below the welds and in between the welds. Figure 3.23a shows the results of the microhardness measurements whereas fig. 3.23b shows a scanning electron micrograph pinpointing the precise location of the welds and micro

indentations. There was no significant change in the microhardness due to the ultrasonic welding procedure.

3.4.3.1.3 Effect of Welding on Fatigue Life

The ACPD probes were to be welded to the CF-18 structural components for monitoring crack initiation and growth during full scale testing and therefore, there was still a considerable concern among DND personnel regarding the effect of welding on the fatigue life of the structure. Six Al 7075 T7351 hourglass specimens with a K_t of 1.03 were machined to investigate the effect of welding on the fatigue life of the base material. The schematic of the specimen geometry shown in fig. 3.24 was provided by DND Canada, representing one of the critical locations (flange fillet region of bulkhead 488) in the CF-18 aircraft structure. The Al wires were welded on both faces of two samples near the edges and at the center for the first batch. In the second batch, welds were made near the four edges on the thickness side of three specimens. One sample was tested without any welds. A total of around four hundred welds were made on the five specimens. An example of the specimen with the welds is shown in fig. 3.25. The fatigue testing conditions were as follows : stress ratio, R = 0, frequency, f = 1 Hz and a maximum stress, σ_{max} = 310MPa. None of the specimens failed at or below the welds. Figure 3.26 shows a typical crack initiation site. Inclusions were always found at the sites where cracks had initiated. These results clearly indicate that the inclusions in the

alloy are more critical from fatigue life perspective than the ultrasonic welds. The fatigue life varied between 49800 cycles to 66850 cycles, which is well within the expected scatter band for the material [107].

Figure 3.25 shows that the Al wires welded on the specimen remain properly attached to the specimen even when the base material fails. This behaviour was expected because the welded Al wires, do not carry any load. Hence, the longevity of the welded wires is not an issue either. This was further confirmed during a four point bend test where the specimen was plastically deformed due to a procedural error. There was an 8 mm permanent deflection on the specimen as shown in fig. 3.27. However, the welded Al wires still remained attached to the specimen. Therefore, the longevity and the integrity of the ultrasonically welded wires and the probes would not prove to be a problem. These issues were the prime requisites for the welding technique because, the CF-18 testing was expected to last for at least three years.

3.5 Performance of the ACPD Technique

3.5.1 Electronics Calibration

The current leads and potential wires were connected to a Al 7075 T651 specimen. The probe arrangement was similar to that shown in fig. 3.16. The gain was fixed at 3000

and the frequency at 30 kHz. The current was varied between 0.5 amp. to 5 amp. in 0.5 amp. steps. The results are shown in fig. 3.28a. It is evident that the ACPD output varies linearly with the current. In another test. the current and frequency were fixed at 1 amp. and 30 kHz respectively. and the gain was changed between four preset values provided in the CGM 6-3. i.e. 1000. 3000. 10 000 and 30 000. The ACPD again changes linearly as shown in fig. 3.28b. In the third experiment. the current and gain were fixed at 1 amp. and 3000 respectively and the frequency was changed between 10 kHz to 240 kHz. The results are plotted as ACPD values versus the square root of frequency in fig. 3.28c because the skin depth is inversely proportional to the square root of the current frequency (equation 1) and the ACPD is inversely proportional to the skin depth. Higher the skin depth. lower will be the ACPD value. Therefore. ACPD should be directly proportional to the square root of the frequency. The results indicate that the ACPD readings are only linear up to 150 kHz and the linearity is lost beyond this point. This deviation is most likely due to the emf picked-up by the potential probes. At higher frequencies. the emf is stronger and therefore the problem of pick up will also be more severe.

3.5.2 Drift Measurements

The drift measurements of the ACPD signal were carried out at different combinations of current. frequency and gain to analyze the performance of the overall ACPD system.

The ACPD probes were attached to an 7075 T651 Al alloy specimen in a similar way to that shown in fig. 3.16 and the readings taken at 30 kHz, 1 ampere and 3000 gain. The measurements were taken over a period of seven days. This was done to see the effect of long term drift on the ACPD signal. The results are plotted in fig. 3.29(a-b). Fig. 3.29a shows the complete measurements taken over the seven day period while fig. 3.29b is a zoom of the first twenty hours. The initial decrease in the ACPD value was due to the time taken by the electronics to warm up. Once the electronics had stabilized, the total noise level is 0.1 mV. These measurements were taken at a gain of 3000, implying that the actual noise is of the order of 33 nano volts. Note that the readings had remained stable (within 0.15 mV) over a seven days period.

Figures 3.30-3.32 show the effect of current, signal amplification (gain) and frequency on the drift measurements. The scale for all the plots has been kept the same (10 mV). Figure 3.30 (a-c) show the drift and noise level for 30 kHz and 3000 gain at different currents of 1, 3 and 5 amperes. Besides, the initial drop for the first four to five hours (time taken by the electronics to warm up) as seen in fig. 3.30c, the noise level remains around 0.1 mV. This implies that increasing the current from 1 amperes to 5 amperes does not increase the noise level. This also confirms that there is a definite advantage in working at higher currents, since it increases significantly the signal to noise ratio.

Figure 3.31 (a-b) shows measurements taken at 30 kHz and 5 amperes at gain levels of 10 000 and 30 000 respectively. The noise level is still around 0.1 mV for the two cases. However, an increase in ACPD signal is seen around eleven and six hours in figs 3.31(a-b) respectively. This increase was found to be related to the difference in temperature between day and night which in our laboratory environment is around 5 to 6° C. Unfortunately, the temperature was not recorded simultaneously. At higher gains, the effect of temperature on the resistivity and therefore on the potential is more visible because of the higher sensitivity of the system. Furthermore, the total change in the signal at 30 000 gain is 3 mV implying that the signal variation due to temperature change is only 0.1 μV.

Figure 3.32 (a-b) shows the drift measurements taken at 5 amperes and 3000 gain while the frequency was kept constant at 120 kHz and 200 kHz. The noise varies in the range of 0.1 mV to 0.15 mV. The variation in the center of the graph is again attributed to temperature changes in the laboratory. In order to verify the effect of the changing temperature on the ACPD values, one set of measurements was carried out at 120 kHz, 5 amperes and 30 000 gain as shown in fig. 3.33. The data acquisition was started around 5 PM (in the month of June) and carried out for 47 hours. At night the ACPD value started increasing because the resistivity of the material increases with temperature. In the morning, the ACPD value started decreasing and reached the same value as before during the day. It again started to increase in the night time and reached the same ACPD

value as the night before. Finally it decreased the next morning and came back to the original value during the day. Overall, the noise level was found to be no more than 0.2 mV with the drift of the signal less than 6 mV (~ 0.2 μV before amplification).

3.6 Probe Design and Strain Calibration

Three different specimen geometries, namely the four point bending, the hourglass and the single edge notch specimen geometries, were selected to study the effect of load cycling on the ACPD.

3.6.1 Four Point Bending Specimen

The four point bending specimens (six inch radius) were machined out of 7075-T651 plate and designed to represent the flange fillet region of the 488 bulkhead in the CF-18 aircraft. This was the location which was to be monitored by the ACPD technique during full scale testing. The schematic of the four point bending specimen is shown in fig 3.34. The grips were specially designed and machined to perform this particular experiment. The grips were made out of heat treated 4340 steel. The load points (or the loading pins) were coated with an oxide coating using a plasma spraying technique to electrically insulate the specimen from the test system. Note that the electrical insulation was not required, as was later found out during the experiments. In fact, it was found

that connecting the specimen to the ground rather than keeping it completely floating produced better results.

Strain gauges were used to obtain the calibration curve of strain versus ACPD. Three strain gauges were installed on the specimen by a qualified technician from "Pratt and Whitney Canada" (PWC). The locations of the strain gauges, along with the location of the ACPD probes, are shown in fig. 3.35. As can be seen, strain gauge 1 is located 10 mm away from the current focusing device. This strain gage was installed at the said location to observe the effect of the emf generated by the high frequency AC on strain gauge readings. The distance of 10 mm was selected because this approximates the shortest distance between the strain gauges and the ACPD sensors installed on the CF-18 aircraft. Strain gauge 2 was placed in the highly stressed region 4 mm away from the edge and 7 mm from the centerline of the specimen. The highly stressed region was identified by carrying out finite element analyses. One quarter of the specimen geometry was modeled because of symmetry. The detailed results are shown elsewhere [108]. Strain gauge 3 was installed approximately at the center of the specimen to verify the strain gauge response by comparing the computed stress gradient.

The ACPD probes were placed on the opposite face of the specimen relative to the strain gauges, with a probe spacing of 7.5 mm, 5 mm away from the centerline and 4 mm from the edge as shown in fig. 3.35. Thus, the ACPD probes were in the same stress domain

as strain gauge 2. The only difference being that the ACPD probe was monitoring a tensile stress whereas strain gauge 2 was measuring the counterpart compressive stress.

A twenty ton servo-hydraulic Instron machine (Model 1333) was used for carrying out the experiments. The ACPD measurements were carried out by a CGM 5 unit, because at that time, CGM 6 was still in its development stage. The CGM 5 was set at 30 kHz, 1 ampere and 70 dB (× 3162) gain. The output of the CGM 5 was connected to a digital voltmeter (DVM-HP 34401A). The DVM was configured to sample the data at an acquisition rate of 100 PLC (power line cycles) with auto zero correction. This configuration of DVM resulted in an acquisition rate of one reading every 3.34 seconds. The DVM readings were directly recorded with the computer. The strain gauge readings were taken manually using the strain gauge measurement system. The system consisted of a ten channel switching and balancing unit (Measurement Group Inc. Model SB1) and a Micro Strain Indicator (Model P3500). Figure 3.36 shows the complete four point bending experimental set up for on-line measurement.

The loading configuration for the test is shown in fig 3.37. The loading was carried out in multiple steps of 400, 2803, 5206, 7609, 10012 and 12415 Newtons, both for the loading and unloading sequence. The loadings were carried out manually and this cycle was repeated three times. At each loading step, the loading was stopped for two minutes and the ACPD and strain gauges measurements were taken. The strain gauge readings

fluctuated within ± $75x10^{-6}$ and the average of the readings was recorded. Finite element analysis was also carried out to determine the strain values associated with each loading step. Figure 3.38 shows the finite element model mesh and the locations where the actual strain measurements were carried out. Element 671 is the location where strain gauge 2 is installed on the specimen, while elements 668 and 657 correspond to the locations of strain gauges 1 and 3 respectively.

Figure 3.39 (a-c) shows the strain gauge readings plotted as a function of the applied load for strain gauges (SG) 1 to 3 respectively. Note that the values of SG 2 and SG 3 have been inverted and then plotted. Fig. 3.40 (a-c), show the strain readings calculated by the FEA for elements, 668, 671 and 657 respectively. Fig. 3.41 compares the computed and the measured strains (SG 1 and element 668). As can be seen, the experimental measurements of the strain gauge and the finite element analysis results are in agreement with one other. Therefore, the ACPD readings can be reliably calibrated against the strain gauge readings or the finite element analysis. Moreover, the emf generated by the high frequency current is not affecting the strain gauge response. One more experiment was conducted at Canadair in which ACPD sensors, acoustic emission sensors and strain gauges were all installed close to each other on the same specimen. The performance of the strain gauges and the acoustic emission sensors was once again not affected by the emf generated by the ACPD sensors. Fig 3.42 shows the ACPD readings as a function of the applied loads. A total of 0.4 mV change was

observed for the elastic strain range (0 to 2.6 x 10^{-3}) imposed during the experiment. A calibration curve between ACPD and strain was obtained using the data from SG 2 and the ACPD readings and this is shown in fig. 3.43. A linear regression analysis was used and the relationship between the strain and the ACPD output was found to be

$$\text{ACPD (volts)} = 0.141\ (\text{strain}) + 0.017 \qquad (3.3)$$

with the reliability of the regression being 97.3 %.

In fig. 3.39. it can be seen that the strain gauge measurements displayed a linear response with the applied load. Thus. the results during the loading and unloading sequence fell (almost) along the same line. The ACPD readings. on the other hand. showed some 'scatter'. To rationalize these results it should be noted that the specimen was loaded to a maximum stress of 28 ksi (193 MPa). which is approximately 40% of the macro yield stress. At this stress level. the stress-strain curves obtained during loading and unloading cannot be expected to follow the same line because of microplasticity [109]. The ACPD readings are. therefore. showing a hysteresis behaviour.

3.6.2 Hourglass Specimen

The specimen design and the material are the same as those used for assessing the performance of the ultrasonic welding procedure. fig. 3.24. The instrument used was a

CGM 5. The ACPD was set up at 30 kHz, 1 amperes and 70 dB (× 3162) gain. The testing was done on a 20 ton servohydraulic Instron machine. The fatigue testing conditions were R = 0, f = 1 Hz and σ_{max} = 310 MPa. Figure 3.44a shows the response of the ACPD as a function of number of fatigue cycles. Since, this section deals with strain, the first part of the curve, i.e. the stable flat line, is discussed here. Fig. 3.44b shows the zoom of the first section of the curve. As can be seen, the ACPD readings are increasing continuously with the number of cycles and then the readings start stabilizing from cycle 10 000 cycles onwards. During continuous cycling, the saturation limit of the material is reached and this is associated with no further change in the overall potential. In essence, a strain hardening curve is observed as indicated in fig. 3.44b. This demonstrates that the ACPD is capable of tracking the behaviour (response) of the material due to cyclic loading, including the microplastic deformation accumulating, demonstrating the sensitivity of the ACPD system.

3.6.3 Single Edge Notch Specimen

The Single Edge Notch specimen geometry shown in fig. 3.45 was selected for testing because it reflected a complicated version of the critical locations on the CF-18 aircraft which were to be eventually monitored with the ACPD technique. The material used was Al 7075 T7351 and the K_t factor was 2.885. The experiments were carried out on 10 ton electromechanical machine (Model 1362). The system used for the ACPD

measurements was CGM 6. The ACPD readings were obtained at 120 kHz, 5 amperes and 3000 gain. The DVM was set at the same conditions as mentioned before. The experiments were carried out by measuring the AC potentials at regular load intervals of 196, 1953, 3711, 5469, 7227 and 8984 Newtons for the loading and unloading sequences. The experiment was fully computerized and the loading and unloading sequence was repeated 276 times. At each loading step, the specimen was held at a constant load for 180 seconds. For the first thirty seconds no readings were taken to ensure that the ACPD readings were stabilized. After 30 seconds the ACPD readings were taken continuously for 150 seconds. The load was then changed to another level and the measurement sequence repeated. The same procedure was repeated during the unloading sequence.

Figure 3.46 shows an example of the feedback load that was actually applied to the specimen as a function of time. Figure 3.47 (a-c) show the corresponding ACPD response as a function of time for the 1-10, 90-100 and 265-275 cycles. It is evident from these plots that the ACPD output is directly proportional to the applied load on the specimen. There is an increase in the ACPD output with increasing load, and vice versa. Figure 3.48 shows the ACPD as a function of load for the 276 load cycles. Figure 3.49(a-c) shows the details of the ACPD versus load for cycles 1-10, 90-100 and 265-275 respectively. The bandwidth, i.e. the scatter, decreases with increasing number of

cycles indicating that the material gradually reaches a saturation limit with the hysteresis behaviour disappearing by the end of the 100^{th} cycle.

3.7 Probe Design and Crack Calibration

The SEN specimen shown in fig. 3.45. was used for carrying out the crack detection and calibration work during the fatigue tests. In one batch of specimens. there were excessively deep machining marks in the notches. The notches in these specimens were re-machined to a radius of 1.27mm (K_t = 2.653) instead of the 1.0668 mm radius(K_t = 2.885) as shown in fig. 3.45. No special surface finish operation was carried out prior to using the ACPD technique.

After investigating a number of probe designs. two different types of probe designs were finally chosen for crack calibration. They are shown in fig 3.50. In both the probe designs (#1 and #2). the current focusing device was glued in the middle of the specimen going all along its length and following the contour of the notch. In the first case (see fig.3.50a). the potential probes were welded on one side of the current focusing device and the wires were directed away from the focusing device. In the other case. fig. 3.50b. the potential probes were welded across the notch, such that one of the probe wires was positioned over the current focusing device The difference between these two

configurations is that the noise pick-up is higher in the second case. However, design # 2 ensures that the sensitivity to crack detection is the same for the entire notch surface.

The other end of the probe wires were welded on copper tracks of a printed circuit board (PCB) which were glued on the back face of the notch as shown in fig. 3.51. The signal wires were then soldered on the PCB and the other end of the wires were connected to the pre amplifier. Two copper pads (1,2) were glued on the top face of the specimen. Both copper pads were electrically connected to the specimen surface through Al wires welded on the specimen surface and copper pads. The conductor of the current wire was soldered to one end of the current focusing device. The other end of the current focusing device was connected to the copper pad 2 with a piece of wire, soldered on both sides. The shield of the current cable was soldered to the other copper pad 1. With this arrangement the current first flows into the current focusing device, jumps into the copper pad 2 and then from the copper pad passes into the specimen. In the specimen, the current flows below the current focusing device in the opposite direction to the flow in the focusing device. The copper pad 1, which was connected to the shield of the current cable, completes the current circuit.

The cracks monitored were naturally initiated fatigue cracks. The fatigue testing was carried out at R = 0, and f = 1 Hz. The maximum remote, far field stress (S) was varied between 131 MPa to 275.7 MPa for different tests. All tests were carried out on a 10 ton

electro-mechanical machine. Woods metal grips were used for testing to ensure proper alignment of the load train assembly.

The CGM-6 was connected to the specimen and the drift measurements were taken during the night. The HP-DVM (model 34401) was set at 100 PLC. The fatigue tests were always started the following morning. This was to ensure that enough time was given for the electronics to stabilize. The experiments were fully computerized. The samples were fatigued until a pre-determined change in potential had occurred. Each specimen was then pried open (by applying a tensile load) and the crack depth was measured using a scanning electron microscope (Model JEOL 820). The dominant crack depth (a), and the corresponding change in potential (δV) were then correlated to produce the calibration curve.

A typical response of the ACPD as a function of number of fatigue cycles (whatever the design used) is shown in fig. 3.52. It is evident that the potential readings are very stable in the beginning and there is a sharp increase as soon as a crack is detected by the ACPD probes. In one particular experiment, the DVM was set at 10 PLC giving a sampling rate of one reading every 0.33 seconds. The results are shown in fig. 3.53. As can be seen the inherent (internal) noise of the DVM is too high when using faster sampling rates.

Fatigue testing was first carried out using probe design # 1(see fig. 3.50a). The results are shown in fig. 3.54a. Here a 12.6 mV change in potential was found to correspond to crack depth of 2.84 mm in the specimen. Similarly, fig. 3.54b shows the results for probe design # 2 (fig. 3.50b) where a 20 mV change in potential corresponded to crack depth of 2.1 mm. These results indicate that the sensitivity of the ACPD signal, with respect to crack depth is higher in the case of design # 2 as compared to design # 1. This is because the entire surface area of the notch (where the crack can grow) is covered in the design # 2 as compared to design # 1. However, the noise level in the design # 1, fig. 3.54a is lower than the design # 2, fig. 3.54b. This is due to the fact that the probe wires are moving away from the current focusing region in design # 1, i.e. from the stronger emf area whereas, in design # 2 one of the wires is passing over the area where the emf is very strong. This shows that a compromise must be made between sensitivity to crack detection and the noise level. If sensitivity is important, as is in the case of short crack detection, then design # 2 should be used and more noise will have to be tolerated. If sensitivity is not important (short crack detection is not particularly needed) then design # 1 should be used. However, for plots 3.54a and 3.54b overall the noise level in both is very low because of proper care that had been taken while laying out the probes.

Four fatigue tests were done with design # 1, and the rest of the experiments were done with design # 2, since the study was also aimed at short crack detection and growth.

Several experiments were carried out to determine the ACPD/crack response under different ACPD conditions in terms of frequency and current. A non-linear relation was observed between the crack depth and the change in potential. The two probe designs. one for which the potential probes were welded on one side of the focusing device (fig. 3.50 a). and the other in which the probes were welded across the focusing device (fig. 3.50b) were tested at 30 kHz. 1 amp. and 3000 gain. Probe design 2 was used in the rest of the experiments. The calibration equation relating crack depth with the change in potential obtained for design # 1 is as follows:

$$\delta V = 0.532\, a^2 + 3.254\, a + 0.388 \qquad (3.4)$$

where δV is the change in potential. and a is the crack depth.

The crack depth. (a) ranged between 1.87 mm to 4.22 mm with the reliability of the regression (r^2) being 98.53%. Figure 3.55a shows the plot of the crack depth (a) versus change in potential for the above equation. All plots relating crack depth with the change in potential were forced through zero. This plot also contains a data point obtained from the test where the data acquisition was carried-out at 10 PLC (see fig.. 3.53). As mentioned earlier. there was too much noise in this particular experiment. Figure 3.55b shows the same plot as in fig. 3.55a. but the data point obtained at 10 PLC was omitted. This omission resulted in the following equation:

$$\delta V = 0.879\, a^2 + 2.003\, a + 0.0068 \qquad (3.5)$$

with $r^2 = 0.999$ and $2.56 \leq a \leq 4.22$ mm.

Figure 3.56a shows the calibration curves obtained using probe design # 2 (fig.. 3.50b). The corresponding calibration equation is :

$$\delta V = 1.422\ a^2 + 4.651\ a - 0.462 \qquad (3.6)$$

with $r^2 = 0.996$ and $0.62 \leq a \leq 6.00$ mm.

As explained earlier. the sensitivity of probe design # 2. (fig. 3.50b) is much higher than that with design # 1.

Figure 3.56 (b-d). shows the plot of crack depth versus the change in potential obtained at 30 kHz. 5 ampere. 3000 gain: 90 kHz. 5 ampere. 3000 gain and 120 kHz. 5 ampere. 3000 gain respectively. All these plots were obtained using probe design # 2. The following calibration equations obtained for the three ACPD settings were respectively:

$$\delta V = 7.0\ a^2 + 25.906\ a - 5.092 \qquad (3.7)$$

with $r^2 = 0.996$ and $0.145\ \text{mm} \leq a \leq 6\ \text{mm}$:

$$\delta V = 43.39\ a^2 - 0.614\ a - 0.016 \qquad (3.8)$$

with $r^2 = 0.997$ and $0.2\ \text{mm} \leq a \leq 0.43\ \text{mm}$:

$$\delta V = 25.42\ a^2 + 20.546 - 0.825 \qquad (3.9)$$

with $r^2 = 0.999$ and $0.14\ \text{mm} \leq a \leq 5.32\ \text{mm}$.

The experiments conducted at 120 kHz frequency were carried out on Al 7075 T7351 material while the rest were conducted on Al 7075 T651 material. Figure 3.57a shows a global view of the fracture surface (scanning electron micrograph) while fig. 3.57b shows a zoom of the dominant crack. The cracks were always semi-elliptical in shape.

All of the above results show that as the current and the frequency increase, the sensitivity to crack detection also increases. A quadratic relationship was found to correlate crack depth with the change in potential as opposed to a linear relationship. The non linearity arises when the crack front approaches the skin depth values. However, the relationship is almost linear when the crack depth is greater than the skin depth. When the crack depth is smaller than the skin depth, the shape of the calibration curve (crack depth and change in potential) should not be very different than that obtained with the DCPD technique. Furthermore, non linearity may also arise due to the fact, that the current is not uniformly distributed throughout the thickness of the solid but rather drops exponentially from the surface into the specimen(see fig., 3.1b).

Hwang and Ballinger [3] and Lu et al [91] have observed a similar non-linear behaviour and reported a second order polynomial and a power law relationship respectively. However, this is in contrast with the observations made by Dai et al [4,89], Charlesworth and Dover [86], Watt [88], Jablonski [90] and Marchand [106]. They reported a linear relationship between crack depth and change in potential. To address these conflicting results a two dimensional finite element analysis was carried out to sort out the effect of crack growth on the change in potential. Details of the analyses are given in Appendix I. Figure 3.58 summarizes the results of the analyses. This plot clearly shows a non linear relationship for the crack depth (normalized with respect to skin depth) versus the change in potential. As mentioned earlier, the non linearity arises

when the crack depth approaches the skin depth. Again, note that the correlation is almost linear when the crack depth is greater than the skin depth. This conclusion is consistent with the observation made by Verpoest et al as well [5].

Multiple cracks were often observed in the fractured specimens as shown in fig. 3.57a. Due to multiple crack initiations, the surface crack length can be much longer than the crack depth. This will affect the ACPD response even if the crack depth is always the same. However, this does not imply that the calibration equations obtained above are wrong, but that some error is introduced as a result of the varying number of initiation sites in a multiple crack situation. Nevertheless, the calibration curve correlating the crack area with the change in ACPD is expected to be very accurate, because it is the crack area which is truly responsible for the change in the ACPD potential. Therefore, the crack areas of all the specimens were measured and correlated with the change in ACPD signal. The crack areas (A), were calculated by assuming perfectly semi-elliptical crack fronts. Figure 3.59 (a-d) show the calibration curves at 30 kHz, 1 amp., 3000 gain; 30 kHz, 5 amp., 3000 gain; 90 kHz, 5 amp., 3000; gain and 120 kHz, 5 amp., 3000 gain. The following calibration equations with the corresponding correlation factors were respectively obtained.

$$\delta V = 0.072\ A^2 + 1.577\ A - 0.55,\ (r^2 = 0.998) \qquad (3.10)$$

$$\delta V = 0.362\ A^2 + 7.819\ A - 2.569,\ (r^2 = 0.998) \qquad (3.11)$$

$$\delta V = 2.097\ A^2 + 5.03\ A + 0.029,\ (r^2 = 0.999) \qquad (3.12)$$

$$\delta V = 1.494\ A^2 + 8.422\ A - 0.209.\ (r^2 = 0.999). \qquad (3.13)$$

3.8 Off-Line Measurements

The measurements and calibration curves were all obtained on-line, i.e. through continuous measurements. In this section, the feasibility of using the ACPD technique as an off-line measurement tool is assessed. This capability is particularly relevant for detecting and sizing cracks using discrete measurements of the potentials during the fatigue life of components. Figure 3.60(a-b) shows plots of ACPD versus time. The first plot (3.63a) shows the data from 0V to 0.8V while the second plot (3.36b) shows a zoom of the same data (0.736 to 0.756V). ACPD measurements were interrupted during fatigue cycling. As can be seen in fig. 3.60a, the cycling was stopped at point A, the system was then brought back to zero load and the CGM 6-3 was disconnected from the specimen. Although disconnected the measurements were taken for some time. Obviously the readings were at zero volts as indicated in fig. 3.60a. The instrument was then connected back and the cycling was resumed. The AC potential returned to its original value. This process was repeated three times and is labelled A, B and C. In all cases, the ACPD signal was not affected by the interruptions. At locations D, E, F, G and H the cycling was stopped again and the load was brought down to zero load. However, the monitoring of ACPD signal was not interrupted. The potential dropped marginally in all cases when the cycling was stopped but returned back to its original

values as soon as the cycling was resumed. When the difference in the potential was around 2.5 mV, the experiment was stopped and the system was brought down to zero load. The difference in the potential at zero load was also observed to be 2.5 mV, (fig. 3.60b). This clearly indicates that the interruptions did not affect the ACPD response and that the ACPD is able to detect and size the cracks even at zero external load.

In another experiment, the measurements were also interrupted during crack growth. Figure 3.61(a-b) shows the plot of ACPD signal as a function of time. At point A, the cycling was stopped and the system was brought down to zero load. The ACPD readings were nevertheless taken for some time. As is evident, the ACPD readings dropped a little. At point B, the CGM 6-3 was disconnected for some time and as expected the readings dropped to zero (location C). The electronics was then connected back to the specimen and fatigue cycling was resumed. The ACPD readings returned to their original value and the difference between the new and original readings was less than 0.1 mV (within noise level). At points D, E, F and G (see fig. 3.61b), fatigue cycling was stopped, the system was brought down to zero load, readings were taken for some time and then the cycling was resumed again. It can be seen that the potential dropped every time the loads were removed but returned to their original values as soon as the cycling (loading) was resumed. When the change in potential during cyclic loading had reached 24.2 mV (due to cracking) the experiment was stopped and load brought down

to zero. Note that a change of 24.2 mV was also observed at zero load due to the presence of the crack.

The above two experiments confirm that the present ACPD/current focusing technique is capable of detecting and sizing cracks in the presence and absence of external loads. Furthermore the interruptions did not affect the ACPD response to crack growth.

In some experiments. prior tc commencing a fatigue test the frequency was scanned between 30 kHz to 240 kHz while the current was fixed at 2 amp. and gain at 3000. The fatigue test was then carried out and the testing was stopped at a pre-determined change in potential due to cracking. The system was then brought down to zero load and the frequency was scanned again between 30 kHz to 240 kHz. The resulting potential differences before and after the fatigue test (at various frequencies) are shown in fig. 3.62. As expected. the sensitivity to crack detection increases with an increase in frequency. i.e. for the same crack depth. the δV at 240 kHz is much higher than at 30 kHz. Note that these results were obtained in the absence of any external load. This may be attributed to the fact that an oxide layer forms on the crack faces. thus making them electrically insulated and therefore the current must still go around the crack faces to complete the circuit. This further provides proof that the ACPD technique can also be effectively used as an off-line or as a Nondestructive Inspection (NDI) tool for crack detection and sizing.

3.9 Residual Stress Measurements

While working on the further development of the ACPD technique the measurements of residual stress turned out to be one of the spin off technologies in the present program. The development of this new capability stemmed from the observations that one batch of SEN specimens (Al 7075 T7351) displayed an 'anomalous' ACPD response during fatigue testing. The ACPD conditions were 120 kHz, 5 amp. and 3000 gain. Figure 3.63 shows one such curve displaying the ACPD response as a function of fatigue cycles. As can be seen, the ACPD value initially decreased with fatigue cycling and increased only when the ACPD probes started to detect the presence of a crack. This behaviour is completely different from the typical response of the ACPD observed in other fatigue tests (see fig. 3.52), where the signal remains fairly stable and increases only when the probes detected a crack. This behaviour has also been reported by other workers in Ni-base superalloys, who however, did not investigate the causes for its occurrence [95]. Therefore, it was decided to investigate this phenomenon further.

Figure 3.64 shows a calibration curve (120 kHz, 5 amp. and 3000 gain) obtained while carrying out the strain testing on Al 7075 T7351 SEN specimens. The maximum stress applied was 448 MPa (65 ksi) and the slope of the curve is 31.56 MPa (4.58 ksi) / mV change. This specimen came from an earlier batch cut from the same plate. Then, one sample from the batch exhibiting a different behaviour was taken and the same strain

testing was carried out. The maximum stress applied was same (448 MPa). The testing was carried out in exactly the same way as explained in section 3.6.3 pertaining to strain calibration (SEN specimen). The change in the ACPD output in this particular specimen was observed to be 12.6 mV as shown in fig. 3.65a. However, based on the calibration curve a change of 14.2 mV should have been observed. There was a difference of 1.6 mV between the two specimens. Using the calibration curve, fig. 3.64, it becomes evident that the relative difference of 1.6 mV corresponds to a stress value of approximately 50 MPa (7.3 ksi).

Another sample from the same batch, showing a different behaviour was stress relieved by subjecting it to a T73 heat treatment. The same strain testing was repeated after the heat treatment. The maximum stress applied was 448 MPa (65 ksi) and the change in output signal was found to be 14.2 mV as shown in fig. 3.65b. The change in the ACPD output was of the same magnitude as that observed in the specimen used for obtaining calibration curve, fig. 3.64.

These results suggest that there were compressive residual stresses present in the specimens that showed a different behaviour. As mentioned earlier, the change in the ACPD signal in this specimen (fig. 3.65a), was 1.6 mV less than expected, implying that the specimen was experiencing a stress of 398 MPa rather than experiencing 448 MPa of stress. Therefore, a compressive residual stress of 50 MPa was present in the specimen.

One more sample from the same batch was strain tested at a low applied stress of 102 MPa. This low maximum stress value was selected to rule out any possibility of the ACPD signal changing due to strain softening or hardening mechanisms normally induced by relatively higher stresses applied in the two previous tests described above. This particular experiment was carried out for 200 cycles. As shown in fig. 3.66 a gradual drop in the ACPD output as indicated by the arrow, occurred during cyclic loading. This was due to the relaxation of residual stresses during testing. The change in the ACPD output value in the first cycle was approximately 1 mV. In accordance with the calibration curve, fig. 3.64, the change in potential corresponding to an applied stress of 102 MPa should have been 3.2 mV. Therefore, a difference of 2.2 mV suggests that compressive residual stress of about 70.3 MPa was initially in the specimen.

To verify the above behaviour further, three specimens from the same batch of specimens were sent out for residual stress measurements using the X-ray diffraction measurement technique. The X-ray diffraction measurements were carried out at Institute for Aerospace Research (IAR), NRC using the $Sin^2\phi$ method and a Rigaku diffractometer. The X-ray diffraction results for the three specimens, verified that there were indeed compressive residual stresses present at the notch roots with these stresses being -40 MPa, -50 MPa and -100 MPa. The ACPD measurements, on the other hand had revealed that compressive residual stresses of the order of -50 MPa and -70.3 MPa

were present. Results from both techniques are therefore in reasonable agreement with one another.

The specimen. which had been used for strain testing. was then subjected to fatigue loading. The only difference was that the compressive residual stresses were expected to have been relaxed during mechanical loading.. The ACPD setting was kept at 120 kHz. 5 amp. and 3000 gain. Figure 3.67 shows the ACPD response with an increase in the number of cycles. As can be seen the ACPD values were initially very stable and increased only towards the end of the test once ACPD probes detected a crack. The crack initiated after only 11.200 cycles whereas in an earlier fatigue test on a specimen from the same batch described above (see fig. 3.63). the crack initiated after approximately 18. 000 cycles. The delay in crack initiation could very well have occurred due to the presence of compressive residual stresses present in the previous specimen. All of these experimental evidence therefore points to the fact that the ACPD technique can be used to quantify residual stresses in the structure.

4.0 PERFORMANCE OF THE ACPD SENSORS IN CF-18 FULLSCALE TESTS

4.1 Introduction

Three locations on three different bulkheads of a CF-18 aircraft were assigned for monitoring with the ACPD technique during the full scale testing.. The full scale testing was being carried out under IFOSTP, a collaborative effort between the Department of National Defence of Canada and the Royal Australian Air Force. The testing was being carried out at the Canadair Defence Division, Bombardier.

The three bulkheads, identified as bulkhead, 470.5, 488 and 497 are also known as wing carry through bulkheads. The three bulkheads are part of the center fuselage of the CF-18 aircraft. A schematic of the CF-18 aircraft, showing the location of the 488 bulkhead along with a more detailed schematic of bulkhead 488 is shown in fig. 4.1. The critical locations to be monitored on these three bulkheads were the center line in bulkhead 470.5, the hydraulic hole on the left side of the bulkhead 488 and the former segment flange radius of the bulkhead 497 on the left hand side.

4.2 Instrumentation and Probe Design

4.2.1 Bulkhead 470.5 - the Center Line Location

A strain gauge was installed in the center, where a crack was expected to initiate according to the finite element analysis carried-out by Canadair/DND. A schematic of the ACPD probe design along with the strain gauge is shown in fig. 4.2. On both sides of the strain gauge a current focusing device was glued. The active probes (channel 1 and channel 2) were attached across the current focusing device covering the critical area. Channel 1 was located on the forward (fwd) and channel 2 on the aft sides of the bulkhead. The reference probe was welded away from the critical area across the current focusing device on the fwd side, and on the left of the active channel 1. The other ends of the probe wires were welded on copper tracks of a PCB (which were glued on the thickness side of this bulkhead).

The voltage signal wires were soldered on the other end of the PCB and these wires were in turn connected to the input of the voltage scanner. The output of the voltage scanner was connected to the input of the pre amplifier at channel X. The reference probe was directly connected to the input of the pre-amplifier at channel Y. The scanner and the pre amplifier were placed six feet away in one of the recesses of the structure. The conductor of the co-axial current cable was soldered directly on one end of the

current focusing device. The other end of the current focusing device was connected to the copper pad through a small piece of wire soldered on both sides. The copper pads were in turn electrically connected to the surface by Al wires welded (ultrasonic welding) on the copper pads and on the structure. The shield of the current cable acting as a return conductor was soldered to another copper pad. Thus, the current from the cable first travels into the current focusing device, then into copper pad 1, then jumps from the copper pad to the structure. In the bulkhead, the current is forced to flow below the current focusing device in the opposite direction and into copper pad 2, thus completing the circuit. The other end of the current cable goes into the output of a three channel scanner which was placed near the pre-amplifier and the voltage scanner. The current scanner can switch the current between current focusing devices 1 and 2. Figure 4.3 shows photographs of the above location.

4.2.2 Bulkhead 488 Hydraulic Hole Location

Figure 4.4 shows a schematic of the probe design installed at this location. The probes cover an area from 12 o'clock to six o'clock position of this hole. This surface area around the hydraulic hole had been identified as the critical area. As can be seen a current focusing device was glued in the center of the location along the circumference covering the area from 12 o'clock to six o'clock position. Five probes were welded across the current focusing device. Channel 1 covered the surface region from 12:30 to

1:30, channel 2 from 1:30 to 2:30, channel 3 from 2:30 to 3:30, channel 4 from 3:30 to 4:30 and channel 5 covered from 4:30 to 5:30 region. The other end of the probes were welded on a PCB, which were glued on the side wall of the structure. Figures 4.5a to fig 4.5c show the location of the hole, a zoom of the area and the PCB respectively. The five potential probes were connected to the input of the voltage scanner (channels 1-5) and the current cable from this location was connected to the output of the current scanner at channel 1.

4.2.3 Bulkhead 497 Former Segment Flange Radius Location

This location contains a corner with a 90° bend. The schematic of the probe design used for this location is shown in fig 4.6. As can be seen, the principle of the probe design is identical to the one installed on the 470.5 location. Figures 4.7a to 4.7c show the location of this area, a zoom of the location with the ACPD sensors and the PCB respectively. The currents from this location were connected to channels 2 and 3 of the current scanner while the voltage probes were connected to channels 6 and 7 of the voltage scanner.

4.3 ACPD Probe Monitoring Plan

The input of the current scanner and output of the pre-amplifier (channel X and channel Y) were both connected to the CGM 6-3 which was installed 30 feet away on top of the platform (which supported the CF-18 aircraft test rig). The CGM 6-3 was set at 30 kHz. 5 amp. and 3000 gain. The output signal of channel X from the CGM6-3 was digitized and recorded into HP DVM (model 3457) and the output signal from the channel Y was connected to the HP DVM (model 34401). The DVM readings were then directly recorded into a computer installed in the control room, which was about 40 feet away from the CGM6-3. The computer also controlled the scanning sequence of the current and voltage scanner. This computer was remotely connected to another computer located at AMRA Technologies Inc. where the data could be monitored on-line. Thus, the data acquisition and scanning sequence could be controlled remotely from the facilities at AMRA Technologies. A schematic of the whole set up is shown in fig. 4.8.

According to the monitoring plan, for the first two blocks of spectrum loading, the voltage and the current scanners were connected to the 470 bulkhead location and for the next two blocks the scanner and the ACPD system were connected to the other two bulkheads (488 and 497). This is because the distance between 470.5 and 488/ 497 was quite large. Therefore, they needed to be monitored separately, otherwise the length of the voltage cables going to the pre-amplifier would have been problematic (noise

problems could have occurred because the signal picked up by the voltage probes was very small).

The current could be switched into one of the two locations in the 470.5 bulkhead or any one of the three locations in the 488 and 497 bulkheads. When current was switched to the fwd current focusing device on 470.5 location, the output from channel 1 was read by the probes and when the current was switched to the focusing device in the aft location then the output from channel 2 was being read by CGM 6-3. The readings from the reference probe were taken continuously. In fact, the channel selection on the voltage scanner controlled the current scanner. For example, if channels 1 to 5 were being read on 488 bulkhead, then channel 1 of the current scanner was activated and the current flowed in the 488 bulkhead. If channel 6 was being read, then channel 2 of the current scanner was activated and current flowed in the fwd side in the 497 bulkhead. When channel 7 was read then current flowed in the aft side location in 497 bulkhead and channel 3 of the current scanner was activated.

4.4 Effect of Strain Survey on ACPD Probe Response

Figure 4.9 shows snapshots of the readings taken at the 470.5 bulkhead for channel 2 and for the reference probe. The active probe (channel 2) was being read at 20 readings/ sec and the reference probe at 3 rdgs /sec. The readings were very stable and the

combined noise and the drift was very low at 0.5 mV. At the end of the plot, jumps appear in the readings for both active as well as reference probes. These jumps occur due to the fact that the aircraft was subjected to strain survey loads. During the strain survey, the structure, was subjected to 100% load spike. This spike (0-100-0%) is imposed to check the response of the structure as well as all the gauges installed on the aircraft to the applied load. After the spike, the aircraft was subjected to stepped loads from 0%-100%. The loading and unloading cycle was applied in fifteen steps. The loading path was similar to the tests carried out in the laboratory for strain testing. However, there are two main differences between the tests carried-out in the laboratory and the full scale test. First, the load steps were not of the same duration. Secondly, the ACPD measurements were carried-out continuously, rather than being synchronized with loading steps.

Figure 4.9b shows the zoom of the last part of the fig. 4.9a, detailing four such loading sequences. The scale on the left side pertains to active probe while the scale on the right pertains to reference probe. The absolute values are different for the reference probe but the scale is the same. The 100% load applied to the structure corresponds to about 70% of the load which was applied during the spectrum loading. The change in the signal due to loading for the active probe and the reference probe is different. The reason being that the active probe was measuring the potential across the critical area and was thus subjected to higher stresses than the reference probe. Note that the difference in the two

readings can give an idea about the stress concentration (K_t) of the critical location compared to the location where the reference probe is installed. Unfortunately, the factor K_t of this location was not provided to us by the Canadair/DND and according to their records has not been calculated (the calculation of K_t, by the finite element analysis would have been quite complicated considering the complexity of the location and the complex interaction of stresses involved). Figure 4.9c shows a zoom of the active probe detailing one complete loading sequence, while fig. 4.9d shows a further zoom on the stepped loading. The solid line shown in fig. 4.9d indicates the percentage of the load applied to the structure (data provided by Canadair) while the dotted line indicates the ACPD response. It can be clearly seen that each loading step is completely characterized by the ACPD signal, indicating that ACPD probes have been successful in tracking the response of the structure due to stepped loading (applied to the structure).

4.5 ACPD Probe Response to Flight Spectrum Loading

The aircraft will be tested for approximately 13000 SFH, while the life of a CF-18 aircraft in actual service condition is estimated to be 6000 SFH. Figures 4.10a and 4.10b show the snapshots of the ACPD response to flight loading spectrum for channel 2, on the 488 location and for channel 6 on the 497 location. The readings are flat, since no crack was detected by the probes.

Figures 4.11a and 4.11b show the readings for channel 1 and channel 2 of the bulkhead 470 for blocks 11 and 12 of the flight loading spectrum. These blocks correspond to 3250-3900 spectrum flight hours (SFH). Each block consists of approximately 325 SFH. The channel 2 readings shown in fig. 4.11b, are no longer flat but are continuously increasing with the flight loadings. This increase in the readings occured due to cracking. When the change in the ACPD was around 1.5 mV, the DND was informed that a crack had been detected on the aft side of the bulkhead 470.5 at the center line. After completion of block 12, the total change was approximately 4 mV. According to the calibration curve, (see fig. 3.56b, equation 3.7), 4 mV change is associated with a 0.350 mm crack depth. The calibration curve (fig. 3.56b and equation 3.7) was obtained for Al 7075 T651 material which has a resistivity of 52.2 nΩ.m [103]. The bulkhead, however is made from Al 7050 T7451 material which has a resistivity of 42.6 nΩ.m [103]. Therefore, to obtain the same change in ACPD due to a crack, 7050 Al T7451 material should have a crack depth 18% higher than that in the Al 7075T651 material. As a result a 4 mV change in the signal in the bulkhead would correspond to a crack depth of 0.415 mm.

The data shown in figs. 4.11a and 4.11b, had been acquired over twelve days. Figure 4.12a shows the same data from fig. 411b on a magnified scale. Fig. 4.12 (b-g) show zooms taken at different times within the twelve days. Fig. 4.12b is an ACPD plot between 63 to 67 hours of monitoring. As can be seen the testing had started around

64.7 hours. Before the start of the test, the ACPD readings were around 83.8 mV while the average ACPD values, just after the start of the test were approximately 85 mV. Figures 4.12c and 4.12d are further zooms, showing the data collected between 65 to 65.33 hours and 65.13 to 65.19 hours. The response of the structure to the spectrum loading is clearly visible in these figures. In the gaps between the three loading cycles, (see fig. 4.12c), the ACPD system was acquiring data for channel 1. Figure 4.12d, shows a detailed view of the flight loading cycle. Figures 4.12e to 4.12g show snapshots of the ACPD plots for monitoring periods ranging between 98-102 hours, 171-175 hours and 248-252 hours respectively. The ACPD readings were increasing slowly with the number of test cycles. The average ACPD readings, during spectrum loading had increased up to 89 mV (see fig. 4.12g). After approximately 251.4 hours of monitoring the test was stopped. The ACPD reading, at the end of the test was around 87.8 mV.

The change in the ACPD signal, both during loading and before and after the test was also approximately 4 mV. Therefore, as far as the ACPD is concerned, whether the structure is under a load or not does not affect the detectability of a crack. The results are very similar to the experiments carried-out during off-line measurements (see figs. 3.60 and 3.61). The results conclusively prove that a specimen or a structure does not have to be under tensile loads for crack detection and quantification. It is noteworthy, that the measurements carried-out in the laboratory with the ACPD technique were reproduced

in a real life scenario (IFOSTP). Thus, the ACPD can be used as an effective NDI tool in the field i.e. on real life structures.

After block 12, the ACPD sensors were removed such that the presence of a crack could be verified by the concerned authorities. The NDI techniques utilized by Canadair/DND authorities were visual inspection, eddy current (EC) and liquid penetration (LPI). These are the most commonly used techniques by the aerospace industry. Acoustic emission (AE) sensors were also placed at the same location and were taking on-line measurements similar to the ACPD sensors. All other techniques which were utilized, failed to verify the presence of a crack and as a result of these findings the testing was continued. The ACPD sensors were not put back on the structure because of the frequent need to inspect the area. The location was inspected every 325 SFH and at 5200 SFH a major NDI inspection was carried out. Again the presence of crack could not be verified.

After block 18, at around 5932 SFH the testing had to be stopped because a crack was detected by the eddy current technique at the same location. The presence of the crack was further verified by the LPI. The details of the crack are shown in fig. 4.13. Note that the crack is located at the location, covered by the channel 2 of the ACPD sensors. There was no crack at the center or on the forward side. The crack length verified by the LPT was 6.26 mm (0.25 inches) long and estimated to be between 0.5 to 0.75 mm (0.020 to 0.030 inches) deep. It is noteworthy that the crack was eventually detected by

eddy current technique almost after 2500 SFH had elapsed since the cracking call was given on the basis of the ACPD technique. The acoustic emission sensors were not able to detect the cracks. The normal usage of a CF-18 aircraft is around 400-500 SFH per year. In terms of this usage, therefore, ACPD technique had detected a crack 5 years before eddy current was able to pick it up.

5.0 CRACK INITIATION AND SHORT CRACK GROWTH BEHAVIOUR IN 7075 AL ALLOY

5.1 Data Processing Methodology

The calibration curves which relate ACPD changes to crack depths (figs. 3.59, 3.60) were used to convert the ACPD signal, varying as a function of number of cycles, into crack depth versus number of cycles plots (Fatigue testing conditions are described in section 3.7). A typical plot of crack depth versus the number of fatigue cycles thus obtained is shown in fig. 5.1. This particular plot only shows data from 9930 cycle onwards. The crack depth data prior to the 9930^{th} cycle was not calculated because there was no detectable change observed in the ACPD signal. This is because below the 40 μm crack depth, crack detection was not possible with the ACPD conditions employed.

To obtain the 'a' versus N plot, such as the one shown in fig. 5.1, the following steps were carried out. Firstly, the initial five to ten cycles (cycle 9920-9930 in fig 5.1), for which a detectable change of ACPD was measured, were ignored. This was done to avoid a sudden change in crack growth rates associated with the detection limit of the technique, i.e. the no crack/ crack transition. Hence, if the initial ten cycles had been used in the data analysis, the initial crack growth rate would have appeared "artificially higher" as shown in fig. 5.2a. Figure 5.2b shows the crack growth (da/dN) versus crack

depth (a) curve if the initial ten cycles were ignored. The inclusion of the ten cycles led to pronounced dips in the beginning of the crack growth rate data, fig. 5.2a which resembled the typical short crack effect (see fig. 2.1) observed by many researchers [8-11]. However, in the present case these dips occurred due to the methodology followed to process the data and not related to any particular physical phenomenon.

Secondly, after the proper selection of the data, a polynomial was fitted through the data points. This polynomial curve fitting was conducted to smoothen the data, such that variations of the ACPD signal which occur due to electrical noise or due to variations in the load cycling are minimized. Note that the loads employed during fatigue cycling would not cause a problem if the data are acquired at the same load level all the time. As mentioned previously, data acquisition was carried out every 3.34 seconds. Therefore, the load levels associated with the ACPD measurements varied from reading to another. Lower order polynomial fits were always preferred over higher order polynomial. While a higher order polynomial may result in precision fitting, the advantage of polynomial fitting to smoothen the data can easily be lost, which may result in unnecessary inflexions (sudden changes in the slope) in the crack growth curve which are not related to the actual crack growth behaviour of the material, but occur as a result of the polynomial fitting procedure followed.

Once the data were processed through these two steps, the calibration equations correlating the change in ACPD with the crack depth were used to convert the data into crack depth versus the number of cycles plots. The crack growth rate was then determined using seven point polynomial fitting procedure as recommended in the ASTM E-647 standard.

5.2 Stress Intensity Factor (SIF) Calculations

The SIFs were calculated using the model proposed by Newman [57]. The model, as described in the Appendix II, was developed for semi-elliptical cracks initiating in the centre of a semicircular notch subjected to a uniform remote tensile load as shown in fig. 5.3. The reason for choosing this model lies in its applicability to the semi elliptical cracks such as those found in our experiments. The other SIF solutions proposed in the literature, all assume through cracks. The equation used to obtain SIF is given by

$$K = S \sqrt{\pi c} / Q \, F_{sn} (c/a, c/t, a/r, a/w, r/t, r/w, \varphi) \qquad (5.1)$$

where

K = stress intensity factor,

S = far field remote stress ,

Q = shape factor, depending on c/a ratio,

F_{sn} = boundary correction factor,

r = radius of the notch.

t = half thickness of the specimen.

w = specimen width.

φ = the angle (radians) with respect to the specimen center line

In the model, the r/w ratio is a variable, but Newman [57] used a constant value of 1/16 in their calculation. The r/w ratio of the specimen used in the present testing program was 1/10. It was however assumed that the SIF calculations made on the basis of Newman's model were applicable for our specimen for thumb-nail cracks. This assumption stems from the fact that the FEA results of Beres and Koul [110], using a r/w ratio of 1/8, showed very little difference relative to the results of Newman using an r/w ratio of 1/16 as long as the cracks were thumb-nail in shape. However, they found that for through-cracks the SIFs varied significantly with r/w ratio.

For short cracks, the crack tip plastic zone can be quite large relative to the crack depth thus invalidating the LEFM assumptions. Newman accounted for the crack tip plasticity by adding one quarter of the crack tip plastic zone to the crack length in order to extend the applicability of LEFM SIF into elastic plastic region of short crack growth [57]. However, upon examining the effect of crack tip plasticity on SIF calculations, it was found out that the SIFs changed by less than 3 % for the data generated in the present study. Therefore, crack tip plastic zone correction was not applied to the experimental data.

Typical variations of the boundary correction factor, (F_{sn}) and stress intensity factor, (K) using Newman's model, as a function of crack depth, 'a' are shown in figs. 5.4 and 5.5 respectively. Note that the variation in the F_{sn} and K are very similar to Beres and Koul's finite element analysis results [110].

5.3 Crack Shape Variation

Figure 5.6 shows the variation of crack aspect ratio (c/a) with the half crack length, c. Only the dominant crack length was taken into account to arrive at this plot. In this plot, there are two data points which revealed unusually high aspect ratios compared to the rest of the data. This discrepancy arises as a result of coalescence of small cracks. Crack coalescence results in a rapid increase in the crack length but not the crack depth and the net result is an increase in the crack aspect ratio. Figure 5.7 shows another plot of c/a versus c/t. As can be seen, the crack aspect ratio, c/a increases with increasing surface crack length, c or c/t. This is in agreement with the results of Newman [57,111]. The calculation of the variation of $K_{\varphi=\pi/2}$ / $K_{\varphi=0}$ with crack depth using Newman's model (see Appendix II) shows that $K_{\varphi=\pi/2}$ increases faster than $K_{\varphi=0}$. Newman's model [57] predicts that surface crack length will grow faster than the crack depth. While the above two plots confirm this behaviour, the increase in c/a is not as prominent. The regression analysis may be strongly influenced by the three data points which show high c/a values.

Figure 5.8 shows another plot of c/a varying as a function of half crack length, c without the three data points (of aspect ratio>2) while keeping the scale of the axis the same as fig. 5.6. It can be seen, that c/a decreases with increasing crack length. This observation is exactly opposite to the predictions of Newman's model [57]. The variation in c/a was further plotted as a function of crack depth, (a) as shown in fig. 5.9 and again the three data points with unusually high c/a were not included in this plot. It can again be seen that c/a decreases with increasing crack depth, suggesting that 'a' is increasing faster than 'c'. To confirm this behaviour, the surface crack length (c) was further plotted against crack depth (a), fig. 5.10. This plot shows that initially, the surface crack length (c) increases faster than the crack depth (a) in accordance with the predictions of Newman [57]. However, when the crack depth is around 2 mm, the crack becomes a through thickness crack and as a result, there is no more increase in the surface crack length. The increase in crack depth beyond the 2 mm mark results in a decrease in the c/a ratio because c is no longer increasing and this introduces an artifact in the overall c/a versus a trend.

Multiple crack initiation can also significantly affect the crack aspect ratio. This effect can be clearly seen in fig. 5.11. In this plot the crack aspect ratio (c/a) was calculated using the total surface crack length of all the cracks, and the c/a ratio increases significantly below ~ 1 mm crack depth. The crack aspect ratio was also plotted as a function of the crack area, fig. 5.12. The c/a ratio decreases with increasing crack area,

but again, these results are influenced by the fact that even when cracks become through thickness cracks, the crack area continues to increase due to an increase in the crack depth alone. Therefore, the true behaviour of the crack shape variation can only be seen in plots where crack length is plotted against the crack depth (for a ≤ 2mm) i.e. fig. 5.10.

The Newman's model, as explained in the previous section is applicable only to thumb-nail cracks. Therefore, when the crack depth reaches 2 mm, this model is no longer applicable. Hence, the data was analyzed only for crack depths up to 2 mm. Furthermore, the variation in c/a ratio as a function of crack depth (a) as shown in fig. 5.9 was used in the analysis rather than assuming a constant c/a ratio.

5.4 Crack Initiation in 7075 Al Alloy

The SEN specimens machined from the plate were cut in such a way that grain orientation relative to crack depth direction varied from one batch of specimen to another. Three main group of specimens at grain orientation angles of 18°, 55° and 70° were machined from 7075 Al alloy with T651 temper and specimens with two grain orientations of 80° and 90° were machined from 7075 Al alloy with T7351 temper as shown in fig. 5.13a - 5.13e respectively. Figure 5.13f shows a specific specimen with T651 temper and 8° grain orientation which was also tested to ascertain certain observations as will become evident later. The crack depth direction is indicated by an

arrow. The corresponding grain size in the crack depth direction were measured to be 25 μm, 38 μm and 80 μm for 18°, 55° and 70° grain orientations respectively for the T651 temper. In the case of T7351 temper, the grain size in the crack depth direction was found to be 85 μm for the 80° orientation and 110 μm for the straight (90°) orientation. The specimen orientation, temper conditions used and corresponding grain sizes are summarized in table 5.1.

As explained earlier in section 3.7, the low cycle fatigue experiments were conducted using different ACPD conditions such as different frequencies, different currents etc. Therefore the sensitivity of the ACPD with respect to the crack depth measurement was different under different ACPD conditions. Taking these variables into account, crack initiation was defined as the number of cycles required to obtain crack depth values of either 200 μm or 300 μm. The 300 μm deep crack initiation criterion was selected for the less sensitive ACPD testing condition, i.e. 30 kHz, 1 ampere and 3000 gain. However, it is very optimistic and sometimes unrealistic to select 300 μm crack depth as the initiation criterion in view of the sensitivity and reliability of the technique for the above mentioned ACPD condition. Nevertheless, this was done to produce a set of data points for the same grain orientation specimens, some of which were also tested at higher ACPD currents and frequencies. In higher ACPD currents and frequency tests, many tests were stopped long before a crack could attain a depth of 300 μm. Since

accurate and reliable data could be obtained at higher currents and frequencies. crack initiation point was defined as a 200 μm deep crack.

Figure 5.14. shows a plot of notch root peak stress (σ. where $\sigma = k_t.S$) versus number of cycles to LCF crack initiation (N_i) using 300 μm crack initiation criterion for the 18° grain orientation. T651 temper specimens. As expected the crack initiation life decreases log-linearly as a function of applied stress. The number of cycles to LCF crack initiation ranged from 4500 cycles at 795 MPa to around 22000 cycles at 400 MPa. Figure 5.15 shows the number of cycles to crack initiation using 300 μm crack initiation criterion for 70° grain orientation and T651 temper specimens. The number of cycles to crack initiation varied from 2700 cycles at 795 MPa to around 13.700 cycles at 466 MPa. At a given stress level. the crack initiation life for the 18° orientation specimen is higher than the 70° orientation specimens. It is noteworthy. that the average grain size of the 18° orientation specimens is finer than the 70° orientation specimens. Finer grain size leads to a more uniform slip dispersal and longer LCF life provided that other microstructural features are similar.

Figure 5.16 shows a plot of notch root peak stress versus (σ) the number of cycles to crack initiation (N_i) using 200 μm crack initiation criterion for the 55° grain orientation. T651 temper specimens. The number of cycles ranged from 1800 cycles at 577 MPa to 12500 cycles at 466 MPa. Figure 5.17 is the same type of plot for 80° grain orientation

as the earlier one but for T7351 temper. The N_i in this case varied from 37186 cycles at 378 MPa to 12116 for 517 MPa.

Figure 5.18 compares the N_i data for T651 and T7351 tempers. The number of cycles required to initiate a 200 μm crack is significantly higher for the T7351 temper as compared to the T651 temper even though the grain size is finer in the case of T651 specimen. However, if the data is extrapolated linearly, the plots will cross over around 450 MPa (assuming the extrapolation is correct). Therefore, below 450 MPa, the N_i will be longer for the T651 temper as compared to the T7351 temper. The notch root peak stress data shown in figure 5.18 was normalized with the respective flow stress of the two tempers and replotted against the number of cycles as shown in the figure 5.19. The flow stress used for normalizing was taken as the average of the yield and the ultimate tensile strengths. The yield and tensile strengths of the two tempers used are provided in table 5.2. The results indicate that T651 has better crack initiation resistance below 0.8 of the flow stress while T7351 has better crack initiation resistance above eighty percent of the flow stress. These result are similar to the results obtained for Al 7XXX series by Sanders, Jr et al [112]. They observed that fatigue lives for total strain amplitudes greater than 10^{-2} generally increased with increasing ductility while for the total strain amplitudes less than 5×10^{-3} the fatigue lives generally increased with increasing strength. From a microstructural perspective, the T7351 temper overages the strengthening precipitates which would be expected to promote wavy slip as opposed to

planar slip in underaged or peakaged microstructures. This behaviour has also been reported in other alloy systems [51].

The crack initiation was invariably associated with inclusions or voids probably created by the removal of inclusions. At the crack initiation site, debonding between the inclusions and the matrix was frequently observed. Figure 5.20 shows an SEM micrograph of crack initiation site (indicated by the arrow) in 55° orientation T651 specimen. The notch root peak stress for this particular specimen was 475 MPa. The notch surface is at the bottom of the micrograph and the crack propagation direction is towards the top of the page. The same arrangement and convention is followed for all the fractographs. It is evident that the crack initiation region is transgranular and possesses distinct crystallographic features. Extrusions can be seen near the crack initiation sites. These extrusions are formed by a mechanism involving crack closure and fracture surface rubbing [113]. The ridges are observed almost parallel to the crack growth and some crack arrest lines (horizontal lines) can also be seen perpendicular to the crack growth direction. Figure 5.21a and fig. 5.21b show the crack initiation sites for other two T651 specimens tested at notch root stress values of 517 and 795 MPa and grain orientation of 8° and 18° respectively. Crack initiation regions are again transgranular containing distinct crystallographic features. Extrusions can again be seen at the crack initiation sites.

Figures 5.22a and 5.22b show the crack initiation sites in 80° grain orientation T7351 temper specimens with a notch root peak stress values of 377 and 447 MPa respectively. The crack initiation sites are transgranular possessing crystallographic features. Some secondary cracking can be observed at the grain boundaries. The smooth appearance of the fracture surfaces may be attributed to the rubbing of the crack faces.

5.5 Short Crack Growth Behaviour of 7075 Al alloy

The crack growth was predominantly transgranular with some secondary cracking observed along the grain boundaries. Figure 5.23 shows a plot of da/dN versus crack depth for the three different grain orientations (8°, 18° and 70°) SEN specimen in T651 condition fatigue tested at same notch root peak stress value of 517 MPa. It is evident that crack growth rate for the 8° orientation specimen is the slowest and and it is highest for 70° orientation. This behaviour can be rationalized on the basis of the interaction of the crack front with the grain boundaries. The number of grain boundaries encountered by the crack front in the crack depth direction will be considerably greater for the 8° orientation specimen (grain size ~ 24 μm) than for other two orientations especially for the 70° grain orientation specimen (grain size ~ 80μm).

A montage of the fracture surface of a 8° orientation specimen tested at 517 MPa is shown in fig. 5.24. The overall crack growth behaviour can be classified as stage I

transgranular. The crack appears to be interacting with the grain boundaries where crack arrest lines seem to coincide with the grain boundaries. The re-initiation sites of the crack can also be observed at several places along the grain boundaries as indicated by the arrows on the montage. The top of the fractograph marked as A. shows the final overload region. The interaction of the crack front with the grain boundaries. which leads to crack arrest and subsequent re-initiation. resulted in slower crack growth in this particular orientation.

Figure 5.25 shows the montage of the fracture surface for the 18° grain orientation specimen in T651 condition tested at 517 MPa. A similar fractographic pattern as that described for the 8° orientation specimen (crack interaction with the grain boundaries) was observed. Although not shown here. the fracture surface for 70° grain orientation specimen also showed a similar fracture pattern with considerably lower incidence of crack arrest along the grain boundaries perpendicular to the crack growth direction. This is because in 70° grain orientation. the crack front in the depth direction encounters lower number of grain boundaries during its advancement.

The crack growth versus crack depth plots for the 18° orientation specimen fatigue tested at 517 MPa (2 tests) and for the 55° orientation specimen tested at a notch root peak stress of 475 MPa (2 tests) are shown in figs. 5.26a and 5.26b respectively. It is evident that the data points for the two tests carried out on the same grain orientation

specimen at the same stress level fall within a reasonable scatter band. These observations confirm that the differences in the crack growth rates shown in fig. 5.23 were indeed due to the difference in the specimen grain orientations and not due to errors associated with the test procedure.

A comparison of da/dN versus crack depth plots for the same grain orientation (18^{o}) specimens but fatigue tested at different notch root peak stress values of 397 MPa and 795 MPa is shown in fig. 5.27. As expected, at a given crack length, the crack growth rates obtained at the higher testing stress are higher than those obtained at the lower stress. The crack growth rates at 795 MPa change somewhat erratically in the beginning up to a crack depth of 0.7 mm. It was not possible to relate this erratic behaviour to any physical phenomenon. Figure 5.28 presents a montage of the fracture surface for a 18^{o} grain orientation specimen tested at 795 MPa. The fracture surface shows evidence of a quasi-static fracture along with the heavily striated fracture surface. These striations become visible within 60 μm from the notch root surface, indicating that stage II crack growth starts much earlier at a higher stress value. Extensive tearing is also visible on the entire fracture surface. At the bottom of the dimples, inclusions can also be seen. Crack arrest along the grain boundaries is not as visible as compared to the fracture surface montage shown in the fig. 5.25 for the same grain orientation specimen tested at a lower stress level of 517 MPa. This indicates that at high notch root stresses, grain boundaries are not as effective barriers to crack advancement as at lower stresses.

Figure 5.29 shows plots of da/dN versus crack depth curves for the T7351 temper. Figure 5.29a shows the crack growth curves for the same grain orientation specimens tested at the same stress level. The curves can almost be superimposed on top of one another indicating that the scatter associated with the experimental technique is very small. Figure 29b shows a plot of da/dN versus crack depth obtained at the same stress level but with different grain orientations of 80° and 90°. The crack growth curve for the 90° orientation changes irrationally (first increases and then decreases with an increase in crack depth) up to 110 μm and the slope of the curve for the other orientation is higher in the beginning (up to ~ 65 μm). The respective grain sizes for the two orientations are 110 μm and 80 μm. It appears that the crack growth rate is higher within the first grain and upon approaching the grain boundary, drops down or slows down. However, these specimens are from the same batch of specimens which had compressive residual stresses induced in them as a result of machining as explained earlier in section 3.9. Furthermore, some of these specimens were initially used for strain testing. Therefore, no conclusive statement can be made from these results at this stage.

Figure 5.30a shows striations in a T651 specimen with 70° grain orientation fatigue tested at a peak stress of 517 MPa. Figure 30b is a zoom of the striations approximately 1 mm away from the notch surface. The crack growth rate measured through striation counting technique is in the range 6.6×10^{-4} mm/cycle. Figure 5.31 shows the

corresponding growth rates versus crack depth plot for the same specimen where crack growth rates were measured by the ACPD technique. The crack growth rate from fig. 5.31 works out to be 7.0×10^{-4} mm/cycle at crack depth of one mm. Figure 5.32 shows the striated fracture surface of another T651 specimen with a grain orientation of 18° fatigue tested at 795 MPa. This fractograph is from an area which lies 550 μm from the notch root. The crack growth rates measured through striation counting technique is 7.4×10^{-4} mm/cycle while the crack growth rate measured by ACPD technique is 8×10^{-4} mm/cycle. fig. 5.27. These results indicate that the ACPD measurements agree reasonably well with the striation counting technique measurements and reinforce the accuracy and sensitivity of the ACPD technique.

The crack growth rates were further correlated with the cyclic stress intensity factor range (ΔK) calculated using the Newman's model [57]. Figure 5.33 (a-c) shows the da/dN versus ΔK curves for T651 specimens possessing grain orientations of 70°, 55° and 18° respectively. Symbols A, B and C on these plots indicate that the data were generated at different notch root stress values of 475 MPa, 517 MPa and 795 MPa respectively. In figure 5.33b the FCGR data were generated at notch root stress of 466 and 475 MPa respectively. The crack growth rate curves depict acceptable scatter for 70° and 55° grain orientation respectively. However, there is considerably more scatter (almost one order in magnitude) in the data generated in the 18° orientation specimens at 795 MPa notch root stress at a $\Delta K = 12$ MPa $\sqrt{m}$. Figure 5.34 plots the data for all three

orientations together on a single graph. The scatter band pertaining to the short crack data generated by Newman et al [111] at notch root peak stress of 378 MPa for Al 7075 T6 L-S orientation is also superimposed on this figure. It should be noted that the data obtained for the 70° orientation lies almost parallel to data of Newman et al [111] because this grain orientation is closest to their grain orientation. It is also evident that the scatter for a given orientation is much less than short crack data of Newman et al [111]. The crack growth rates measured at a given ΔK are higher in our case than that measured by Newman et al [111]. figure 5.34.

Careful examination of the data generated in the current test program shows that in addition to the stress intensity range. the crack growth rates are also strongly influenced by the applied notch root stress particularly at high stress (see figs. 5.33 a-c). This implies that ΔK alone does not describe the short crack growth in 7075 Al alloy. Figures. 5.35a -5.35c show all the da/dN versus ΔK curves obtained at the same stress levels of 475. 517 and 795 MPa respectively but each plot contains data from different grain orientation specimens. All plots show that the higher the stress level the higher the growth rate at the same ΔK. Similar conclusion was reached by Dubensky [114] while working on 7075 T6 material at stresses ranging between 380 to 500 MPa. He observed that the higher the value of maximum gross stress the higher were the crack growth rates for a given value of ΔK. Similar behaviour could be seen in the data generated by

Newman [57] on 2024 T3 aluminium alloy at stresses ranging between 63.75 MPa to 255 MPa at stress ratio, R = -1.

The ΔK factor was normalized with respect to peak stress (σ) and the da/dN plotted as a function of $\Delta K^2 / \sigma$. This figure also includes the scatter band associated with the data of Newman et al [111]. It is evident that the data collapses into a narrow scatterband as compared to the data shown in fig. 5.34. The data pointed by the arrow in fig. 5.36 shows some discrepancy with respect to the rest of the data i.e. slower growth rates at same ΔK value. However it should be emphasized that the data pointed by the arrow corresponds to the grain orientation of 8° and 18° obtained at stress level of 517 MPa. As mentioned earlier at this stress level, there was a strong interaction between the crack front and the grain boundaries (see fig. 5.24 and 5.25).

The ΔK factor was also normalized with a constant C, with C taken as the ratio of notch root peak stress to the flow stress of the material. Figure 5.37 is a plot of da/dN versus $\Delta K/C$. The scatter band has become somewhat narrower. The effectiveness of this normalization procedure is more visible for the data generated at a peak stress of 795 MPa. The better convergence of the data obtained at higher stresses, implies that constant C takes into account the effect of notch root plasticity.

Figures 5.38(a.b) show the da/dN versus ΔK for T7351 temper for the two same orientations of 80° and 90° while fig. 5.39 shows the data for both the orientations on a single plot. There is much less scatter in T7351 specimens as compared to the T651 temper specimens. One of the reason for having much less scatter is that all the experiments on T7351 temper were carried out using only one set of ACPD conditions (120 kHz and 5 amperes). Furthermore. the probe design was same for all specimens and the tests were carried out far later during the study than when the T651 temper specimens were tested. All data on T7351 specimens correspond to cracks of 40 μm in depth onwards and this was not the case with the T651 temper because different ACPD conditions were used at different stages during the program. Fig. 5.40(a.b) show the plots da/dN versus $\Delta K^2/\sigma$ and $\Delta K/C$ for T7351 temper. The data collapses into narrow scatter bands for both the cases.

In 7075 alloy with both T651 and T7351 tempers. $\Delta K^2/\sigma$ and $\Delta K/C$ parameters are better able to correlate the data than ΔK alone. This is because the crack growth rates show a strong stress dependence. This also implies that LEFM parameter. ΔK calculated using Newman's model may not entirely characterize the crack driving force.

6.0 CONCLUSIONS

- An advanced ACPD system using current focusing technique for on-line as well as off-line measurements was successfully implemented in laboratory and industrial scale test environments.

- A simple and flexible ACPD probe design methodology was developed to conduct stress, strain and crack measurements on a wide variety of specimen geometries and actual airframe structural parts. The pros and cons of the current focusing technique were fully established and the technique was successfully incorporated in ACPD probe design. The effectiveness of the current focusing technique and the resulting three-dimensional control of the current density distribution have been demonstrated.

- Ultrasonic welding technique was extensively modified to weld ACPD probes to specimens as well as large structural components on F-18 aircraft. It was demonstrated that the ultrasonic welding does not affect the base material performance under fatigue loading condition.

- Crack calibration curves detailing crack depths versus potential difference were obtained at three different frequencies. A quadratic function was used for

correlating crack depths with potential change. The reliability of the regression were better than 99%. The smallest crack depth detected was 140 μm at 120 kHz. 5 amp. and 3000 gain. The experimental results were in agreement with the finite element calculations (also showing a quadratic relation) which related the surface potential with normalised crack depth.

- Potential differences due to cracks were also correlated with crack areas since the potential difference is affected by the overall crack area rather than just the crack depth. The calibration curves (also quadratic functions) relating crack area with potential difference were obtained with the reliability of the regression being better than 99%. This is important in the case of multiple site damage studies (multiple cracks).

- It was demonstrated that the effect of load cycling on stress/strain response could be easily followed with the ACPD signal. Strain calibration curve were obtained for a four point bending specimen with the reliability of the regression being better than 97%.

- Residual stress measurements were also carried out using the ACPD technique. This is one of the most significant spin-off of this study. The ACPD technique was able to detect the relaxation of residual stresses due to step loading (static

loading) and fatigue cycling. The residual stress measurements carried out with the ACPD technique were also verified by the X-ray diffraction measurements. Another spin-off of this program was the ability of the ACPD technique to perform case depth measurements [115] in carburized and heat treated components.

- It was demonstrated that the interruptions in the fatigue test did not adversely affect the ACPD response. The change in the potential due to crack was same during load cycling and at zero load. Thus, ACPD technique can also be effectively used as an off-line measurement system. It can thus become a valuable NDI tool and be used for preventive maintenance scheduling under RFC management philosophy.

- The ACPD sensors were installed on a CF-18 aircraft undergoing full scale testing (IFOSTP). The sensors were able to measure the response of the structure to load cycling. A crack was detected by the sensors on one of the critical locations monitored by the ACPD technique. The crack was detected at the fracture critical location almost 2500 SFH (~ five years in real life) before any other established techniques (visual inspection, Eddy Current, Liquid Penetration and acoustic emission) utilized by the DND/Canadair was able to detect the

crack. The magnitude of the signal was able to size the cracks using calibration curves established on the laboratory experiments.

- ACPD technique was used to characterize the short crack growth behaviour of naturally initiated fatigue cracks in 7075 Al alloy (for a $\geq$ 40 μm crack depth).

- The variation of crack aspect ratio showed that surface crack length grew faster than the crack depth with the c/a ratio being approximately 1.3. It was found that the best way to characterize this behaviour was to study crack length versus crack depth variations rather than plotting c/a ratio as a function of 'a' or 'c' because through-cracks create an artifact in the c/a versus 'a' or 'c' data. It has also been demonstrated that data processing procedures used for converting the ACPD signal versus number of fatigue cycles into crack depth versus number of fatigue cycles curves can introduce artificial trends in the data.

- A comparison of the crack initiation life data generated on Al 7075 T651 and Al7075 T7351 condition showed that T651 had better crack initiation resistance at lower stresses ($\leq$ 0.8 flow stress) whereas the T7351 temper had better crack initiation resistance at higher stresses. The crack initiation regions in both cases revealed the presence of a transgranular fracture and distinct

crystallographic stage I fracture features. As expected, increasing the fatigue load reduced the degree of stage I growth.

- The fatigue crack growth rates were strongly influenced by the grain orientations. The crack growth rates in T651 material were slower for the 8^{o} grain orientation specimen than in 70^{o} grain orientation specimen. At lower stresses, the grain boundaries were found to be effective barriers to crack propagation. At higher stresses (~ 795 MPa) no interaction between crack front and grain boundaries was clearly visible in the fractographs.

- The fatigue crack growth rates were plotted as a function of the SIF, (K) calculated using Newman's model for thumb-nail cracks. Specimens possessing various crack depths but loaded to the same ΔK level at the crack front showed that crack growth rates increased with increasing applied stress. Therefore, K may not be an adequate measure for the crack driving force in 7075 Al alloy. Modified parameters $\Delta K^2/\sigma$ and $\Delta K/C$ were found to be better for correlating the fatigue crack growth rates because both of these parameters led to a reduction in the scatter.

7.0 RECOMMENDATIONS FOR FUTURE WORK

- Off-line measurements carried out in the present study have demonstrated that ACPD readings can detect and size cracks without the presence of external loads. This conclusion was further supported by the results obtained during on-line monitoring of the full scale test carried out on the F-18 aircraft. Therefore, the applicability of ACPD as an NDI tool should be thoroughly investigated.

- The results detailing the measurements of residual stresses using ACPD technique appear promising. Further investigations need to be carried out to verify the possibility of measuring residual stresses by the ACPD technique.

- Statistically significant short crack growth data bases need to be generated to assess the applicability and effectiveness of $\Delta K^2/\sigma$ and $\Delta K/C$ parameters for describing the short crack growth behaviour of Al alloys and other engineering alloy systems.

8.0 REFERENCES

[1] WANHILL, R.J.H. (1986). "Short Cracks in Aerospace Structures". The Behaviour of Short fatigue Cracks. Eds., K.J.Miller and E.R. de los Rios. EGF Pub. 1. Mechanical Engineering Publications. 27-36.

[2] KOUL, A.K., WALLACE, W. and THAMBURAJ, R. (1984). "Problems and Possibilities for Life Extension in Gas Turbine Components". National Research Council Canada. LTR-ST-1503.

[3] HWANG, I.S. and BALLINGER, R.G. (1992). " A Multi-Frequency AC Potential Drop Technique for the Detection of Small Cracks". Measurement Science Technology, Vol. 3, 62-74.

[4] DAI, Y., MARCHAND, N.J. and HONGOH, M. (1995). " Fatigue Crack Growth Measurements in TMF Testing of Titanium Alloys using an ACPD Technique". Special Applications and Advanced Techniques for Crack Size Determination STP 1251, Eds., J.J.Ruschau and J.K.Donald, ASTM, Philadelphia, 17-32.

[5] VEROPEST. I.. AERNOUDT. E.. DERUYTTERE. A. and NEYRINCK. M. (1982). "An ACPD Method for Detection and Measurement of Surface Microcracks during Fatigue Testing of Wires". Advances in Crack Length Measurement. Ed. C.J.Beevers. EMAS Publications. West Midlands. U.K.. 295-322.

[6] DOVERS.W.D.. RUDLIN. J.R. and TOPP. D.A. (1991). "Fatigue Crack Measurements in Offshore Structures". Fatigue Crack Measurement Techniques and Applications. Eds.. K.J.Marsch and R.O.Ritchie. EMAS Publications. West Midlands. U.K.. 487-507.

[7] PEARSON, S. (1975). "Initiation of Fatigue Cracks in Commercial Aluminium Alloys and the Subsequent Propagation of Very Short Cracks". Engineering Fracture Mechanics. 7. 235-247.

[8] BOLINGBROKE. R.K. and KING. J.E. (1986). "A Comparison of Long and Short Fatigue Crack Growth in a High Strength Aluminium Alloy". The Behaviour of Short fatigue Cracks. Eds.. K.J.Miller and E.R. de los Rios. EGF Pub. 1. Mechanical Engineering Publications. 101-114.

[9] SONIAK. F. and REMY. L.. (1986). " Fatigue Growth of Long and Short Cracks in a Powder Metallurgy Nickel Base Superalloy". The Behaviour of Short Fatigue Cracks. Eds.. K.J.Miller and E.R. de los Rios. EGF Pub. 1. Mechanical Engineering Publications. 133-142.

[10] SURESH. S.. and RITCHIE. R.O. (1984). "Propagation of Short Fatigue Cracks". International Metals Review. American Society for Metals. Vol. 29. No. 6. 445-476.

[11] WANG. S.Z.. MILLER. K.J.. BROWN. M.W. and DE LOS RIOS. E.R. (1991). "A Statistical Analysis of Short Fatigue Crack Growth". Fatigue Fract. Engng. Mater. Struct.. Vol. 14. No. 2/3. 351-368.

[12] TANAKA. K. (1987). "Mechanisms and Mechanics of Short Fatigue Crack Propagation" JSME Int. Journal.. 30. 1-13.

[13] MILLER. K.J. and DE LOS RIOS E.R. Eds. (1986). "The Behaviour of Short Fatigue Cracks". EGF Pub. 1. Mechanical Engineering Publications. London.

[14] RITCHIE, R.O. and LANKFORD. J. Eds. (1986). "Small Fatigue Cracks". Metall. Soc., Warrendale, PA.

[15] MILLER. K.J. and DE LOS RIOS. E.R. Eds. (1992). "Short Fatigue Cracks". ESIS 13. Mechanical Engineering Publications. London.

[16] MILLER. K.J. Ed. (1991). "Short Fatigue Cracks". Fatigue Fract. Engng. Mater. Struct., Vol. 14, No. 2/3.

[17] MILLER. K.J.. (1987). "The Behaviour of Short Fatigue Cracks and their Initiation. Part II - A General Summary" Fatigue Fract. Engng. Mater. Struct., Vol. 10. 93-113.

[18] RITCHIE. R.O. and LANKFORD. J. (1986). "Overview of the Small Crack Problem". Small Fatigue Cracks. Eds.. R.O.Ritchie and J.Lankford. Metall. Soc.. Warrendale. PA.. 1-5.

[19] LANKFORD. J.. DAVIDSON. D.L. and CHAN. K.S. (1984). "The influence of Crack Tip Plasticity in the Growth of Small Fatigue Cracks". Metallurgical Transactions A, Vol. 15A. 1579-1588.

[20] BROWN. C.W.. KING. J.E. and HICKS. M.A. (1984). "Effect of Microstructure on Long and Short Crack Growth in Nickel Base Superalloys". Metal Science. Vol. 18. 374-380.

[21] BLOM. A.F., HEDLUND. A., ZHAO. W., FATHULLA. A., WEISS. B. and STICKER. R. (1986). "Short Fatigue Crack growth Behaviour in Al 2024 and Al 7475". The Behaviour of Short fatigue Cracks. Eds., K.J.Miller and E.R. de los Rios. EGF Pub. 1. Mechanical Engineering Publications. London. 37-66.

[22] HOLM. D.K. and BLOM. A.F. (1984). "Short Cracks and Crack Closure in Al 2024-T3". FFA TN 1984-40. The Aeronautical Research Institute of Sweeden.

[23] BROWN. M.W. (1986). "Interfaces between Short. Long and Non-Propagating Cracks". The Behaviour of Short fatigue Cracks. Eds., K.J.Miller and E.R. de los Rios. EGF Pub. 1. Mechanical Engineering Publications. London. 423-439.

[24] WEERTMAN. J. (1986). "Short Crack Theory".(1986). Small Fatigue Cracks. Eds., R.O.Ritchie and J.Lankford. Metall. Soc., Warrendale. PA., 363-375

[25] TAYLOR. D. and KNOTT. J.F. (1981). "Fatigue Crack Propagation Behaviour of Short Cracks : The Effect of Microstructure". Fatigue of Engineering Materials and Structures. Vol. 4. No. 2. 147-155.

[26] LANKFORD, J., COOK, T.S. and SHELDOW, G.P. (1981). "Fatigue Micro-Crack Growth in a Nickel-Base Superalloy", Int. J. of Fracture, Vol. 17, 143-145.

[27] NEWMAN JR., J.C. and EDWARDS, P.R. (1988). "Short Crack Growth in an Aluminium Alloy-an AGARD Co-Operative Test Programme". AGARD report No. 732.

[28] LANKFORD, J. (1985). "The Influence of Microstructure on the Growth of Small Fatigue Cracks". Fatigue Fract. Engng. Mater. Struct., Vol 8, 161-175.

[29] KITIGAWA, H. and TAKAHASHI, S. (1976). "Applicability of Fracture Mechanics to Very Small Cracks or the Cracks in the Early Stage". Proc. Second International Conference on Mechanical Behaviour of Materials, Boston, MA, 627-631.

[30] MILLER, K.J. and DE LOS RIOS, E.R. (1986). "An Introduction". The Behaviour of Short fatigue Cracks. Eds., K.J.Miller and E.R. de los Rios, EGF Pub. 1, Mechanical Engineering Publications, 1-3.

[31] TAYLOR. D. (1986). "Fatigue of Short Cracks : The Limitations of Fracture Mechanics". The Behaviour of Short fatigue Cracks. Eds.. K.J.Miller and E.R. de los Rios. EGF Pub. 1. Mechanical Engineering Publications. 479-490.

[32] LANKFORD. J. and DAVIDSON. D.L. (1986). "The Role of Metallurgical Factors in Controlling the Growth of Small Fatigue Cracks". Small Fatigue Cracks. Eds.. R.O.Ritchie and J.Lankford. Metall. Soc.. Warrendale. PA. 51-71.

[33] ZUREK. A.K.. JAMES. M.R. and MORRIS. W.L. (1983). "The Effect of Grain Size on Fatigue Growth of Short Cracks". Metall. Trans. A. 14A. 1697-1705.

[34] TOKAJI. K.. OGAWA. T.. HARADA. Y. and ANDO. Z. (1986). "Limitations of Linear Elastic Fracture Mechanics in respect of Small Fatigue Cracks and Microstructure". Fatigue Fract. Engng. Mater. Struct.. 9. 1-14.

[35] BOLINGBROKE. R.K. and KING. J.E. (1987). "The Effect of Microstructure on the Surface Length: Crack Depth Relationship for short Cracks". Fatigue 87. Eds.. R.O. Ritchie and E.A. Starke Jr.. EMAS Publications. West Midlands. U.K.. 281-290.

[36] GRABOWSKI, L. and KING, J.E. (1992). "Modelling Short Crack Growth Behaviour in Ni-Base Superalloys". Fatigue Fract. Engng. Mater. Struct., 15, 6, 595-606.

[37] WEISS, B., STICKLER, R. and FATHULLA, R. (1986). "Initiation and Transition of Short to Long Fatigue Cracks in Technical Alloys". Small Fatigue Cracks. Eds., R.O.Ritchie and J.Lankford, Metall. Soc., Warrendale, PA, 471-497.

[38] BROWN, C.W. and KING, J.E. (1986). "The Relevance of Microstructural Influences in the Short Crack Regime to Overall Fatigue Resistance". Small Fatigue Cracks. Eds., R.O.Ritchie and J.Lankford, Metall. Soc., Warrendale, PA, 73-96.

[39] NEWMAN, P. and BEEVERS, C.J. (1986). "Growth of Short Fatigue Cracks in High Strength Ni-base Superalloys". Small Fatigue Cracks. Eds., R.O.Ritchie and J.Lankford, Metall. Soc., Warrendale, PA, 97-116.

[40] WAGNER, L., GREGORY, J.K., GYSLER, A. and LUTJERING, G. (1986). "Propagation Behaviour of Short Cracks in a Ti-8.6 Al alloy". Small Fatigue

Cracks. Eds.. R.O.Ritchie and J.Lankford. Metall. Soc.. Warrendale. PA. 117-128.

[41] BOLINGBROKE. R.K. and KING. J.E. (1986). "The Growth of Short Fatigue Cracks in Titanium Alloys IMI 550 and IMI 318". Small Fatigue Cracks. Eds.. R.O.Ritchie and J.Lankford. Metall. Soc.. Warrendale. PA. 129-144.

[42] MANFRED. A. D. and THOMPSON. A.W. (1986). "Microstructural Effects on Short Fatigue Cracks in Eutectoid Steels". Small Fatigue Cracks. Eds.. R.O.Ritchie and J.Lankford. Metall. Soc.. Warrendale. PA. 157-166.

[43] NAVARO. A. and DE LOS RIOS. E.R. (1987). "A Model for Fatigue Crack Propagation with an Interpretation of the Short-Long Crack Transition". Fatigue Fract. Engng. Mater. Struct.. Vol. 10. No. 2. 169-186.

[44] PLUMTREE. A. and SCHAFER. S. (1986). "Initiation and Short Crack Behaviour in Aluminium Alloy Castings". The Behaviour of Short fatigue Cracks. Eds.. K.J.Miller and E.R. de los Rios. EGF Pub. 1. Mechanical Engineering Publications. 215-227.

[45] ZHANG. Y. H. and EDWARDS. L.. (1992). "Measurement of Plastic Zones Associated with Small Fatigue Cracks by Selected Area Channelling Patterns". Materials Characterization. 29. 313-320.

[46] ZHANG. Y. H. and EDWARDS. L.. (1992). "The Effect of Grain Boundaries on the Development of Plastic Deformation ahead of Small Fatigue Cracks". Scripta Metallurgica et Materialia. 26. 1901-1906.

[47] RADHAKRISHNAN. V.M. and MUTOH. Y. (1986). "On Fatigue Crack Growth in Stage I". The Behaviour of Short fatigue Cracks. Eds.. K.J.Miller and E.R. de los Rios. EGF Pub. 1. Mechanical Engineering Publications. 87-99.

[48] NAVARRO. A. (1988) "An Alternative Model of the Blocking of Dislocations at Grain Boundaries". Philosophical Magazine A. Physics of Condensed Matter. Defects and Mechanical Properties. Vol. 57. No. 1. 37-42.

[49] YATES. J.R.. ZHANG. W. and MILLER. K.J. (1993). "The Initiation and Propagation Behaviour of Short Fatigue Cracks in Waspalloy Subjected to Bending". Fatigue Fract. Engng. Mater. Struct.. Vol 16. No. 3. 351-366.

[50] TANAKA. K.. KINEFUCHI. M. and YOKOMAKU. T. (1992). "Modelling of Statistical Characterization of the Propagation of Small Fatigue Cracks". The Behaviour of Short fatigue Cracks. Eds.. K.J.Miller and E.R. de los Rios. EGF Pub. 1. Mechanical Engineering Publications. 351-368.

[51] KOUL. A.K.. IMMARIGEON. J.P. and WALLACE.W. "Microstructural Control in Ni-based Superalloys". Advances in High Temperature Structural Materials and Protective Coatings. Eds. A.K. Koul. V.r. Parameswaran. J.P. Immarigeon. W. Wallace. National Research Council. Canada. Ottawa. Canada. 95-125.

[52] ELBER. W. (1971). "The Significance of Fatigue Crack Closure". Damage Tolerance in Aircraft Structures. ASTM STP 486M. 230-242.

[53] EWALDS. H.L. and WANHILL. R.J.H. (1984). "Fracture Mechanics" Edward Arnold Publishers Ltd. 174-179.

[54] LIAW. P.K. and LOGSDON. W.A. (1985). "Crack Closure : An Explanation for Small Fatigue Crack Growth Behaviour". Engineering Fracture Mechanics. Vol. 22. No. 1. 115-121.

[55] SCHIJIVE. J. (1981). "Differences Between the Growth of Small and Large Fatigue Cracks. The Relation to Threshold K-Values". Department of Aerospace Engineering. Delft University of Technology. Delft- The Netherlands.

[56] JAMES. M.R. and MORRIS. W.L. (1983). "Effect of Fracture Surface Roughness on Growth of Short Fatigue Cracks". Metall. Trans. A. 14A. 153-155.

[57] NEWMAN. JR. J.C. (1992). "Fracture Mechanics Parameters for Small Fatigue Cracks" Small-Crack Test Methods. ASTM STP 1149. Eds.. J.M. Larsen and J.E. Allison. American Society for Testing and Materials. 6-33.

[58] LEE. J.J. and SHARPE. JR. W.N. (1986). "Short Cracks in Notched Aluminium Specimens". Small Fatigue Cracks. Eds.. R.O.Ritchie and J.Lankford. Metall. Soc.. Warrendale. PA. 323-339.

[59] OBABUEIKI. A.O.. LEE. C.H. TANAKA. T. and MILLER. A.K. (1987). "A Unified Model for Fatigue Crack Initiation. Short Crack Growth. Long Crack Propagation and Closure Effects". Fatigue 87. Eds.. R.O.Ritchie and E.a. Starke Jr. EMAS Publications. U.K. 381-391.

[60] OGURA, K., MIYOSHI, Y. and NISHIKAWA, I. (1985). "Fatigue Crack Growth and Closure of Small Cracks at the notch root". Current Research on Fatigue Cracks. Ed. T. Tanaka. Materials Research Series 1. Soc. Material Science, Japan. 67-91.

[61] USAMI, S. (1986). "Engineering Applications of Small Crack Fatigue Properties". Small Fatigue Cracks. Eds., R.O.Ritchie and J.Lankford. Metall. Soc., Warrendale, PA. 323-339.

[62] NEWMAN, J.C JR., SWAIN, M.H. and PHILLIPS, E.P. (1986). "An Assessment of the Small Crack Effect for 2024-T3". Small Fatigue Cracks. Eds., R.O.Ritchie and J.Lankford. Metall. Soc., Warrendale, PA. 427-452.

[63] SHIN, C.S. and SMITH, R.A. (1985). "Fatigue Crack Growth from Sharp Notches". Int. J. Fatigue. 7. 87-93.

[64] RITCHIE, R.O., YU, W., HOLM, D.K. and BLOM, A.F. (1986). "Developement of Fatigue Crack Closure with the Extension of Long and Short Cracks in Aluminium Alloy 2124:A Comparison of Experimental and Numerical Results". The Aeronautical Research Institute of Sweeden, FFATN. 58.

[65] MENDEZ, J., VIOLAN, P. and GASC, G. (1986). "Initiation and Growth of Surface Micro-Cracks in Polycrystalline Copper Cycled in Air and Vacuum". The Behaviour of Short fatigue Cracks. Eds., K.J.Miller and E.R. de los Rios. EGF Pub. 1. Mechanical Engineering Publications. 145-161.

[66] PETIT, J. and ZEGHLOUL, A., (1986). "On the Effect of Environment on Short Crack Growth Behaviour and Threshold". The Behaviour of Short fatigue Cracks. Eds., K.J.Miller and E.R. de los Rios. EGF Pub. 1. Mechanical Engineering Publications. 163-177.

[67] DE MIRANDA, P.E.V. and PASCAL, R. (1986). "Initial Stages of Hydrogen Induced Short Fatigue Crack Propagation". The Behaviour of Short fatigue Cracks. Eds., K.J.Miller and E.R. de los Rios. EGF Pub. 1. Mechanical Engineering Publications. 179-190.

[68] GANGLOFF, R.P. (1982). "Electrical Potential Monitoring of the Formation and Growth of Small Fatigue Cracks in Embrittling Environments". Advances in Crack Length Measurement. Ed., C.J.Beevers. EMAS Publications. U.K. 175-229.

[69] FROST. N.E. (1959). "A Relation Between the Critical Alternating Propagation Stress and Crack Length for Mild Steel". Proc. Inst. Mech. Engg.. 173. No. 35. 811-827.

[70] BROEK. D. (1972). "The Propagation of Fatigue Cracks emanating from Holes". National Aerospace Lab.. NLR. Netherlands. NLRTR. 72134 U.

[71] SMITH. R.A. and MILLER. K.J. (1978). "Prediction of Fatigue Regimes in Notched Components". Int. J. Mech. Sci.. vol. 20. 201-206.

[72] DAI. YI. (Dec. 1992). "Thermal Mechanical Fatigue Crack Growth in Aircraft Engine Materials". Doctorate Thesis. Ecole Polytechnique.

[73] SWAIN. M.H. and NEWMAN. J.C. JR. (1984). "On the Use of Marker Loads and replicas for Measuring Growth Rates for Small Cracks". Fatigue Crack Topography, an AGARD Conference Proceedings No. 376. 12-1 - 12-9.

[74] MARDER. A.R. (1989). "Replication Microscopy Techniques for NDE". Nondestructive Evaluation and Quality Control. Metals Handbook. Ninth Edition.Vol. 17. 52-56.

[75] SCHULTE. K.. TRAUTMAN. K.H. and NOWACK. H. (1984). "New Analysis Aspects of the Fatigue Crack Propagation by SEM- Insitu Microscopy". Fatigue Crack Topography, an AGARD Conference Proceedings No. 376. 16-1 - 16-10.

[76] PISHVA. M.R.. BELLINGER. N.C.. TERADA. T. and KOUL. A.K. (1987). "DC-PD Technique for Crack Length Measurements at Elevated Temperatures". Laboratory Technical Report. LTR-ST-1635. National Research Council. Canada.

[77] INSTRUCTION MANUAL. (1994). "Matelect Pulsed DCPD Crack Growth Monitor". Version 6. Matelect Limited. 33 Bedfords Gardens. London. U.K.

[78] GANGLOFF. R.P. (1981). "Electrical Potential Monitoring of Crack Formation and Subcritical Growth from Small Defects". Fat. Engg. Mater. Struct.. Vol. 4. No. 1. 15-33.

[79] HARTMAN. G.A. and JOHNSON. D.A. (March 1987). "D-C Electric-Potential Method Applied to Thermal/Mechanical Fatigue Crack Growth". Experimental Mechanics. 106-112.

[80] HICKS, M.A. and PICKARD, A.C. (1982). "A Comparison of Theoretical and Experimental Methods of Calibrating the Electrical Potential Drop Technique for Crack Length Determination". Int. Journ. of Fracture 20, 91-101.

[81] CHANG, M., TERADA, T. and KOUL, A.K. (1992). "Calibration of a DCPD Technique for Fatigue Crack Initiation and Short Crack Growth in Double Edge Notched Specimens". Internal Report (unpublished), SML, IAR, National Research Council, Canada.

[82] DONALD, J.K. and RUSCHAU, J. (1991). "Direct Current Potential Difference Fatigue Crack Measurement Techniques". Fatigue Crack Measurement Techniques and Applications, Eds., K.J.Marsch and R.O.Ritchie, EMAS Publications, West Midlands, U.K., 11-37.

[83] BURGERS, A. and KEMPEN, P.D. (1982). "Automatic Crack Length Measurement by the Electrical P.D. Method with Computer Control". Advances in Crack Length Measurement, Ed. C.J.Beevers, EMAS Publications, West Midlands, U.K., 325-342.

[84] KRAUS, J.D. (1984). "Electromagnetics", McGraw Hill, Third Edition, 449-450.

[85] VEROPEST. I.. AERNOUDT. E.. DERUYTTERE. A. and NEYRINCK. M. (1981). "An Improved A.C. Potential Drop Method for Detecting Surface Microcracks during Fatigue Tests of Unnotched Specimens". Fat. Engg. Mater. Struct.. Vol. 3. 203-217.

[86] CHARLESWORTH. F.D.W. and DOVER. W.D. (1982). "Some Aspects of Crack Detection and Sizing using A.C. Field Measurements". Advances in Crack Length Measurement. Ed. C.J.Beever. EMAS Publications. West Midlands. U.K.. 253-276.

[87] DOVER. W.D.. CHARLESWORTH. F.D.W.. TAYLOR. K.A.. COLLINS. R. and MICHAEL. D.H. (1980). "A.C. Field Measurement-Theory and Practice" The Measurement of Crack Length and Shape during Fracture and Fatigue. Ed. C.J.Beever. EMAS Publications. WestMidlands. U.K.. 222-260.

[88] WATT. K.R. (1980). "A Consideration of an A.C. Potential Drop Method for Crack Length Measurement". The Measurement of Crack Length and Shape during Fracture and Fatigue. Ed. C.J.Beever. EMAS Publications. WestMidlands. U.K.. 202-221.

[89] DAI. Y.. MARCHAND. N. and HONGOH. M. (March 1993). "Study of Fatigue Crack Initiation and Growth in Titanium Alloys using an ACPD Technique". Canadian Aeronautics and Space Journal. Vol. 39. No. 1. 35-44.

[90] JABLONSKI. D.A. (1995). "Measurement of Multiple-Site Cracking in Simulated Aircraft Panels Using AC Potential Drop". Special Applications and Advanced Techniques for Crack Size Determination. ASTM STP 1251. Eds.. J.J. Ruschau and J.K. Donald. American Society for Testing and Materials. PA. 33-50.

[91] LU. Z.-J.. NICHOLAS. P.J. and EVANS. W.J. (1995). "Calibration of an ACPD Monitoring System for Small Crack Growth in Corner Crack Specimens". Engineering Fracture Mechanics. Vol. 50. No. 4. 443-456.

[92] MARCHAND. N.J.. DORNER. W. and ILSCHNER. B. (1990). "A Novel Procedure to Study Crack Initiation and Growth in Thermal Fatigue Testing". Surface-Crack Growth:Models. ASTM STP 1060. Experiments and Structures. Eds.. W.G. Reuters. J.H. Underwood. and J.C. Newman Jr.. PA. 237-259.

[93] GENDRON. S. and MARCHAND, N.J. (1994). "On-Line Damage Assessment of Turbine Airfoil-Like Test Coupons under Simulated Service Conditions"

Testing under Simulated Conditions Part 2. Oberflachen Werkstoffe. No. 3. 12-16.37-38.

[94] GENDRON. S.. MARCHAND. N.J. and IMMARIGEON. J.P. (1995). "Thermal Fatigue Damage Accumulation in a Coated Turbine Blade Material Tested under Simulated Service Conditions". Elevated Temperature Coatings:Science and TechnologyI. Eds.. N.B. Dahotre. J.M. hamikian and J.J. Stiglich. The Minerals. Metals and Materials Society. 135-144.

[95] FULEKI. D.M. (1995). "Crack Initiation and Short Crack growth Characteristics of Notched MERL 76 Specimens" Masters Thesis. Carleton University. Ottawa. Canada.

[96] CECCO. V.S.. FRANKLIN. E.M.. HOUSERMAN. H.E.. KINCAID. T.G.. PELLICER. J. and HAGEMAIER. D. (1989). "Eddy Current Inspection". Nondestructive Evaluation and Quality Control. Metals Handbook. Ninth Edition.Vol. 17. 164-194.

[97] HAGEMAIER. D.J. (1991). "Application of Crack Detection to Aircraft Structures". Fatigue Crack Measurement Techniques and Applications. Eds..

K.J.Marsch and R.O.Ritchie. EMAS Publications. West Midlands. U.K.. 419-455.

[98] BELLINGER. N.C.. FAHR. A.. KOUL. A.K.. GOULD. G. and STOUTE. P. (1988). "The Reliability and Sensitivity of NDI Techniques in Detecting LCF Cracks in Fastener Bolt Holes of Compressor Discs" Laboratory Report. LTR-ST-1651.

[99] BORUCKI. J.S. and JORDAN. G. (1989). "Liquid Penetrant Inspection". Nondestructive Evaluation and Quality Control. Metals Handbook. Ninth Edition.Vol. 17. 71-88.

[100] ONO. K. (1991). "Acoustic Emission". Fatigue Crack Measurement Techniques and Applications. Eds.. K.J.Marsch and R.O.Ritchie. EMAS Publications. West Midlands. U.K.. 173-205.

[101] POLLOCK. A.A. (1989). "Acoustic Emission Inspection". Nondestructive Evaluation and Quality Control. Metals Handbook. Ninth Edition.Vol. 17. 278-294.

[102] SCRUBY, C.B. and BUTTLE, D.J. (1991). "Quantitative Fatigue Crack Measurement by Acoustic Emission". Fatigue Crack Measurement Techniques and Applications. Eds., K.J.Marsch and R.O.Ritchie, EMAS Publications. West Midlands, U.K., 207-287.

[103] METALS HANDBOOK (1990). "Properties and Selection: Nonferrous alloys and Special-Purpose Materials." Vol. 2, 10th edition. ASM International.

[104] UNVALA, B.A., "U.S. Patent No. 5,202,641", 13th April, 1993.

[105] Private Communication with Dr. Bikhu Unvala, Director Matelect Ltd.

[106] MARCHAND, N.J. (Sept. 1990). "Feasibility Study of a Damage Measurement Sensor Based on the ACPD Technique". Prepared for: Maj. P. Beaudit, DAS Eng. 6-6. Department of National Defense, Canada.

[107] STARKE Jr., E.A. and LÜTJERING (1986). "Alloys 7075 and 7475: Effect of Inclusion Density on Cycles to Failure". Atlas of Fatigue Curves. Edited by Howard E. Boyer. ASM, Metals Park,Ohio 44073, pp 355.

[108] MARCHAND. N.J.. TIKU. S. and SCHULZE. H. (Aug. 1992). "On-Line Strain and Damage Measurement System". First Annual Report for Department of National Defense. Canada. c/o DSS. Re: DSS file 18SVo. W8477-O-AC59.

[109] DIETER. G.E. (1986). "Mechanical Metallurgy" McGraw-Hill Publishing Company. Third Edition. 138-139.

[110] BERES. W. and KOUL. A.K. (1994). "Finite Element Validation of Stress Intensity Factor Calculation Models for Thru-Thichness and Thumb-Nail Cracks in Double Edge Notch Specimens". Engineering Fracture Mechanics. Vol. 49. No. 2. 165-177.

[111] NEWMAN Jr. J.C.. WU. X.R.. VENNERI. S.L. and LI. C.G. (May.1994). "Small-Crack Effects in High-Strength Aluminium Alloys". A NASA/CAE Cooperative Program" Nasa Reference Publication 1309.

[112] SANDERS. Jr.. T.H. and STALEY. J.T. (1986). "7XXX Alloys: Cyclic Strain vs Crack Initiation Life". Atlas of Fatigue Curves, Edited by Howard E. Boyer. ASM. Metals Park.Ohio 44073, pp 351.

[113] DICKSON. J.I.. BAILON. XIA. J. and BUREAU. M. (1993). "Extrusion-Intrusion Formation in Cu and 70Cu-30Zn". Fatigue 93.1883-1892.

[114] DUBENSKY. R.G. (March 1971). "Fatigue Crack Propagation in 2024-T3 and 7075-T6 Aluminium Alloys at High Stresses". NASA Contractor Report. NASA Cr-1732.

[115] TIKU. S.. MARCHAND. N.J. and UNVALA. B. (April 1994). "On-Line Strain and Damage Measurement System". Third Annual Report for Department of National Defense. Canada. c/o DSS. Re: DSS file 18SVo. W8477-O-AC59.

TABLES

Al 7075 T 651		Al 7075 T 7351	
Grain Orientation	Grain size (in the crack depth direction)	Grain Orientation	Grain size (in the crack depth direction)
18°	25 μm	80°	85 μm
55°	38 μm	90°	110 μm
70°	80 μm		
8°	23 μm		

Table 5.1 Details of the material with the grain orientation and respective grain size used in the present program.

Material	Yield Strength	Tensile Strength
Al 7075 T651	462 MPa	538 MPa
Al 7075 T7351	393 MPa	476MPa

Table 5.2 The average values used for yield strength and tensile strength [103].

FIGURES

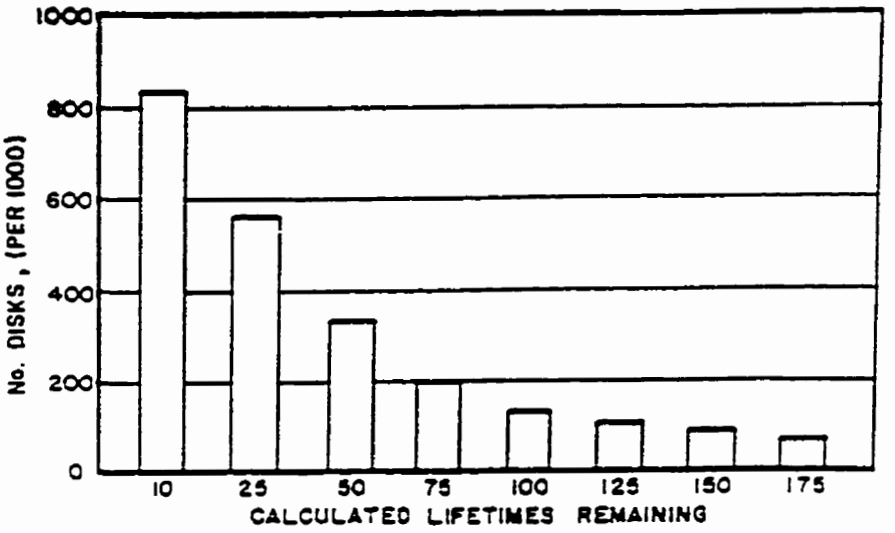

Figure 1.1 The majority of the discs have useful life after retirement. The retirement criterion is based on Safe Life Approach.

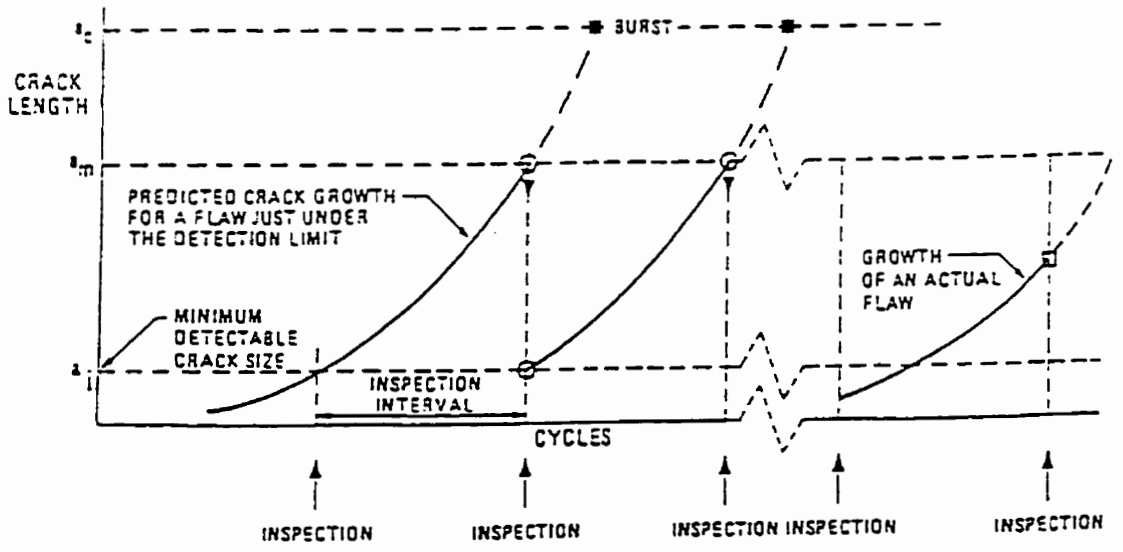

Figure 1.2 Schematic of Damage Tolerant Methodology showing the application of the Safe Inspection Interval.

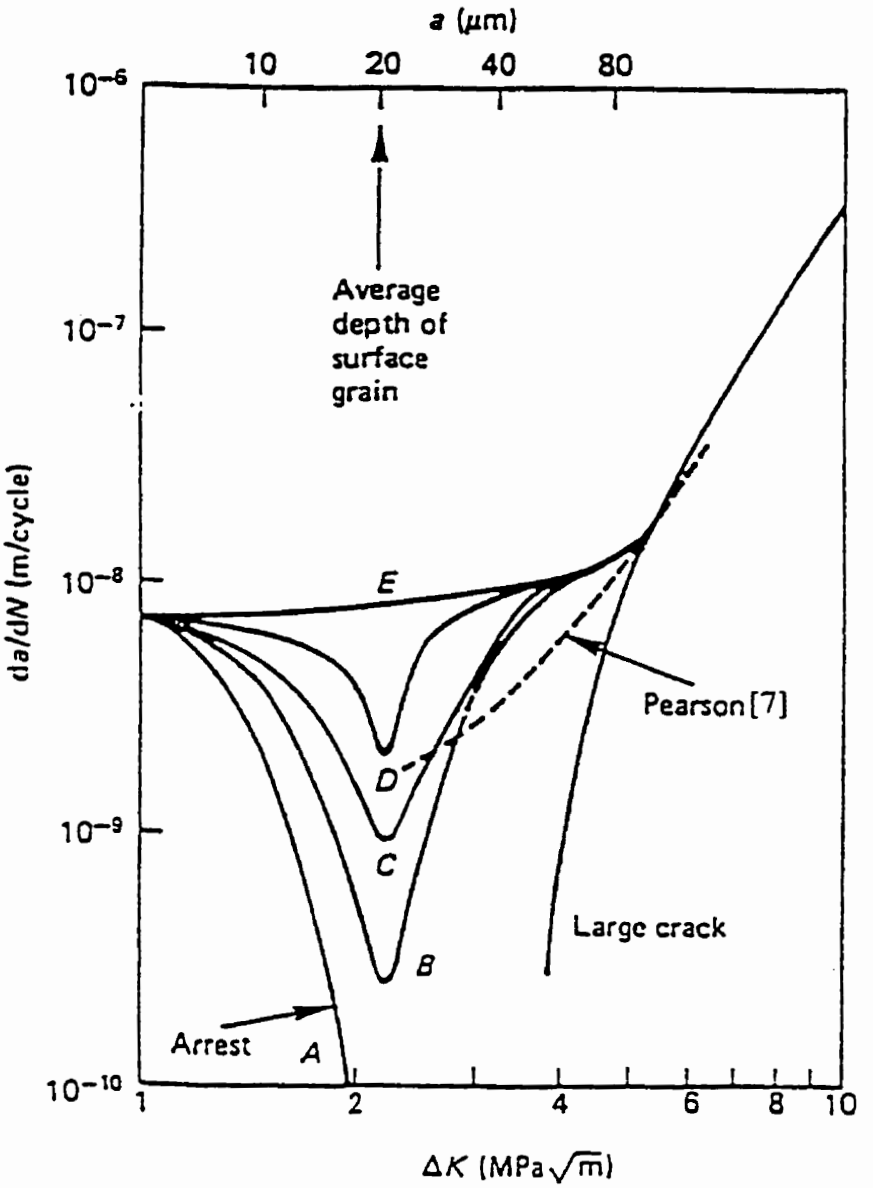

Figure 2.1 A comparison of short crack growth versus long crack growth in Al 7075[28].

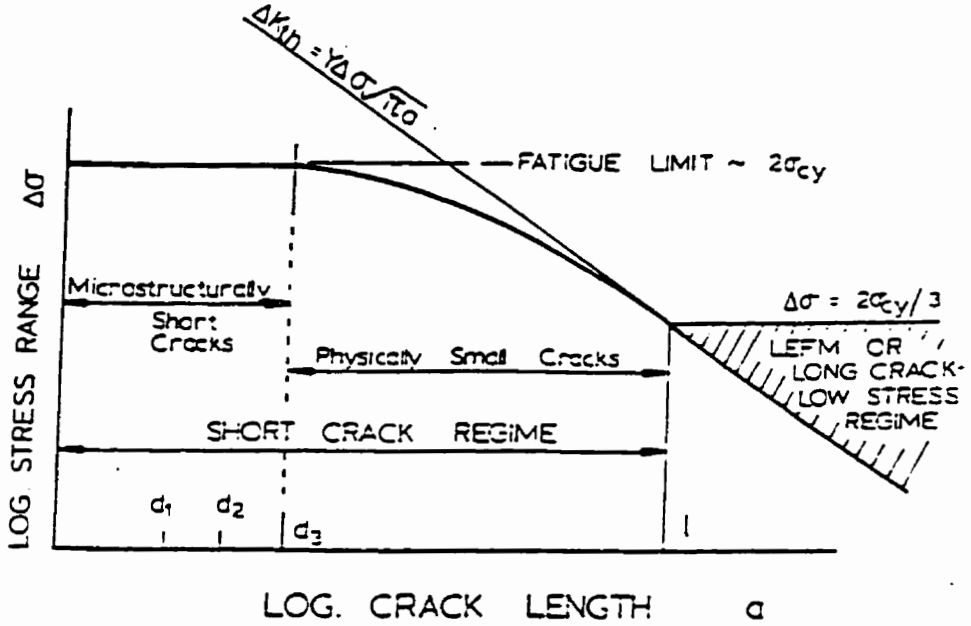

Figure 2.2 A schematic of the Kitigawa Takahashi diagram showing the two regions of short crack growth where σ_{cy} is the cyclic yield stress in a reversed stress test. d_1, d_2, d_3 represent sizes of microstructural elements and l represents the crack length at which LEFM principles are valid[30].

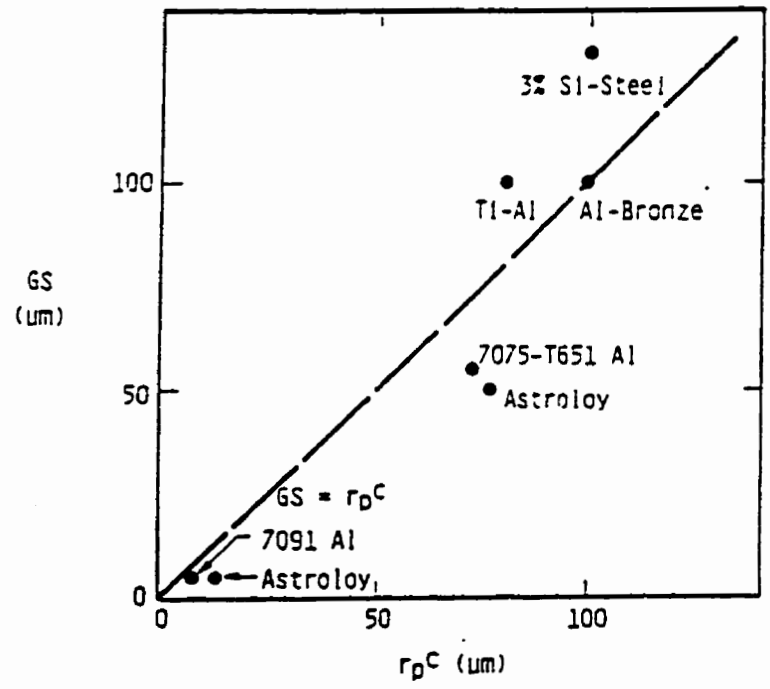

Figure 2.3 A plot of grain size versus plastic zone size at convergence of da/dN versus Δ K curves for small and large cracks[32].

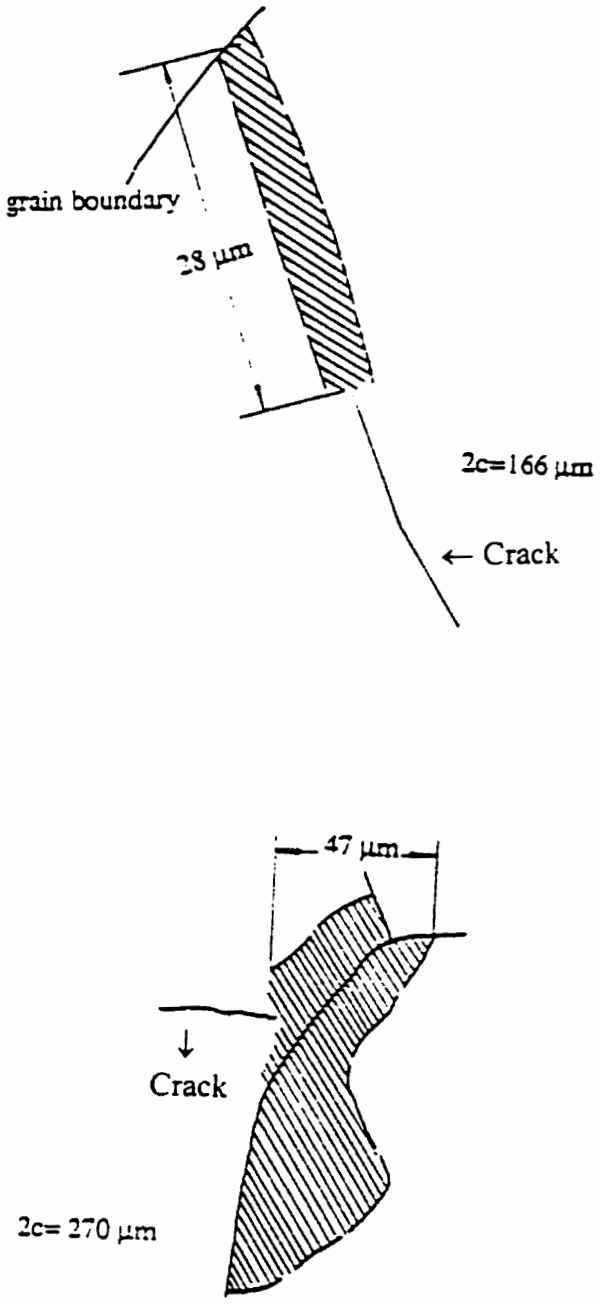

Figure 2.4 Typical shapes of plastic zone size associated with (a) short cracks and (b) long cracks [45].

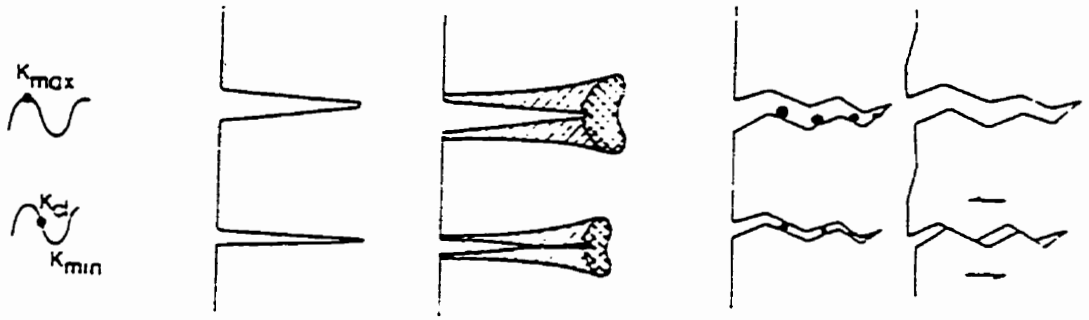

Figure 2.5 A schematic depicting crack closure mechanisms. (a) no closure, (b) plasticity induced closure, (c) closure induced by oxide debris (d) roughness induced closure [52].

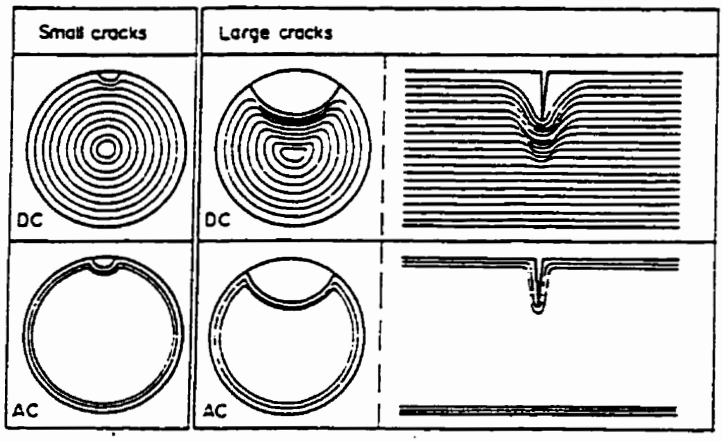

Figure 2.6 Schematic representation of current configuration around a crack in (a) DCPD and (b)ACPD measurements [5].

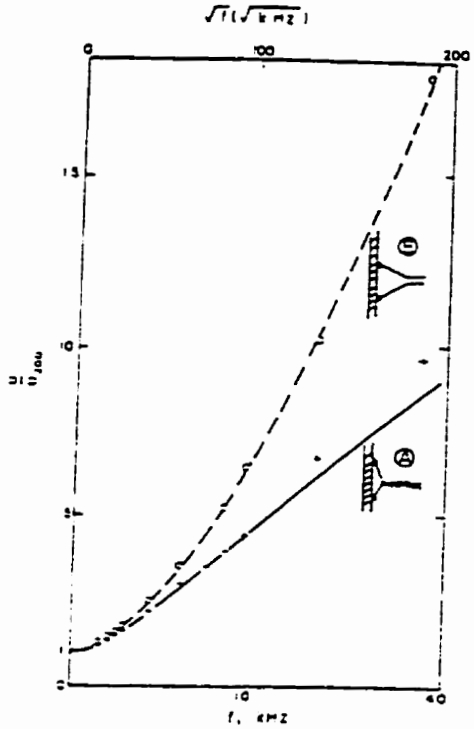

Figure 2.7 Effect of probe loop on AC potential difference measurements [85].

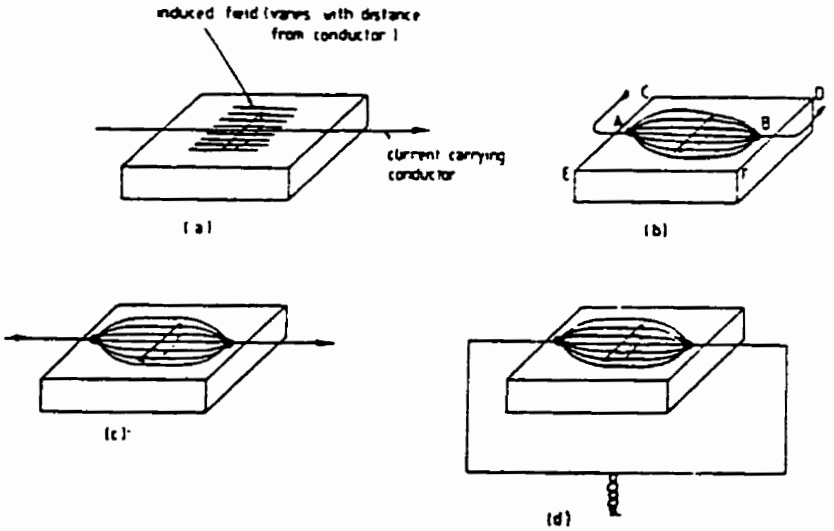

Figure 2.8 Schematic of possible current input arrangements [86].

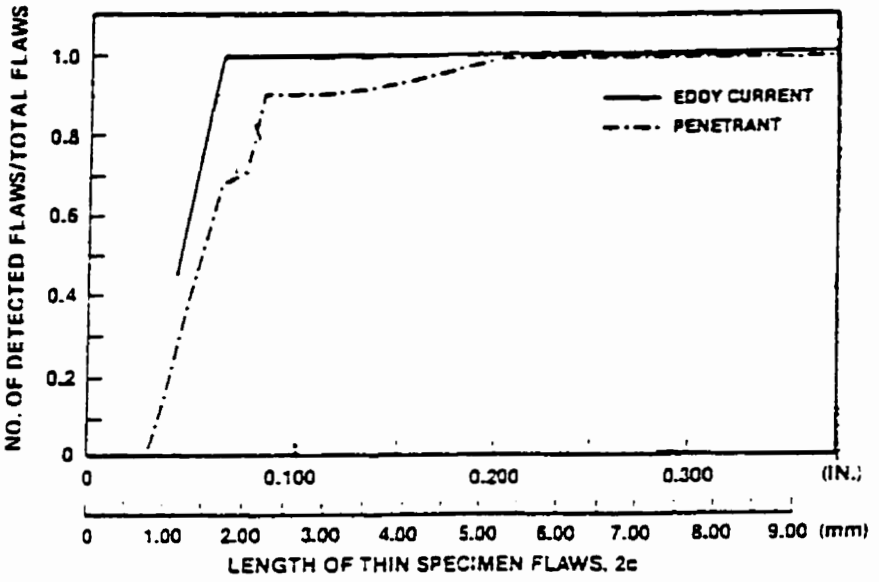

Figure 2.9 A plot of POD versus crack lengths in thin aluminium specimens for eddy current and liquid penetrant [97].

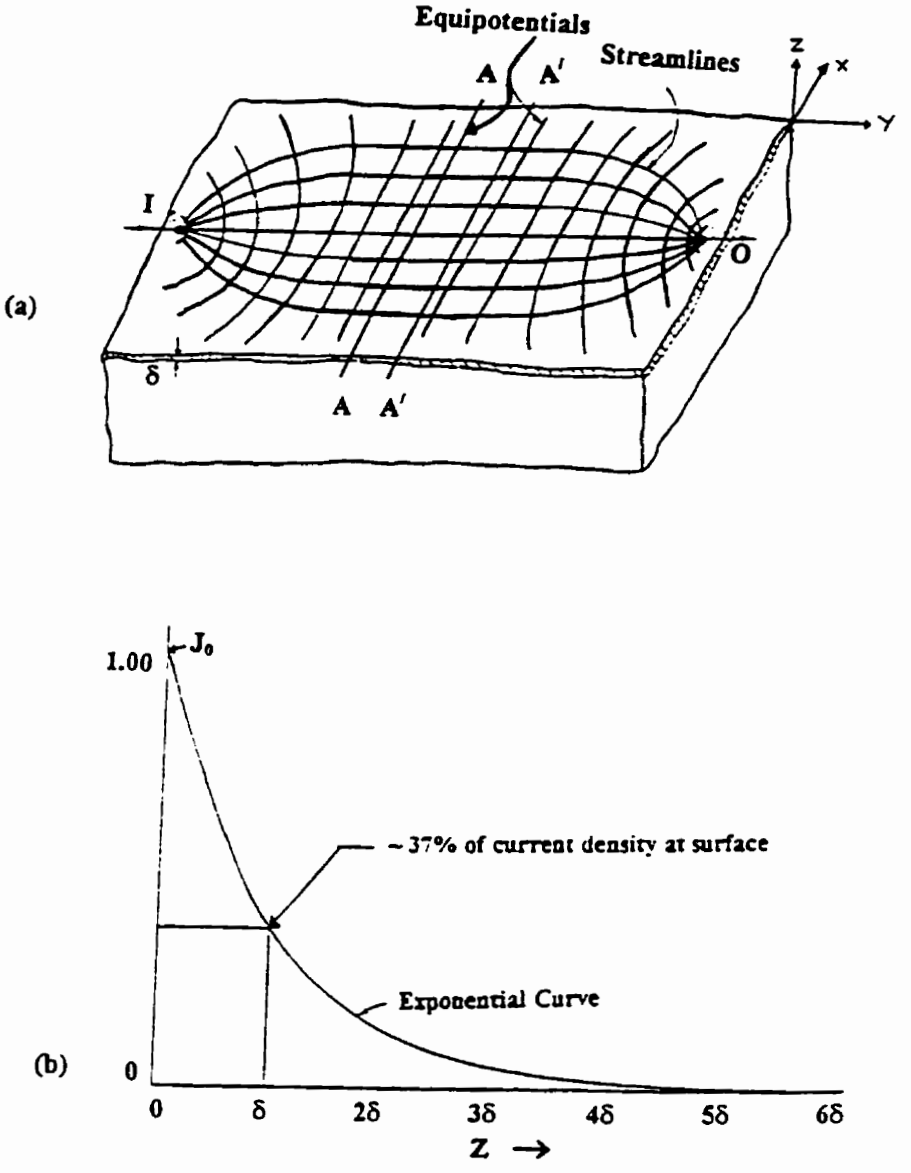

Figure 3.1 (a) AC current distribution in a solid (b) Skin Effect

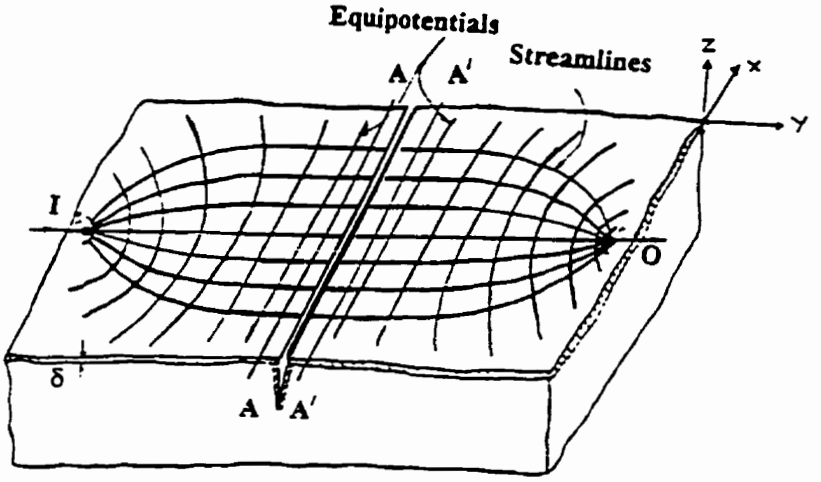

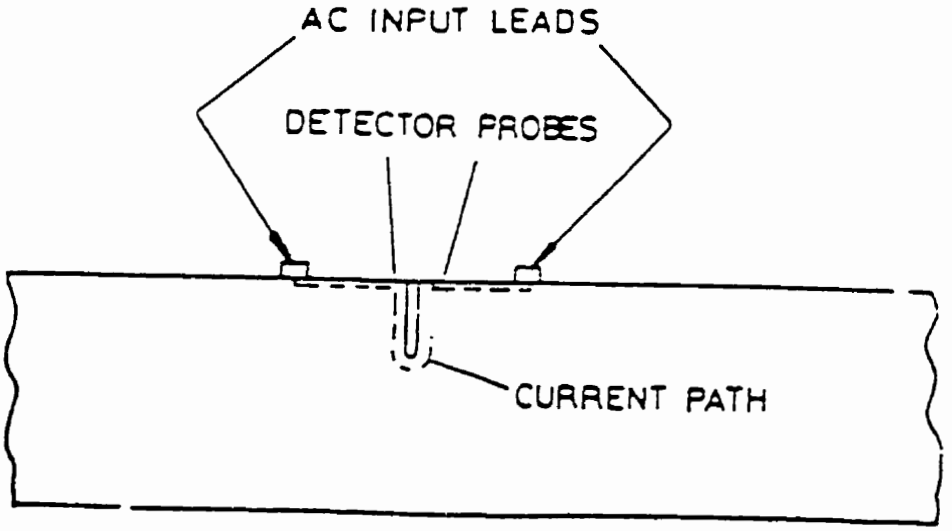

Figure 3.2 Modified current distribution around a crack.

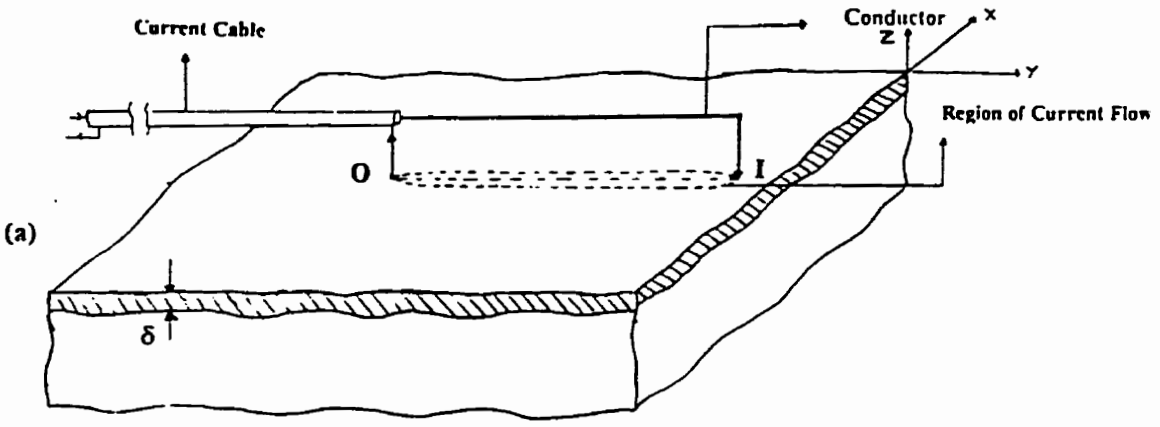

Figure 3.3a Modified current distribution due to current focusing device

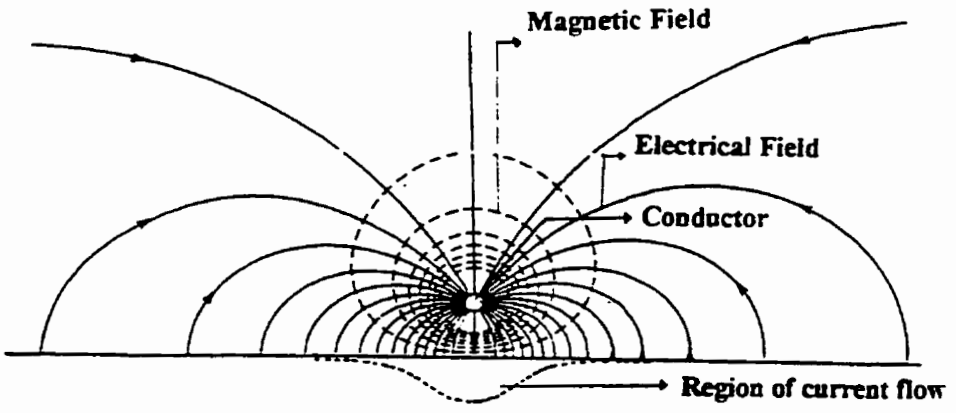

Figure 3.3b A schematic of current focusing effect.

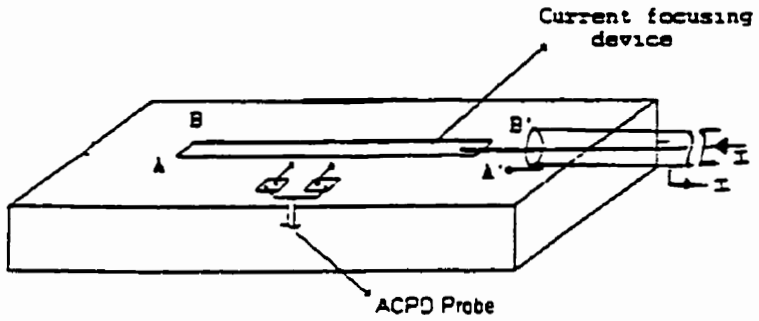

Figure 3.4a Schematic of ACPD probe arrangement.

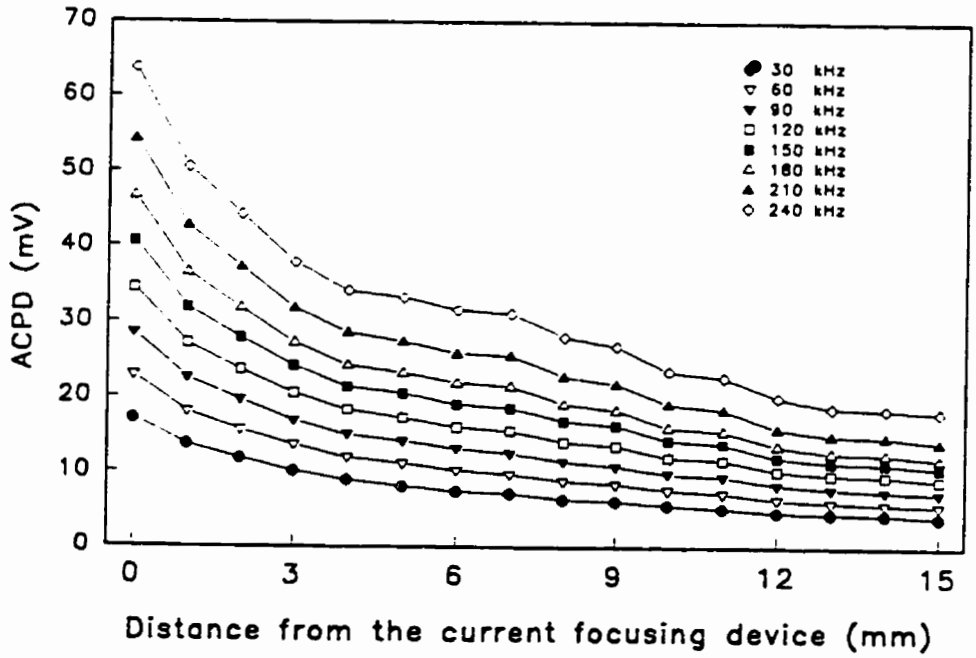

Figure 3.4b A plot of ACPD versus probe distance from the current focusing device.

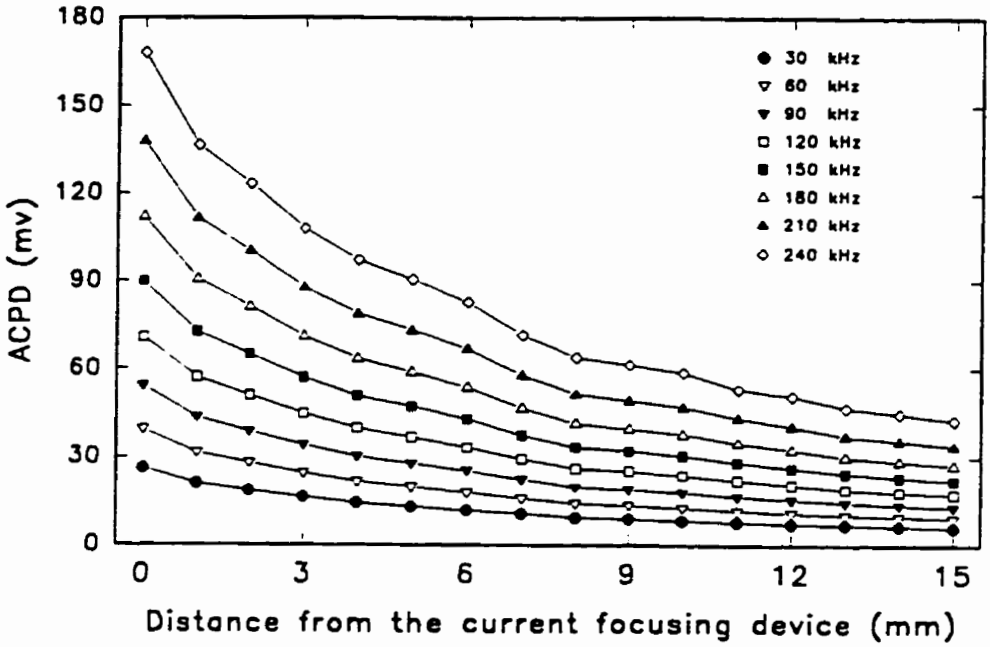

Figure 3.5a A plot of ACPD versus probe distance from the current focusing device (the device is at a height of 0.9 mm).

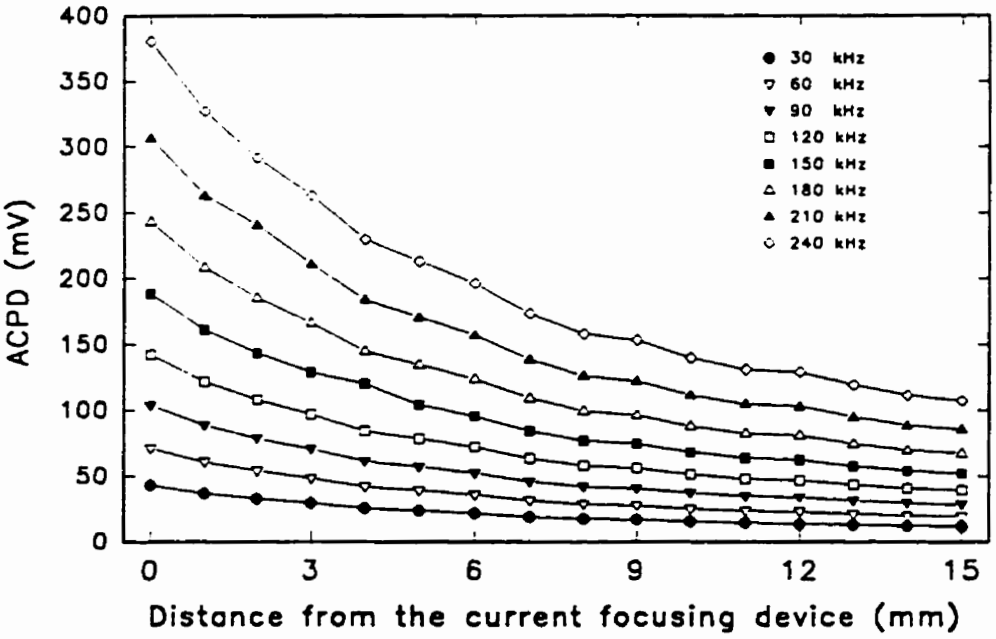

Figure 3.5b A plot of ACPD versus probe distance from the current focusing device (the device is at a height of 3.0 mm).

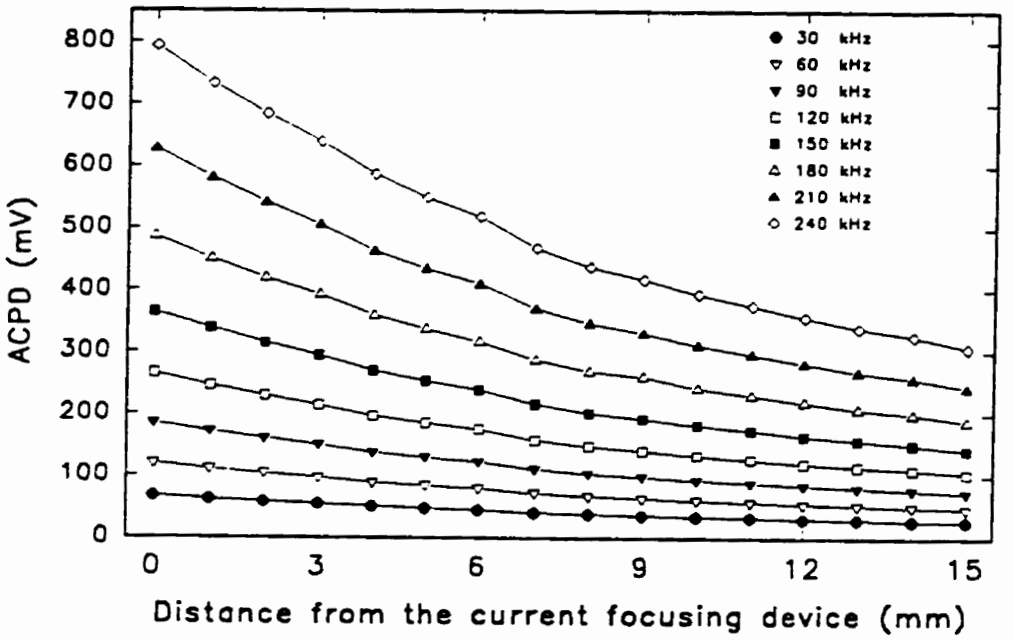

Figure 3.5c A plot of ACPD versus probe distance from the current focusing device (the device is at a height of 9.3 mm).

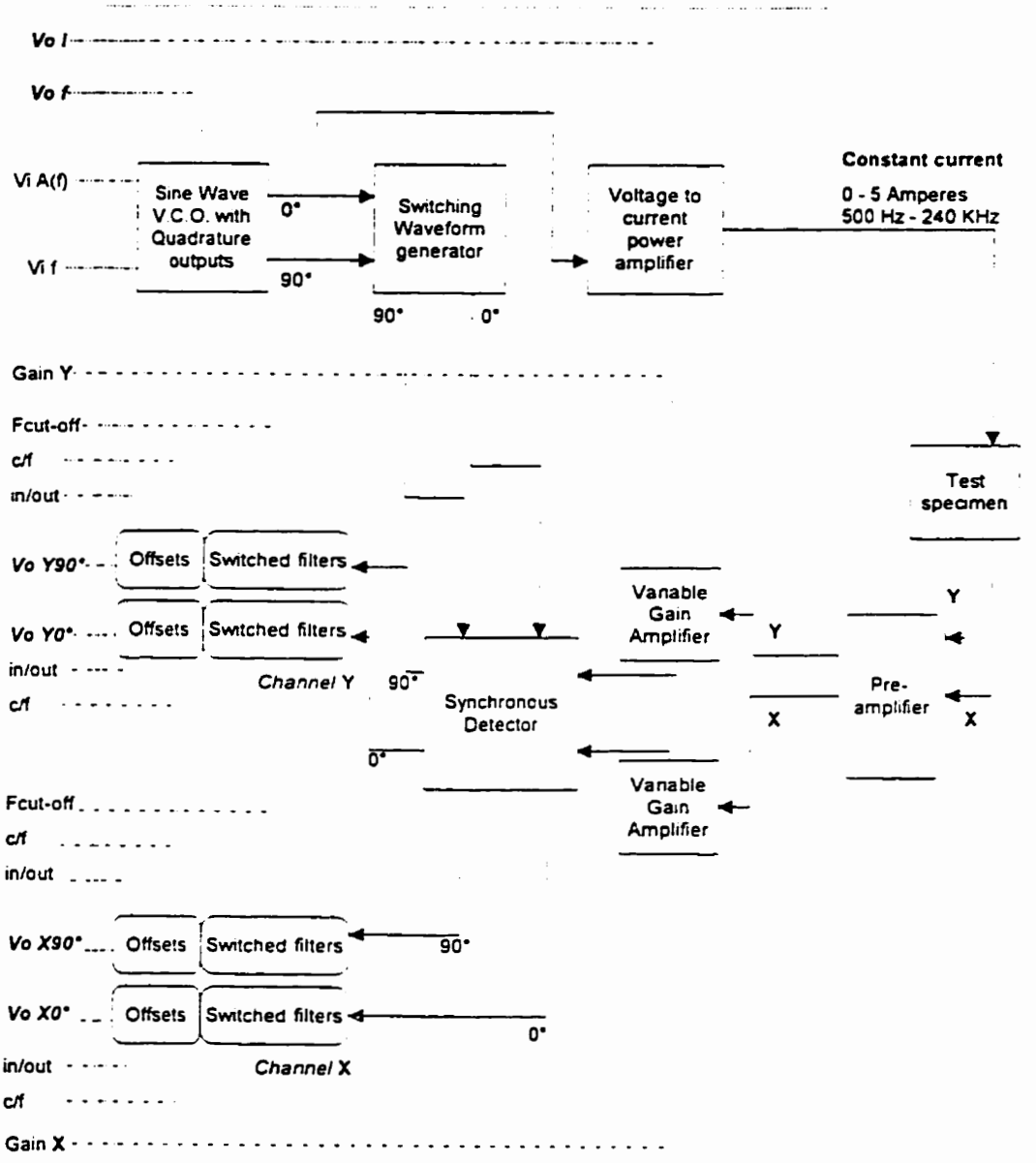

Figure 3.6 A simplified block diagram of ACPD system.

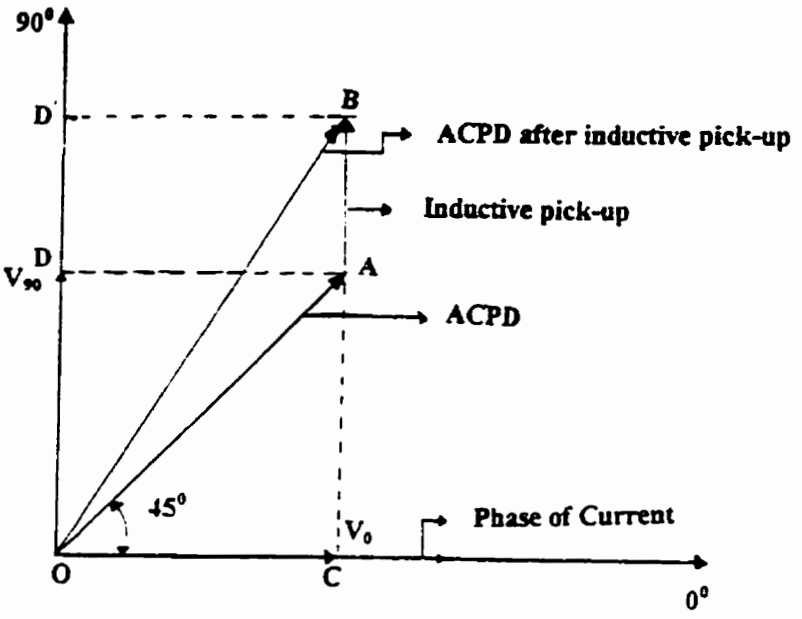

Figure 3.7 Schematic view of ACPD component.

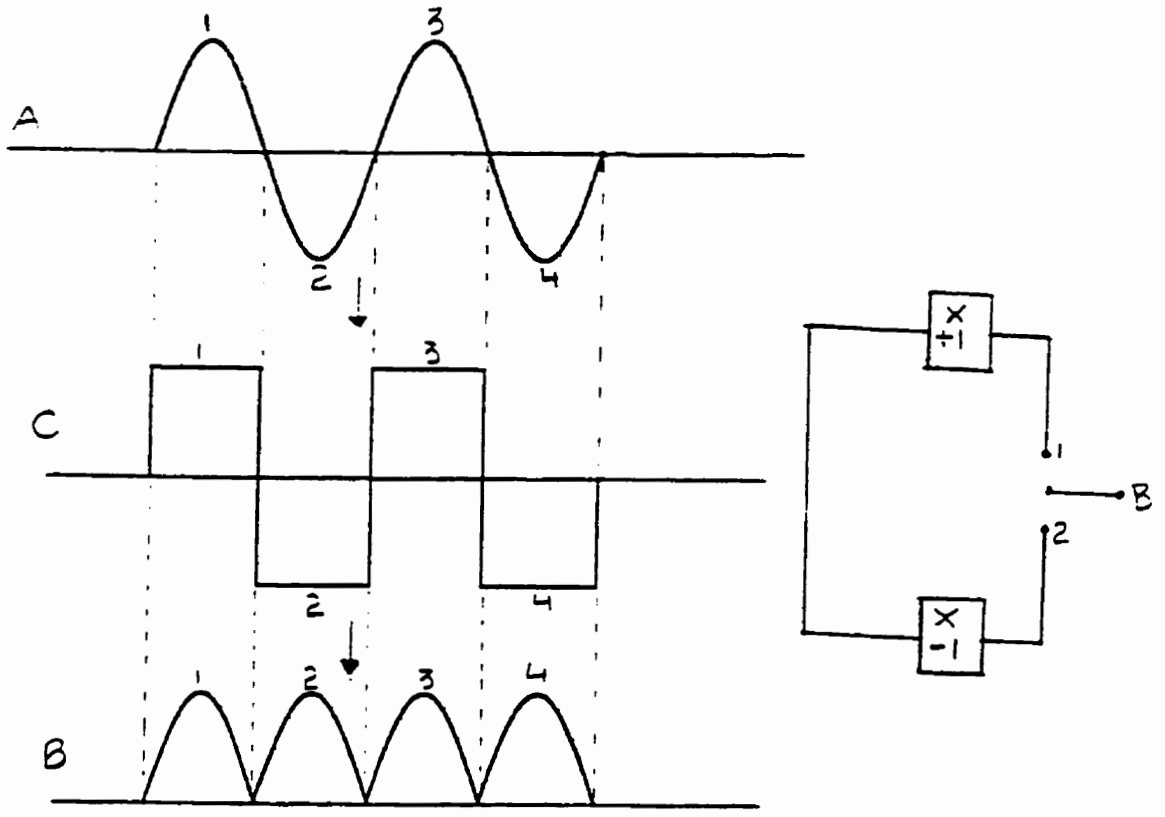

Figure 3.8 Schematic illustrating the principle of PSD (when signal is in phase with the phase of current).

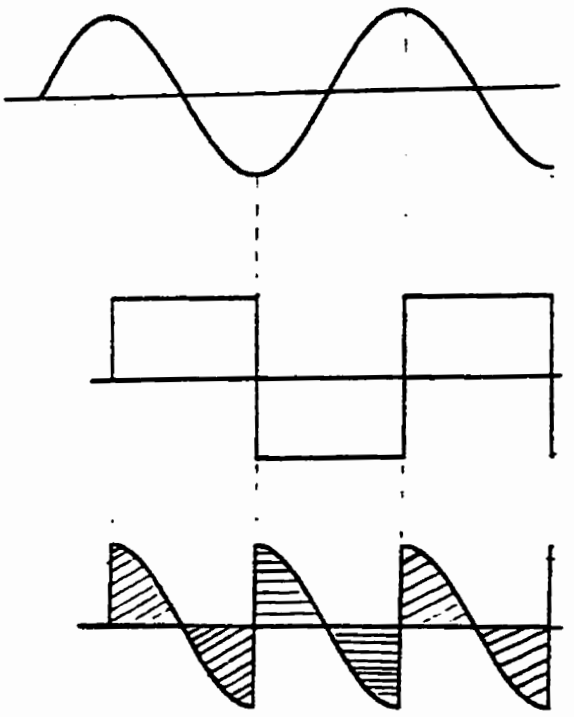

Figure 3.9 Schematic illustrating the principle of PSD (when signal is at 90^{O} to the phase of current).

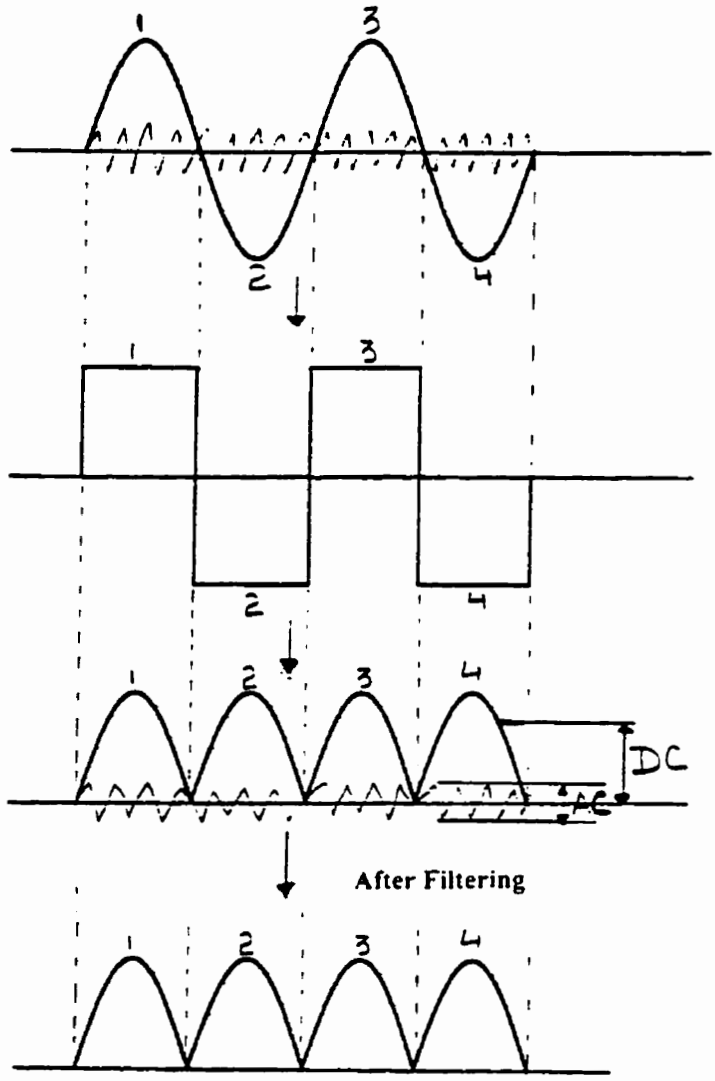

Figure 3.10 Schematic illustrating how PSD removes noise.

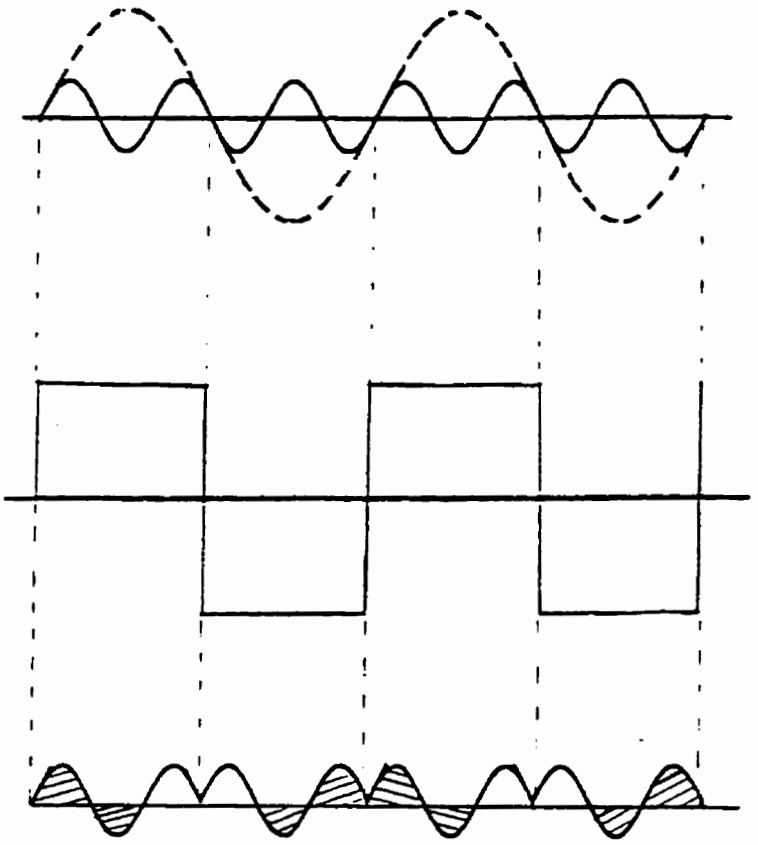

Figure 3.11 Schematic showing the inability of PSD system involved to block odd harmonics.

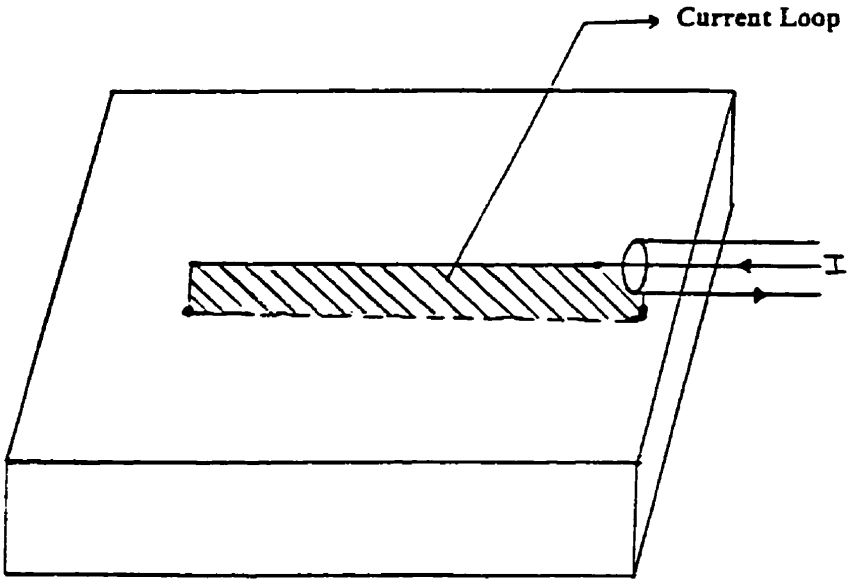

Figure 3.12 Schematic of current loop.

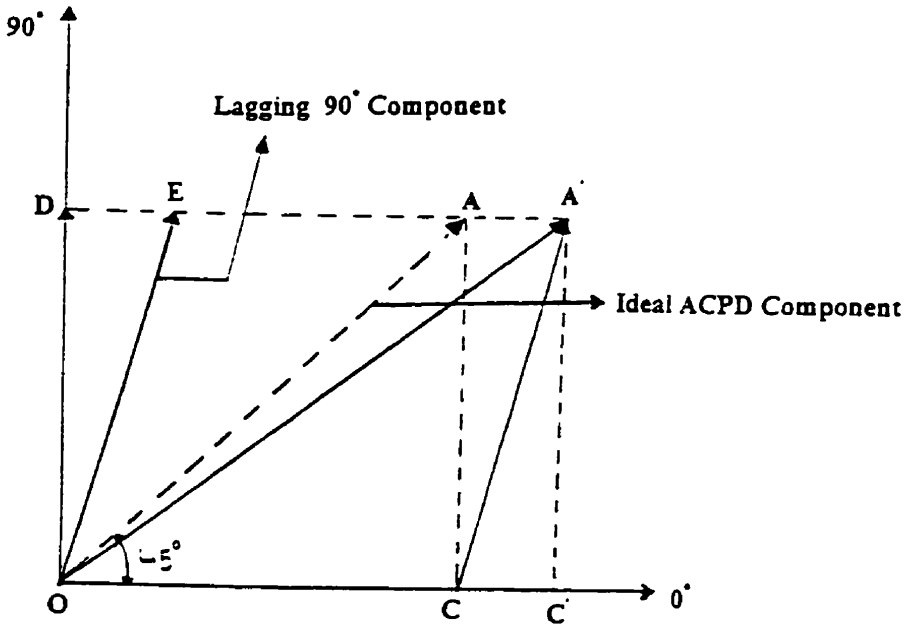

Figure 3.13 Schematic illustrating the effect of current diffusion on ACPD component.

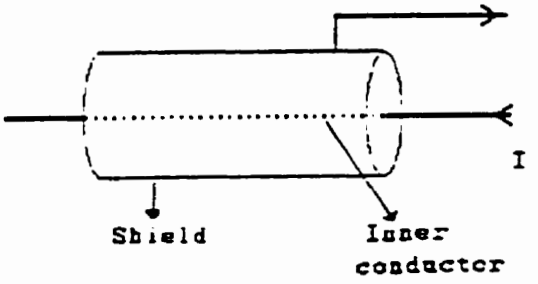

Figure 3.14a A co-axial current arrangement.

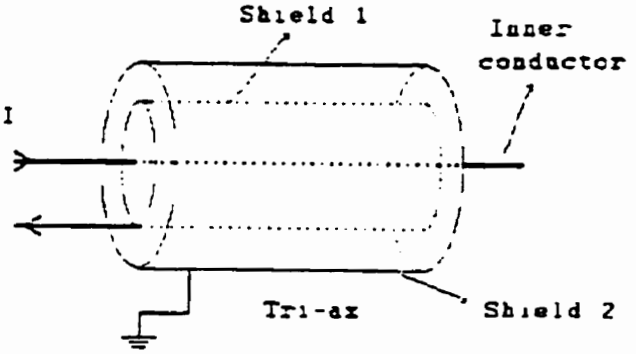

Figure 3.14b A tri-axial current arrangement.

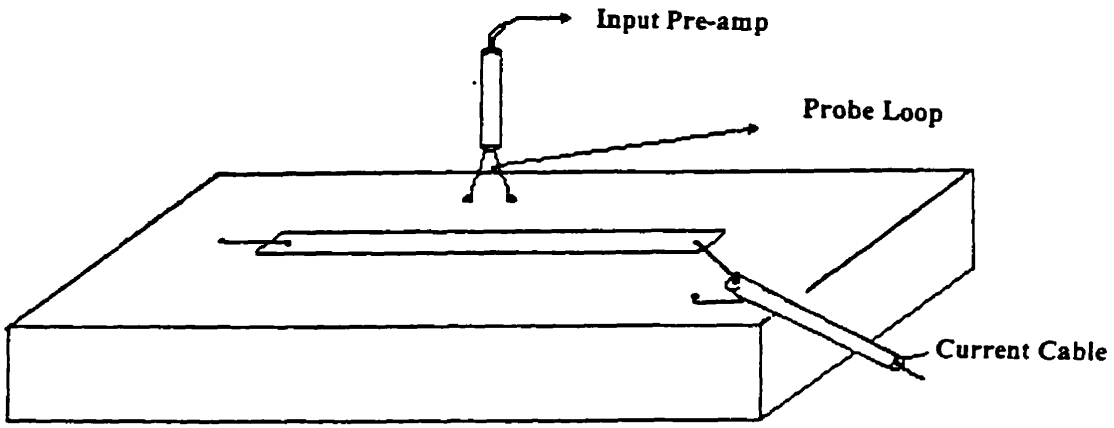

Figure 3.15 A schematic showing probe loop.

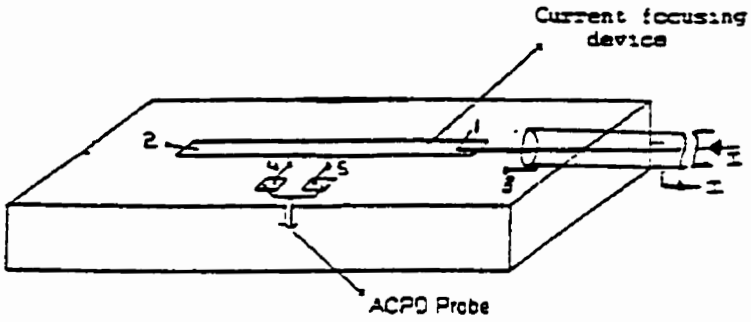

Figure 3.16 Schematic showing probe design developed in this program.

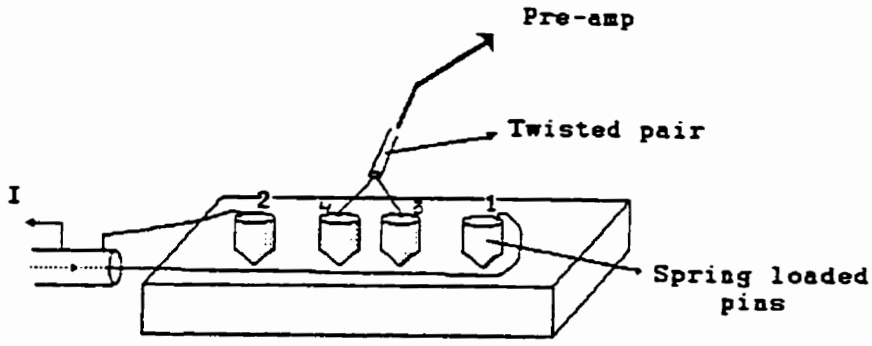

Figure 3.17 Schematic of hand held probe.

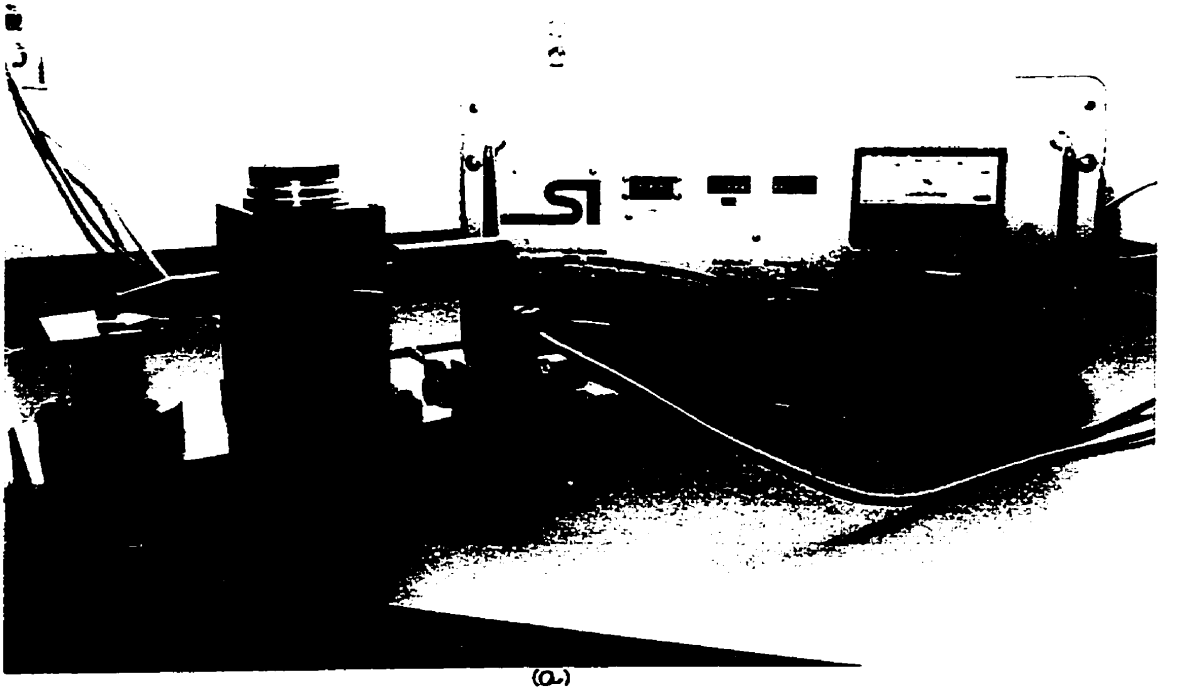

(a)

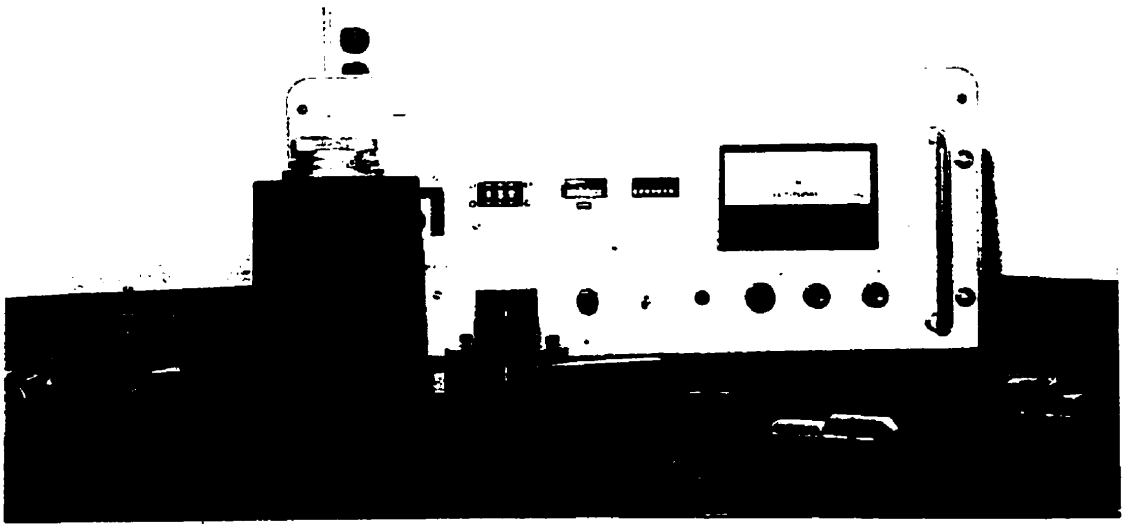

(b)

Figure 3.18 (a) Original welding set up, (b) Disassembled welding set up.

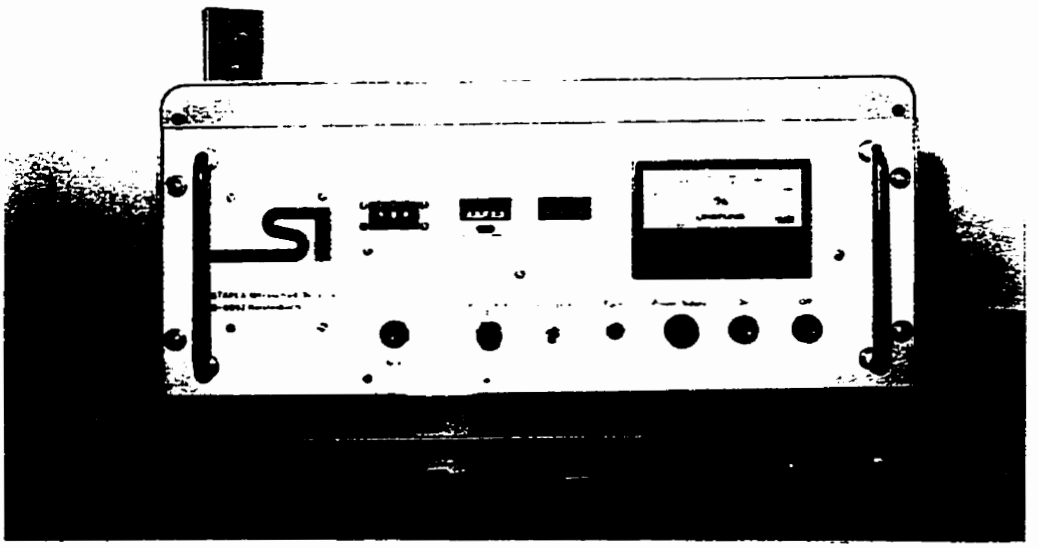

Figure 3.18 c Modified welding set up.

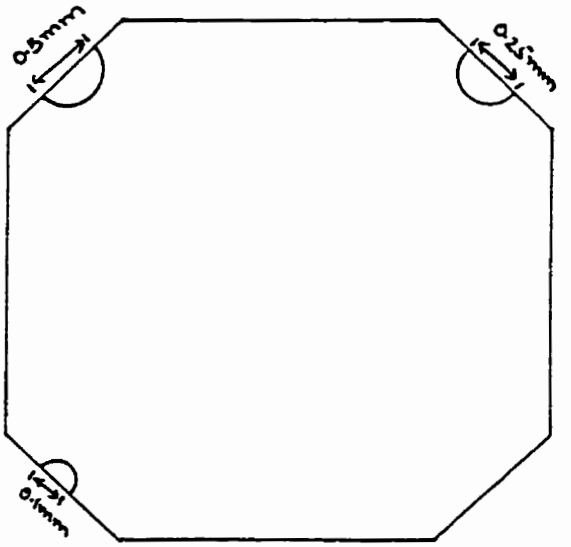

Figure 3.19 Modification done to the welding head.

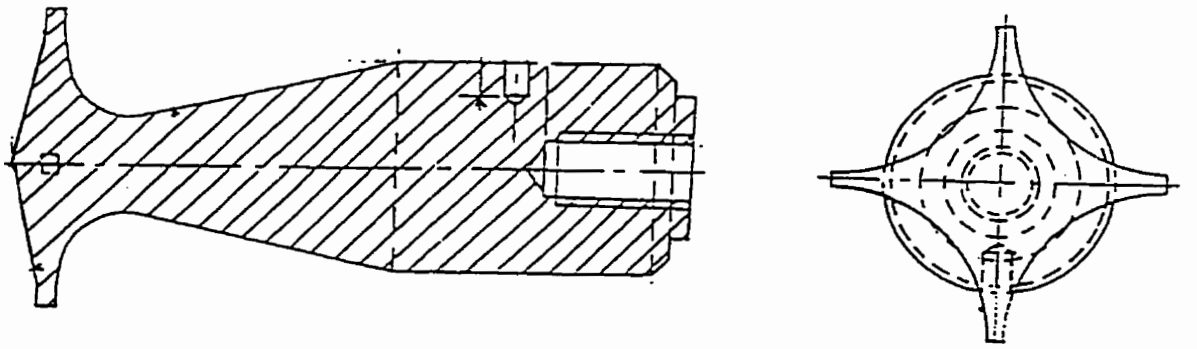

Figure 3.20a Schematic showing the new welding head.

(b)

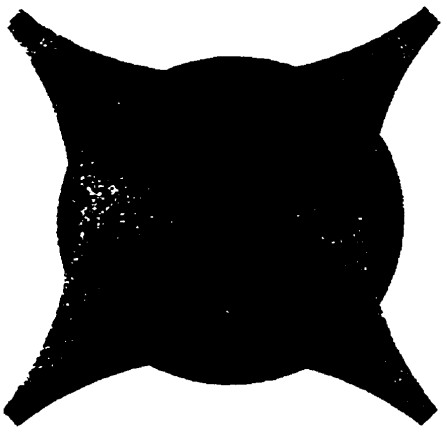

(C)

Figure 3.20 Photographs showing (b) side view (c) top view of the welding horn

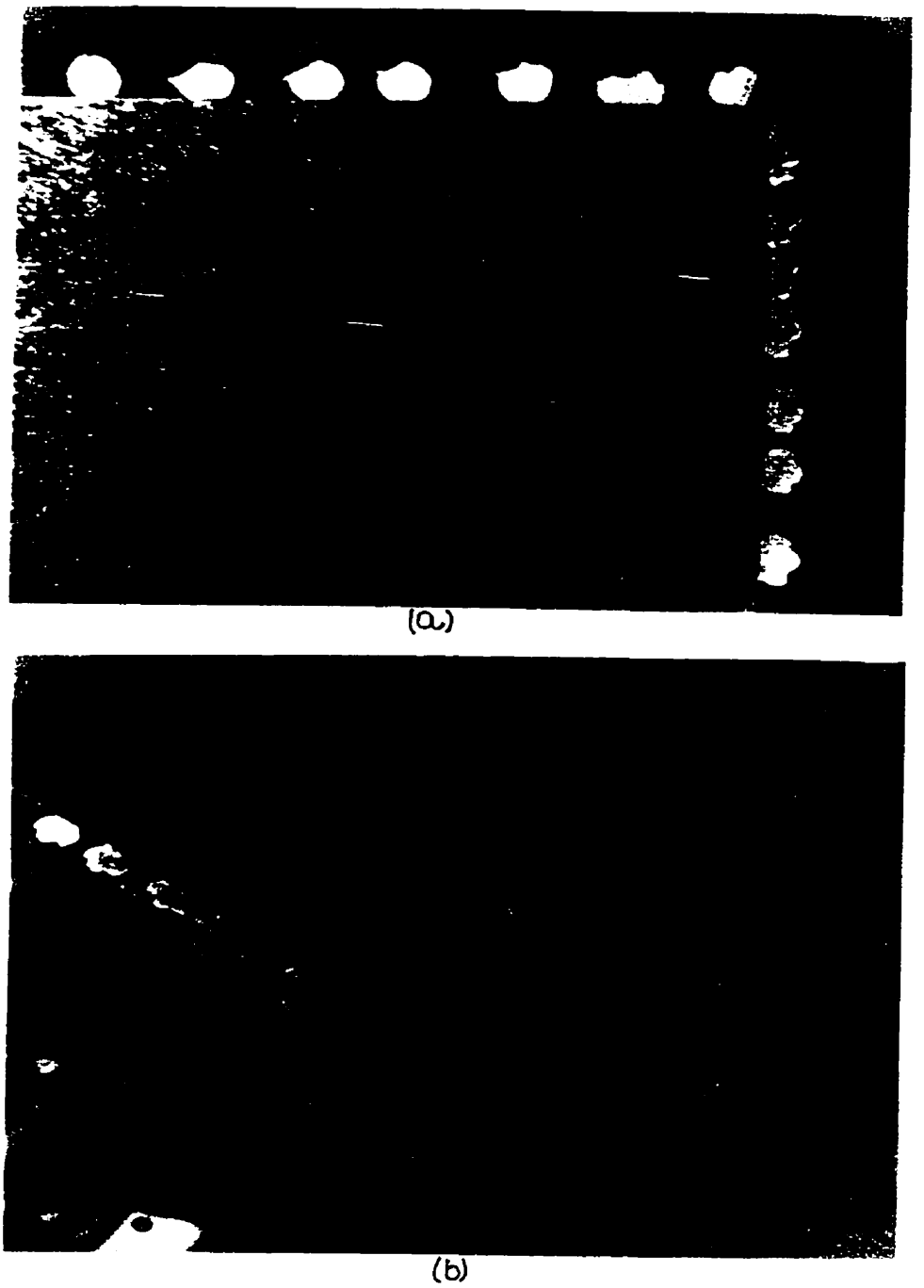

Figure 3.21 Photographs showing Al wires welded on a test specimen (a) top view (b) side view. Mag. 14 ×.

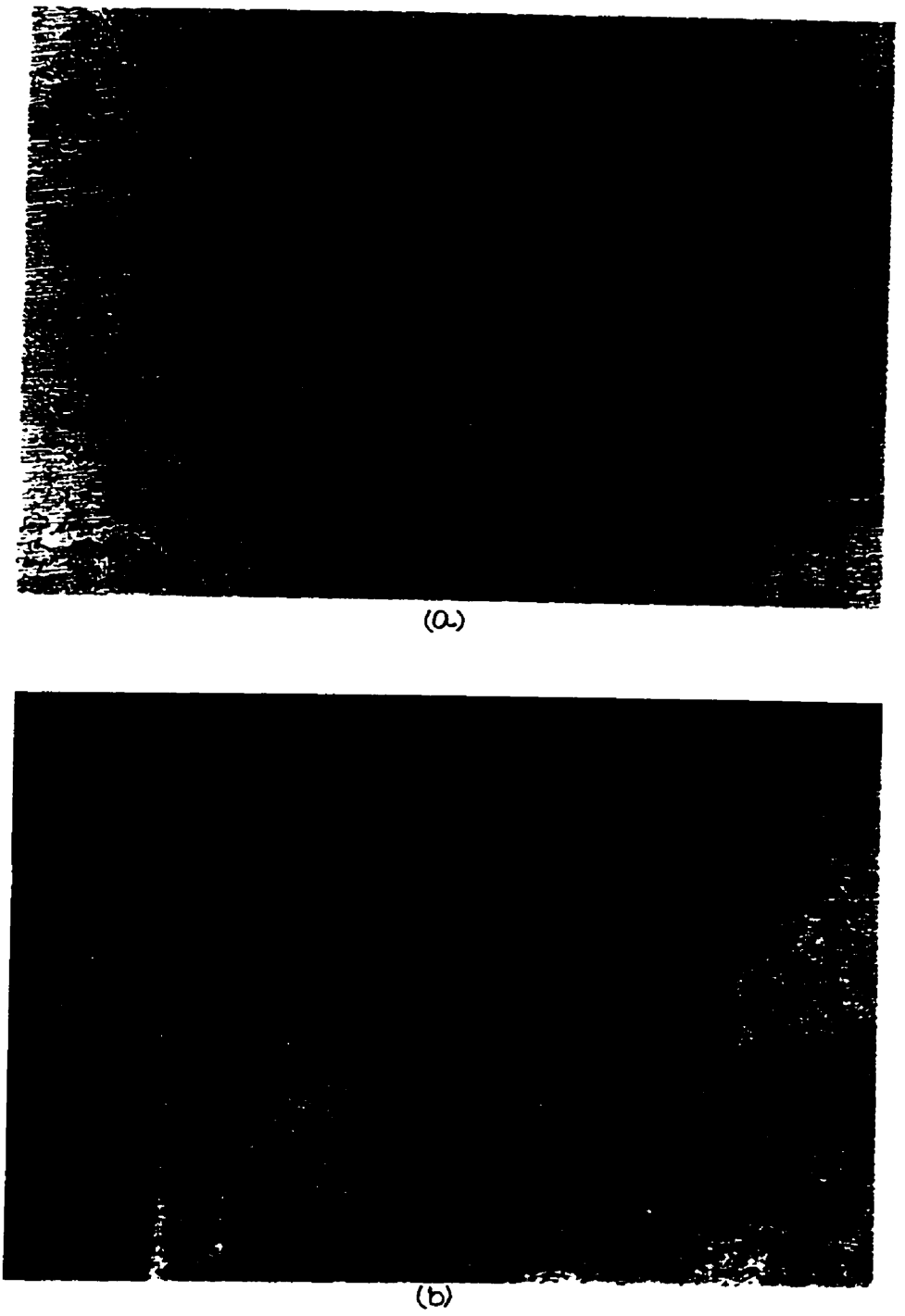

Figure 3.22 Micrographs showing effect of welding on the microstructure (a) away from the welds (b) near the welds. Mag. 200 ×.

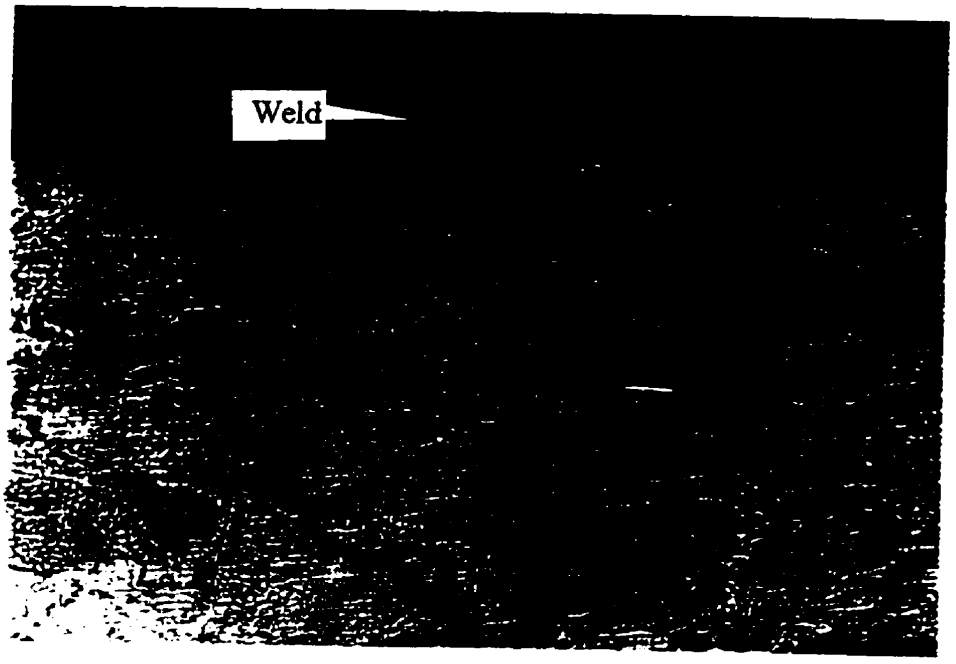

Figure 3.22 (c) below the welds. Mag. 200 ×.

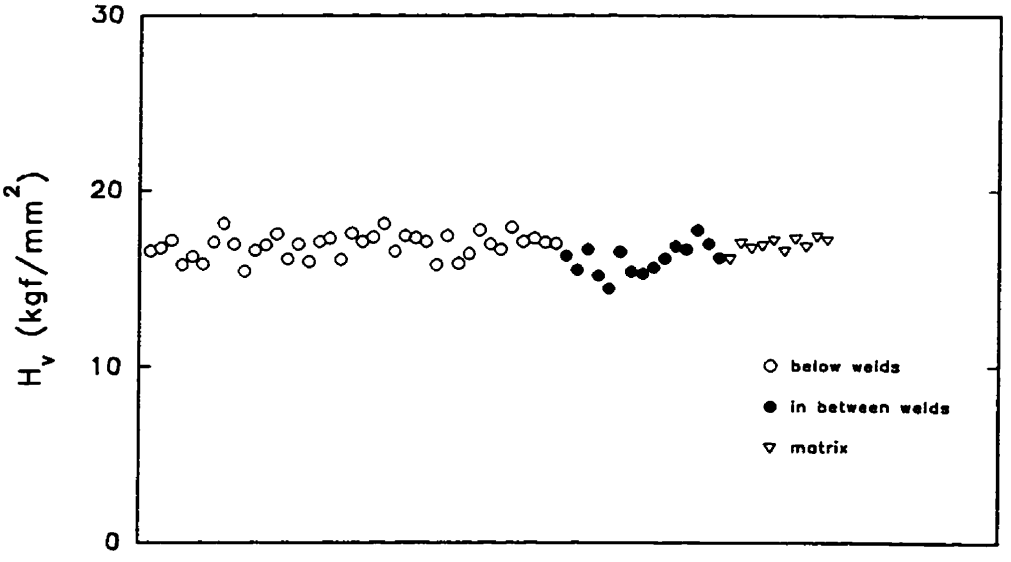

Figure 3.23a A plot showing microhardness measurements taken below the welds, in between the welds and matrix (away from the welds)

Figure 3.23b A SEM micrograph showing the indentations of microhardness measurement Mag. 250 ×.

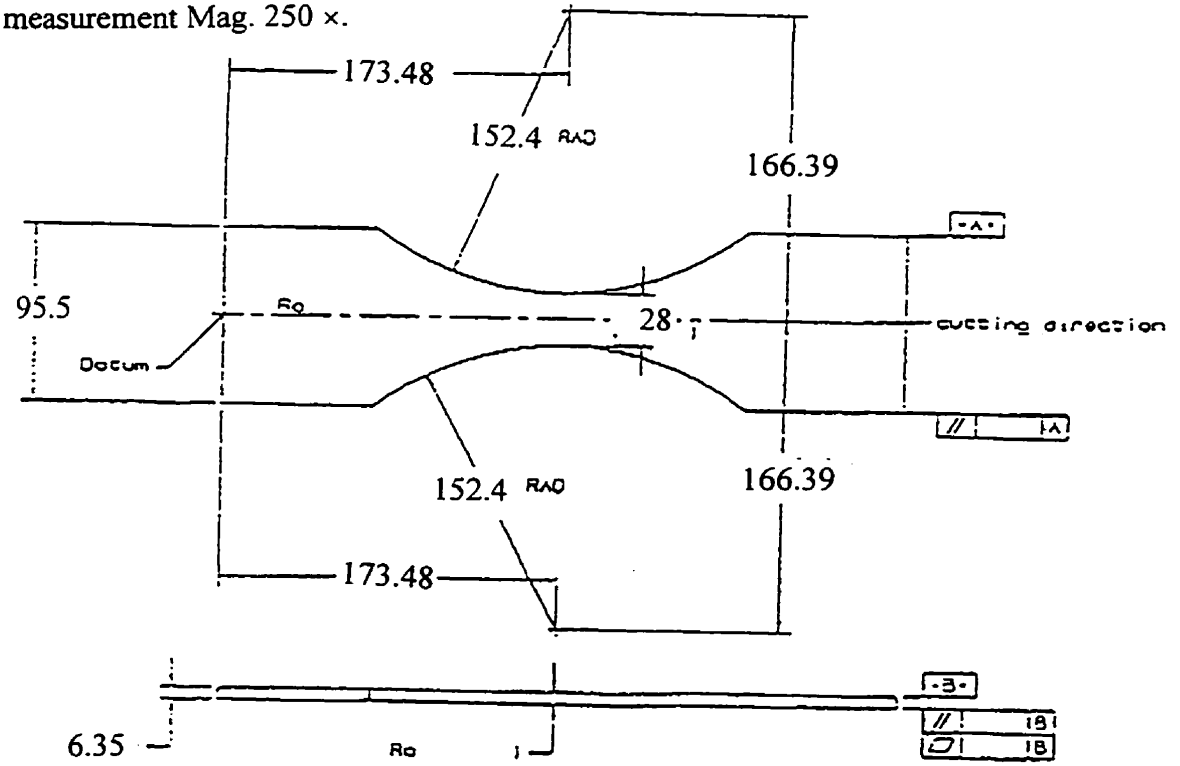

Figure 3.24 Schematic of Hourglass specimen used in the testing program.

(a)

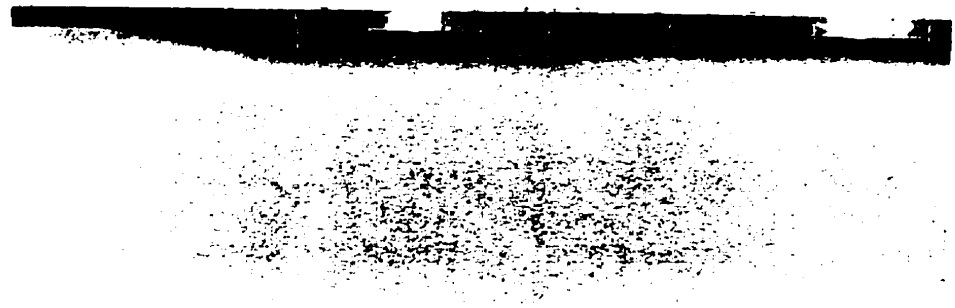

(b)

Figure 3.25 Photographs showing Al wires welded on the specimen (a) on the face (b) on the thickness side.

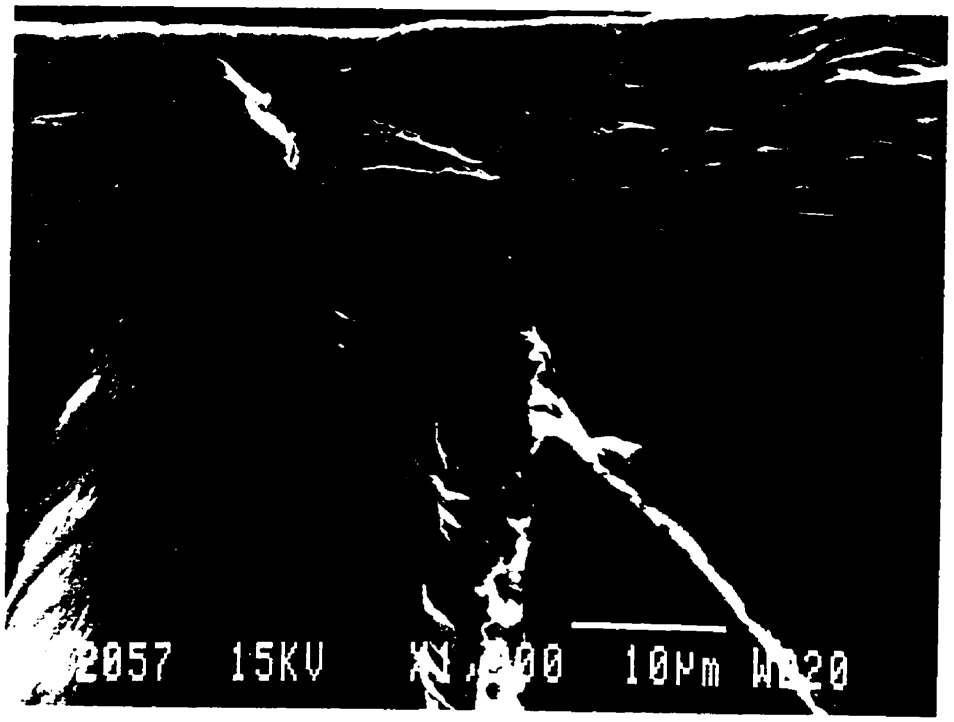

Figure 3.26 Crack initiation site in the hourglass test specimen

Figure 3.27a Photograph showing the four point bending specimen plastically deformed.

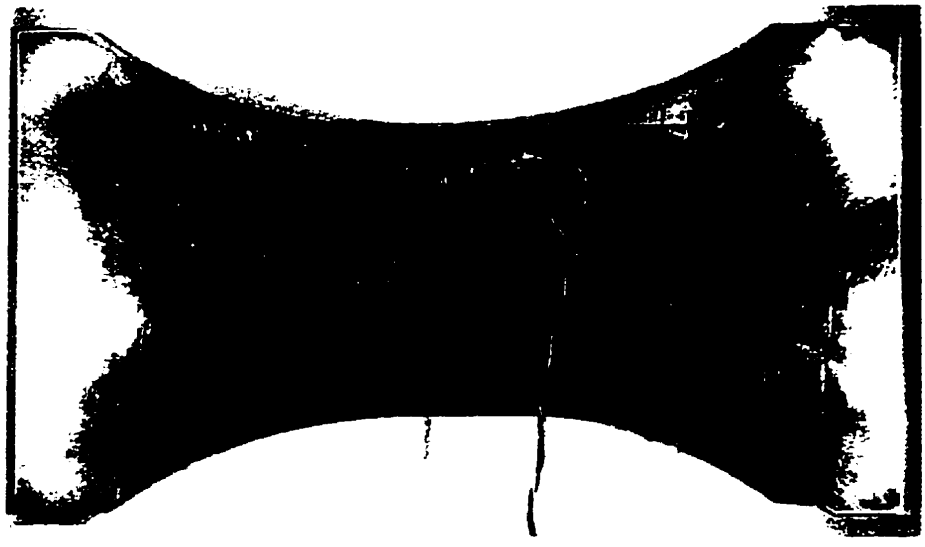

Figure 3.27b Photograph showing that the probe wires are still attached to the specimen after extensive plastic deformation.

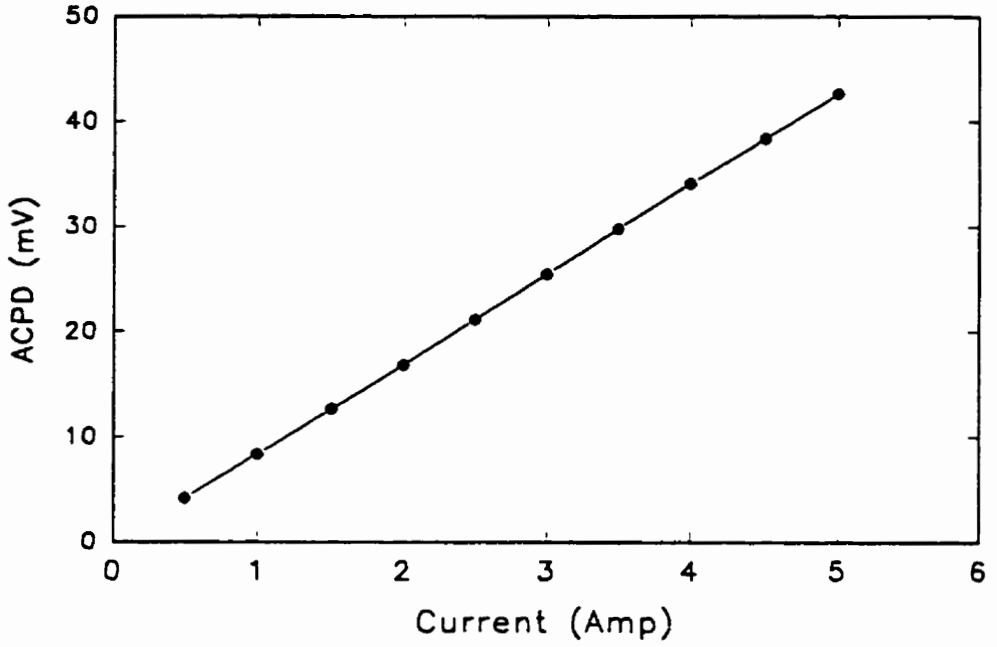

Figure 3.28a A plot of ACPD versus current.

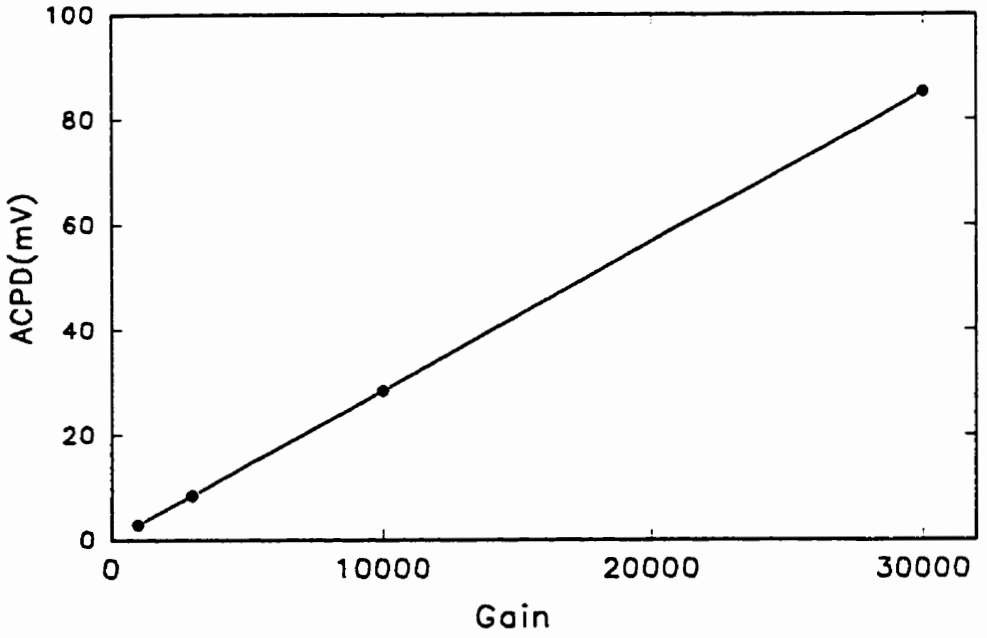

Figure 3.28b A plot of ACPD versus gain.

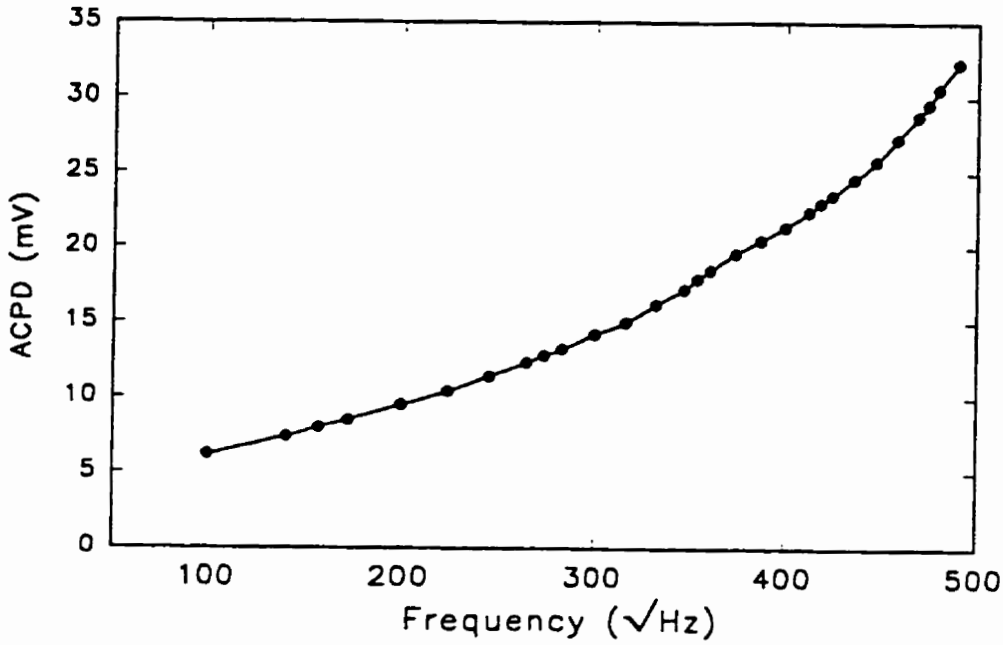

Figure 3.28c A plot of ACPD versus frequency.

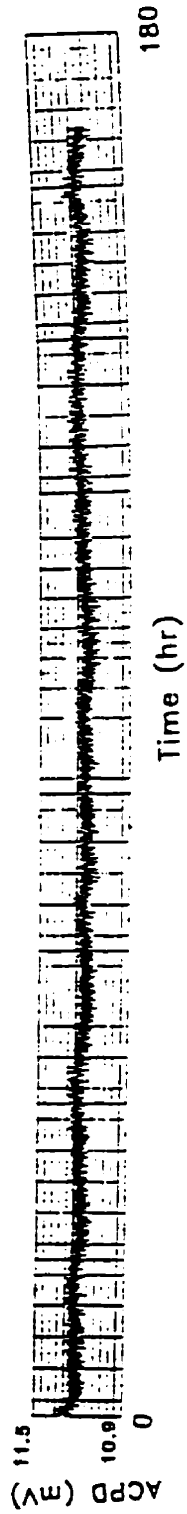

Figure 3.29a A plot of ACPD versus time for seven days.

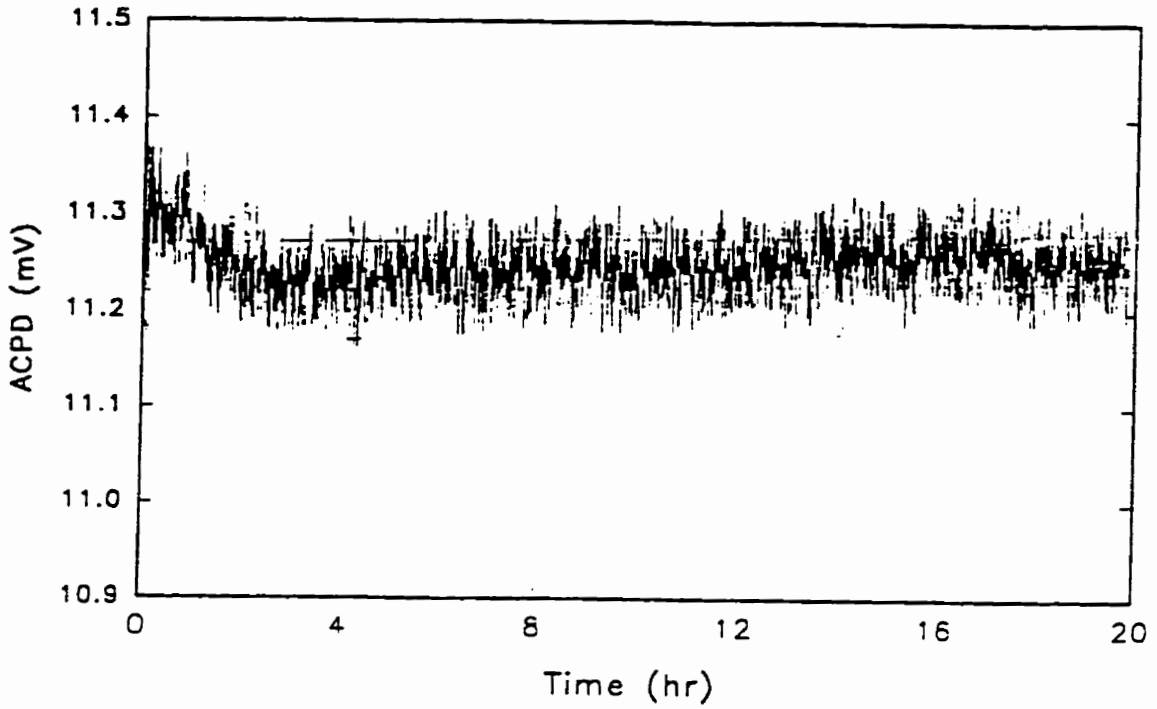

Figure 3.29b A plot of ACPD versus time (zoom of 1-20 hrs).

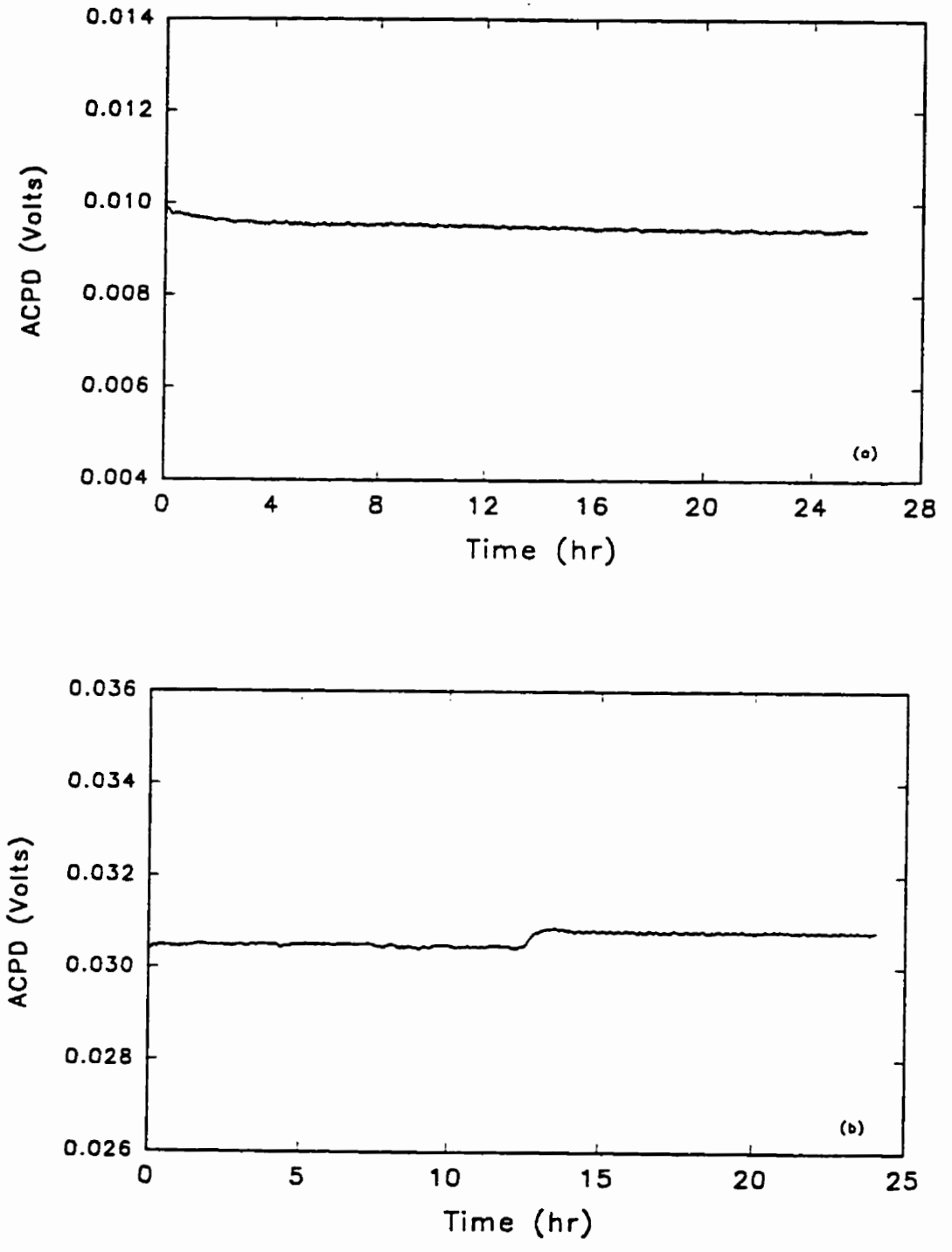

Figure 3.30 Drift measurements, showing the effect of current on ACPD signal at 30 kHz frequency and 3000 gain (a) 1 ampere current (b) 3 ampere current.

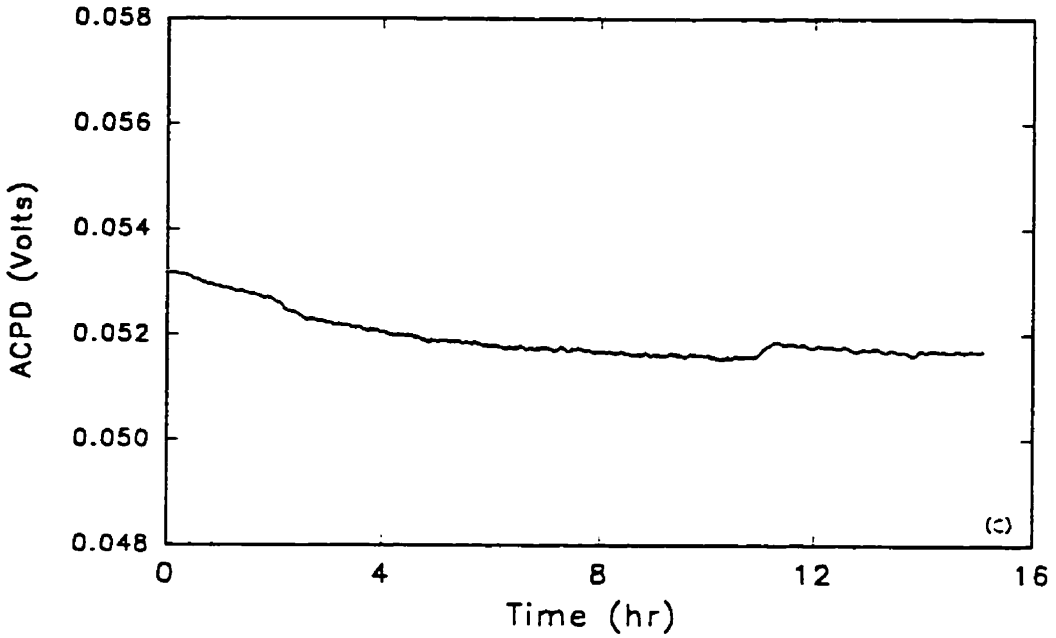

Figure 3.30 (c) 5 ampere current.

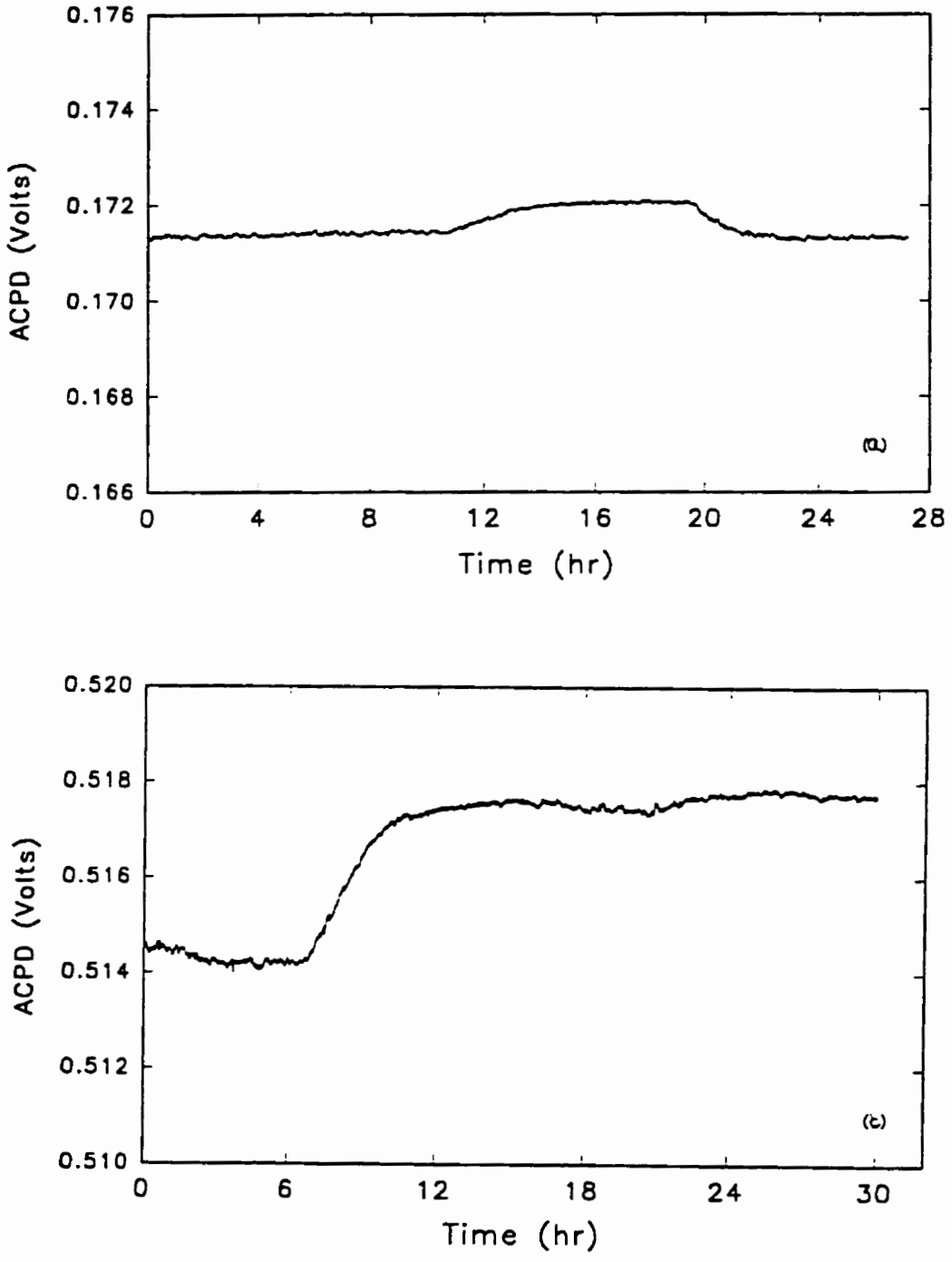

Figure 3.31 Drift measurements, showing the effect of gain on ACPD signal at 30 kHz and 5 amperes. (a) 10 000 gain, (b) 30 000 gain.

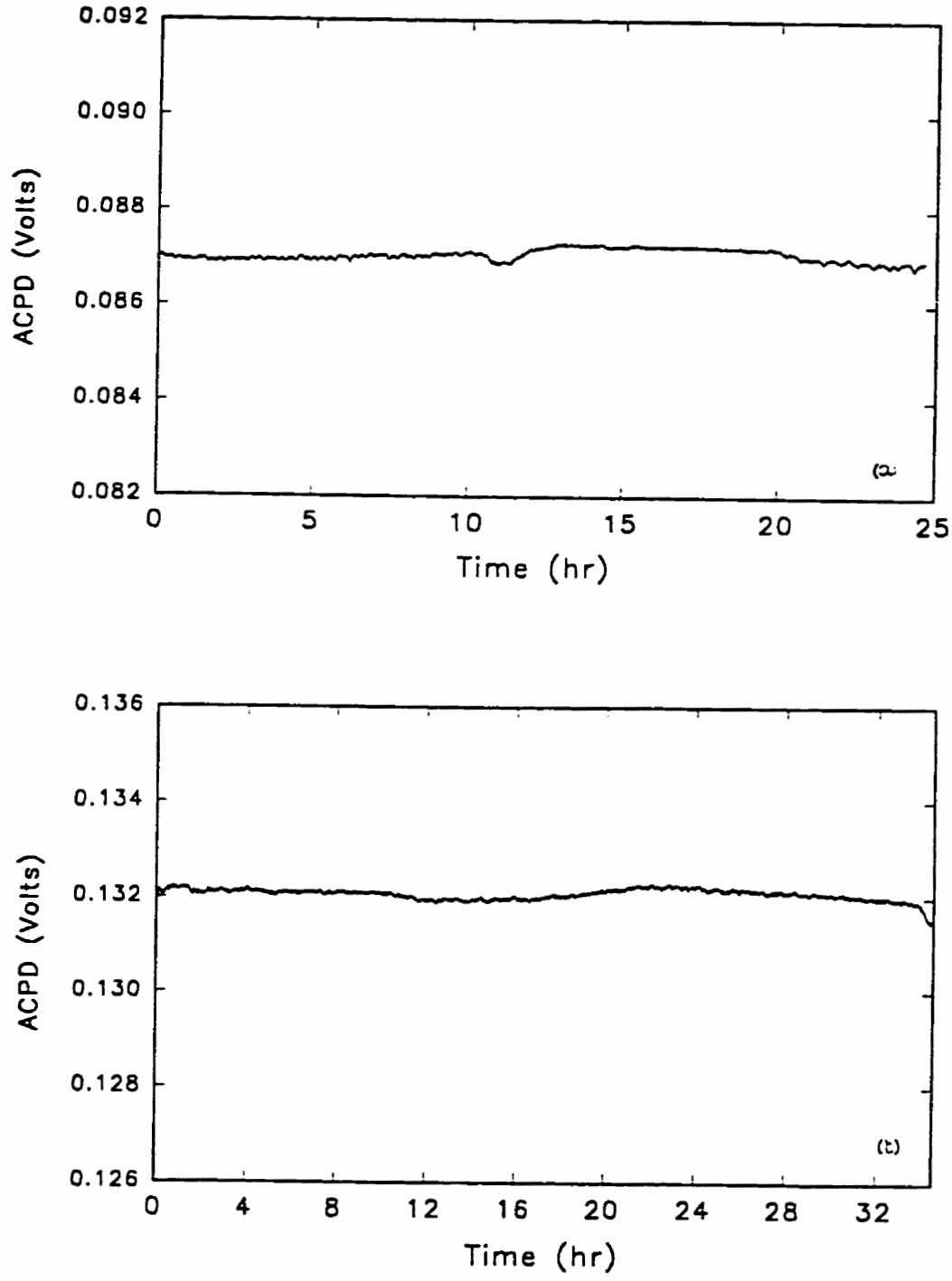

Figure 3.32 Drift measurements, showing the effect of frequency on ACPD signal at 5 amperes and 3000 gain (a)120 kHz, (b) 200 kHz.

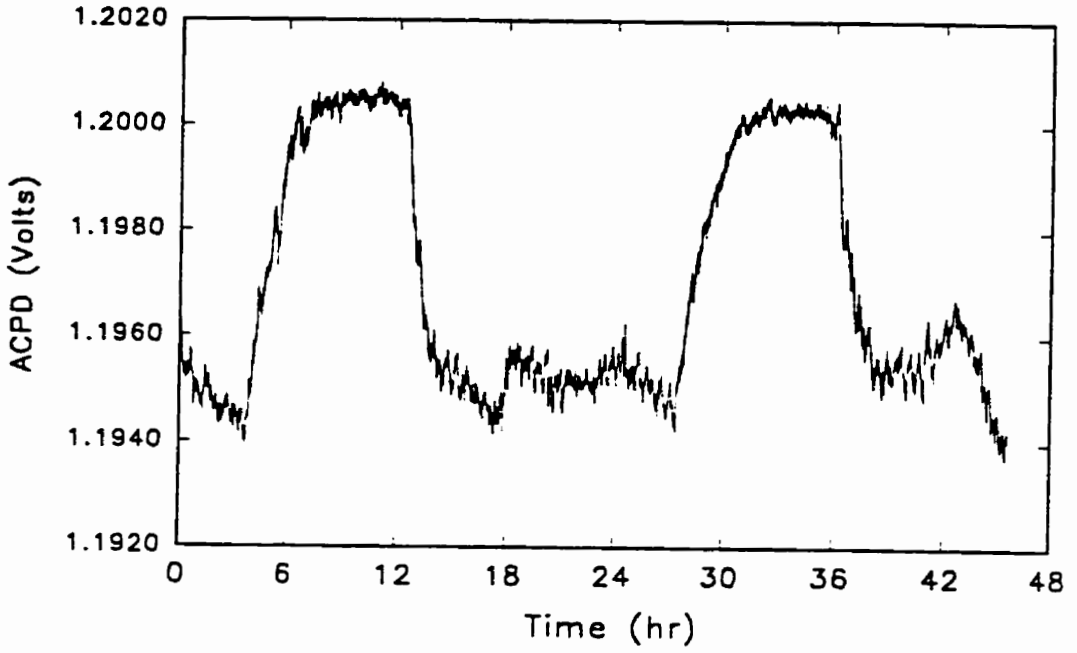

Figure 3.33 Drift measurements, showing the effect of temperature on ACPD signal at 120 kHz, 5 ampere and 30 000 gain.

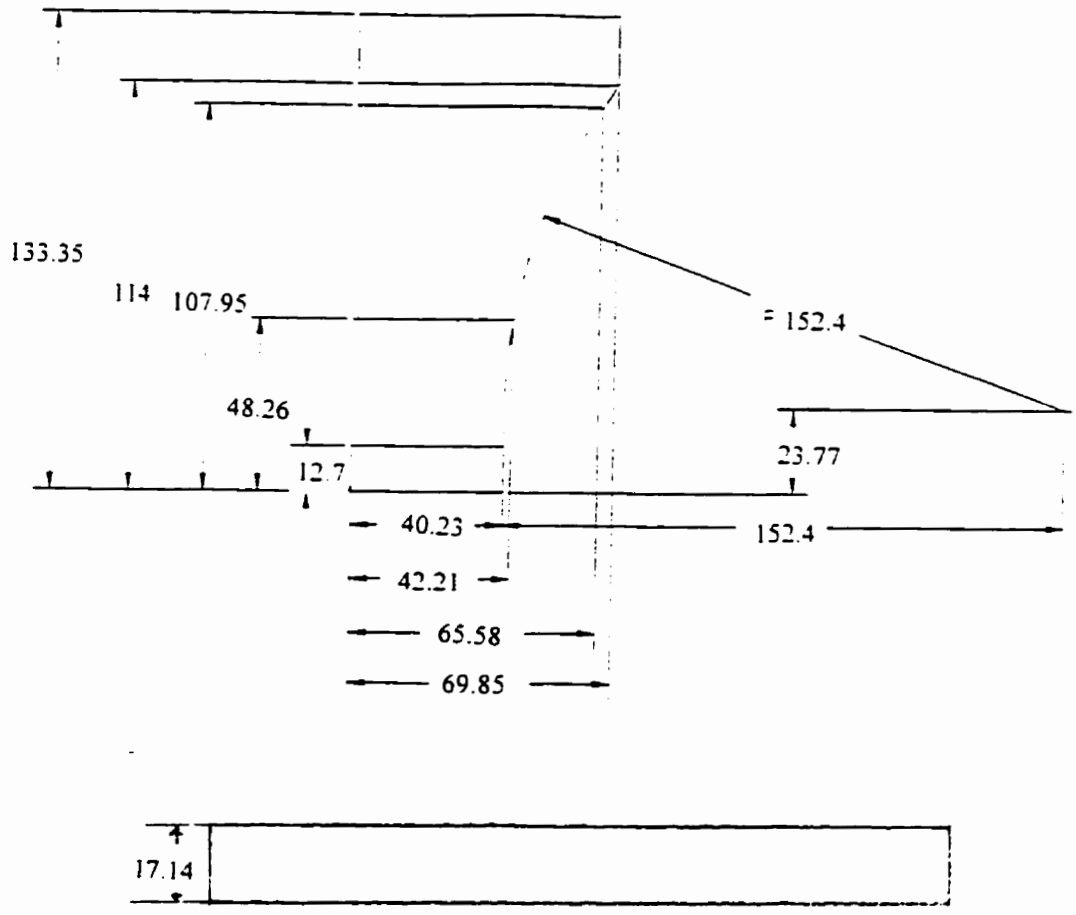

Figure 3.34 A schematic showing a quarter of four point bending specimen.

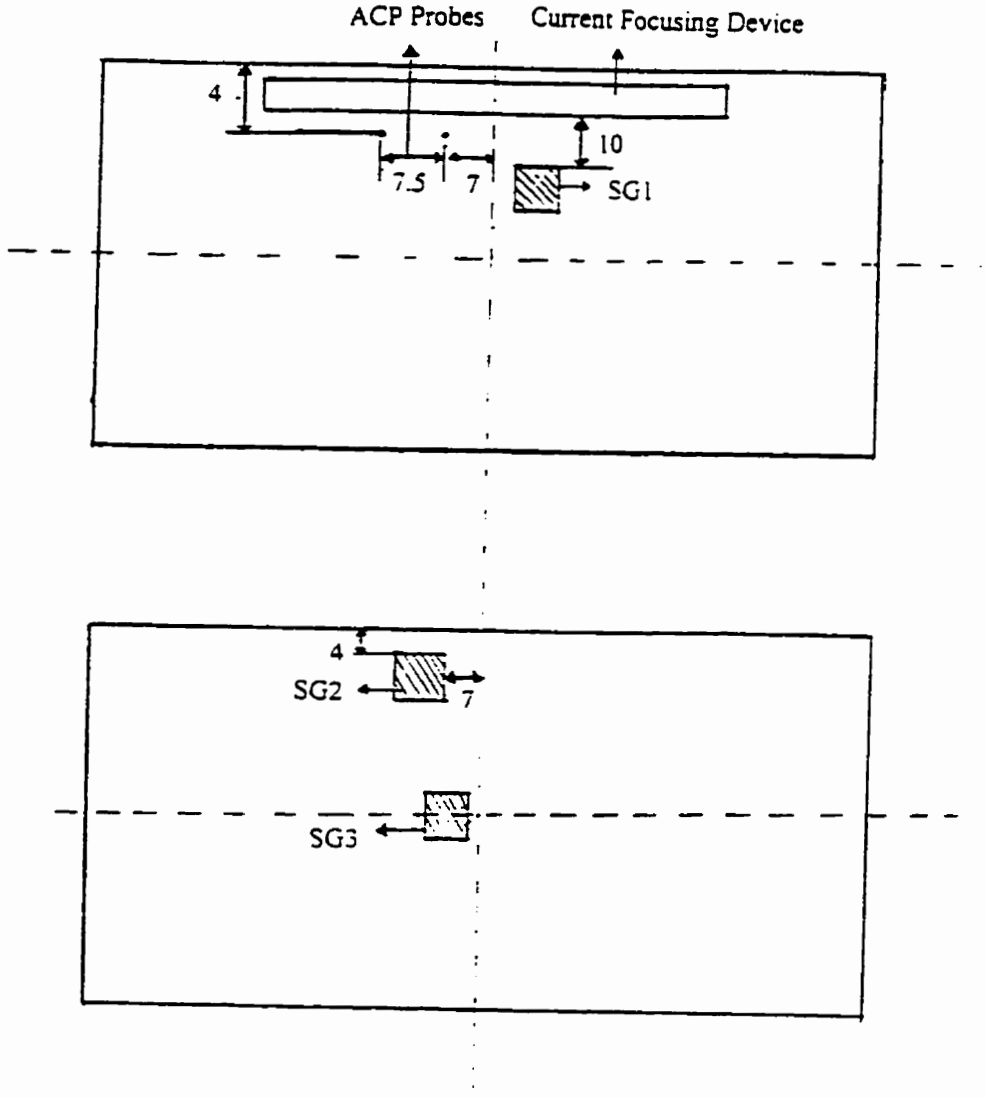

Figure 3.35 Schematic showing locations of ACPD probes and strain gauges.

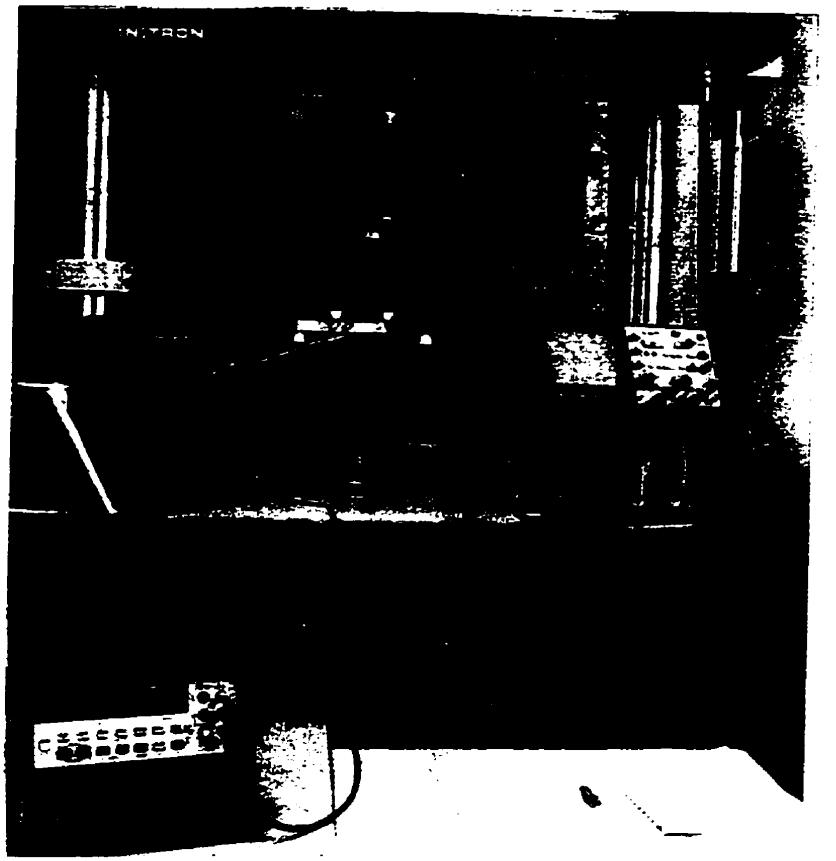

Figure 3.36 Photograph showing close up of four-point bending test.

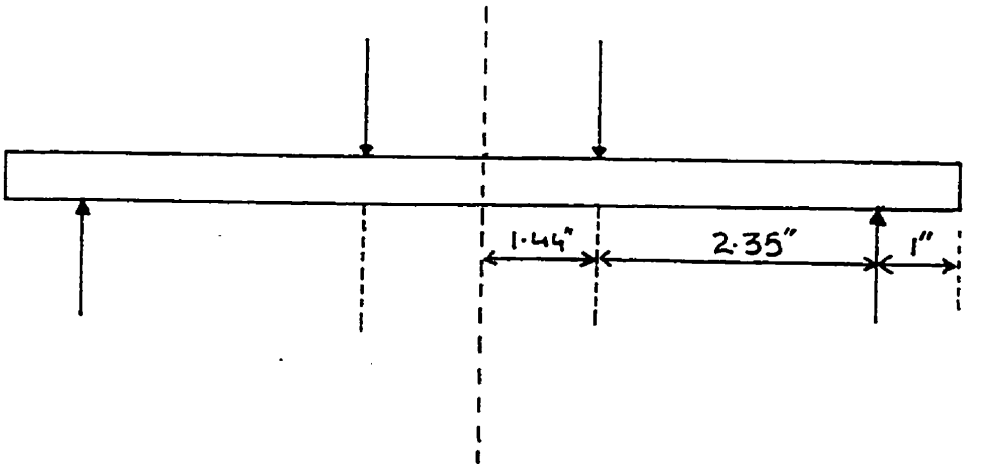

Figure 3.37 Schematic of four contact points on four point bending specimen.

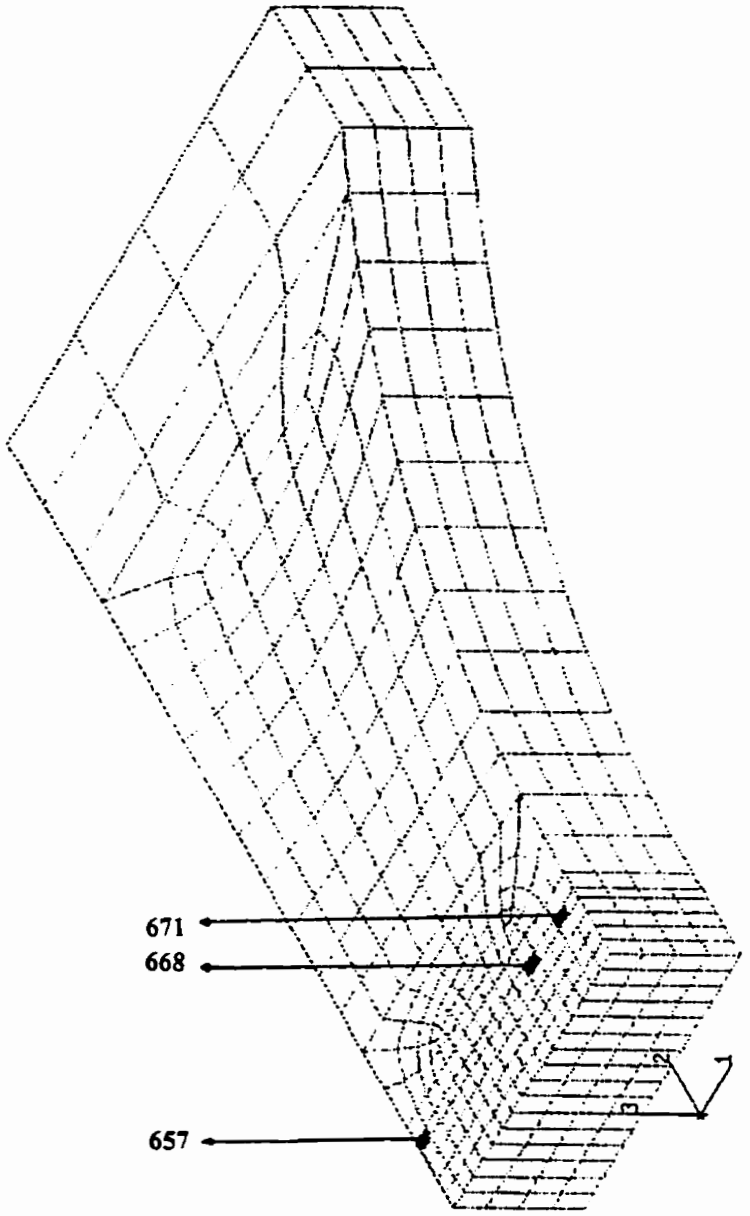

Figure 3.38 Finite element mesh showing locations where strain measurements were carried out.

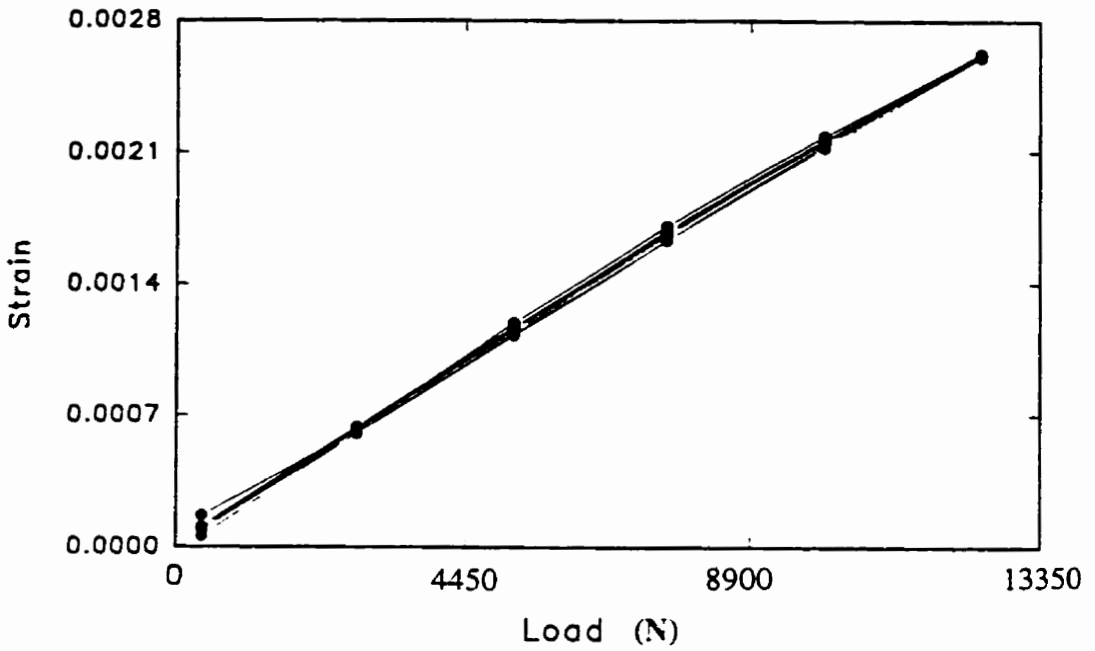

Figure 3.39a A plot of strain versus load for SG1.

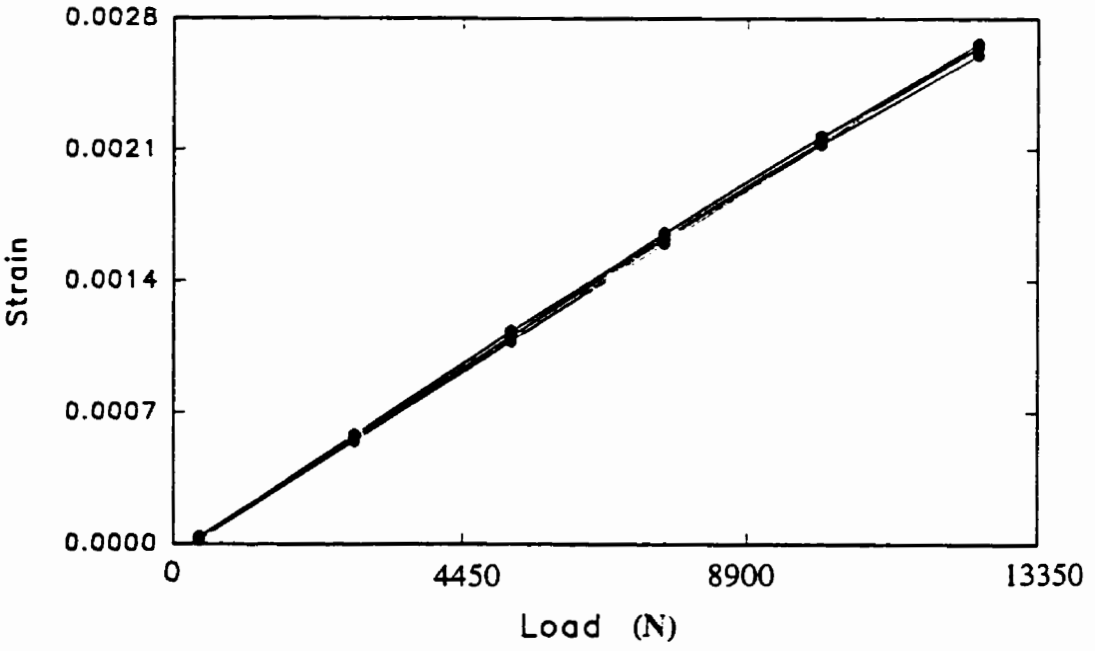

Figure 3.39b A plot of strain versus load for SG2.

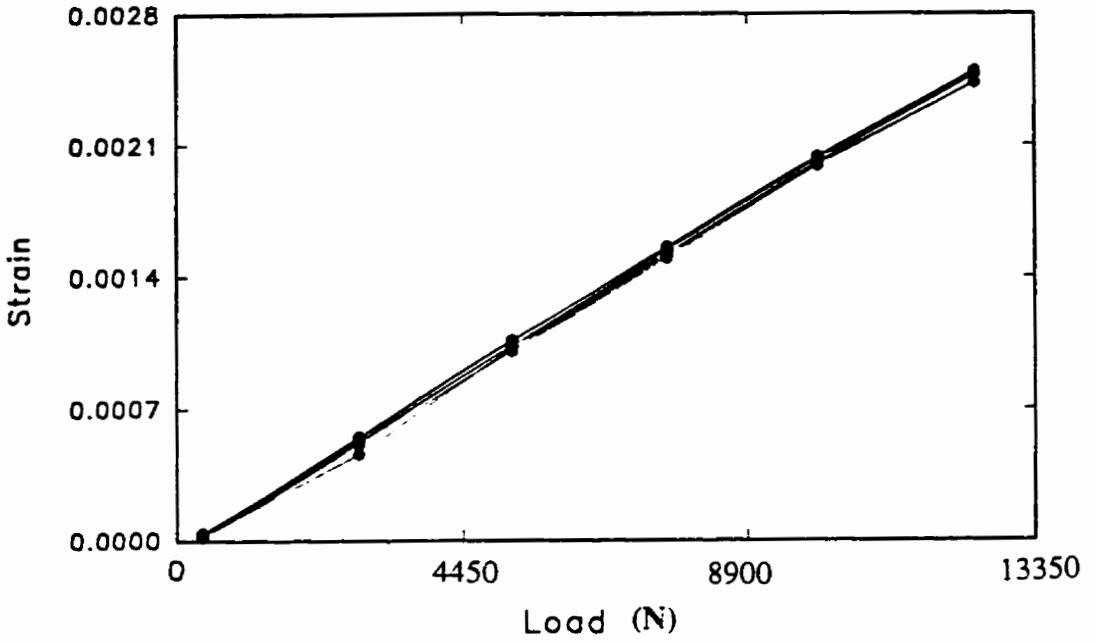

Figure 3.39c A plot of strain versus load for SG3.

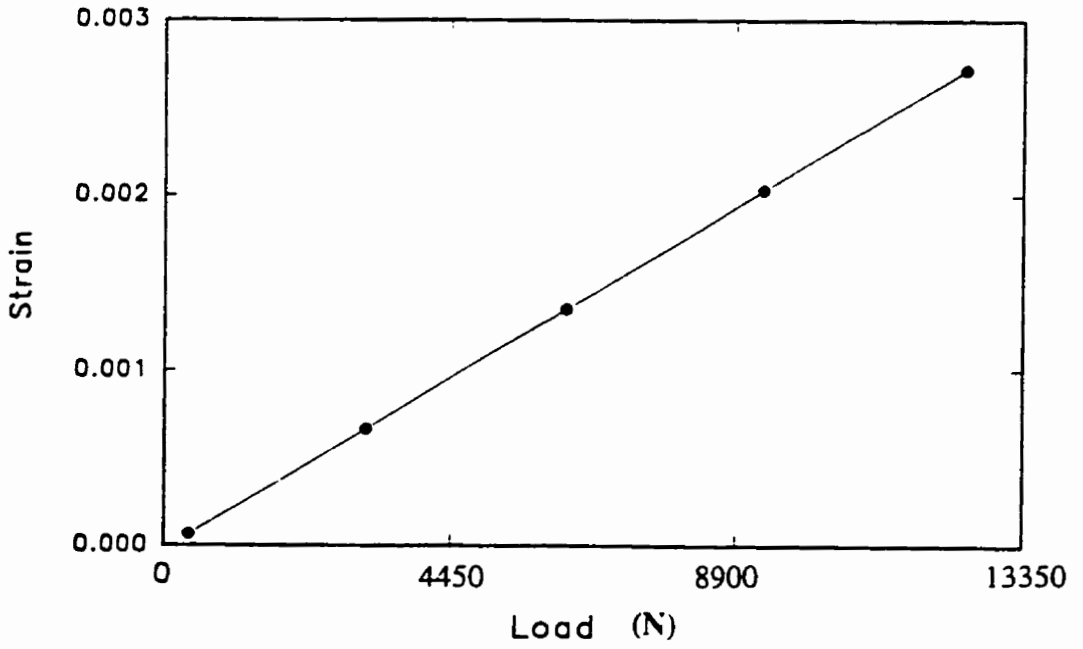

Figure 3.40a A plot of strain versus load for element 668.

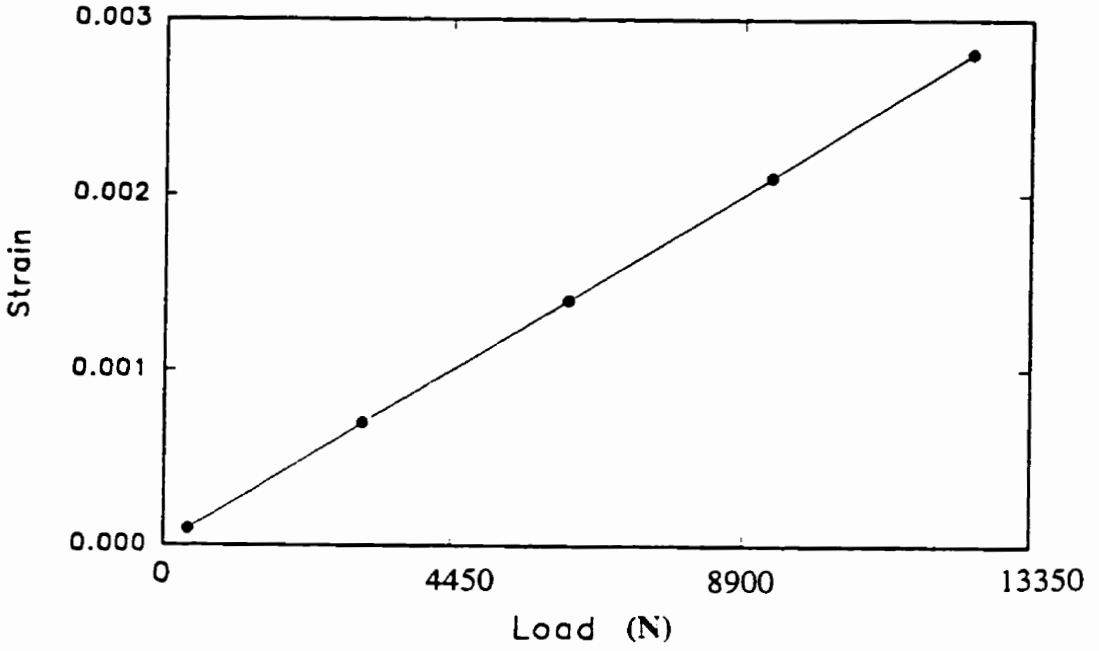

Figure 3.40b A plot of strain versus load for element 671.

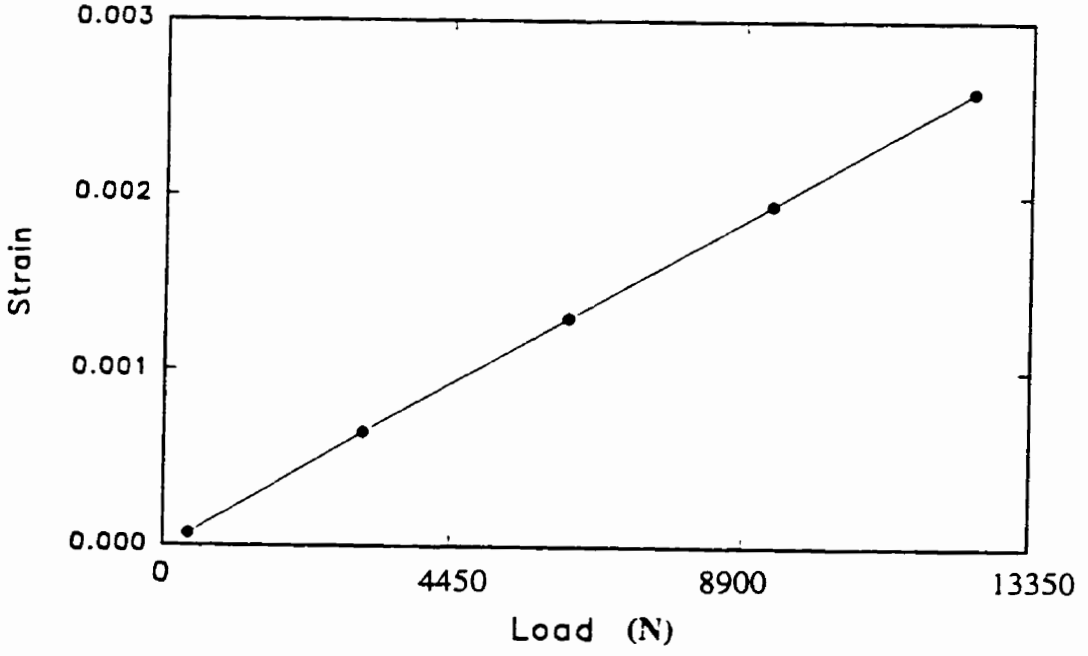

Figure 3.40c A plot of strain versus load for element 657.

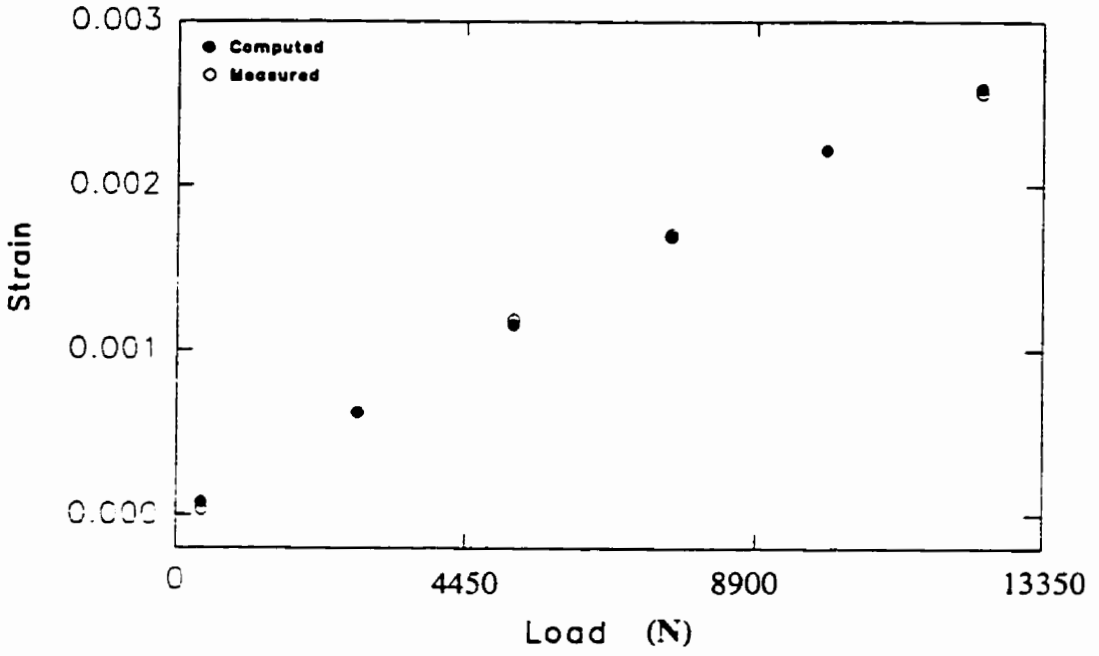

Figure 3.41 A comparison of strain versus load for SG1 and element 668.

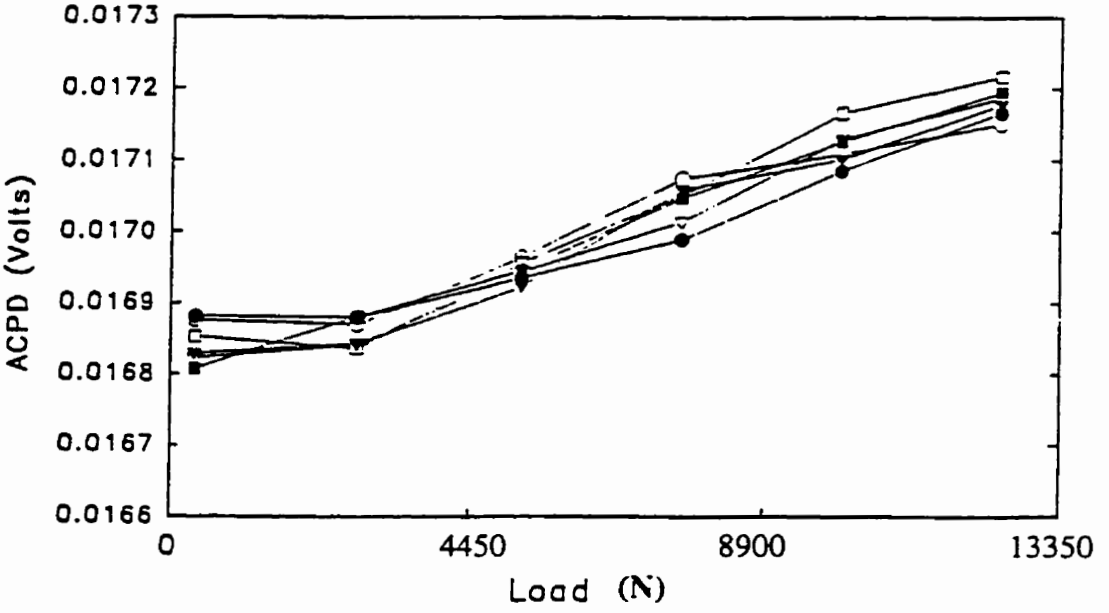

Figure 3.42 A plot of ACPD versus load.

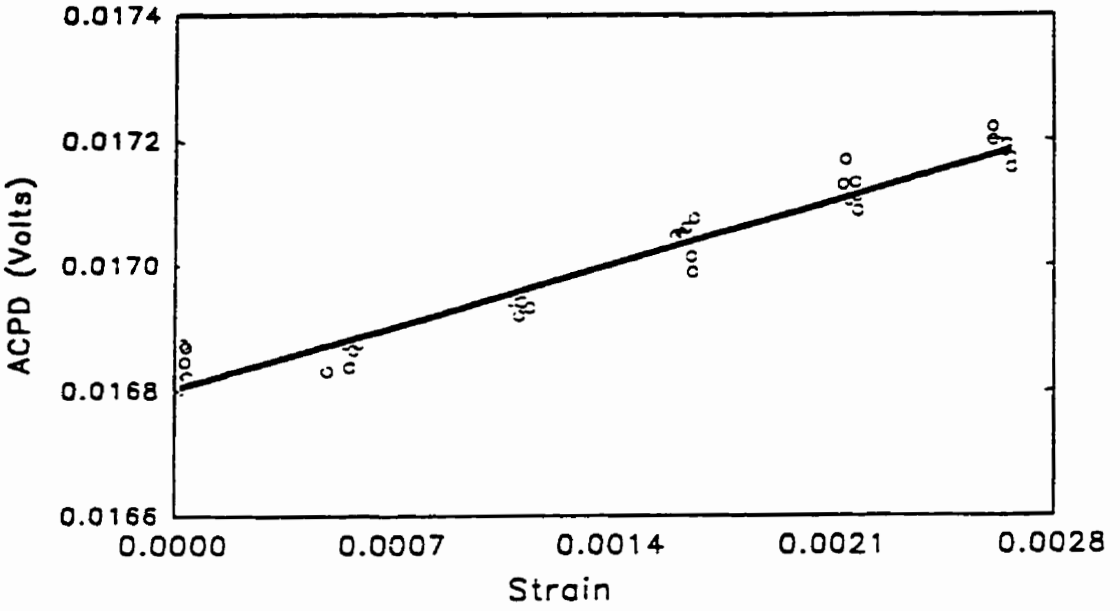

Figure 3.43 Strain calibration curve, a plot of ACPD versus strain.

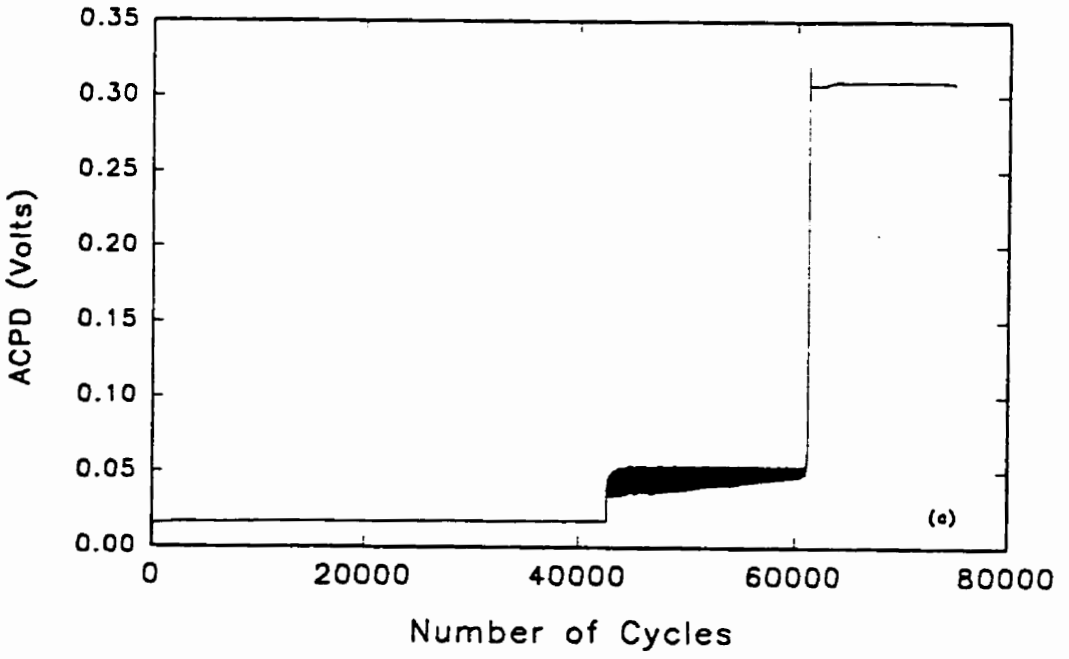

Figure 3.44a A plot of ACPD versus number of fatigue cycles.

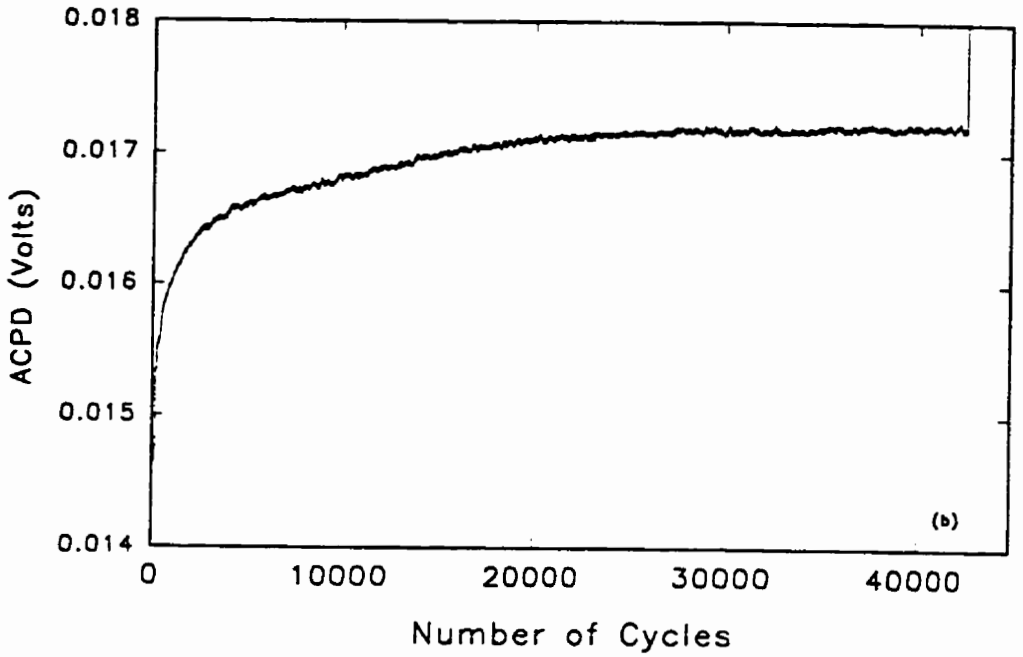

Figure 3.44 (b) Zoom of a.

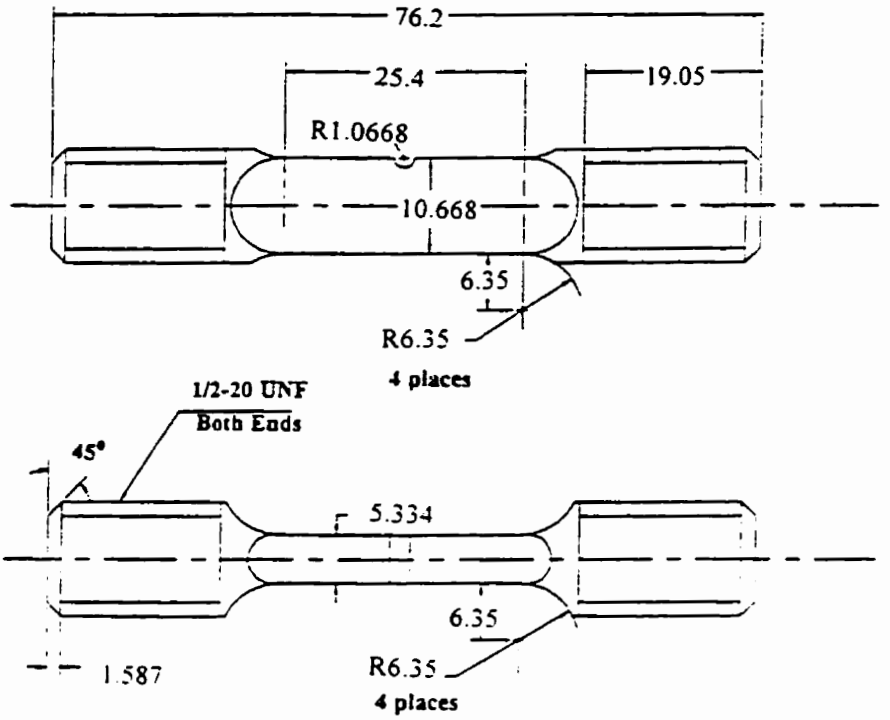

Figure 3.45 A schematic of SEN specimen used in the testing program.

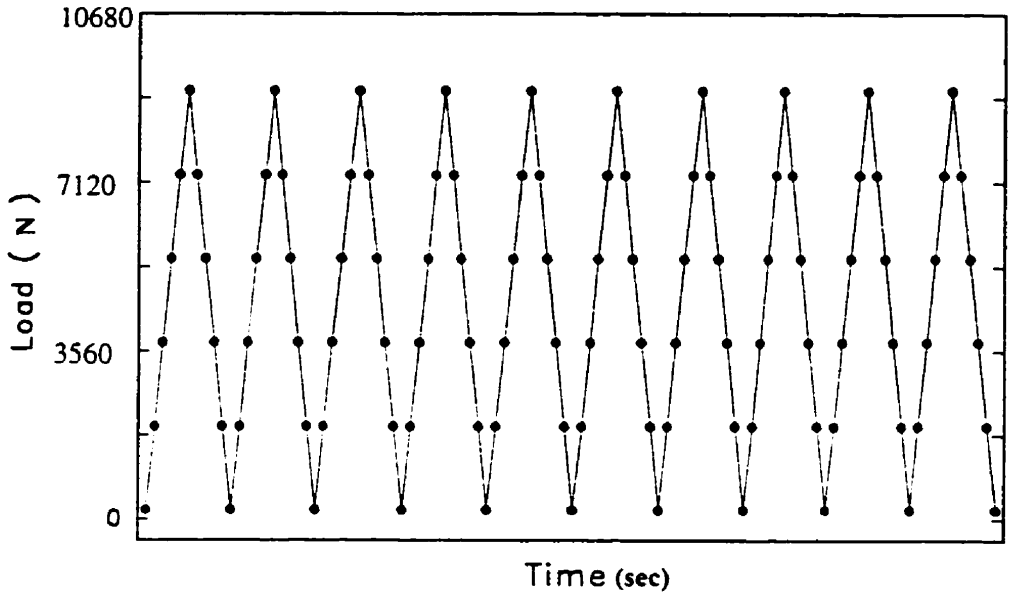

Figure 3.46 A plot of load (feedback) versus time applied on the SEN specimen.

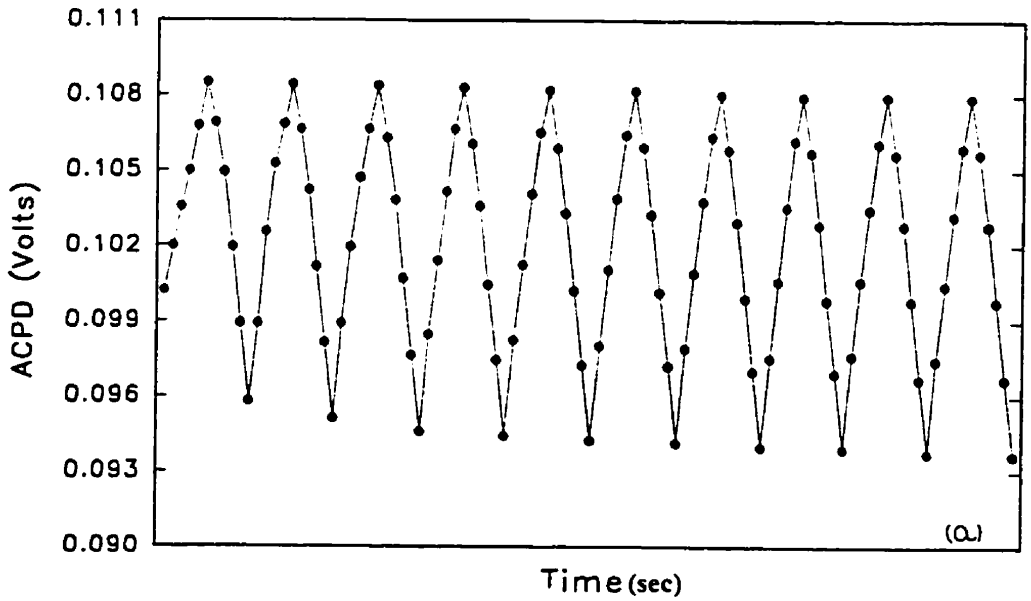

Figure 3.47 A plot of ACPD versus time (a) cycles 1-10.

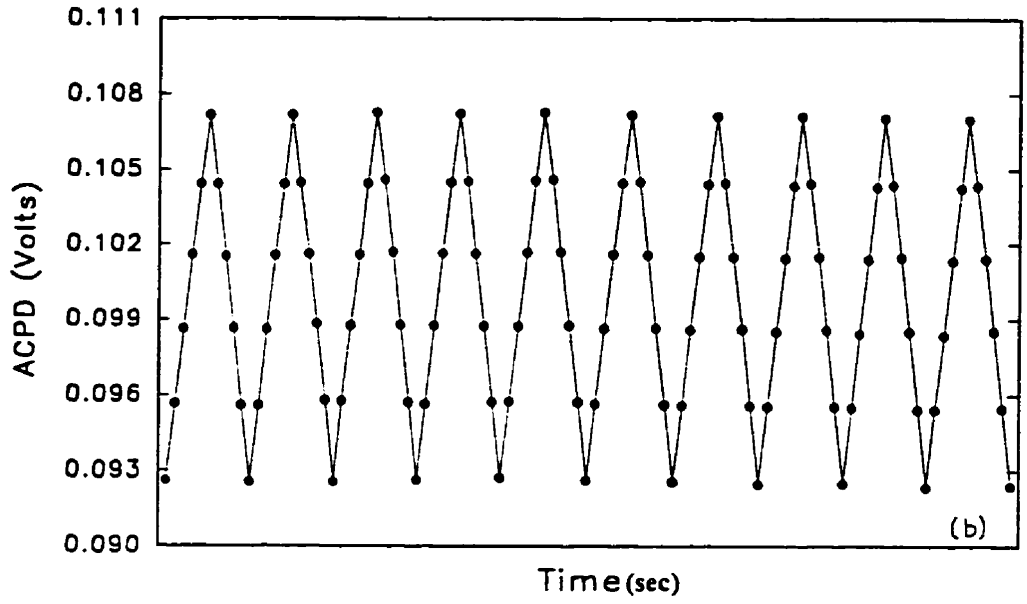

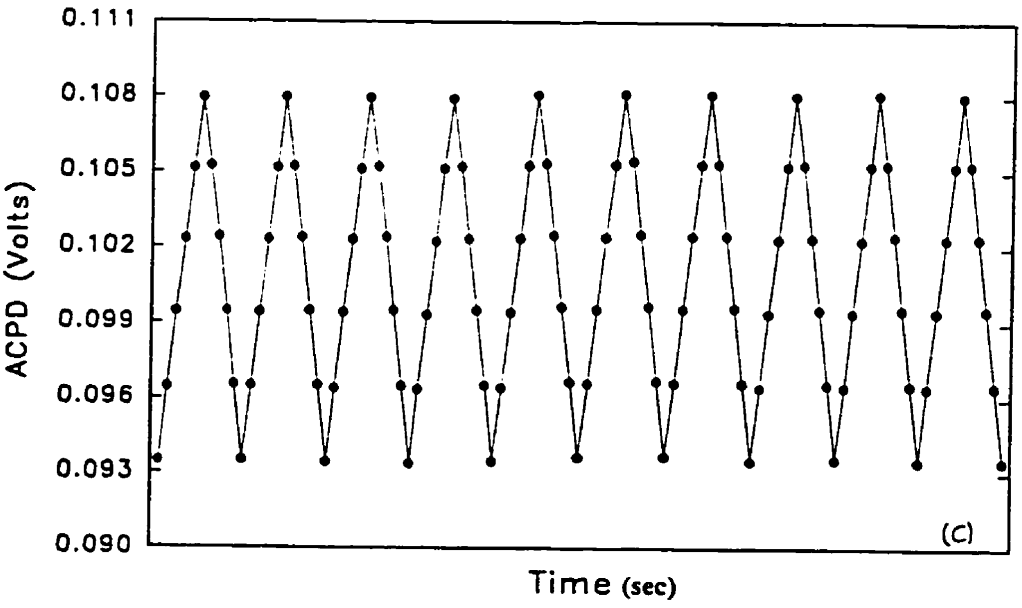

Figure 3.47 A plot of ACPD versus time (b) cycles 90-100 (c) cycles 265-275.

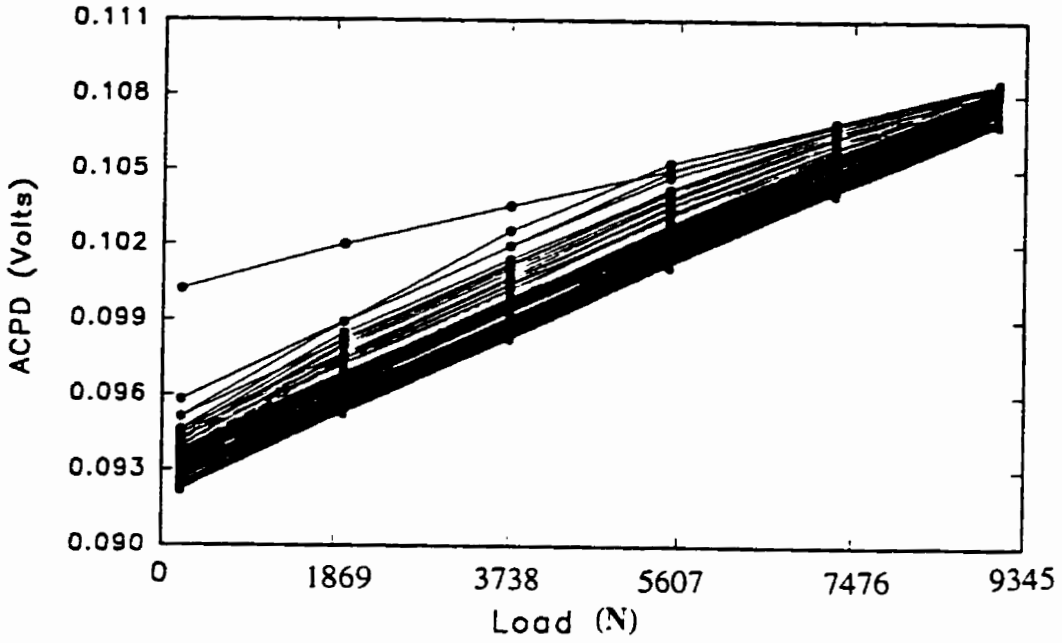

Figure 3.48 A plot of ACPD versus load cycles (1-275)

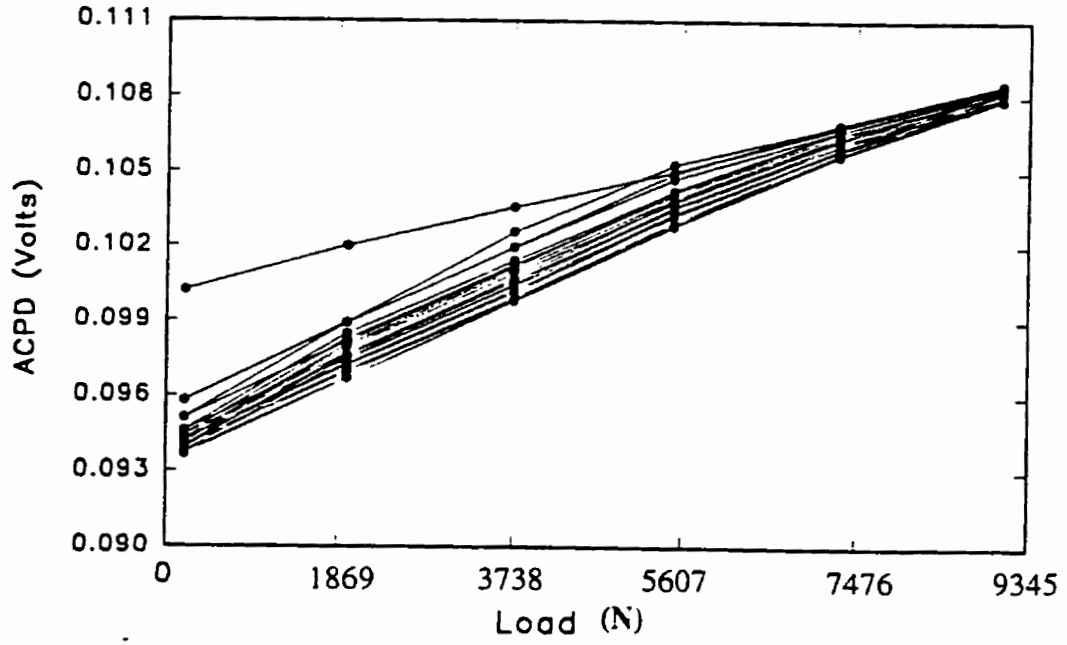

Figure 3.49 A plot of ACPD versus load (a) cycles 1-10.

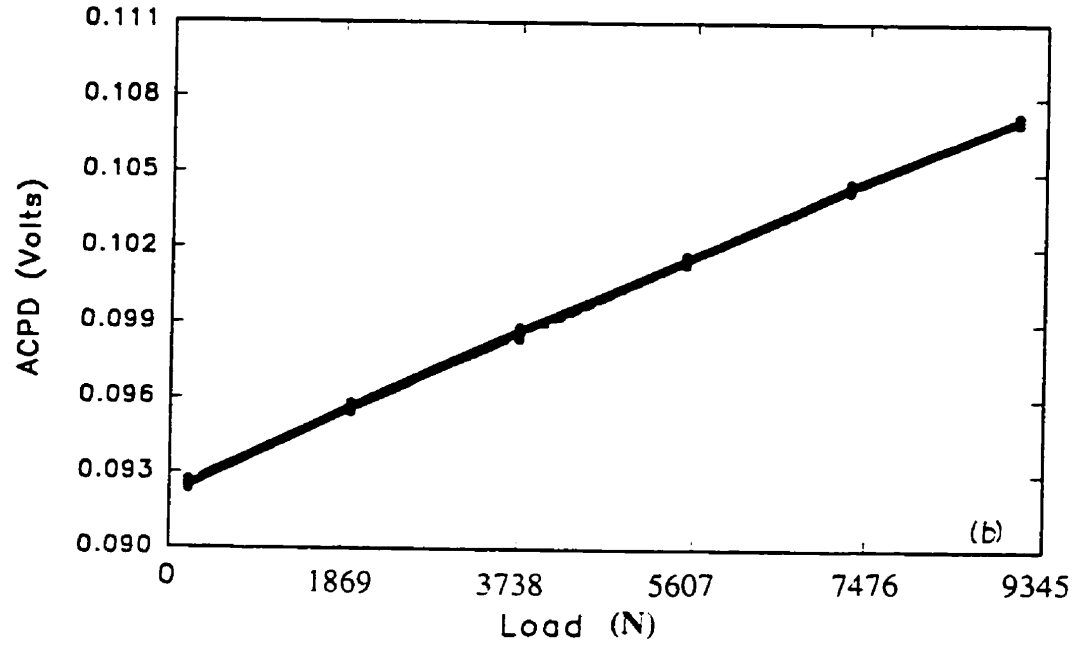

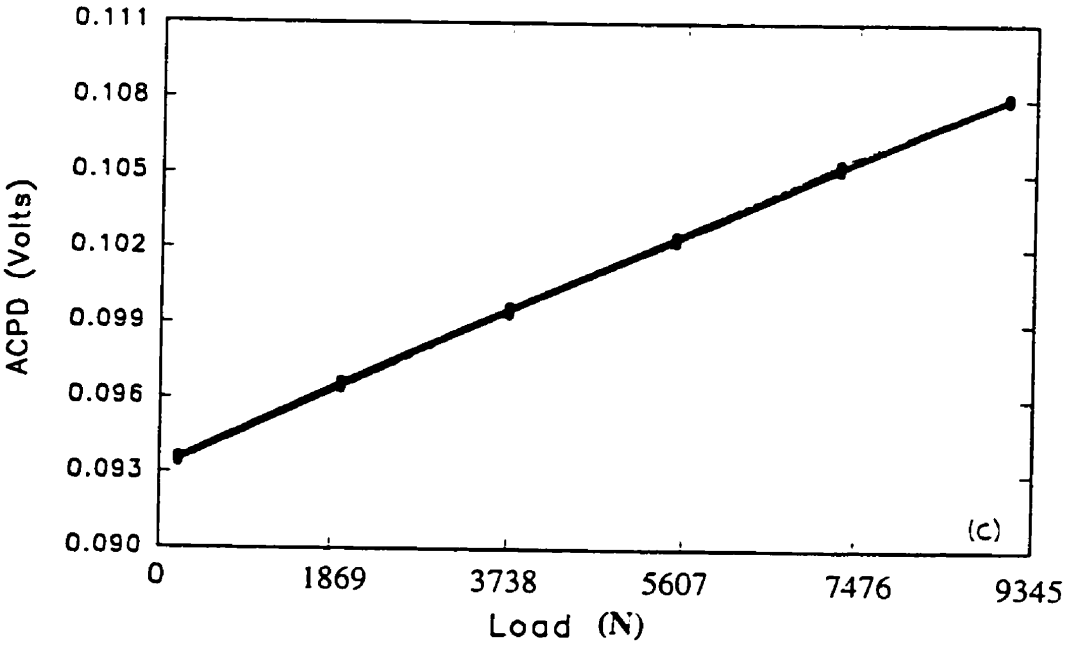

Figure 3.49 (b) cycles 90-100 and (c) cycles 265-275.

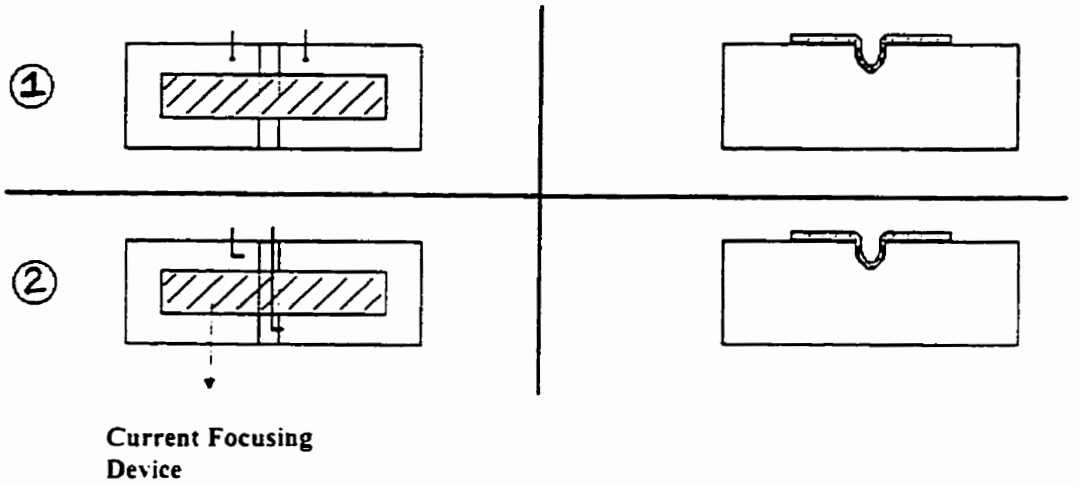

Figure 3.50 Schematic showing different probe arrangements studied in the program.

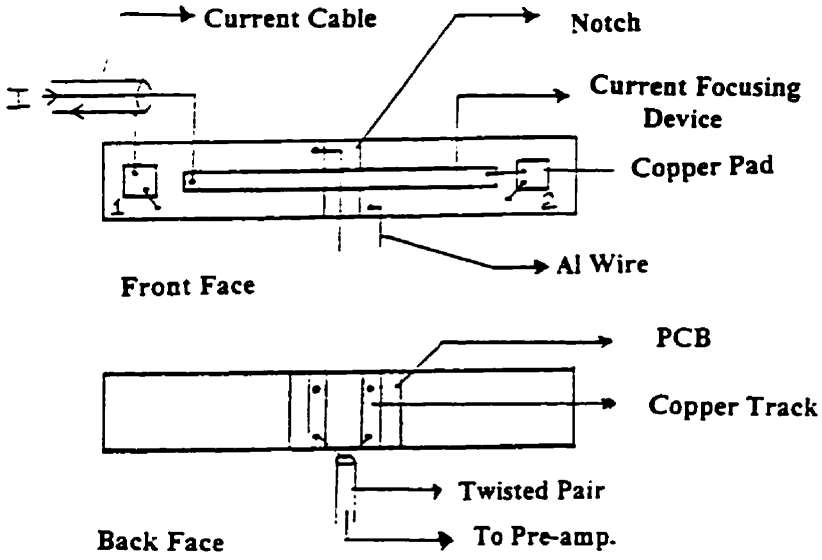

Figure 3.51 A detailed schematic of final probe design used on the SEN specimen.

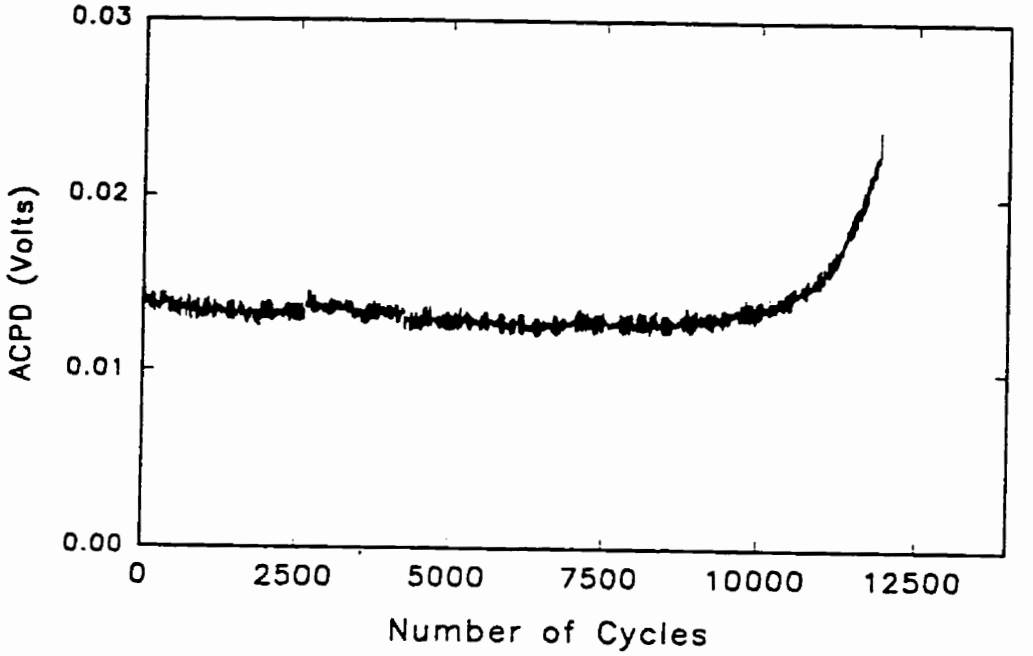

Figure 3.52 A typical plot of ACPD versus number of fatigue cycles.

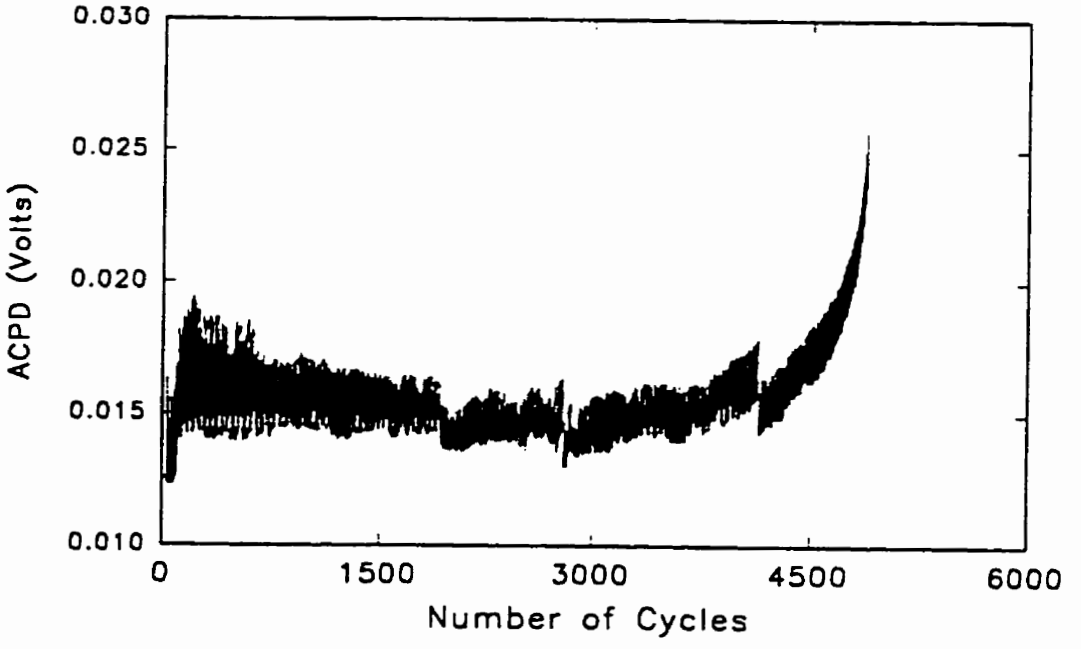

Figure 3.53 A plot of ACPD versus number of cycles for faster data acquisition (10 PLC).

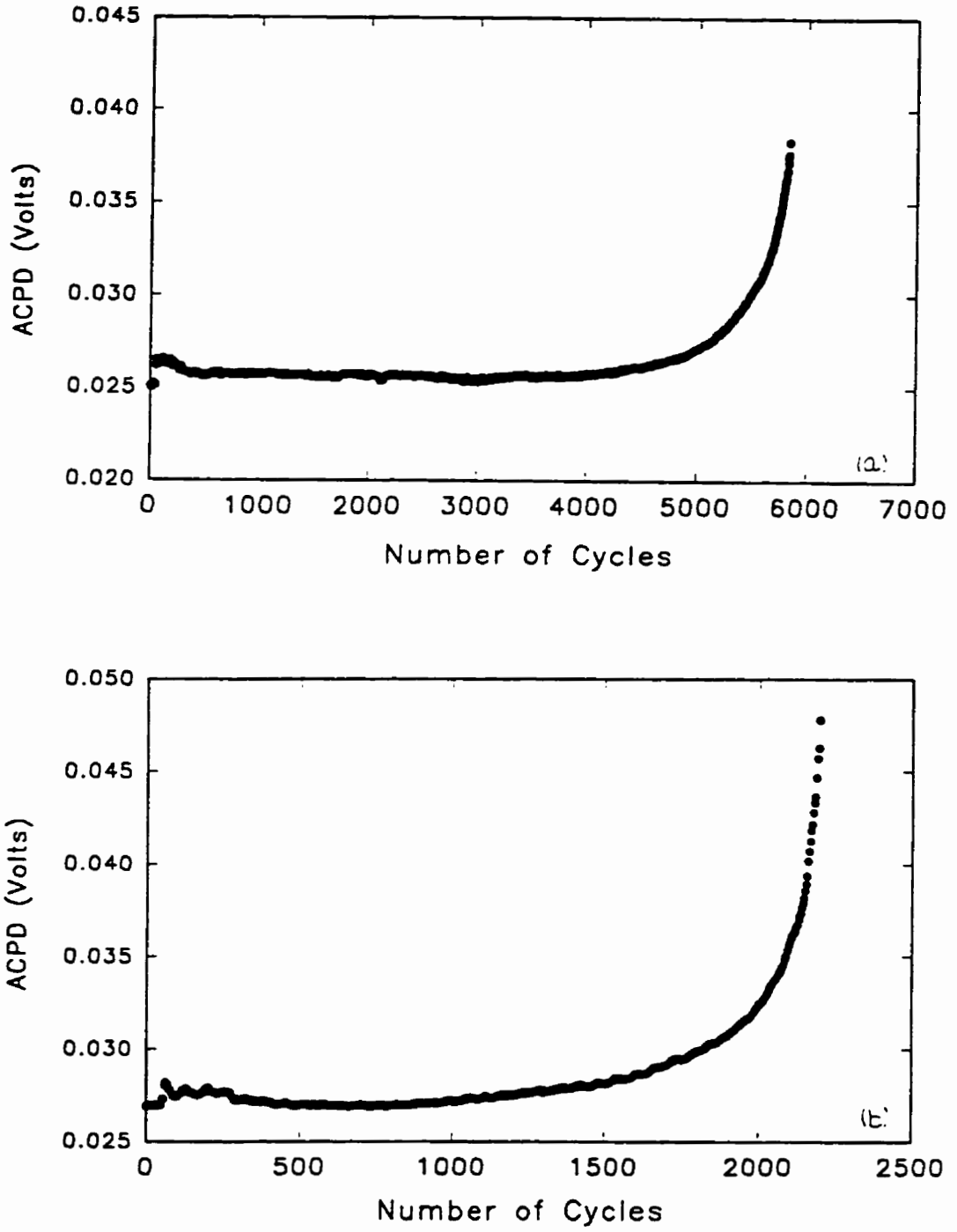

Figure 3.54 Plots of ACPD versus number of fatigue cycles (a) using probe design # 1 (b) using probe design # 2.

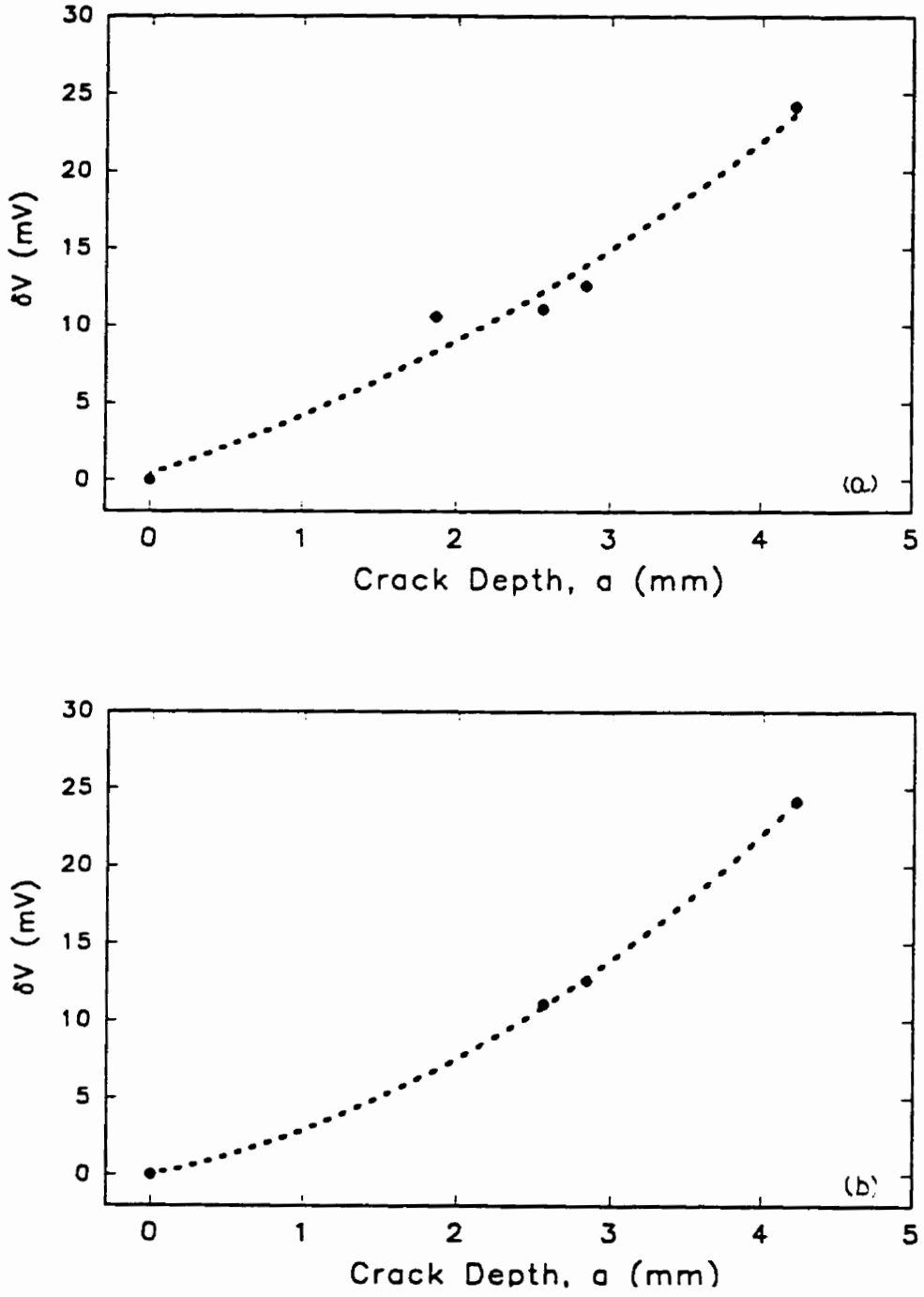

Figure 3.55 Crack calibration curves relating potential change with dominant crack depth at 30 kHz, 1 amp. and 3000 gain using probe design # 1 (a) Includes all data points (b) data point obtained at 10 PLC acquisition rate rejected.

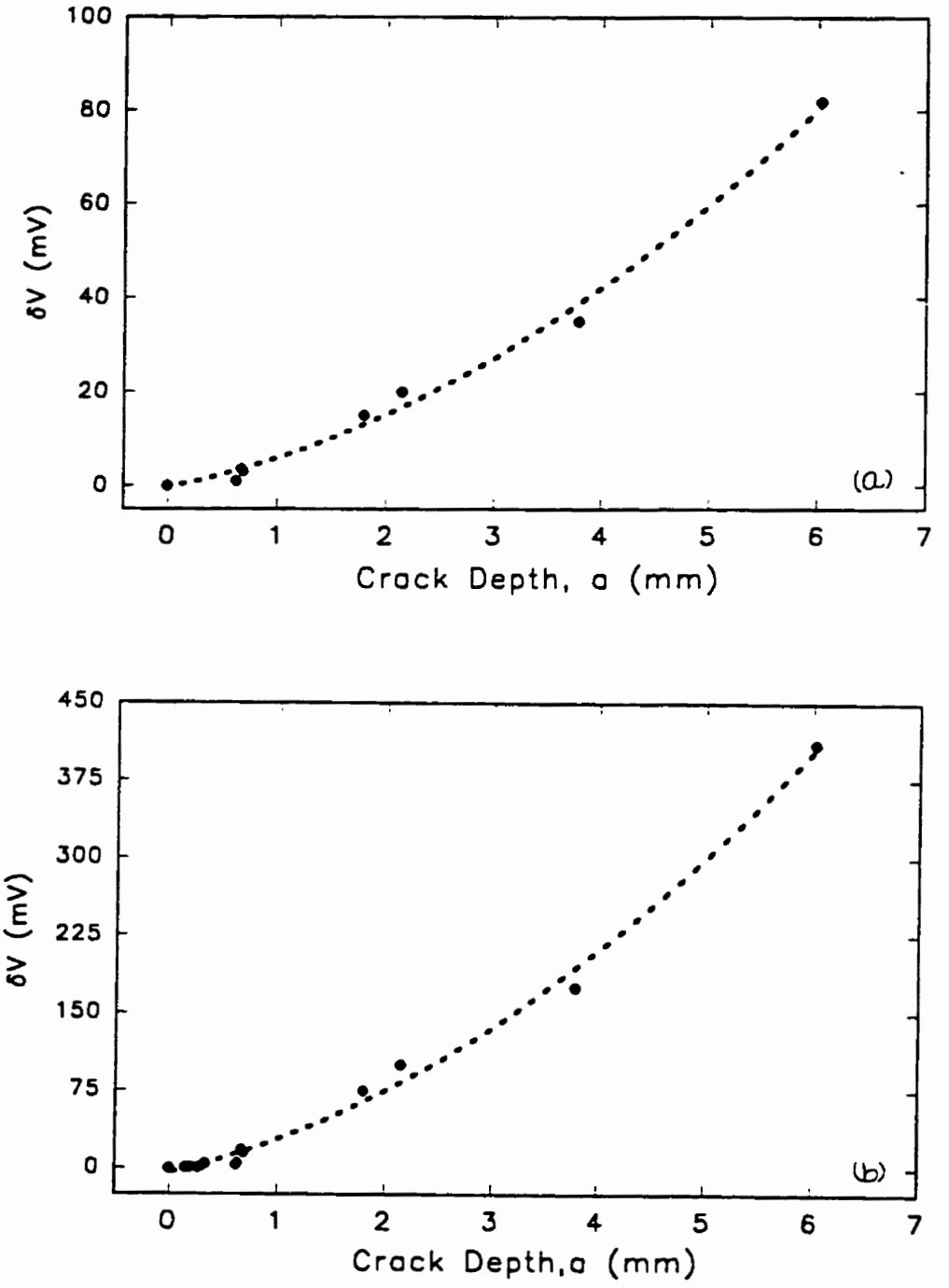

Figure 3.56 Crack calibration curves relating potential change with dominant crack depth using probe design # 2. (a) 30 kHz, 1 amp. and 3000 gain, (b) 30 kHz, 5 amp. and 3000 gain.

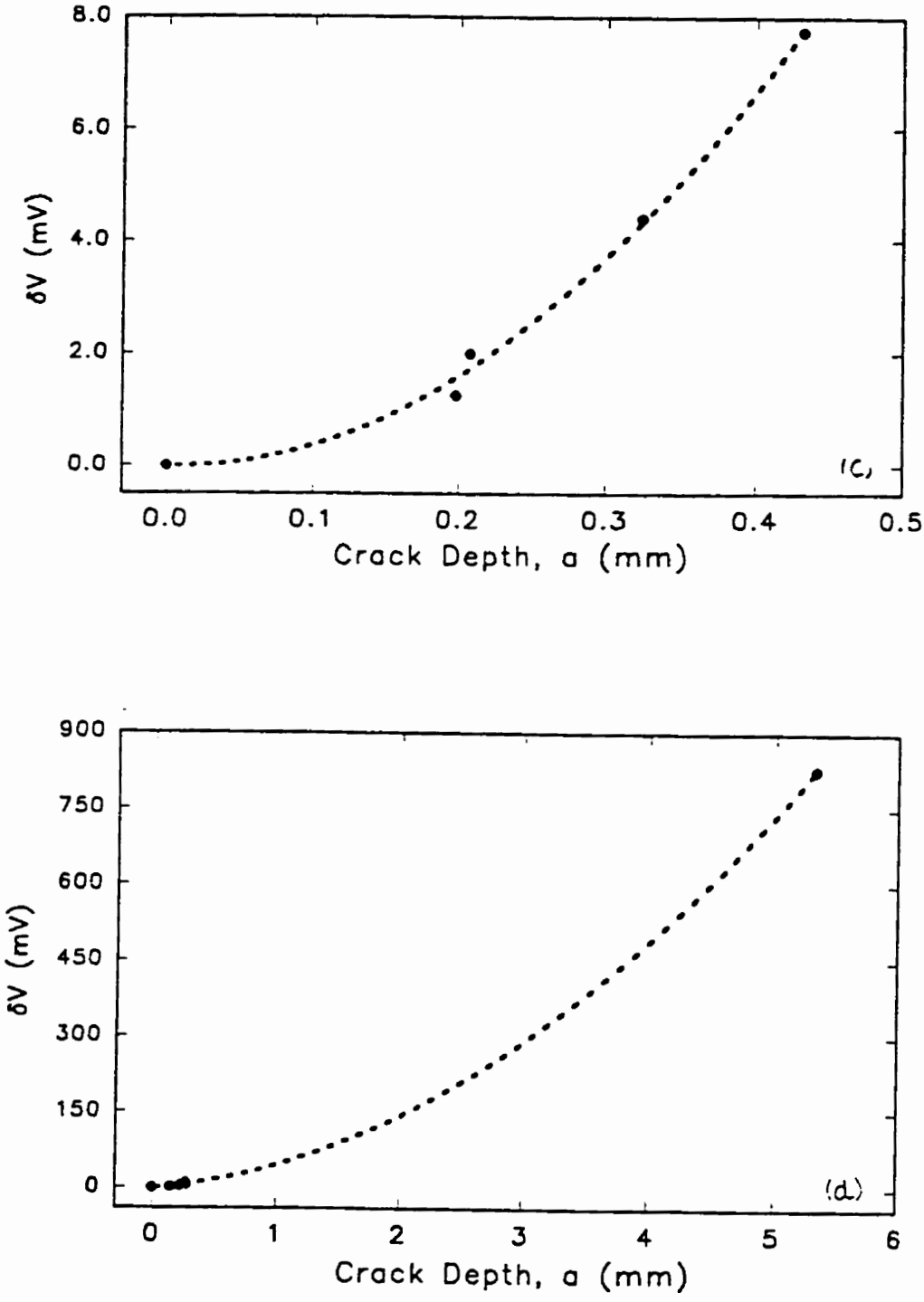

Figure 3.56 (c) 90 kHz, 5 amp. and 3000 gain, (d) 120 kHz, 5 amp. and 3000 gain.

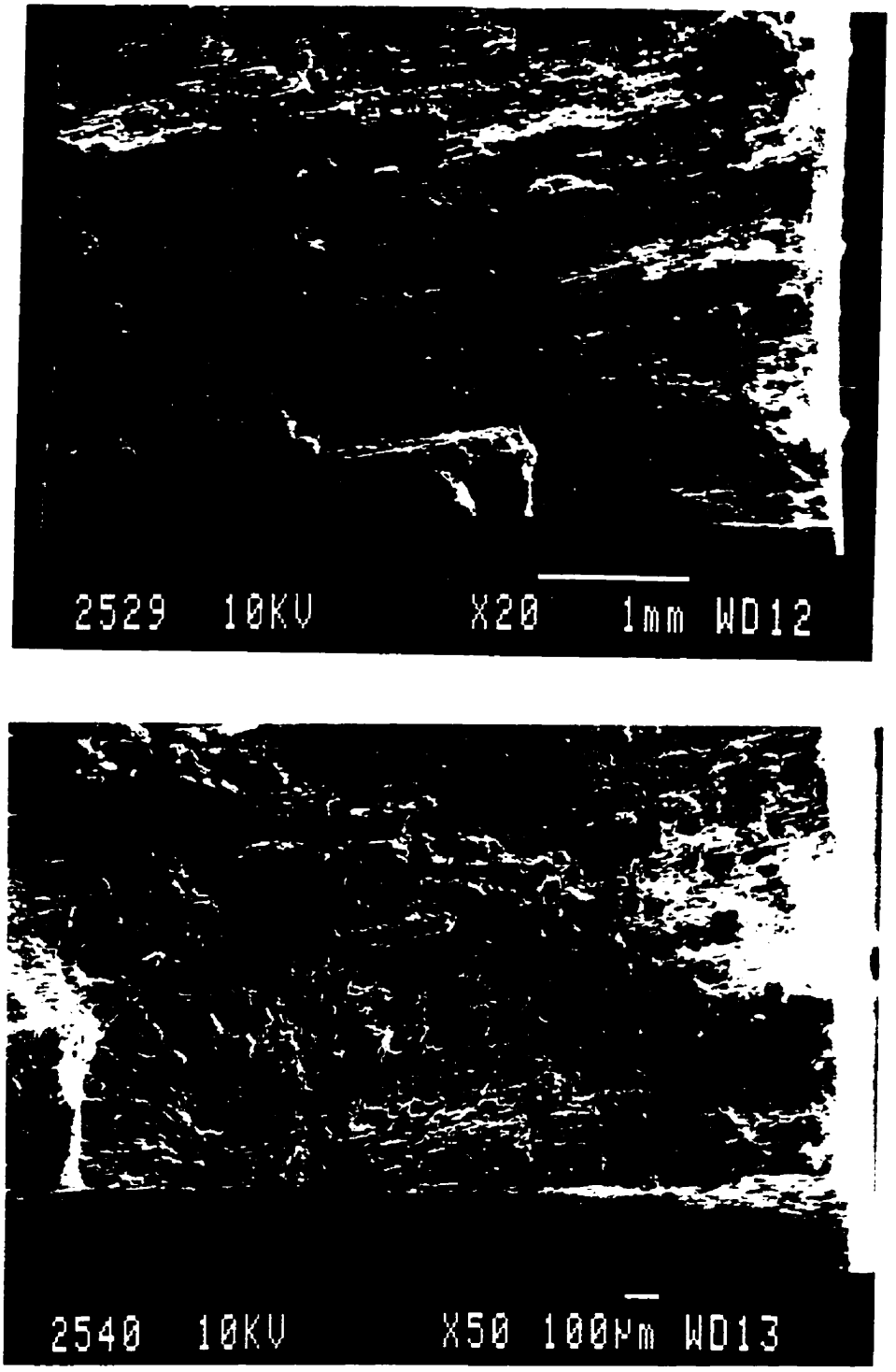

Figure 3.57(a) A global view of the fracture surface showing multiple crack initiations, (b) Zoom on the dominant crack.

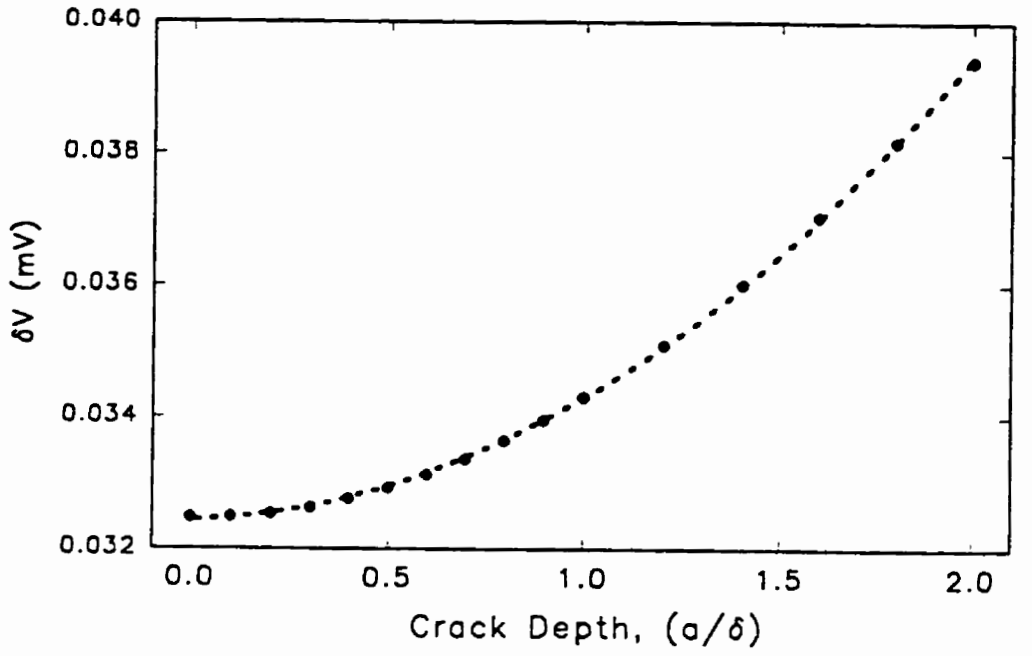

Figure 3.58 A plot of change in potential versus normalised crack depth obtained by a finite element analysis (2D).

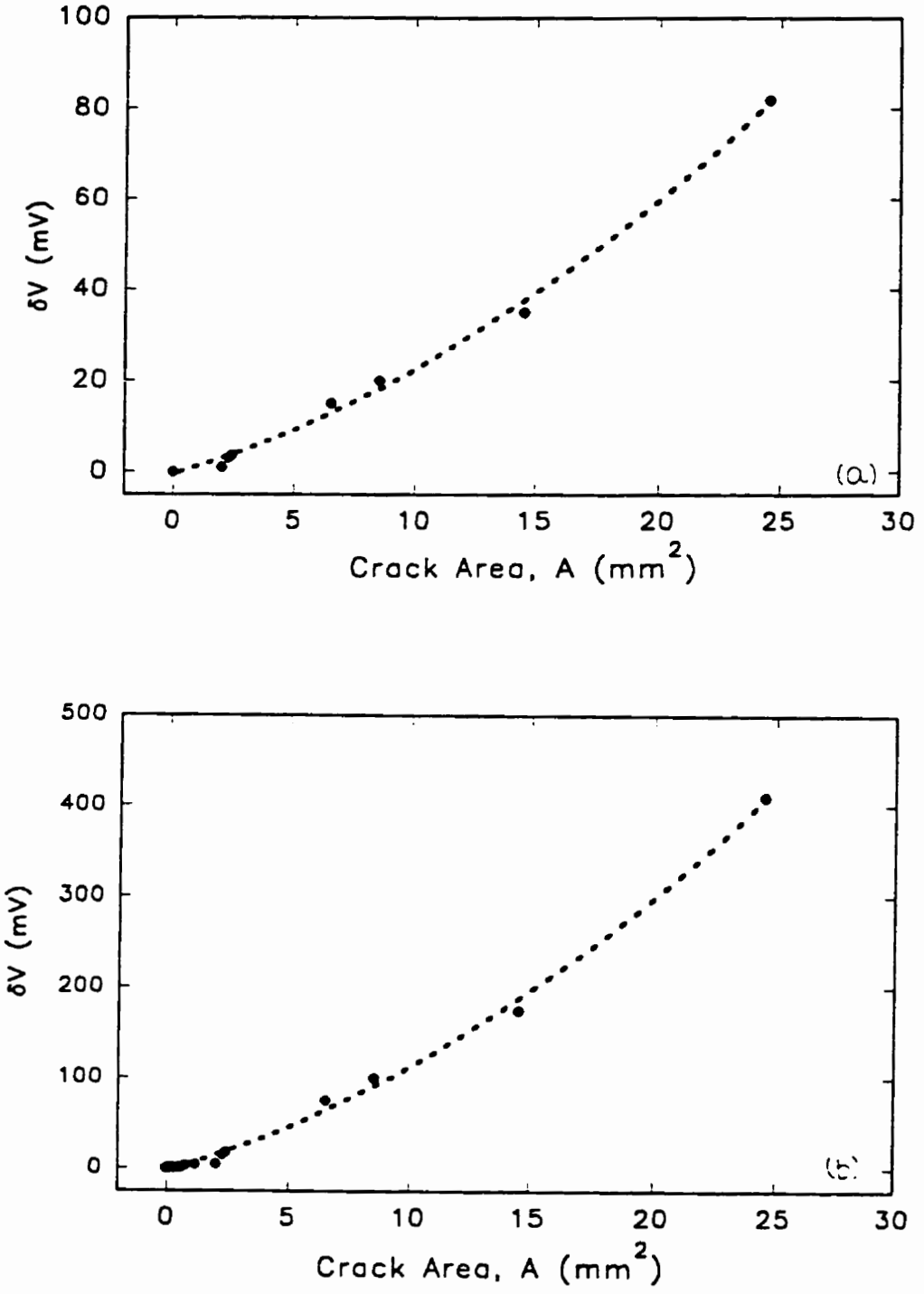

Figure 3.59 Calibration curves relating potential change with crack area (a) 30 kHz, 1 amp. and 3000 gain, (b) 30 kHz, 5 amp. and 3000 gain.

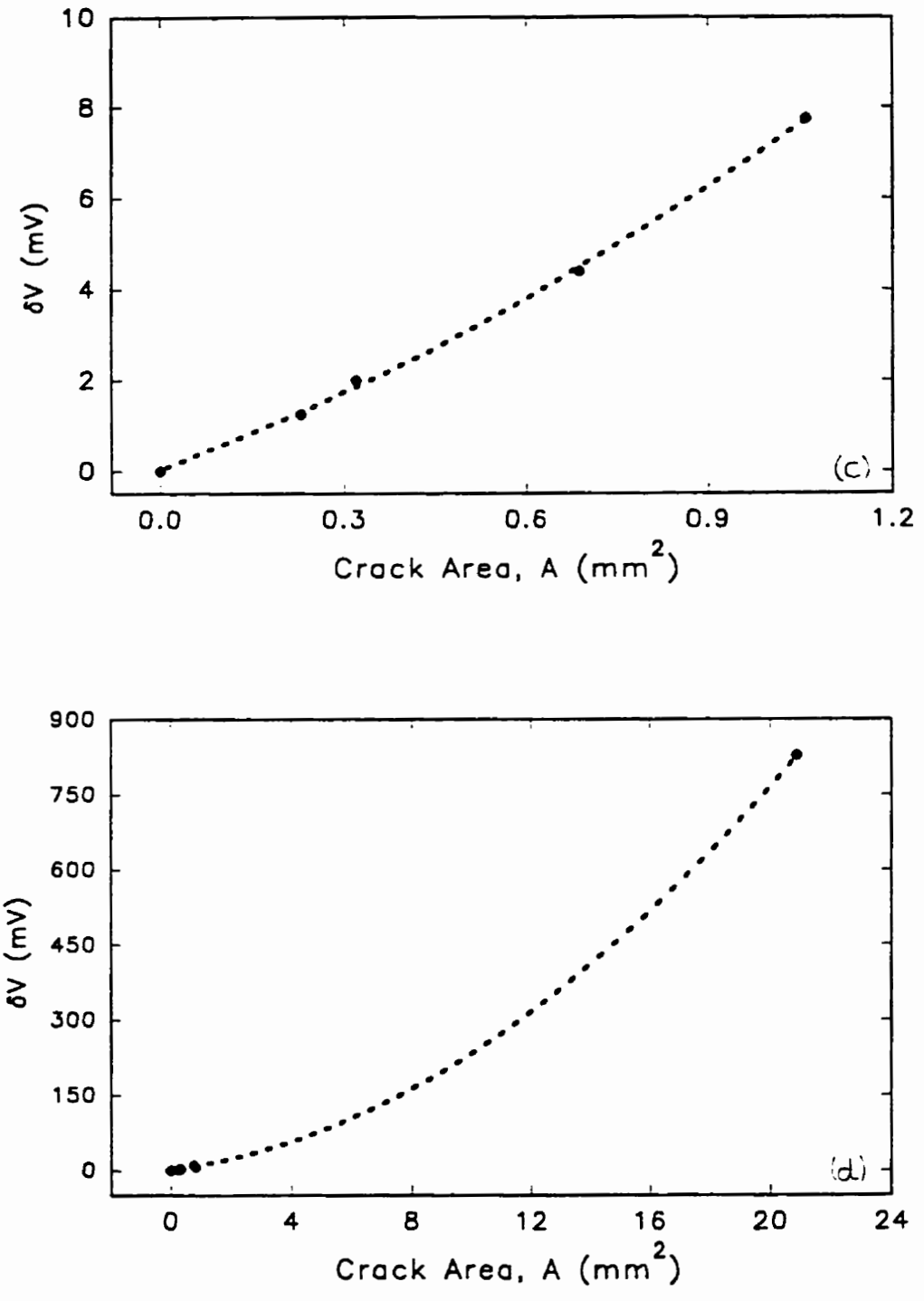

Figure 3.59 (c) 90 kHz, 5 amp. and 3000 gain, (d) 120 kHz, 5 amp. and 3000 gain.

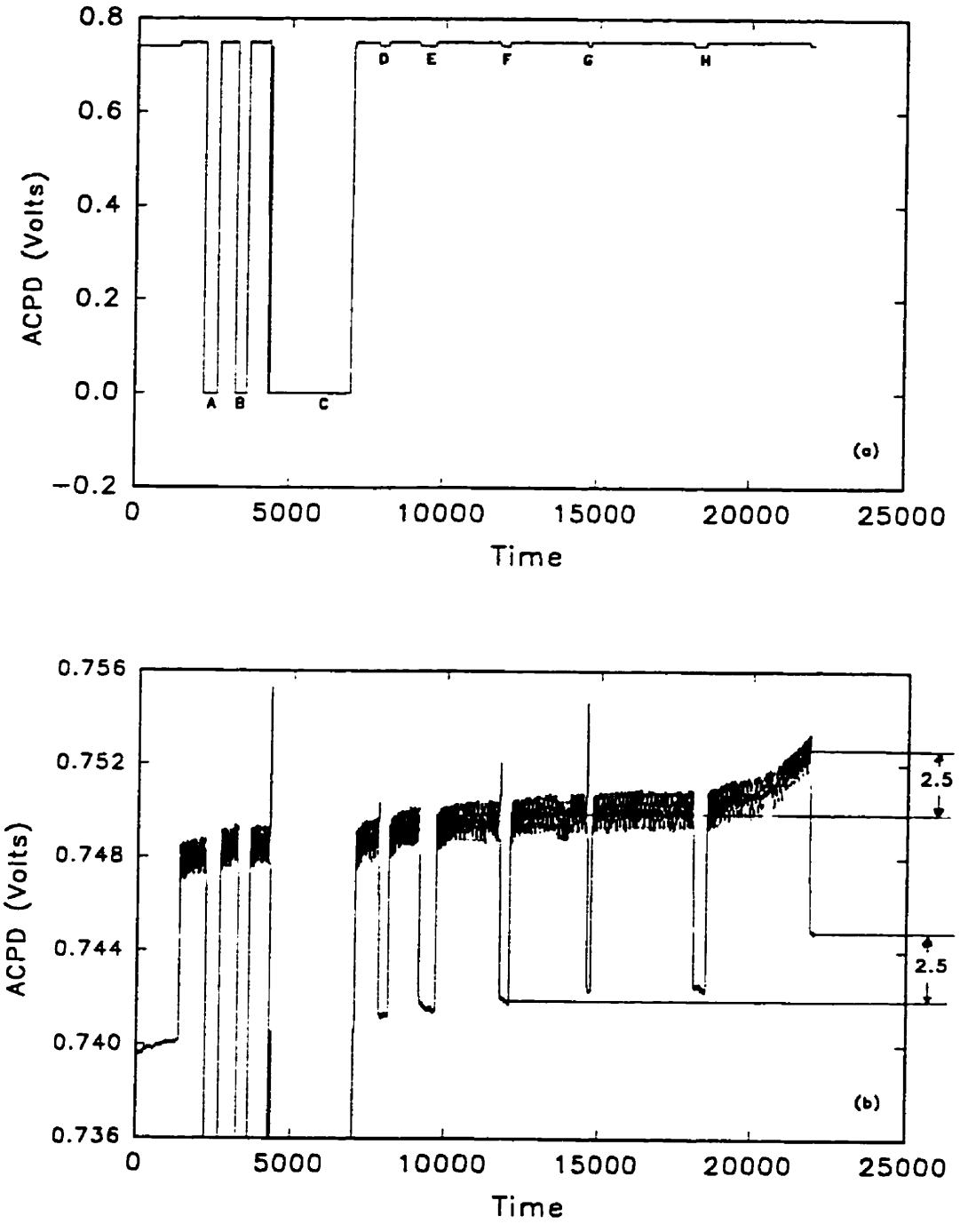

Figure 3.60 Interrupted (Off line) measurements during fatigue cycling (a) Plot of ACPD versus time, (b) Zoom of (a).

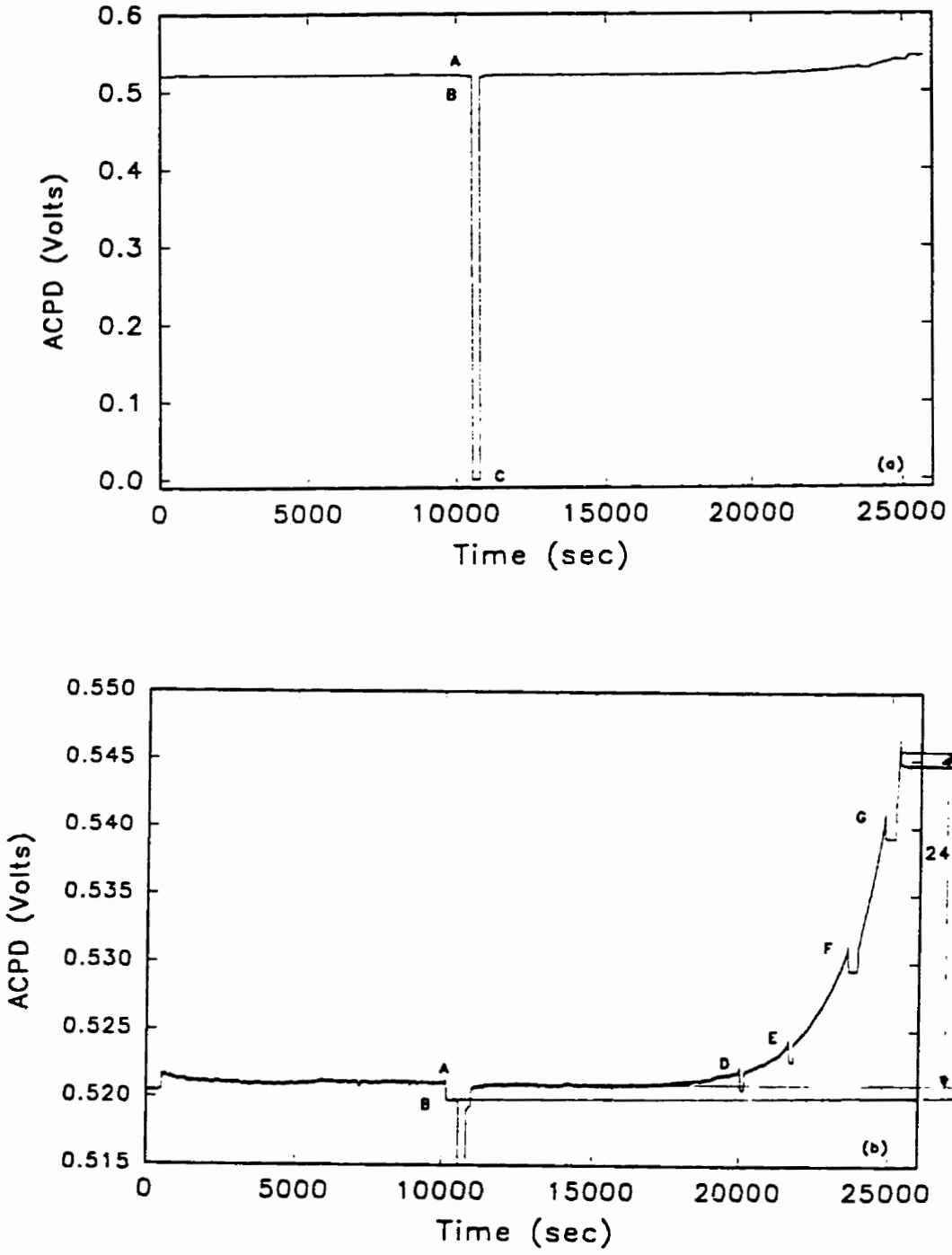

Figure 3.61 Interrupted (Off line) measurements during fatigue cycling (a) Plot of ACPD versus time, (b) Zoom of (a).

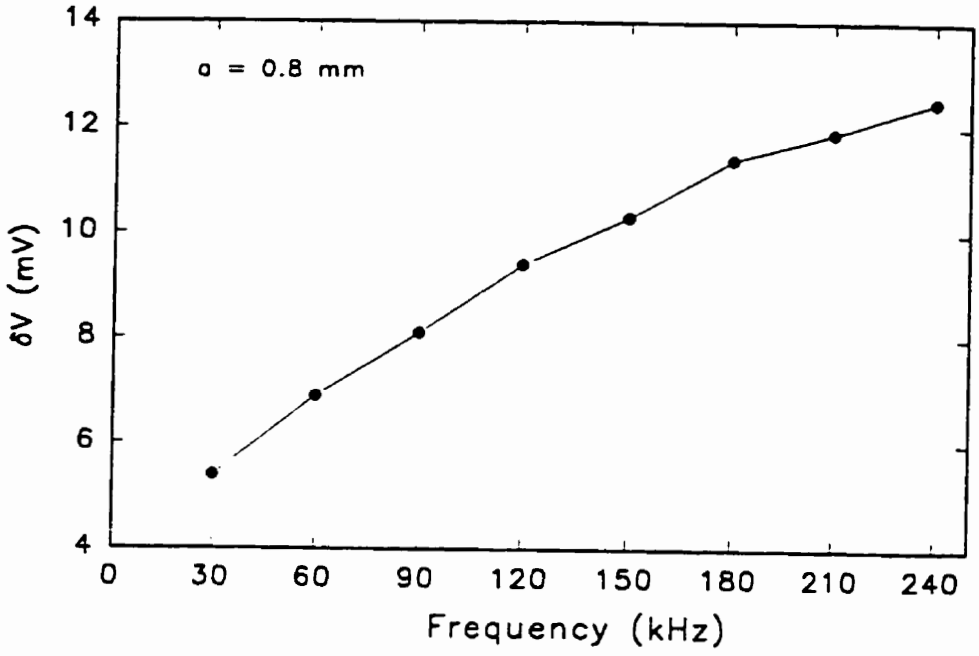

Figure 3.62 A plot of frequency versus change in potential due to crack.

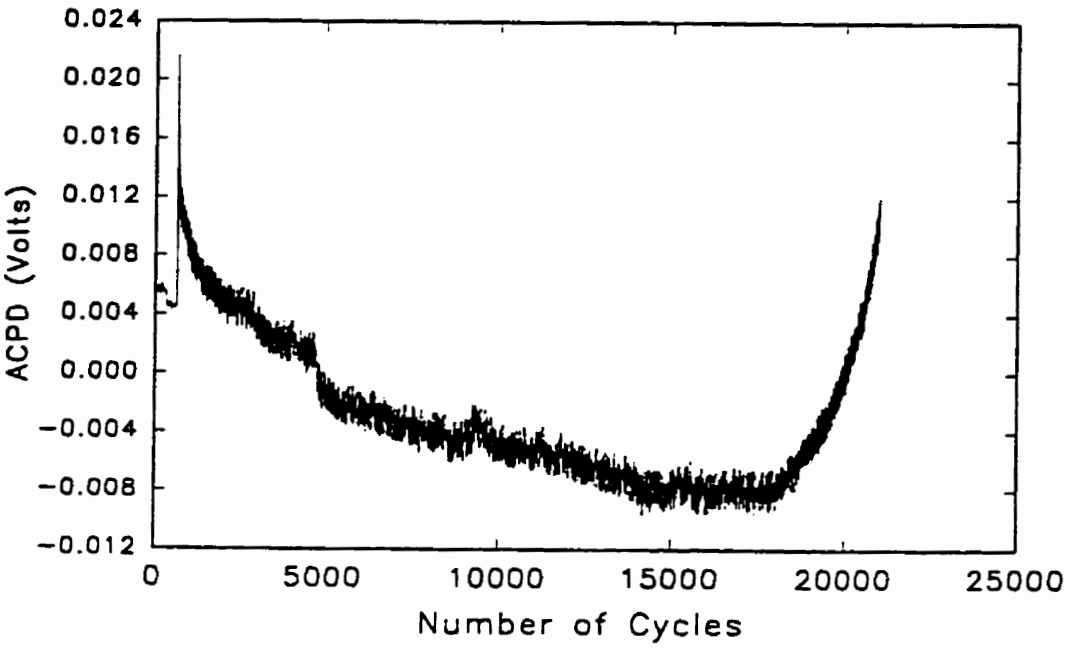

Figure 3.63 A plot of ACPD versus number of cycles demonstrating relaxation of residual stresses due to fatigue.

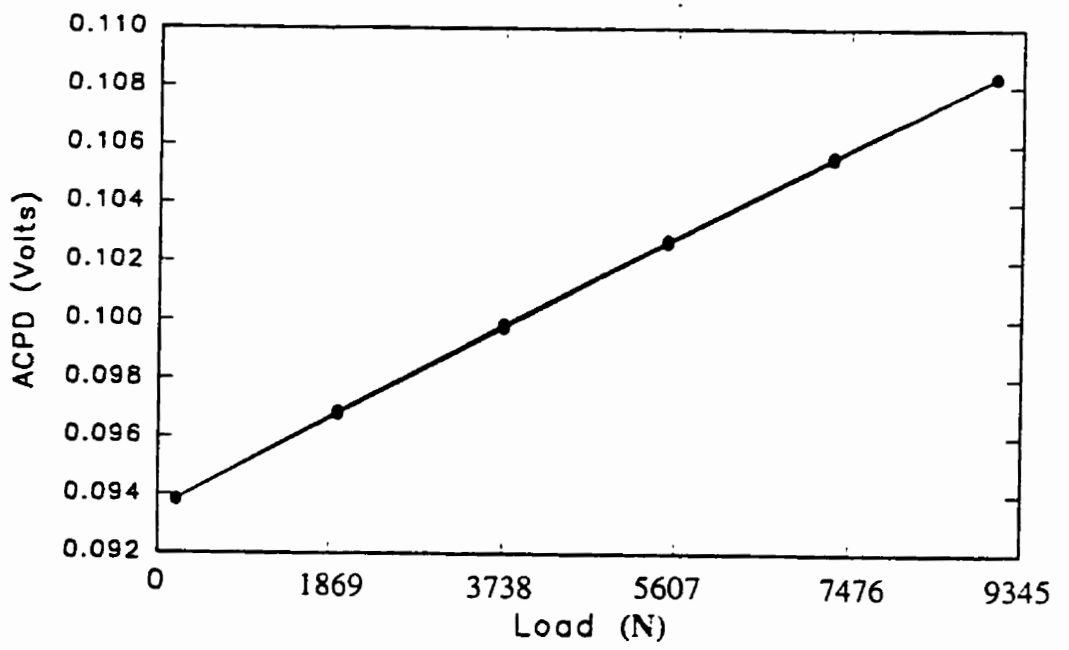

Figure 3.64 Calibration curve : A plot of ACPD versus load.

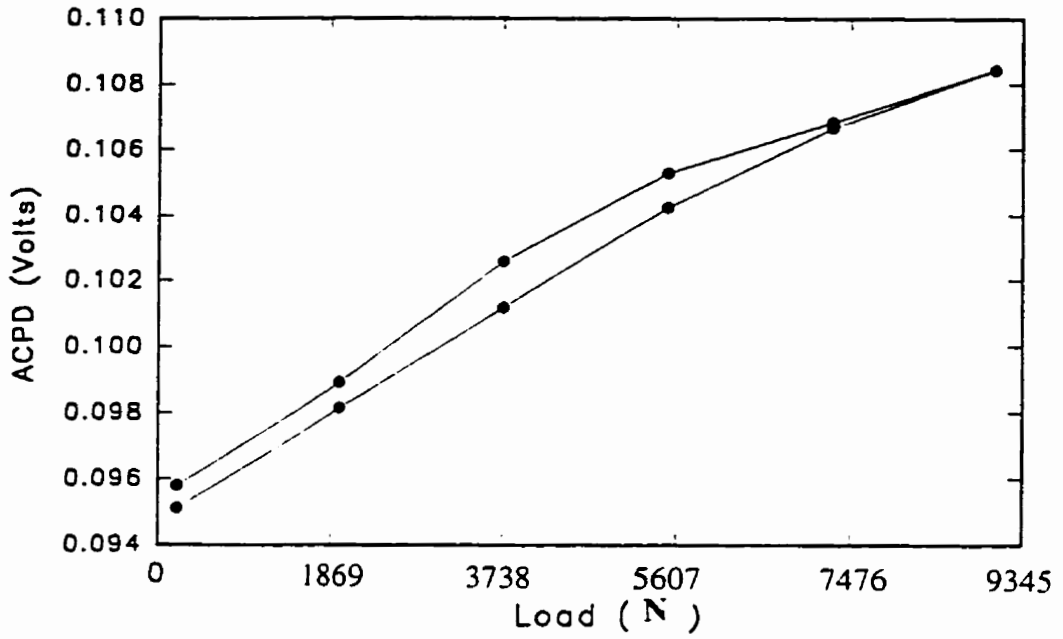

Figure 3.65a A plot of ACPD versus load for a specimen with compressive residual stresses.

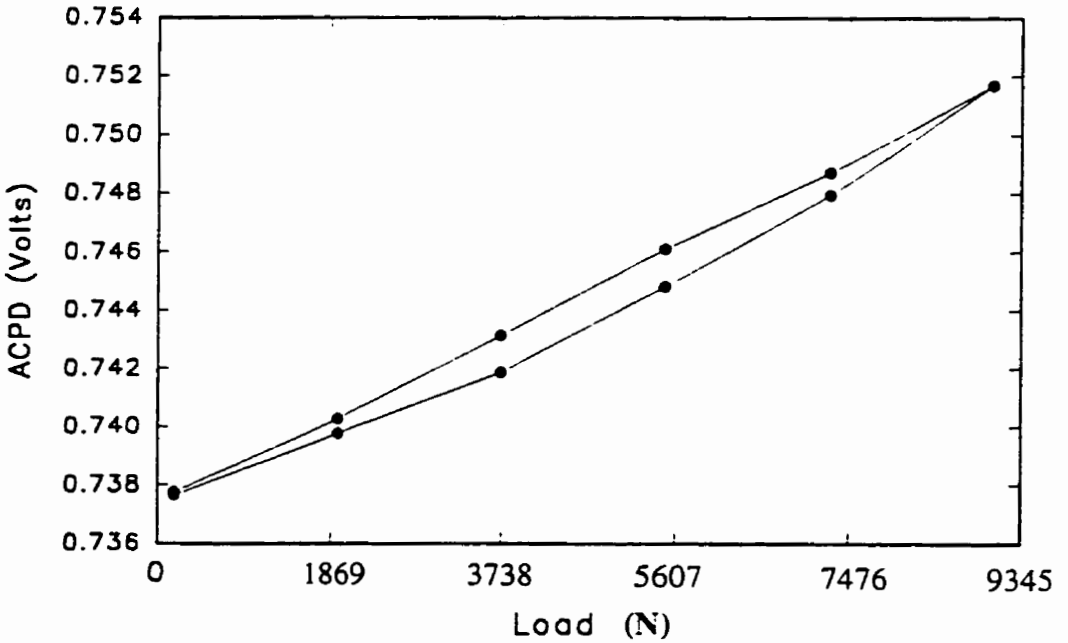

Figure 3.65b A plot of ACPD versus load for a stress relaxed specimen.

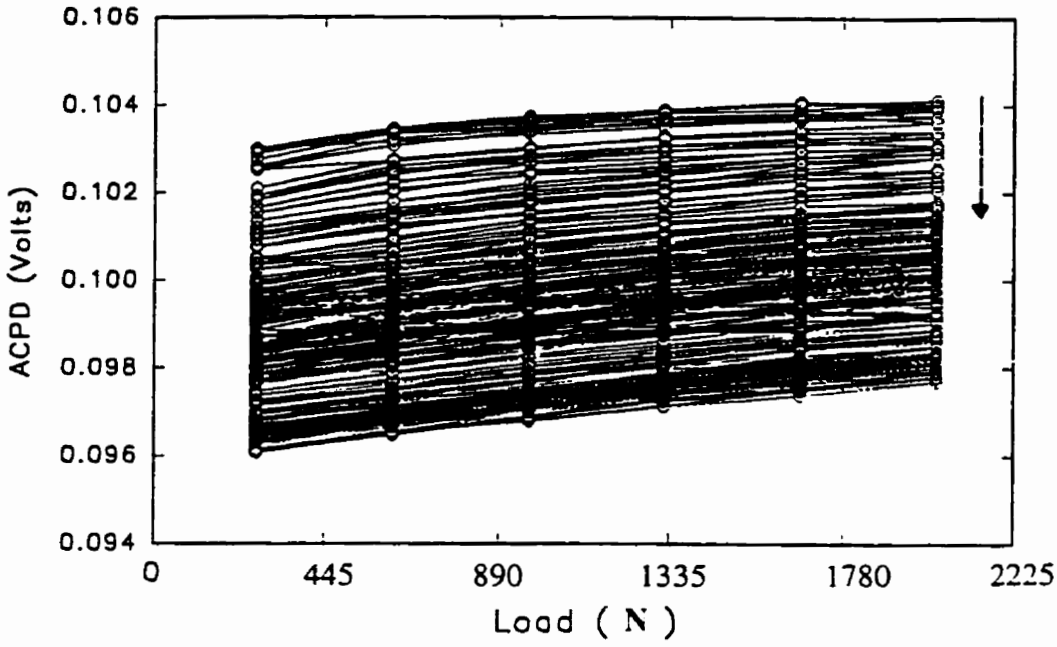

Figure 3.66 A plot of ACPD versus load for 200 cycles showing relaxation of compressive residual stresses due to mechanical loading.

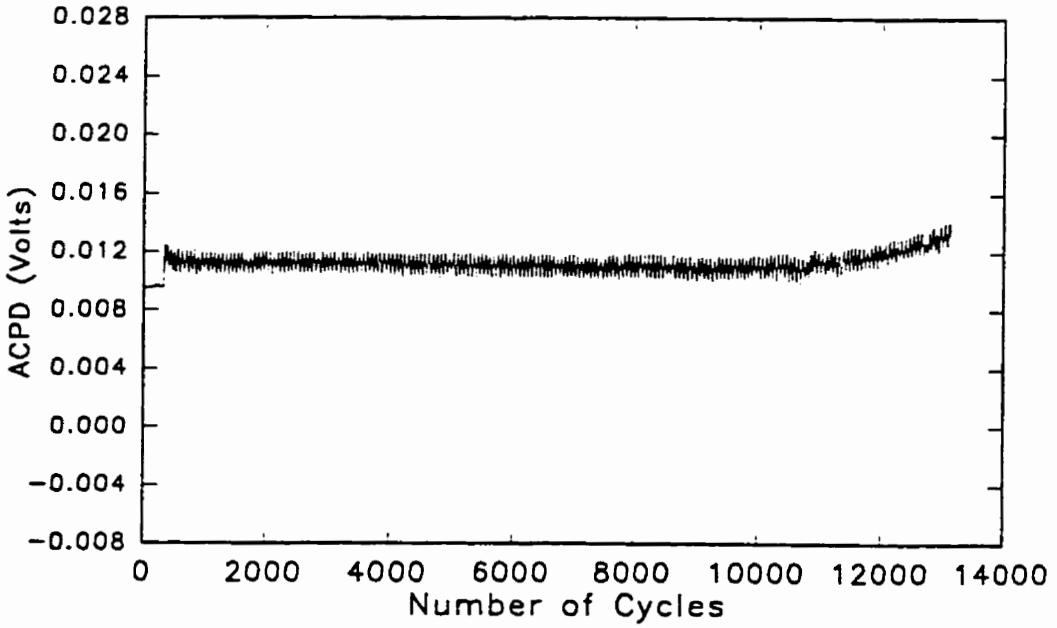

Figure 3.67 A plot of ACPD versus number of fatigue cycles for a stress relaxed specimen.

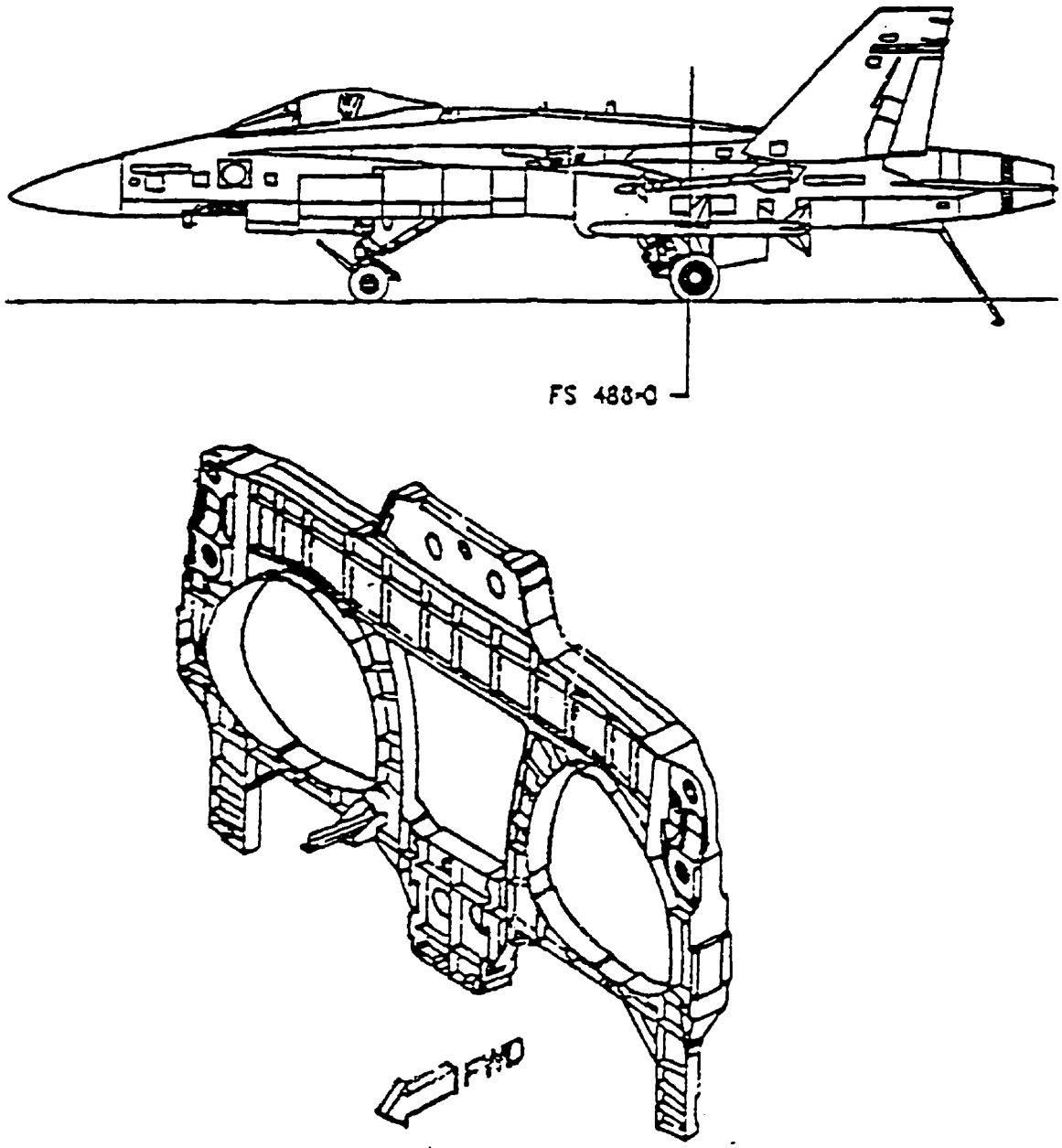

Figure 4.1 Schematic showing the bulkhead 488 and the location of bulkhead 488 in a CF- 18 aircraft.

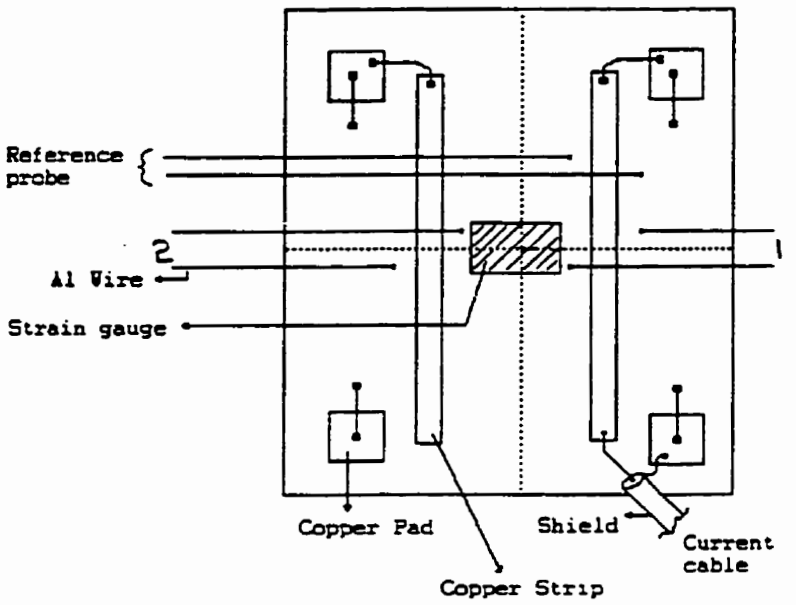

Figure 4.2 Schematic of the probe design installed on the bulkhead 470.5 at the centre line. Strain gauge present at the center was installed by the Canadair.

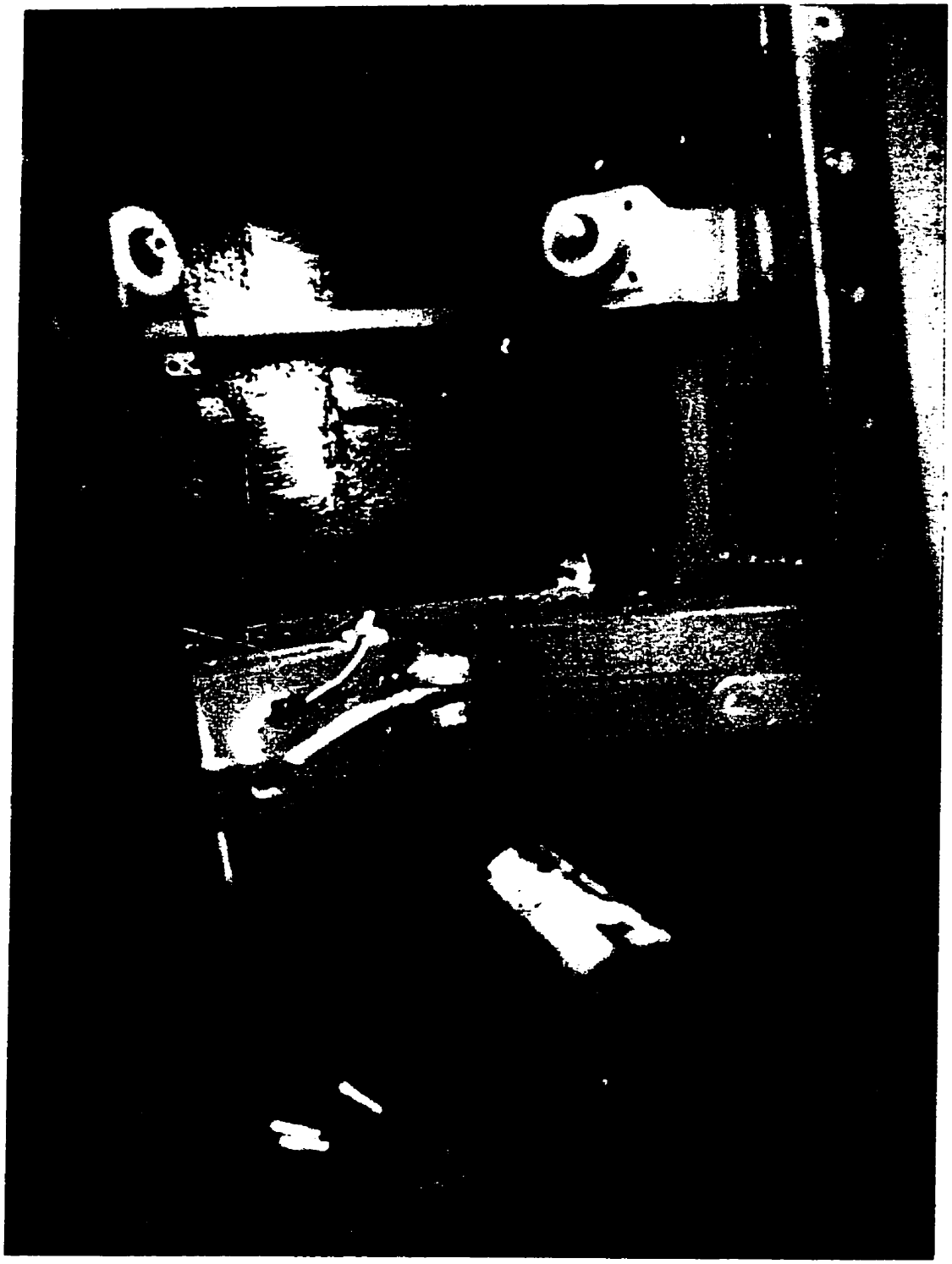

Figure 4.3a Photographs showing the center-line location on bulkhead 470.5 as well as the ACPD sensors.

Figure 4.3b Close view of the center-line location on bulkhead 470.5 along with ACPD probes and the strain gauge (in the center).

Figure 4.3c Zoom of the fig. 4.3b identifying the area covered by the ACPD probes and strain gauge on bulkhead 470.5 center line location.

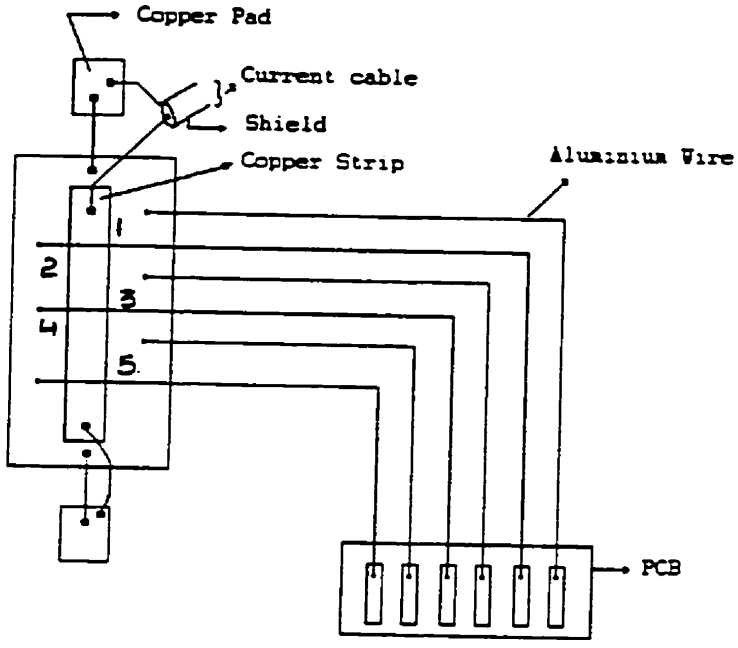

Figure 4.4 Schematic of the probes installed on the bulkhead 488 at the hydraulic hole (L.H.S).

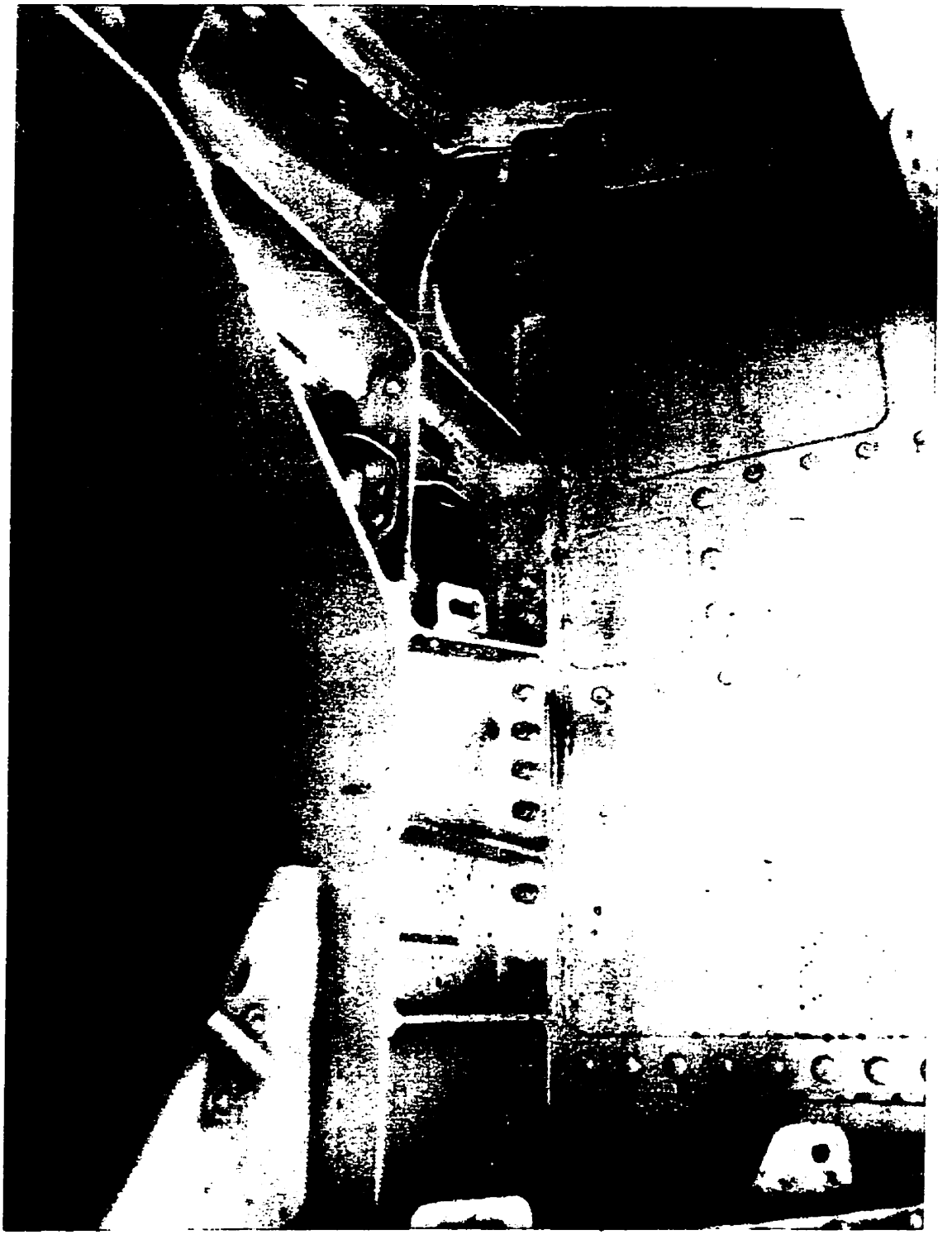

Figure 4.5a Photograph showing the location of the hydraulic hole on the bulkhead 488.

Figure 4.5b Close View of the Hydraulic hole and the ACPD probes.

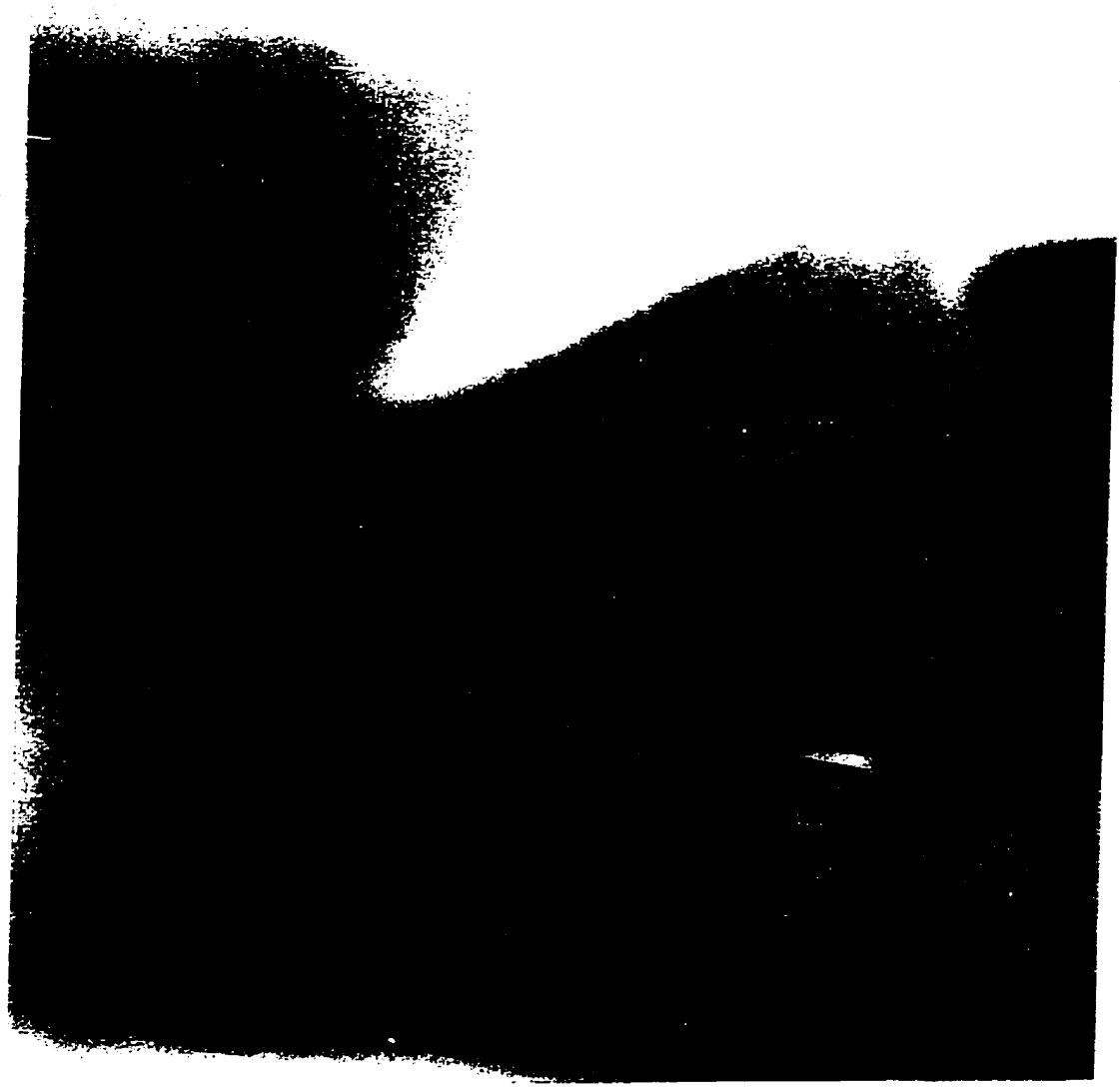

Figure 4.5c Zoom of the fig.4.5b showing the PCB installed on the bulkhead 488.

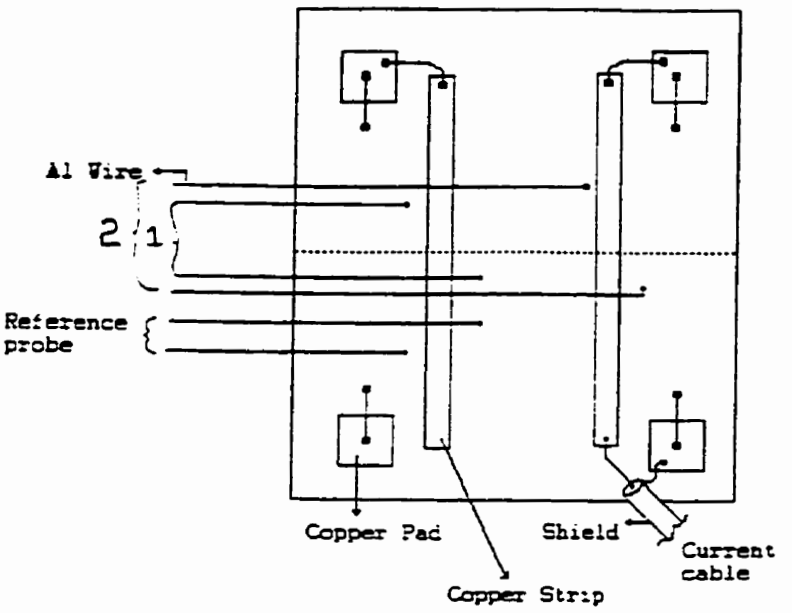

Figure 4.6 Schematic of the probes installed on the bulkhead 497 at the former segment flange radius.

Figure 4.7a Photograph showing the location of the former segment flange radius on bulkhead 497 (L.H.S) and the ACPD probes installed on the location.

Figure 4.7b Closer view of the location on the bulkhead 497 which were monitored by ACPD sensors.

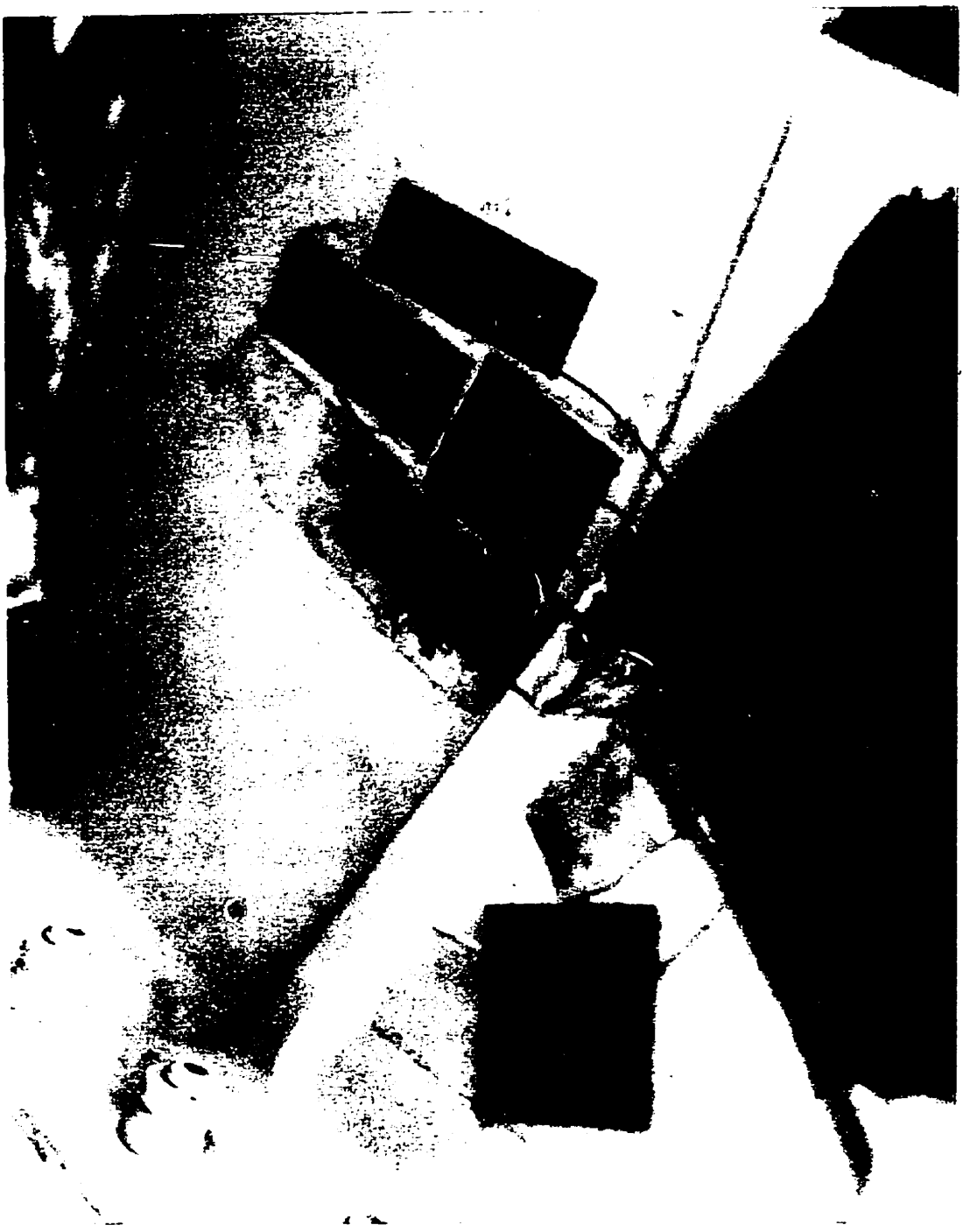

Figure 4.7c Photograph showing PCB installed on the former segment flange radius of bulkhead 497.

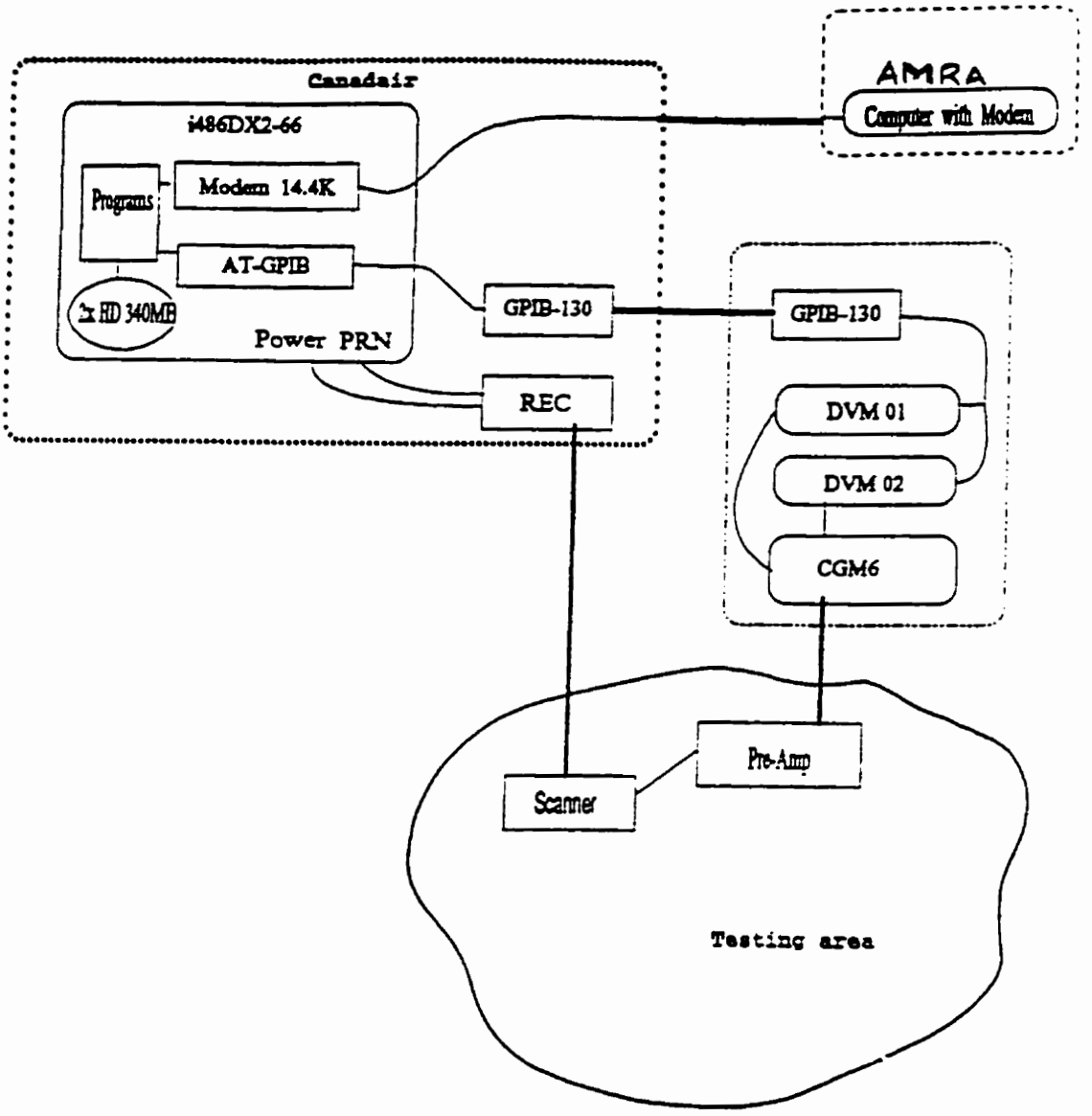

Figure 4.8 A schematic showing the complete monitoring set up at Canadair.

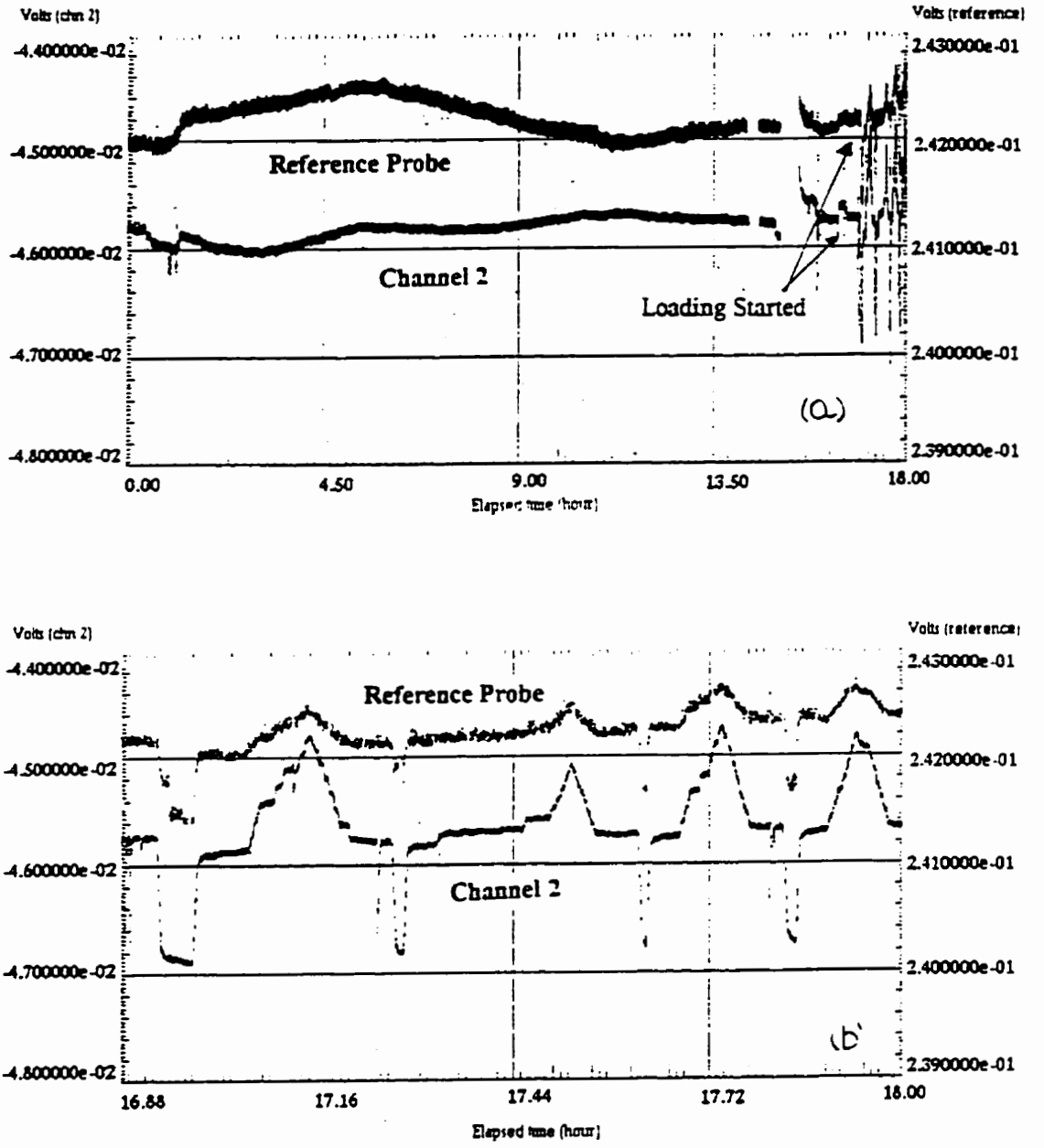

Figure 4.9 Snap shot of strain survey, bulkhead 470.5. (a) A snap shot of the reference probe and active probe (channel 2), (b) Zoom of (a) showing four loading sequence for reference probe and active probe,

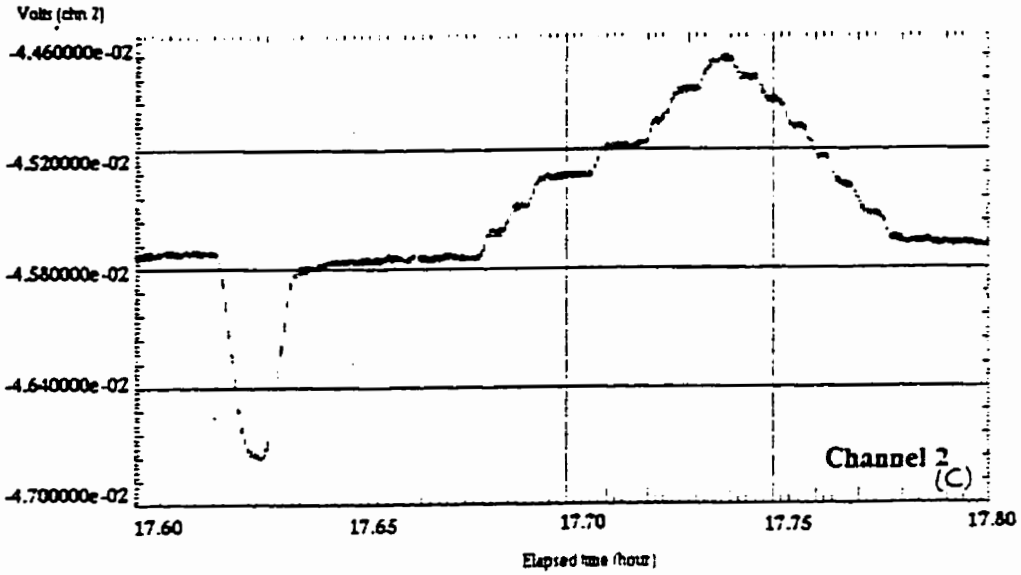

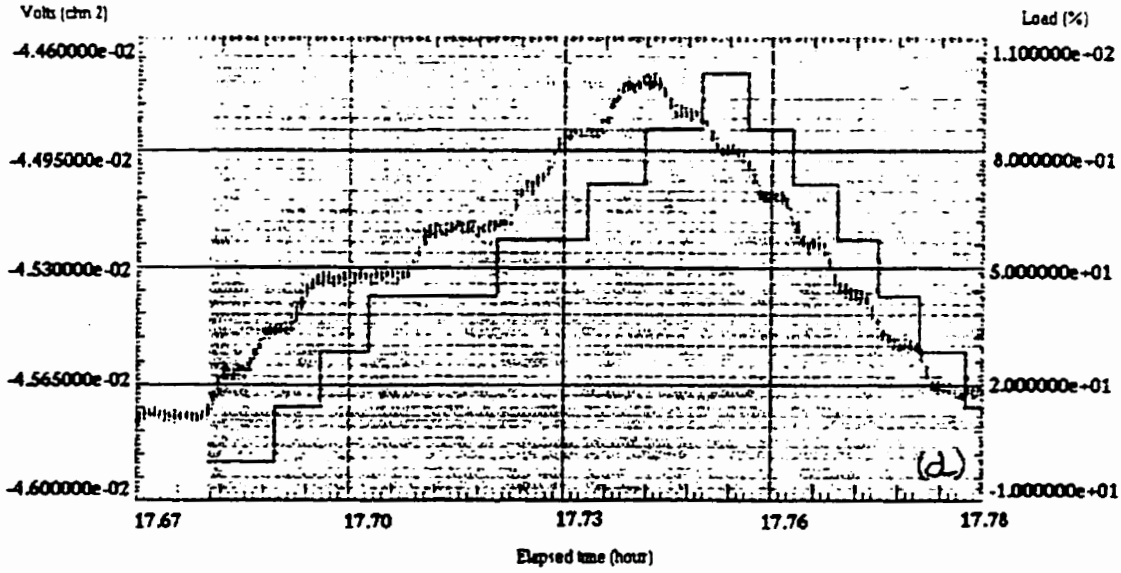

Figure 4.9 (c) Further zoom of active probe showing one loading sequence, (d) Further zoom of fig. 4.9c showing the fifteen loading steps.

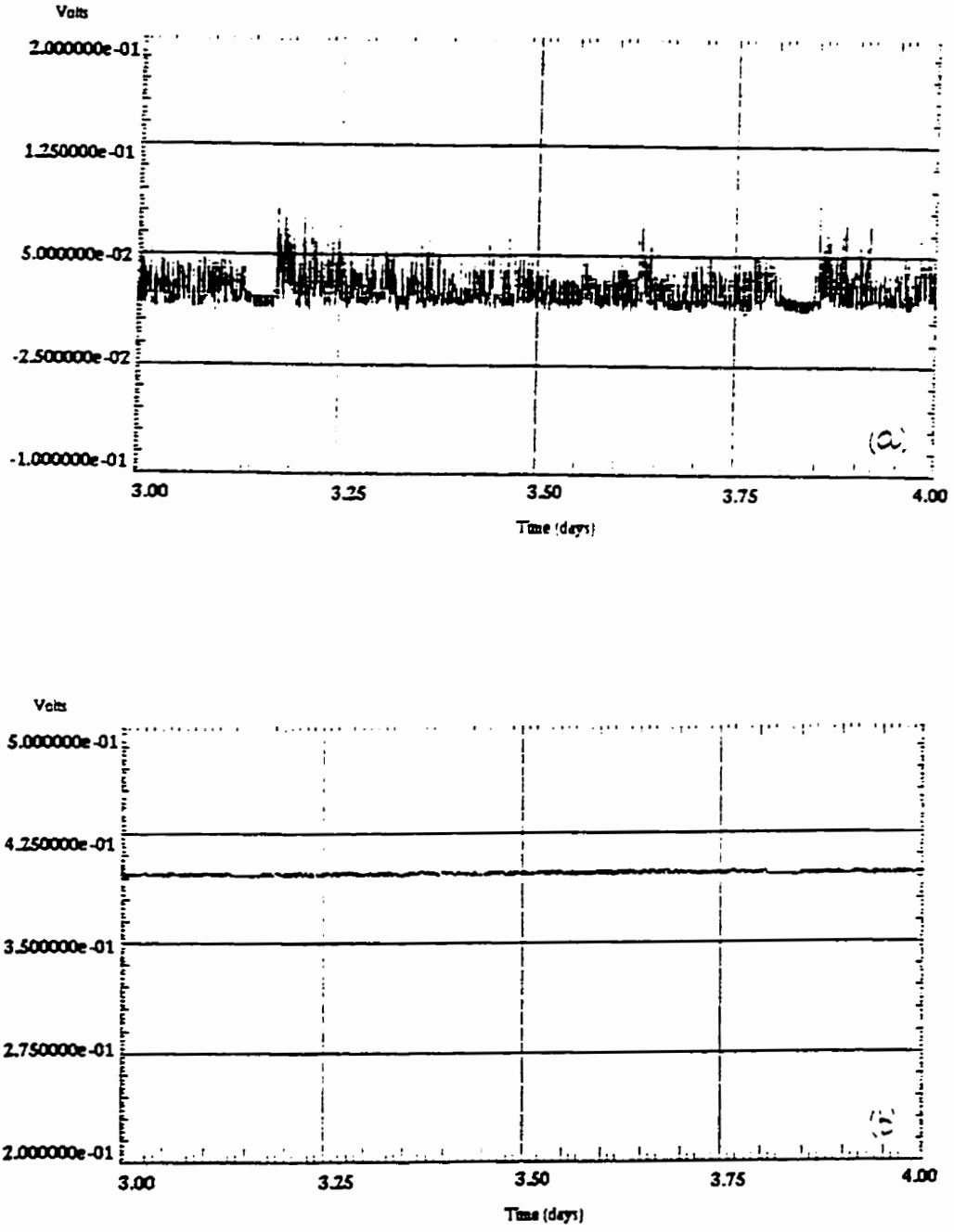

Figure 4.10 Snap shots of flight spectrum loading of block 9. (a) Bulkhead 488, channel 2, (b) Bulkhead 497 channel 6.

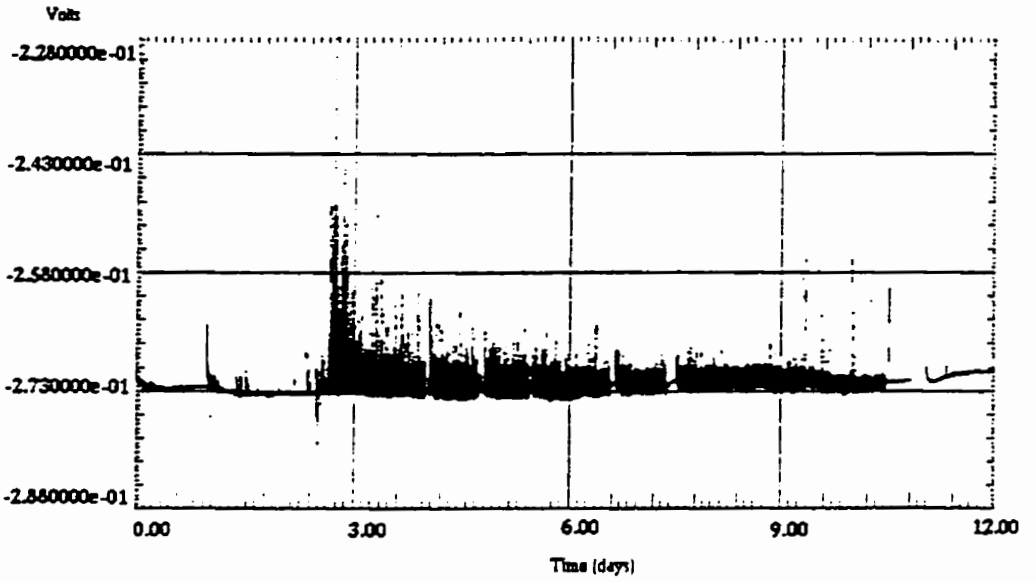

Figure 4.11a A snap shot of ACPD versus time for blocks 11 and 12 (3250-3900 SFH). bulkhead 470.5 channel 1.

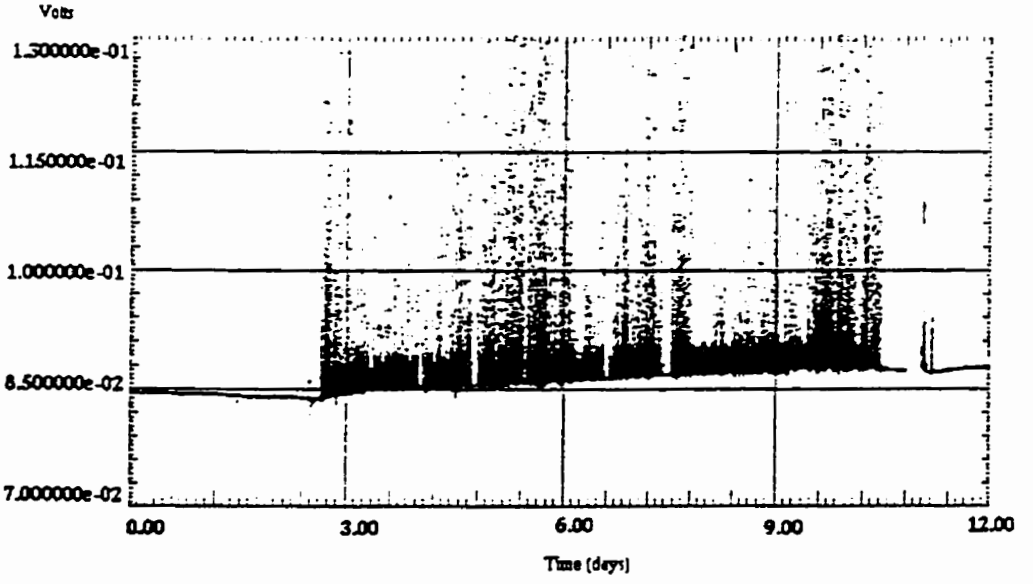

Figure 4.11b A snap shot of ACPD versus time for blocks 11 and 12 (3250-3900 SFH). bulkhead 470.5 channel 2.

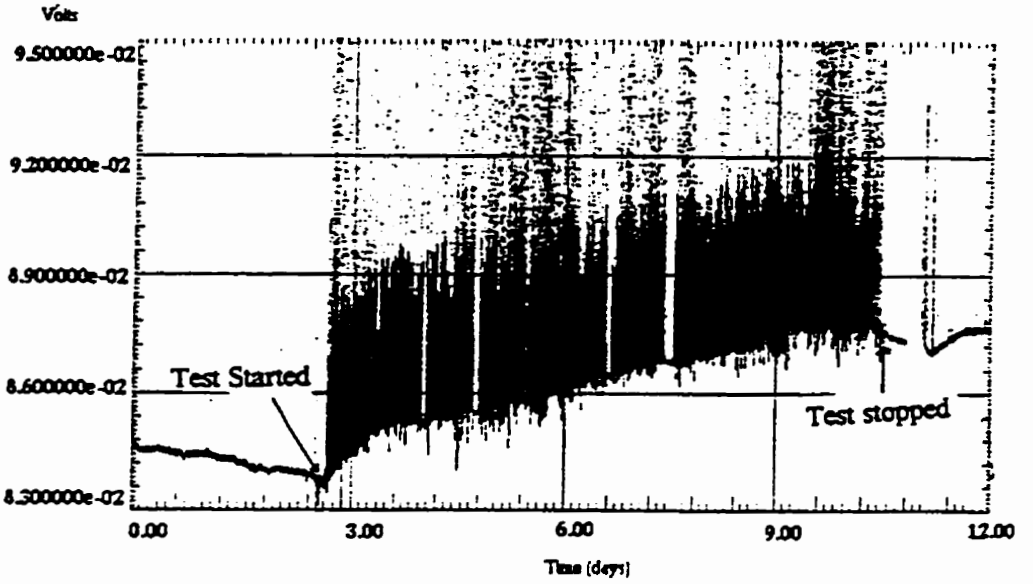

Figure 4.12a Zoom of figure 4.11b.

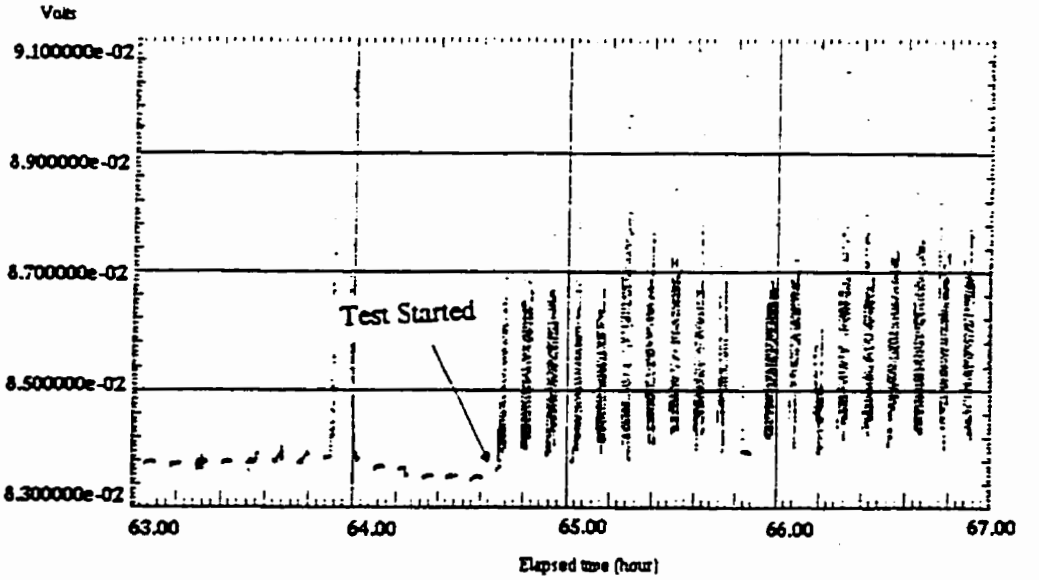

Figure 4.12b Further zoom (63-67 hours) of fig. 4.12a showing the start of block 11.

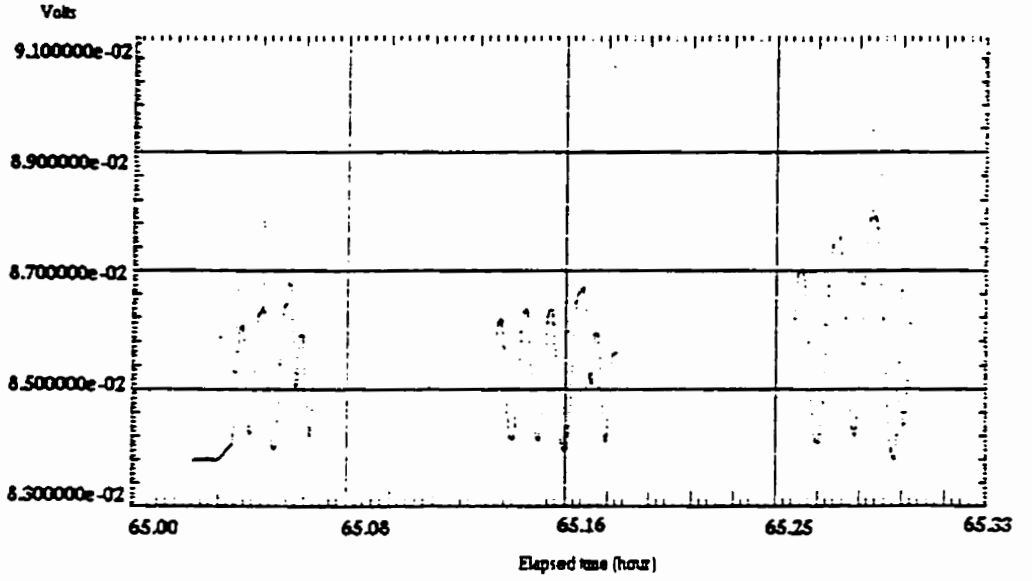

Figure 4.12c Further zoom (65-65.33 hours) showing three flight loading cycle.

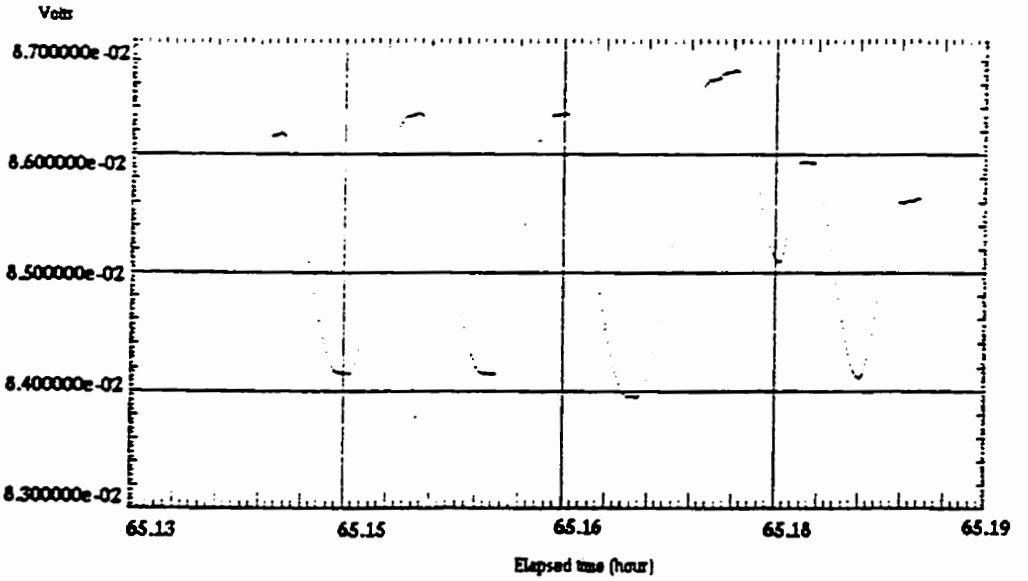

Figure 4.12d Further zoom (65.13- 65.19 hours) showing one loading sequence.

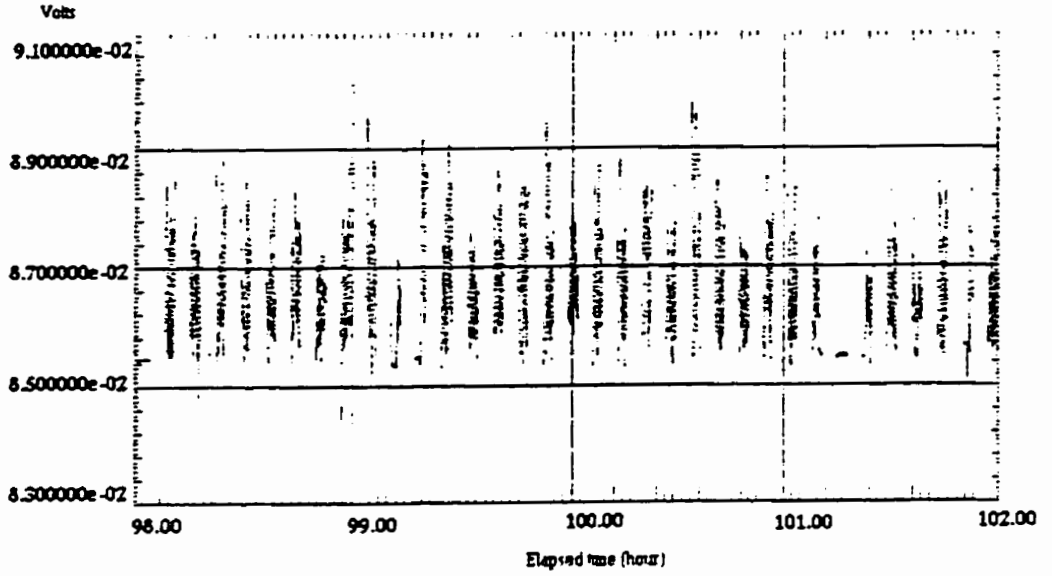

Figure 4.12e A snapshot (98-102 hours) of block 11, channel 2, bulkhead 470.5.

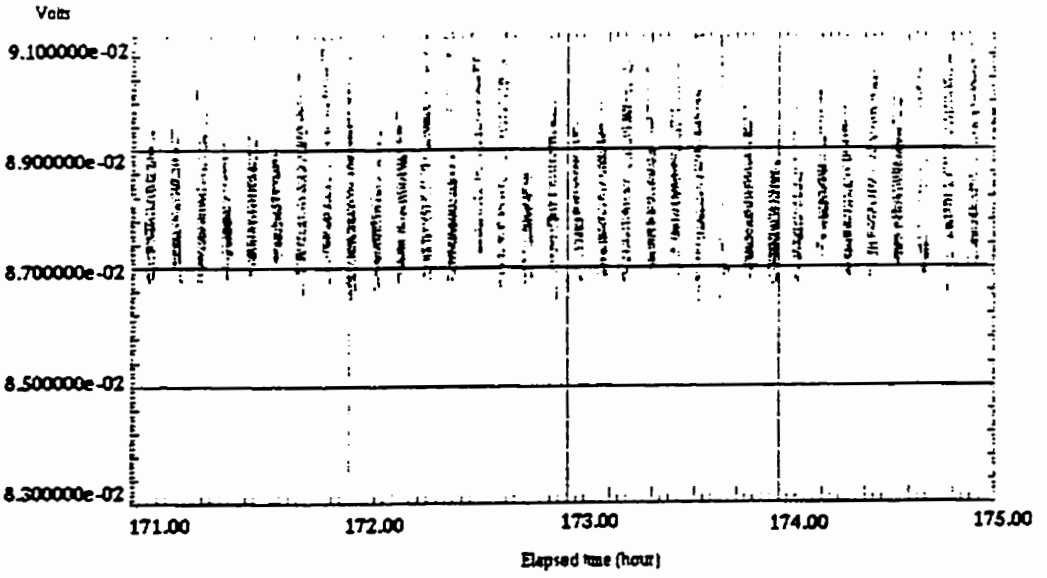

Figure 4.12f A snapshot (171-175 hours) of block 12, channel 2, bulkhead 470.5.

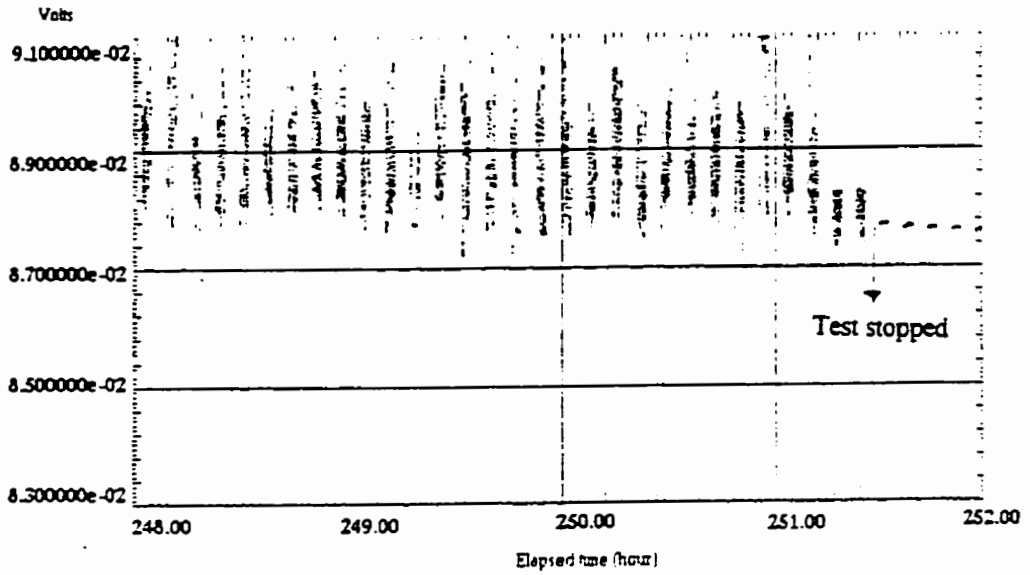

Figure 4.12g A snapshot (248-252 hours) of block 12, channel 2, bulkhead 470.5, showing the end of flight loading.

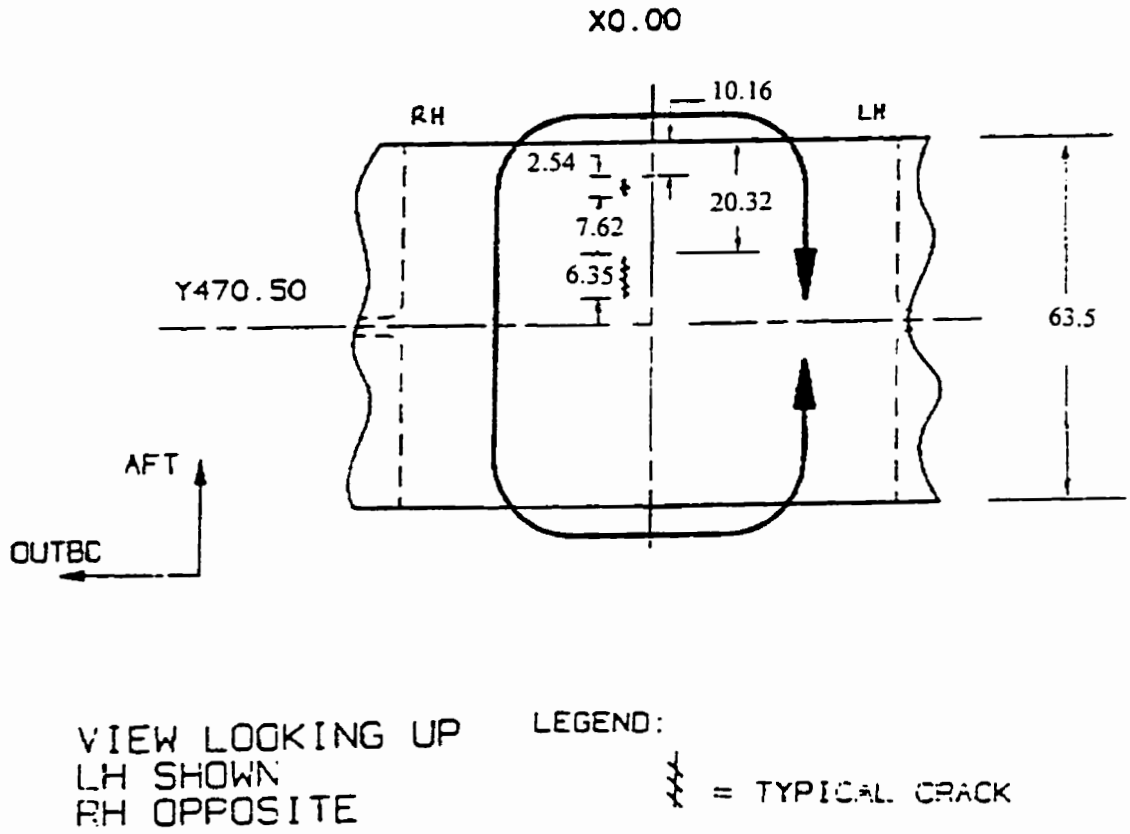

Figure 4.13 A schematic of the bulkhead 470.5 at the centre line detailing the presence of cracks at the aft side.

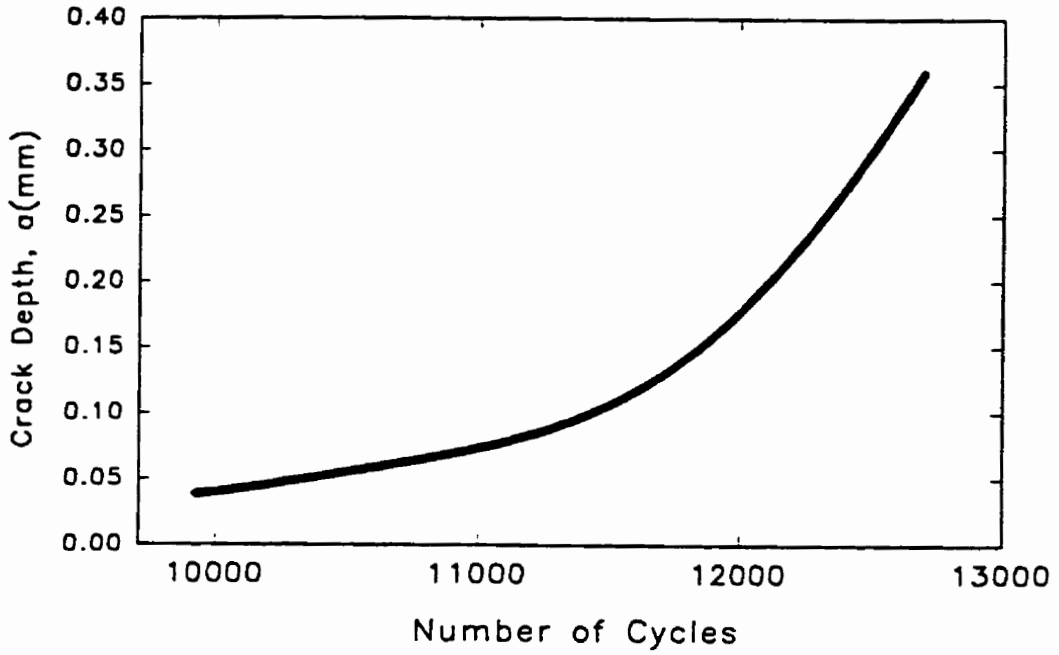

Figure 5.1 A plot of crack depth versus number of cycles.

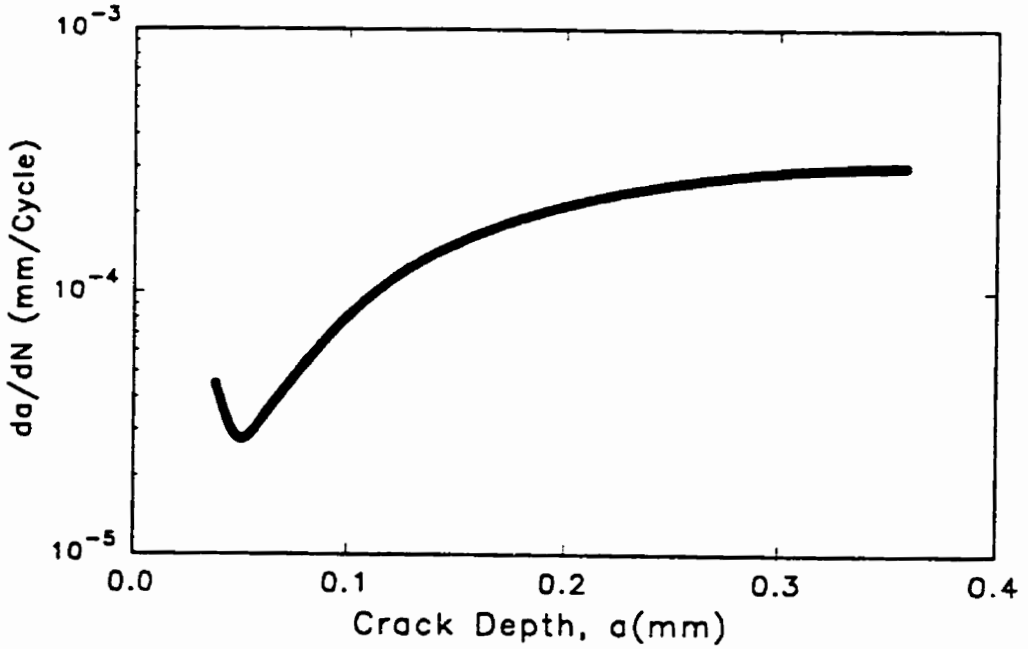

Figure5.2a da/dN versus crack depth curve. The crack growth appears artificially higher due to an artifact created, because of the inclusion of no crack /crack transition data.

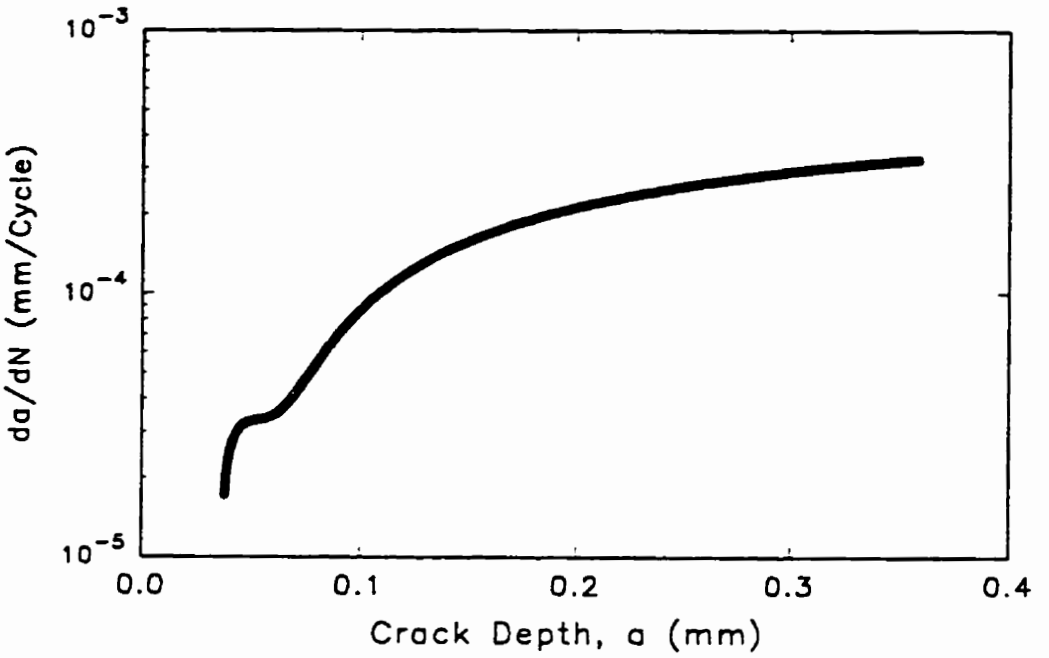

Figure 5.2a da/dN versus crack depth curve when the first ten data points are ignored.

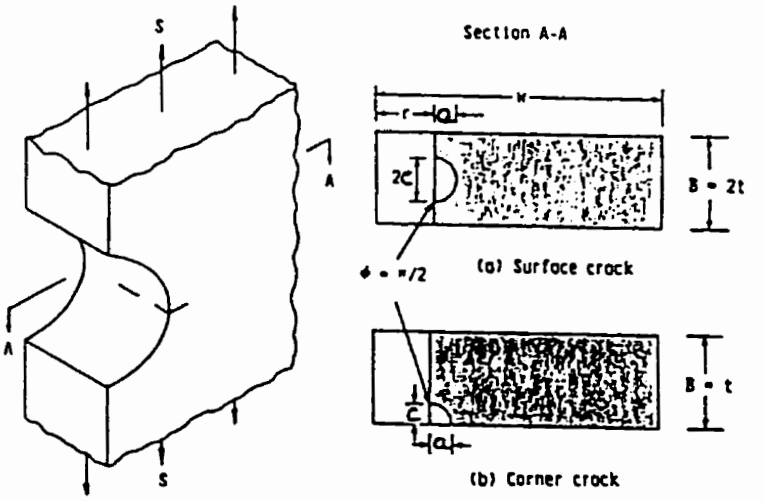

Figure 5.3 Parameters, used for SIF calculation (Swain and Newman's model) of semi-elliptical cracks for SEN specimen geometry.

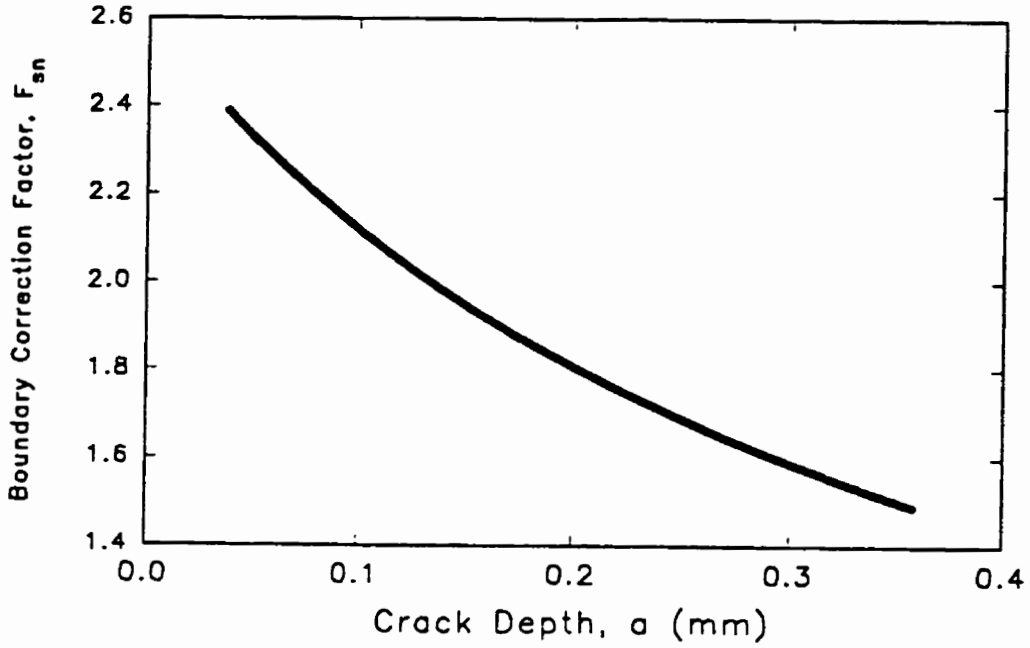

Figure 5.4 Typical variation of boundary correction factor, F_{sn} with the crack depth.

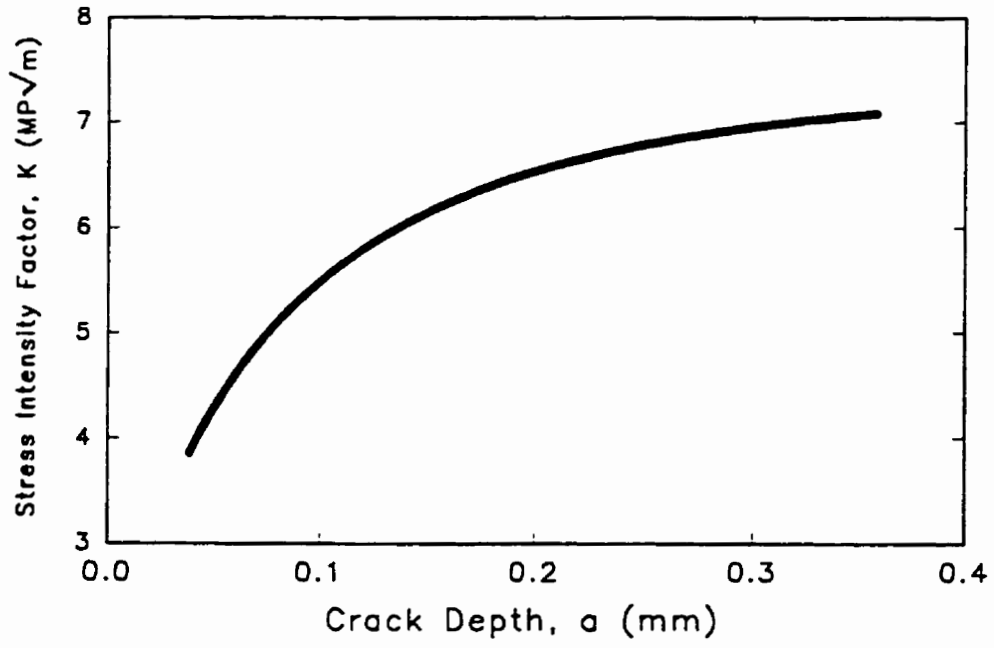

Figure 5.5 Typical variation of SIF, K with the crack depth.

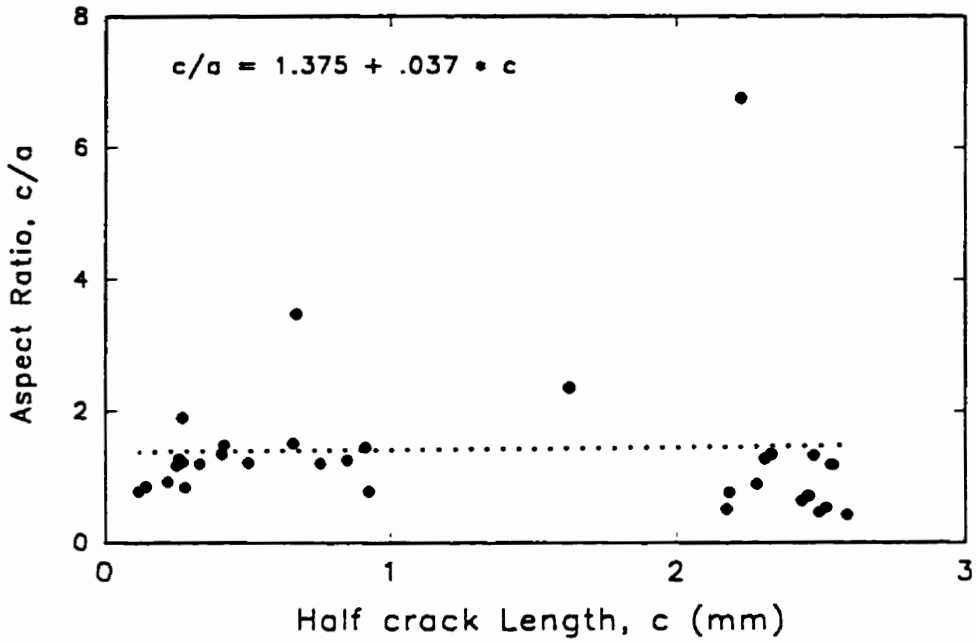

Figure 5.6 Plot of crack aspect ratio with the half surface crack length. Note that three data points showing higher c/a ratio were due to crack coalescence.

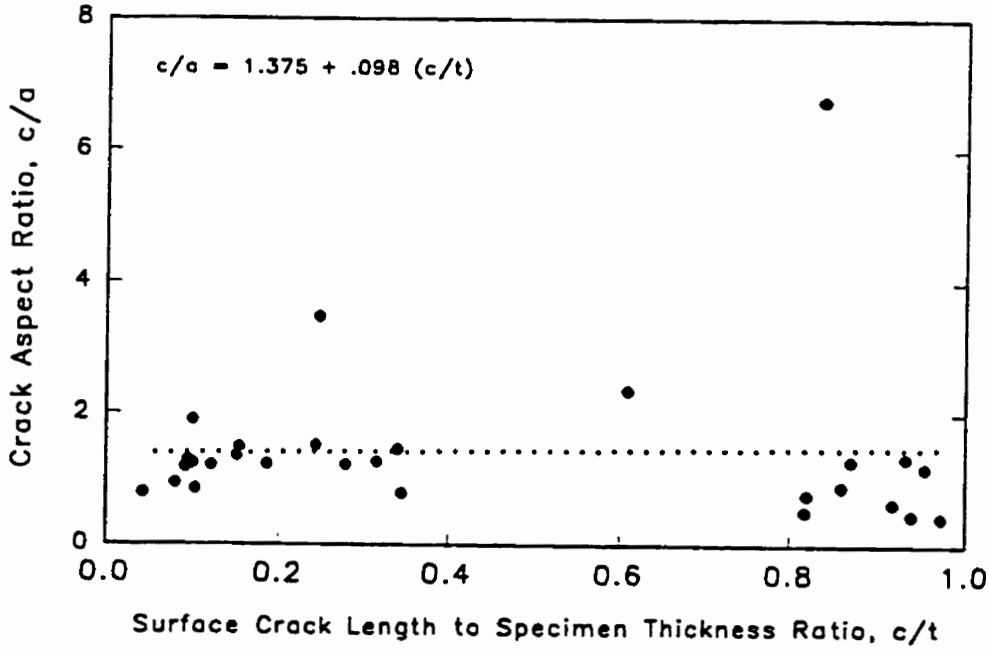

Figure 5.7 Variation of crack aspect ratio with half surface crack length normalised with the half specimen thickness.

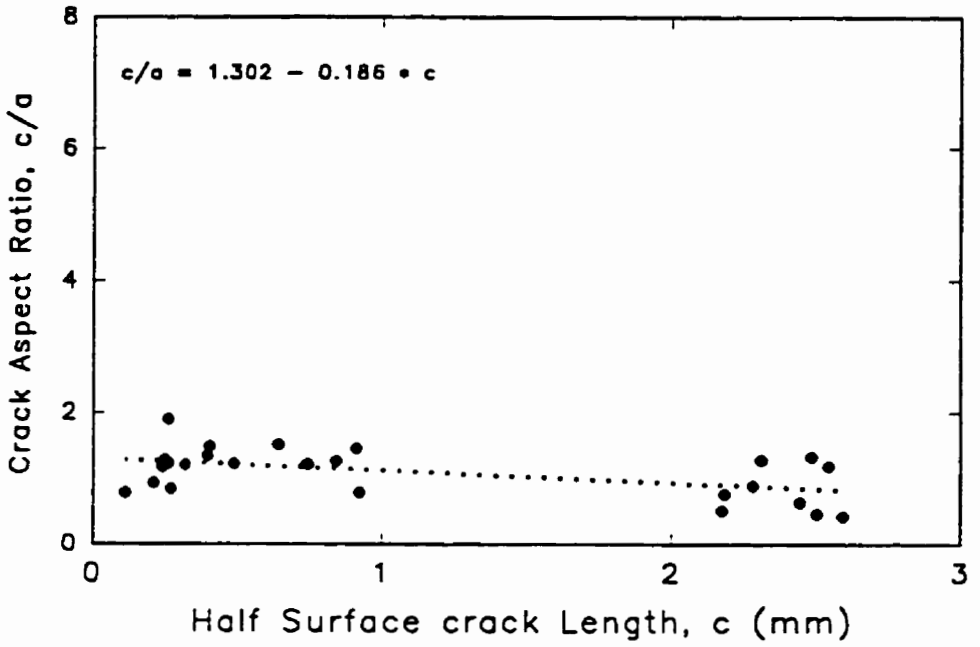

Figure 5.8 Variation of crack aspect ratio with half surface crack length (three data points showing higher aspect ratio were omitted).

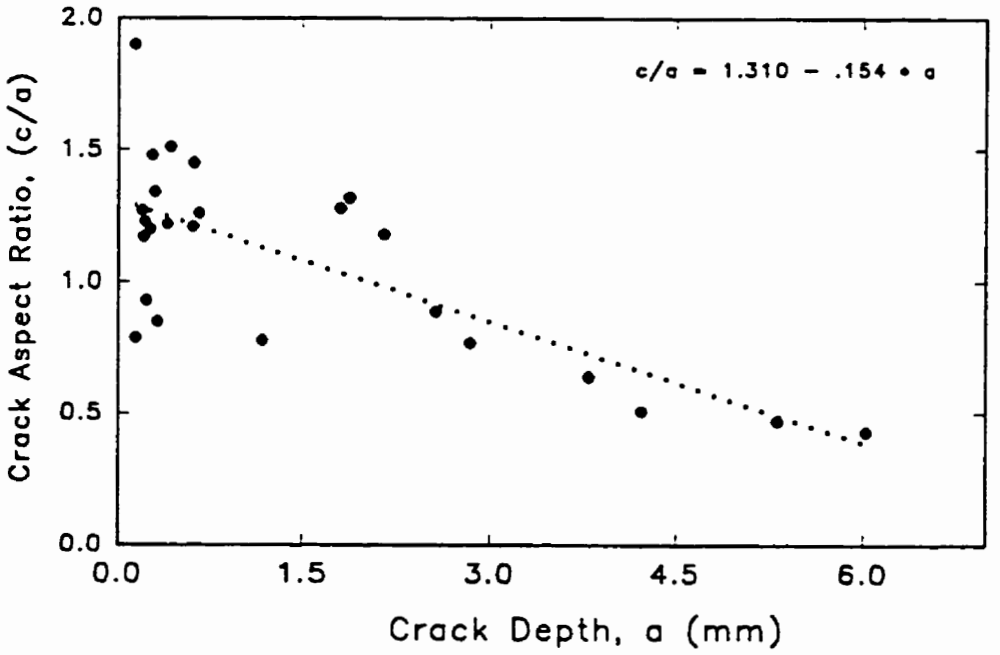

Figure 5.9 Variation of crack aspect ratio (c/a) with the crack depth (three data points showing higher aspect ratios were not included).

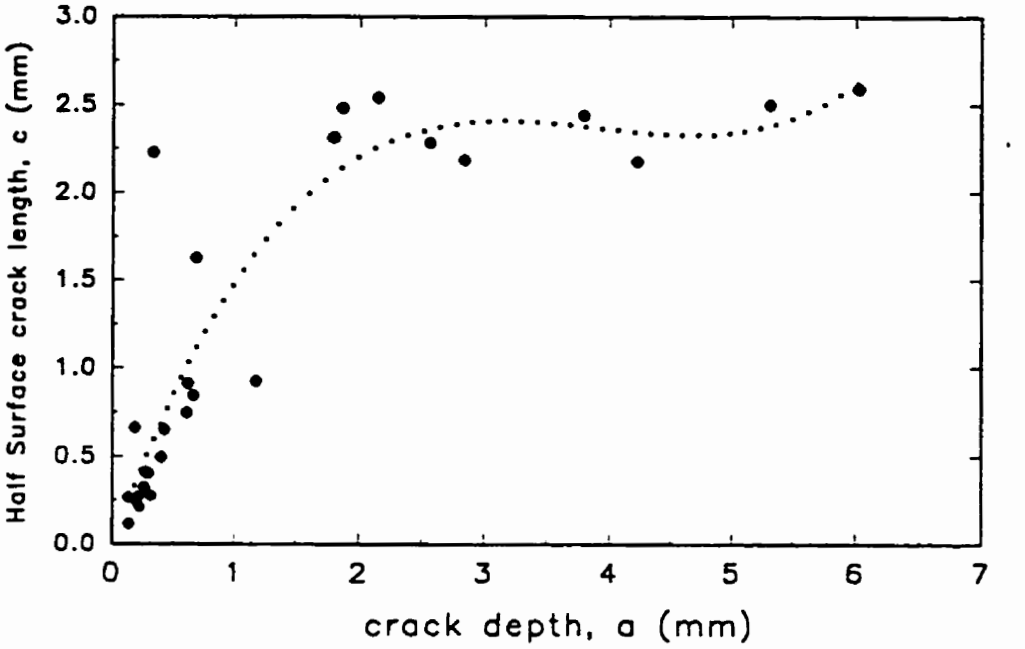

Figure 5.10 Variation of half surface crack length with crack depth.Note : Half surface crack length is increasing faster than crack depth untill crack depth is 2mm.

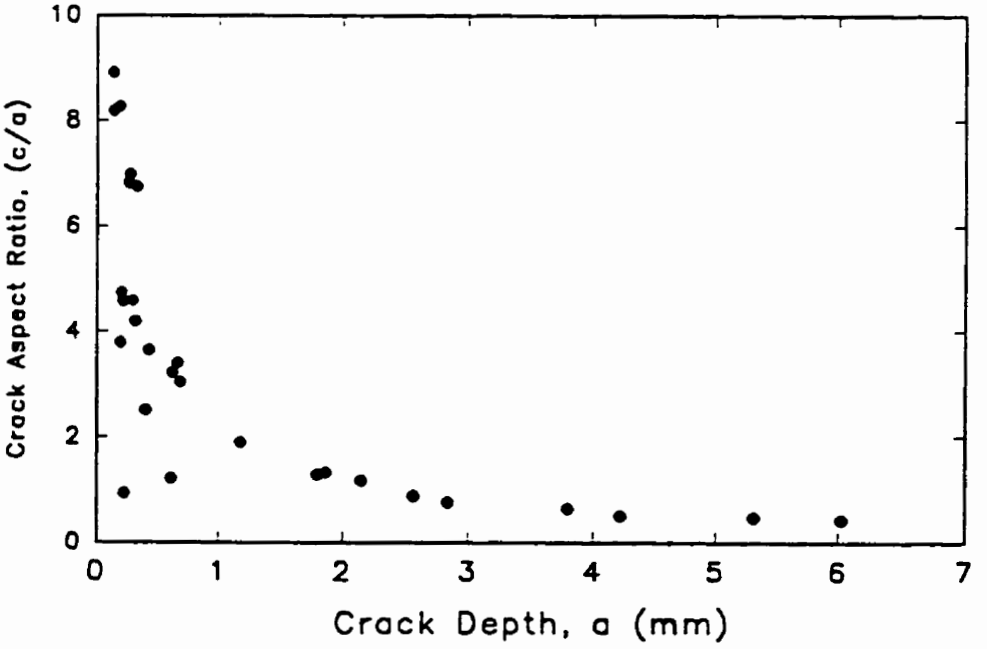

Figure 5.11 Variation of crack aspect ratio with the crack depth. Note: Higher surface crack lengths are due to the crack coalescence of all the cracks

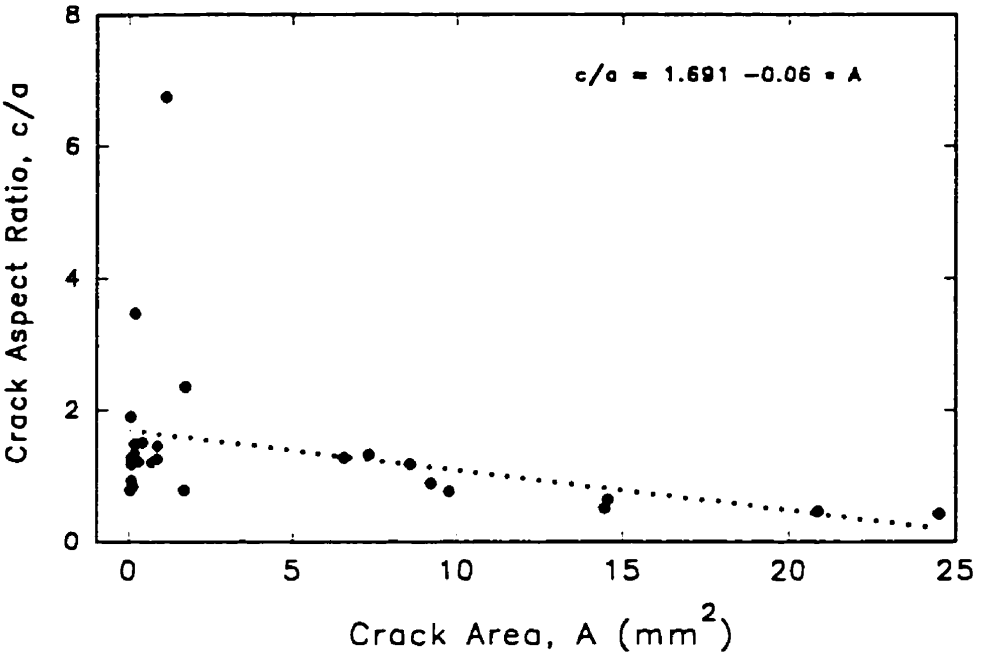

Figure 5.12 Variation of crack aspect ratio with crack area.

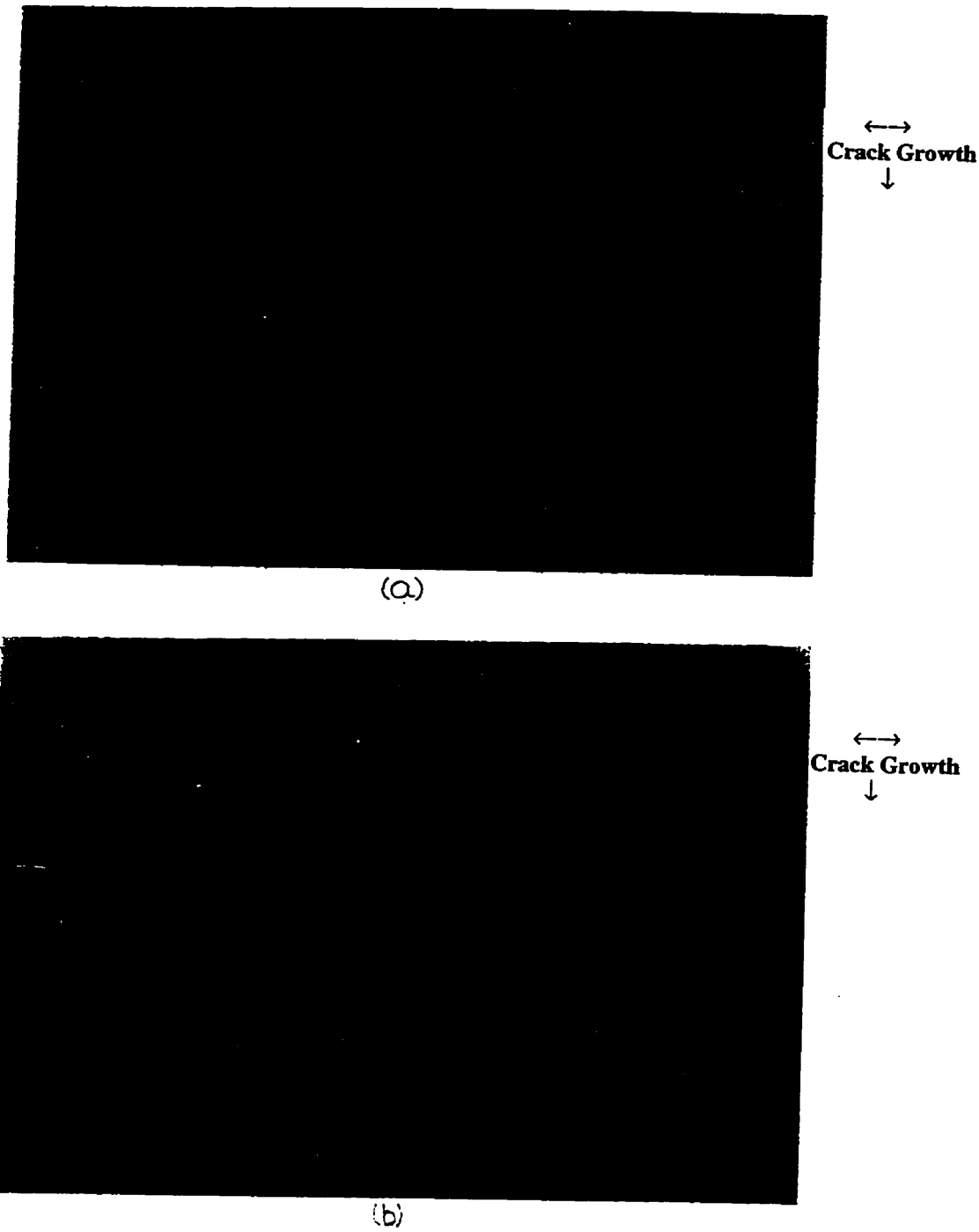

Figure 5.13 Optical micrographs showing different grain orientations (a) 18^{O}, (b) 55^{O} for alloy Al 7075 T651.

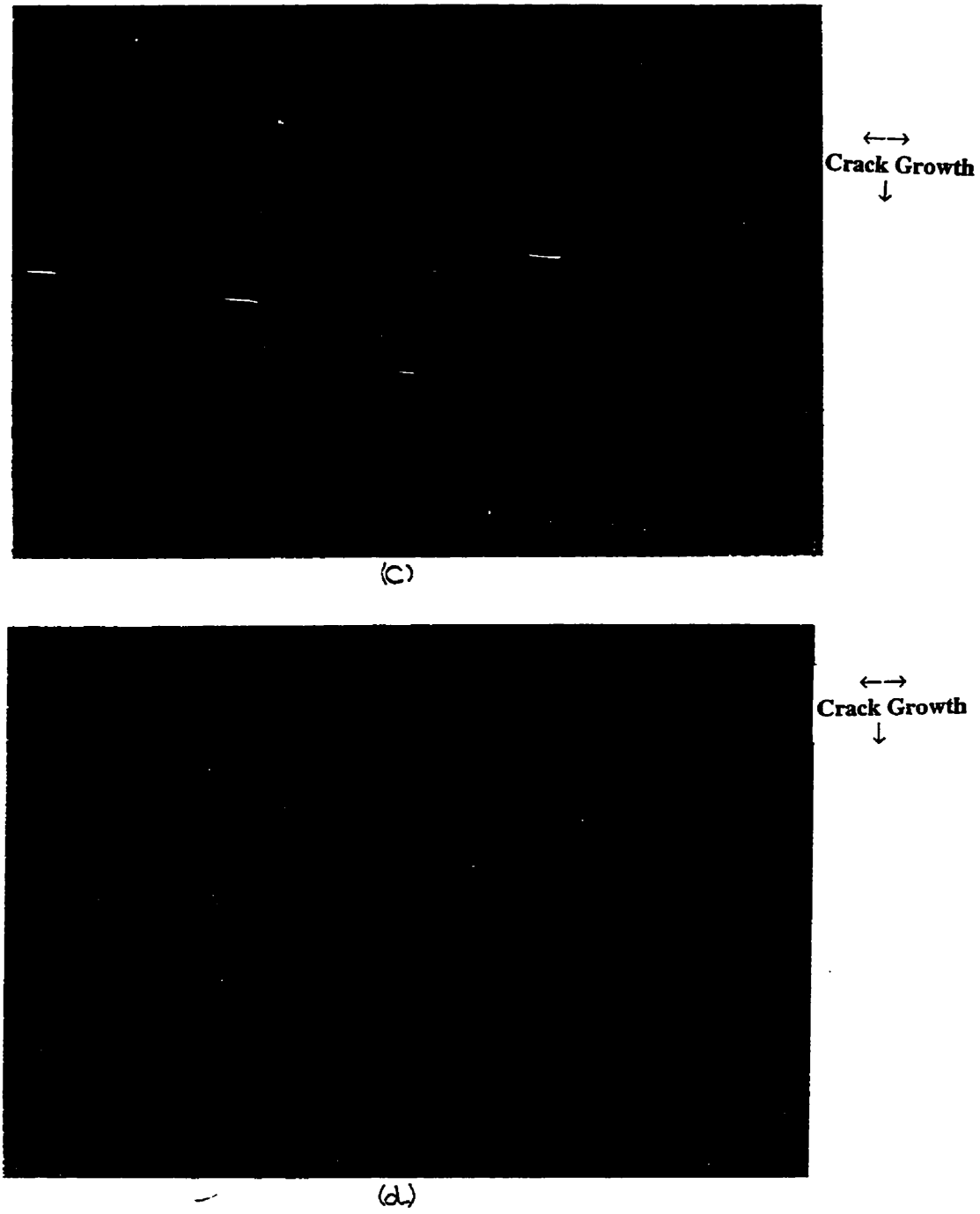

Figure 5.13 Optical micrographs showing different grain orientations (c) 70^{o} and (d) 8^{o} for alloy Al 7075 T651.

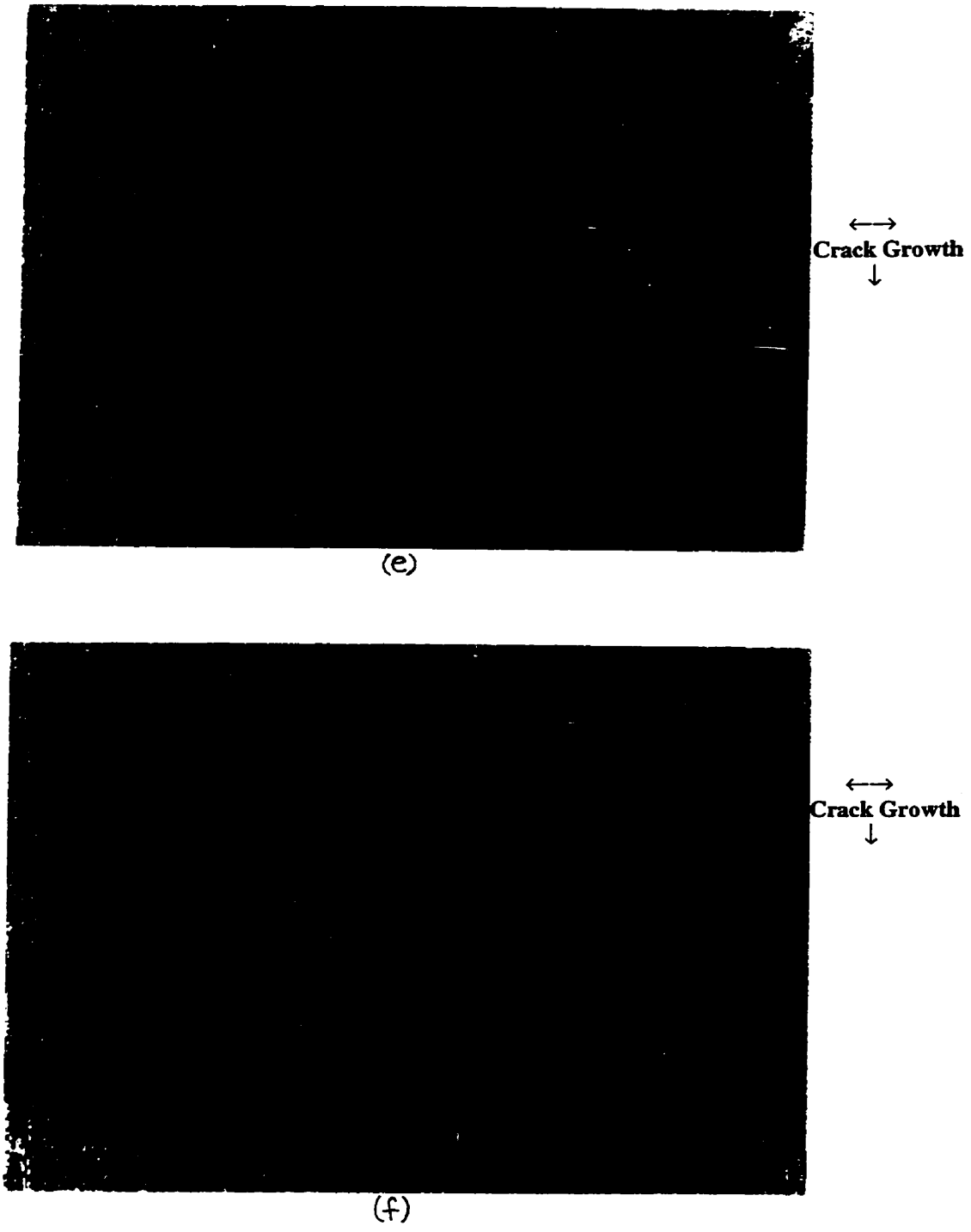

Figure 5.13 Optical micrographs showing different grain orientations (e) 80^{O}, and (f) 90^{O} for Al 7075 T7351 material.

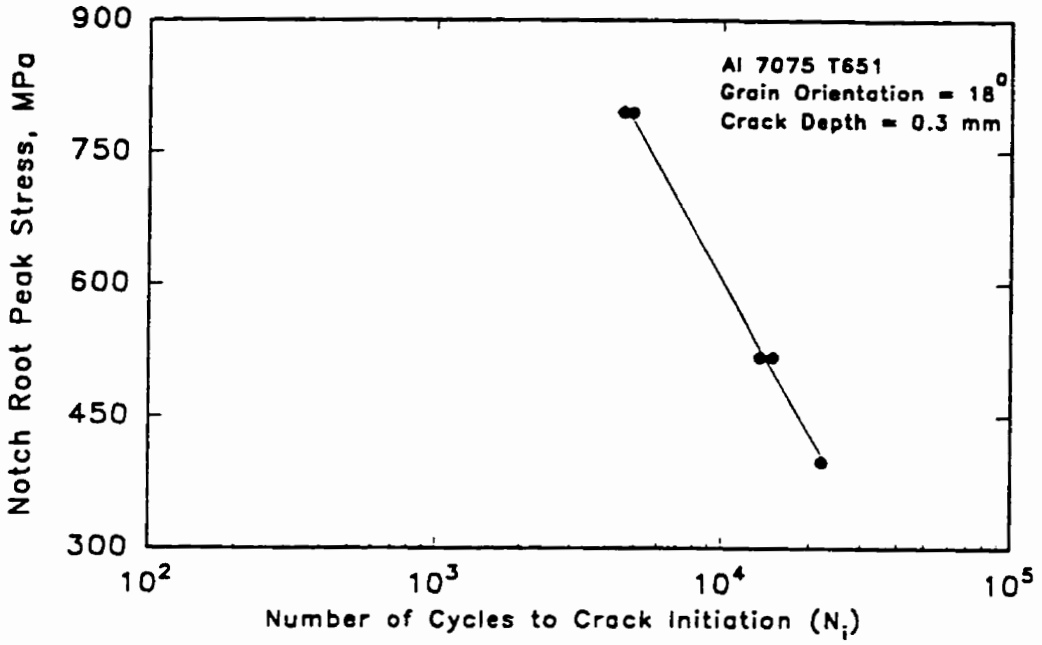

Figure 5.14 Fatigue crack initiation data for Al 7075 T651 material, for 18^{O} grain orientation using 300 μm crack initiation criterion.

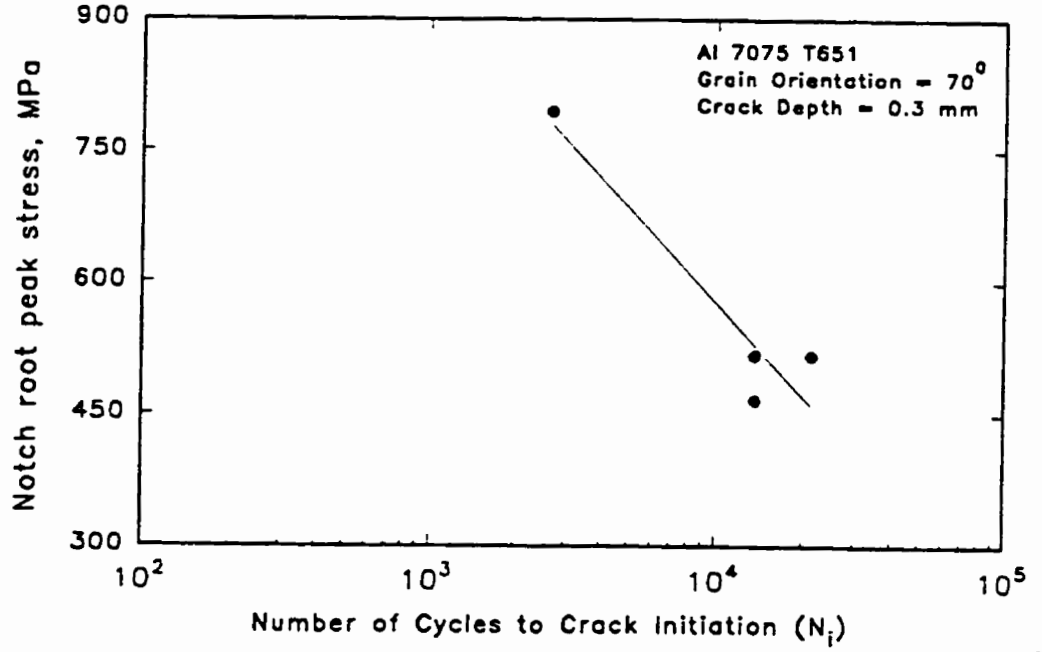

Figure 5.15 Fatigue crack initiation data for Al 7075 T651 material, for 70^{O} grain orientation using 300 μm crack initiation criterion.

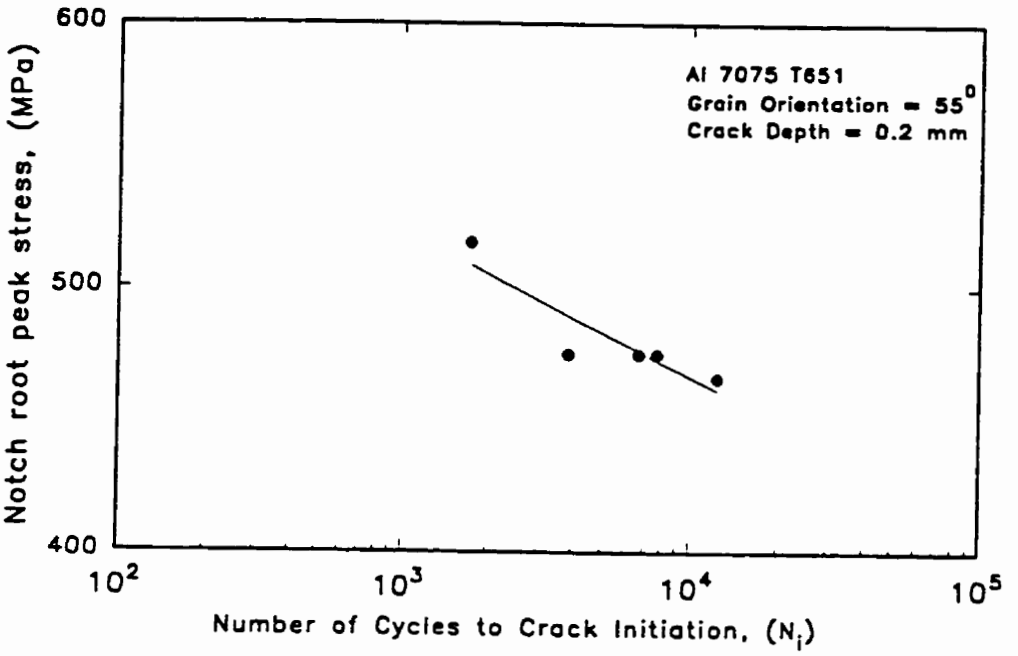

Figure 5.16 Fatigue crack initiation data for Al 7075 T651, for 55^{O} grain orientation using 200 μm crack initiation criterion.

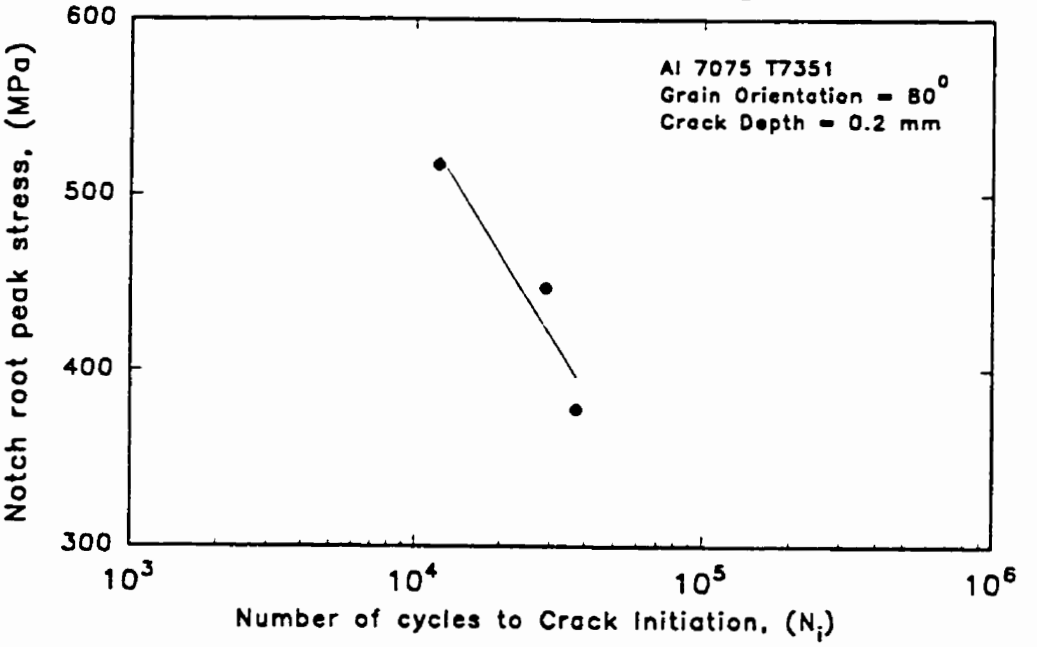

Figure 5.17 Fatigue crack initiation data for Al 7075 T7351, for 80^{O} grain orientation using 200 μm crack initiation criterion.

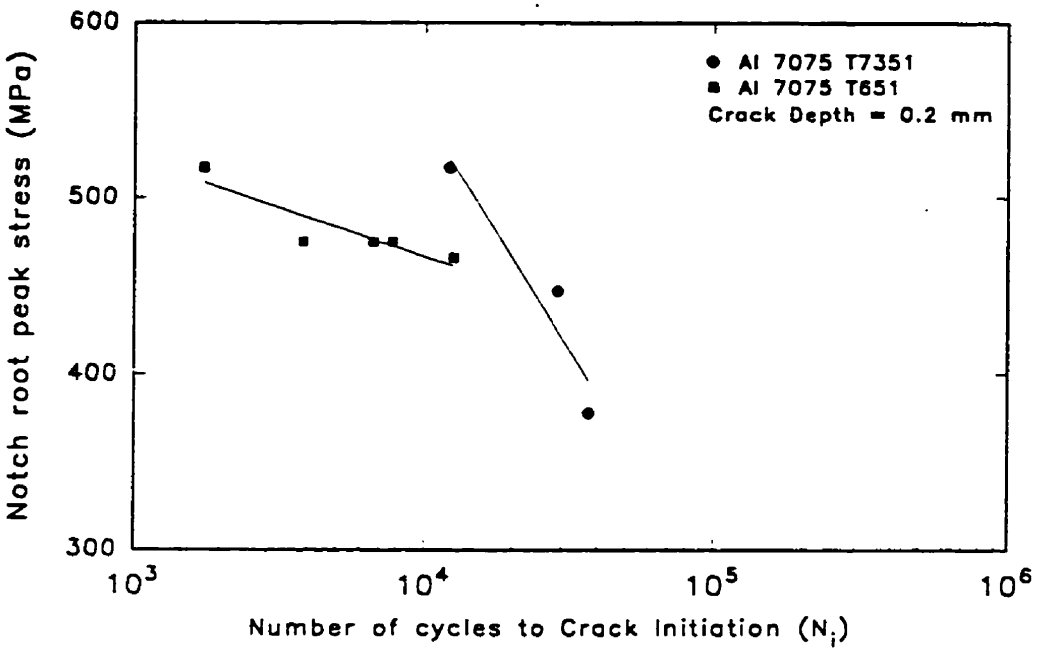

Figure 5.18 Comparison of the fatigue crack initiation data of T651 and T7351 temper. Note: 200 μm crack initiation criterion has been used.

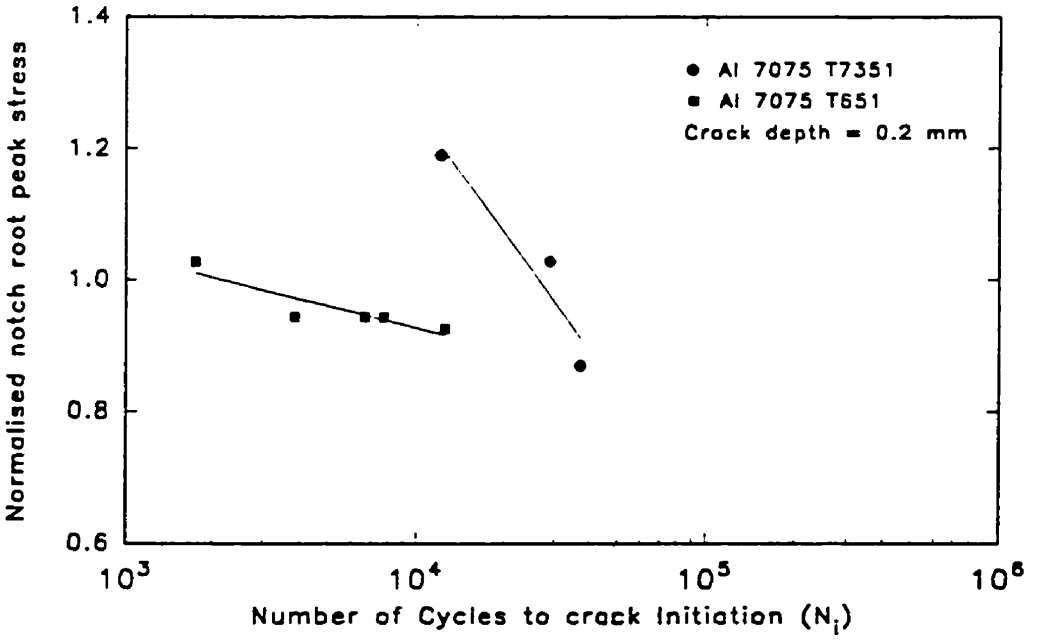

Figure 5.19 Comparison of the fatigue crack initiation of T651 and T7351 temper using 200 μm crack initiation criterion. Note: Notch root peak stress is normalised with the flow stress of the respective materials.

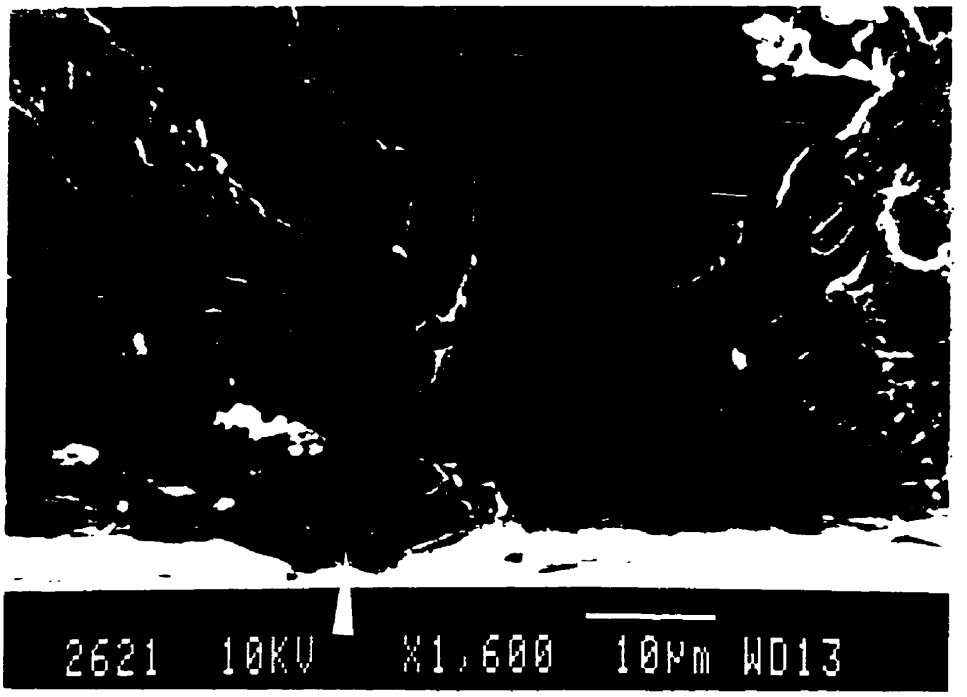

Figure 5.20 Fractographs showing crack initiation region of T651 material in 55^{O} grain orientation specimen. Notch root peak stress was 475 MPa.

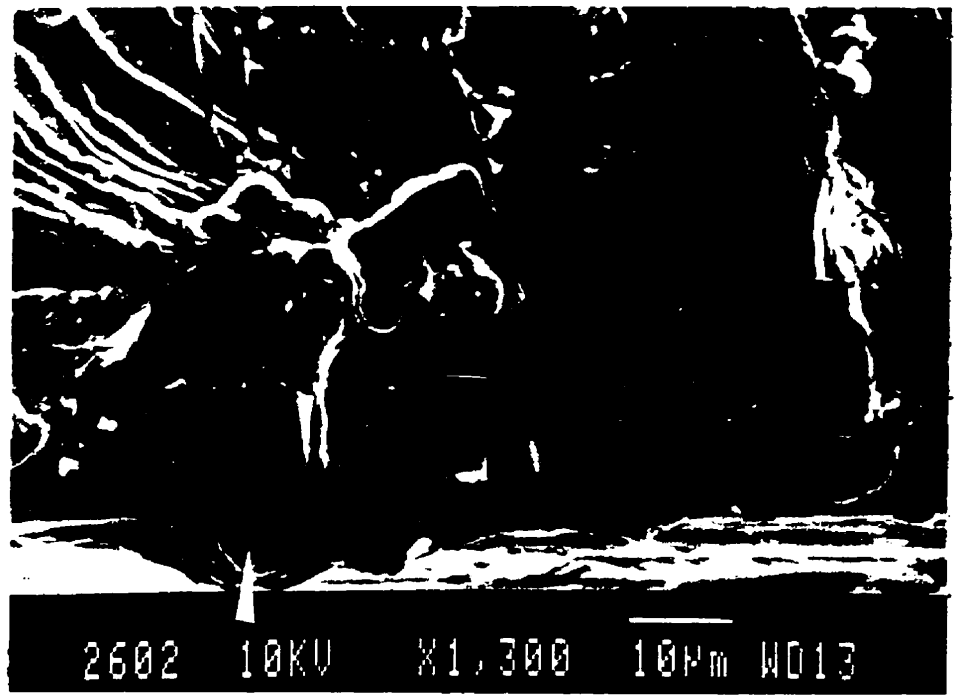

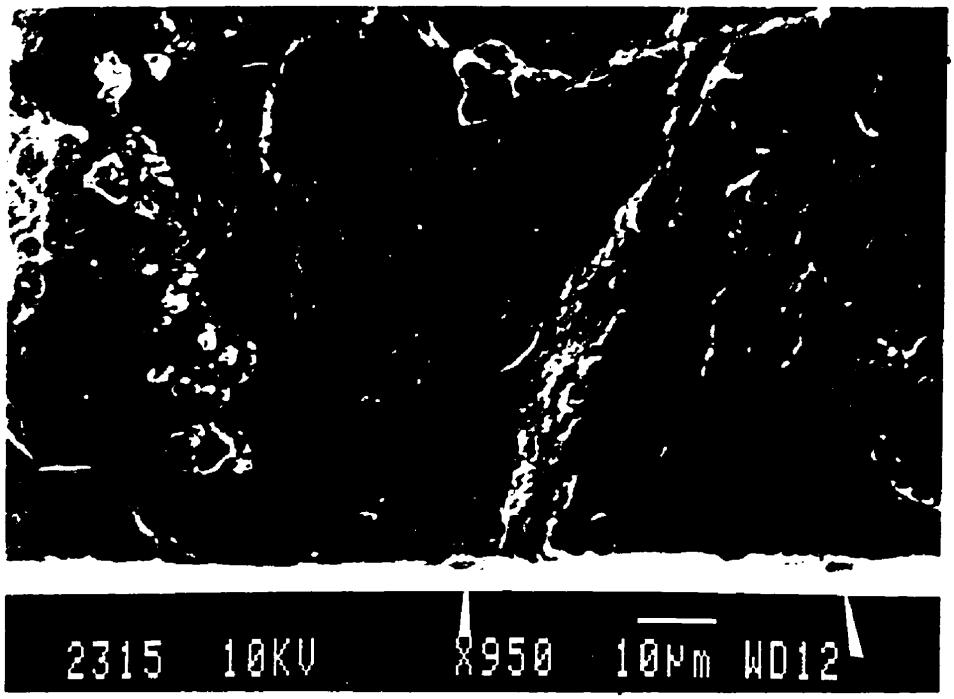

Figure 5.21 Fractographs showing crack initiation region, T651 temper (a) 8^{o} grain orientation, 517 MPa stress (b) 18^{o} grain orientation, 795 MPa stress.

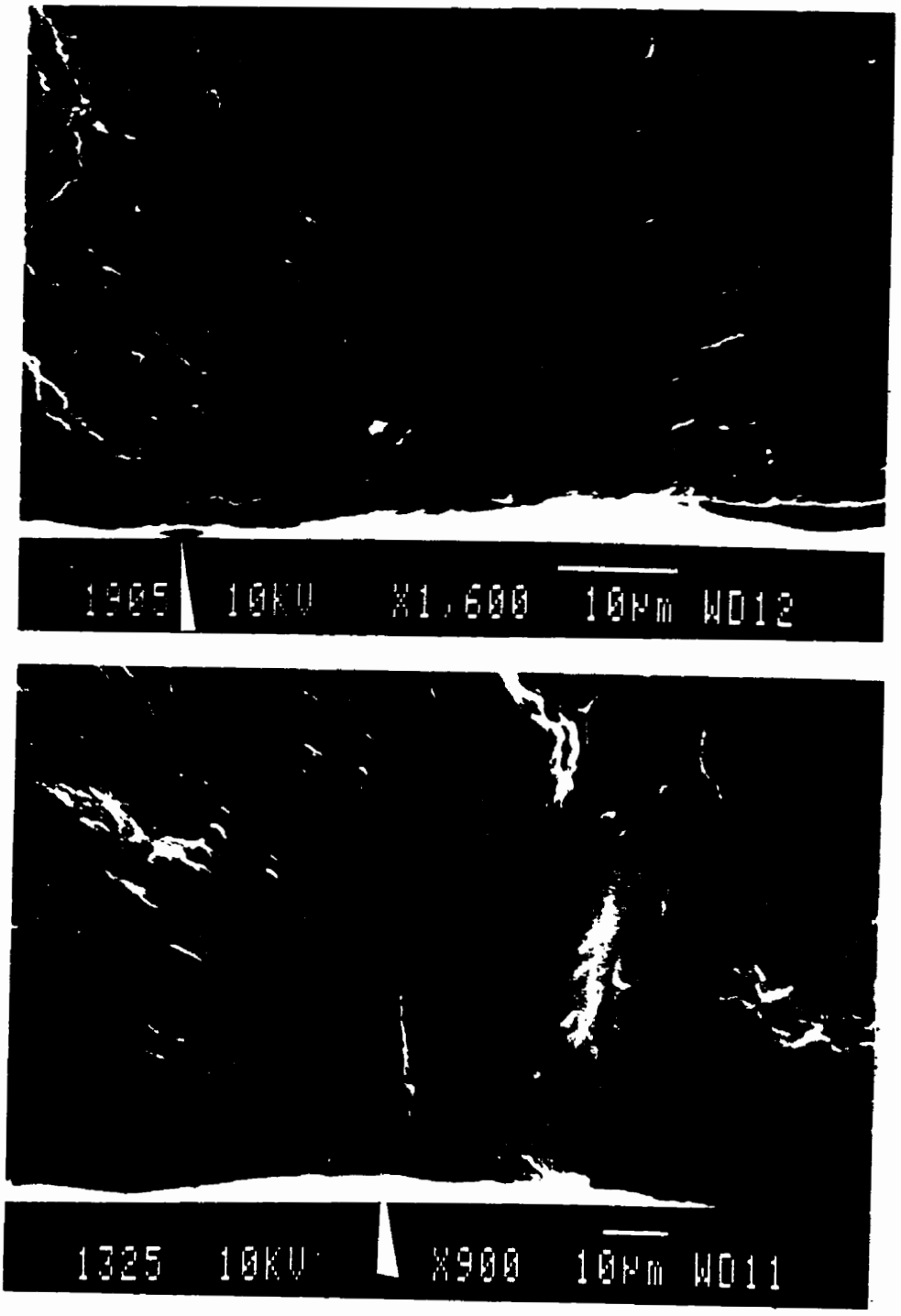

Figure 5.22 Fractographs showing crack initiation regionfor T7351 temper for 80^{O} grain orientation (a) 377 MPa stress (b) 447 MPa stress.

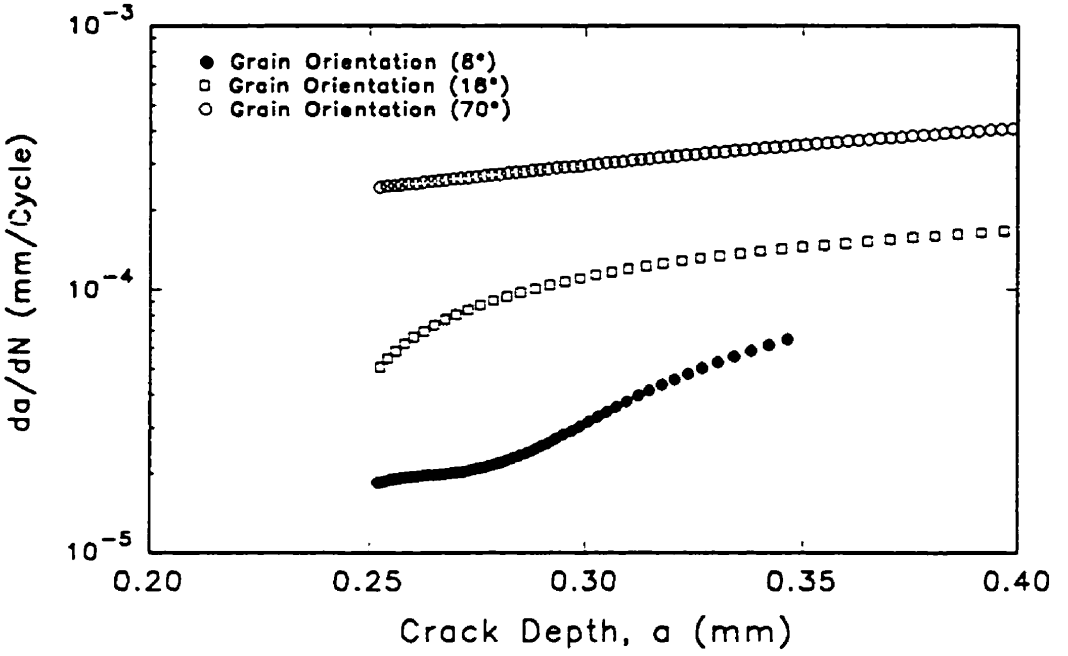

Figure 5.23 Variation of da/dN with crack depths due to different grain orientations in T651 temper.

Figure 5.24 A montage of fracture surfaces of T651 material having 8^{O} grain orientation. The notch root peak stress was 517 MPa.

Figure 5.25 A montage of fracture surfaces of T651 material having 18^{o} grain orientation. The notch root peak stress was 517 MPa.

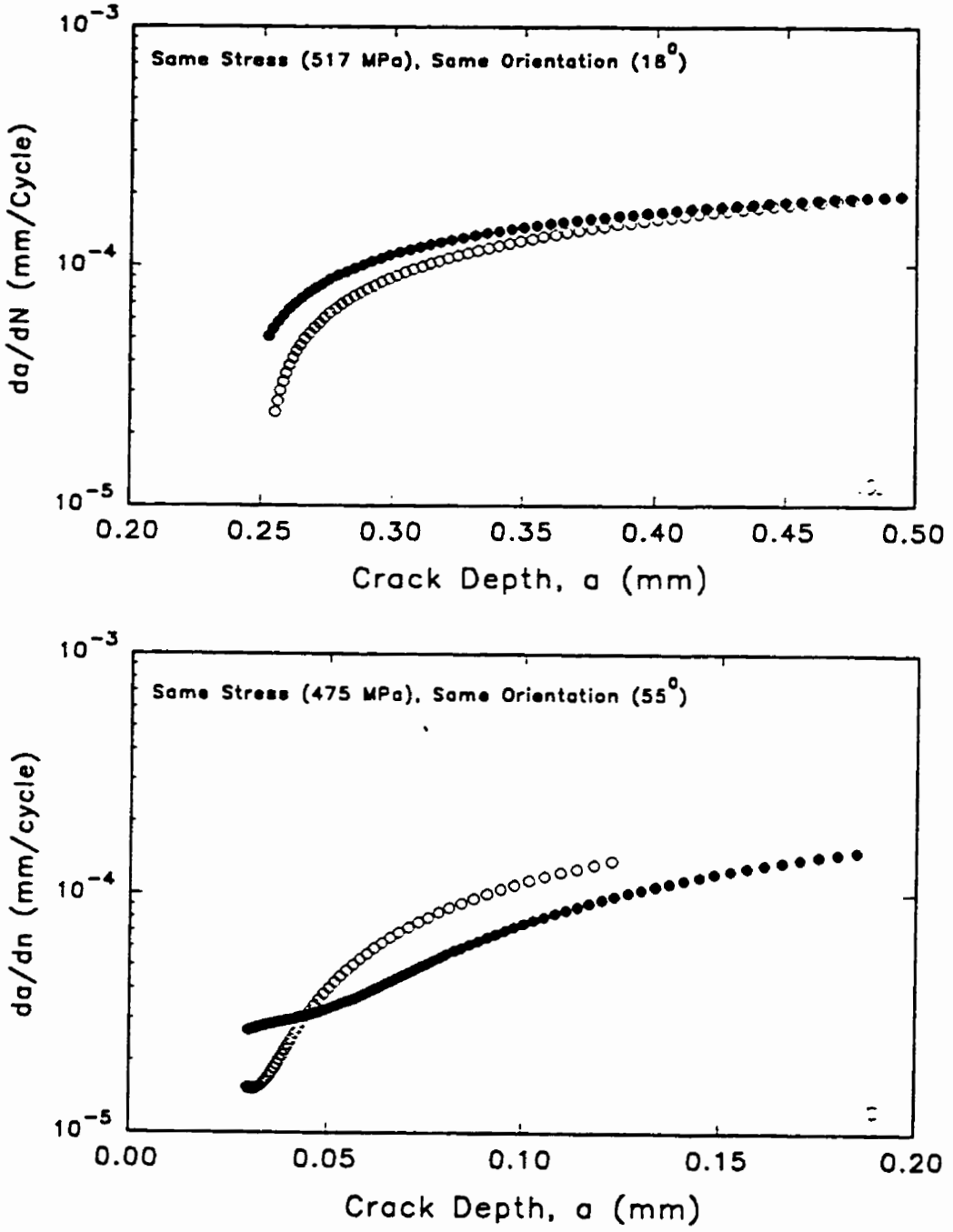

Figure 5.26 Variation of da/dN with crack depths for same stress and same grain orientation in T651 temper. (a) 517 MPa, 18^{O} grain orientation, (b) 475 MPa, 55^{O} grain orientation.

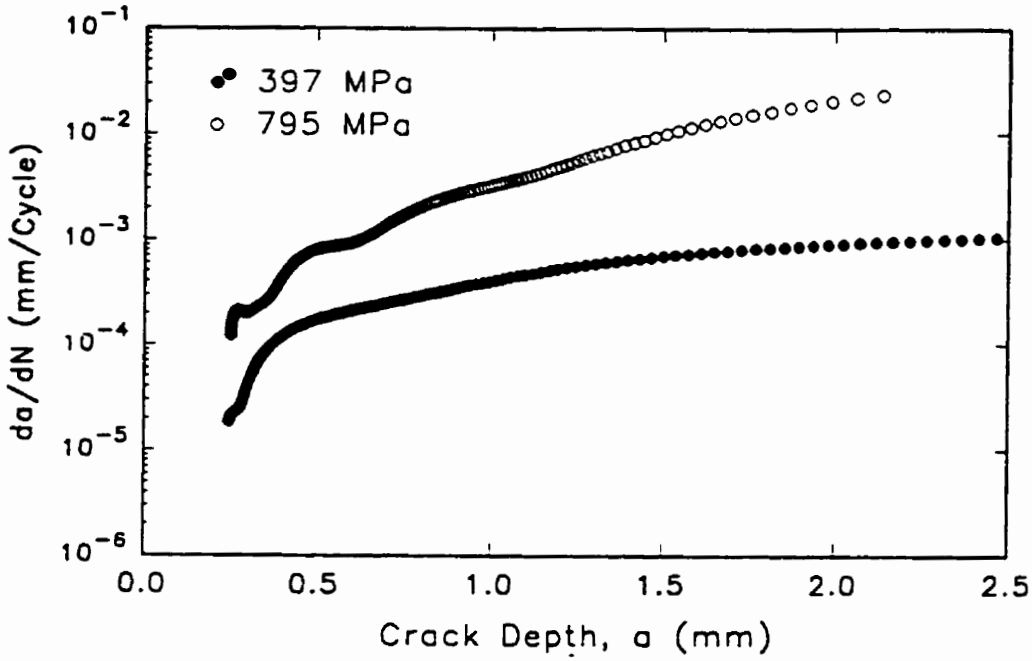

Figure 5.27 A comparison of variation of da/dN with crack depths for different stress.

Figure 5.28 A montage of fracture surfaces in T651 material for 18^{O} grain orientation. The notch root peak stress was 795 MPa.

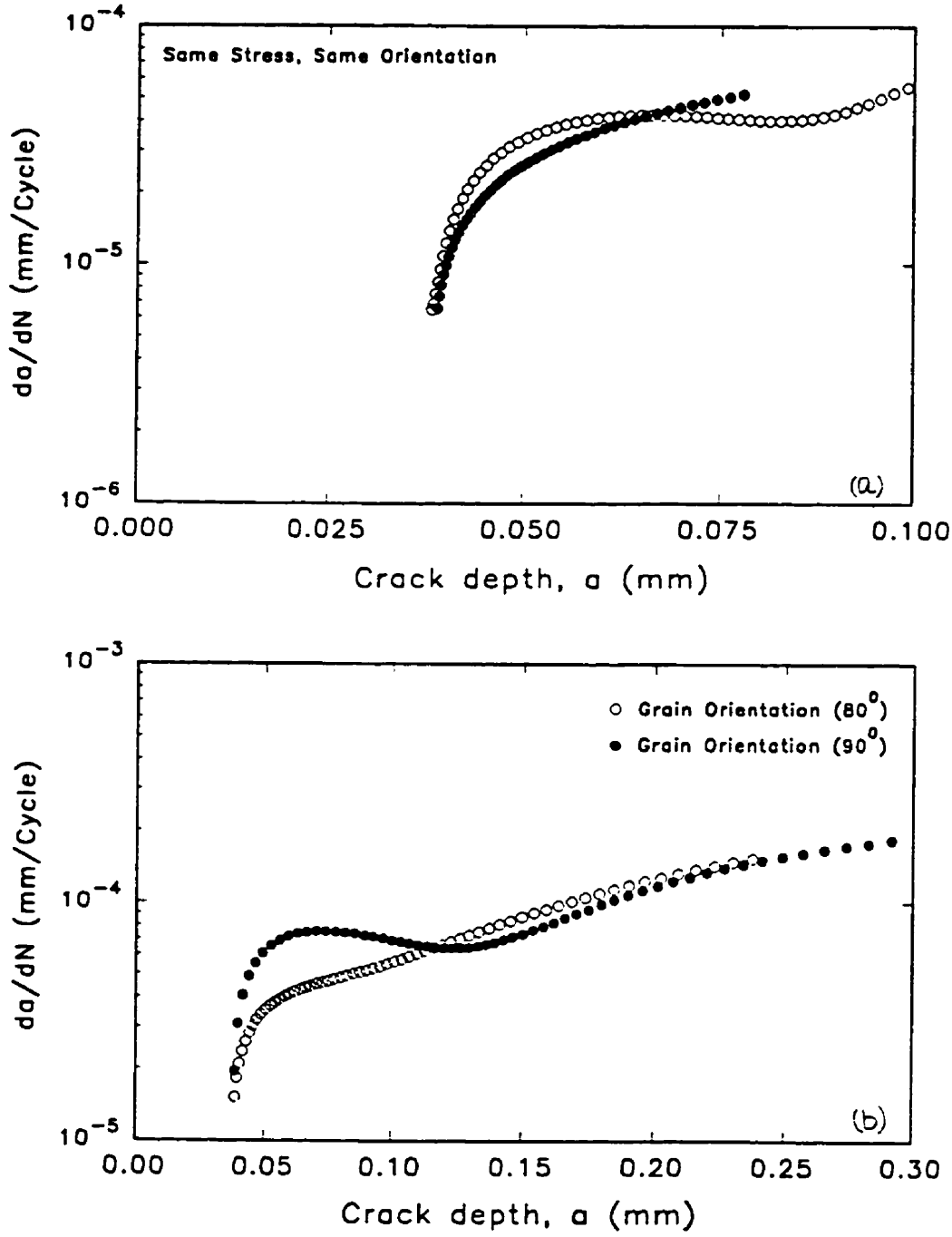

Figure 5.29 Variation of da/dN with crack depths in T7351 temper. (a) for same stress, 155 MPa and same grain orientation, 80^{O} (b) same stress, 131 MPa and two different grain orientations of 80^{O} and 90^{O}.

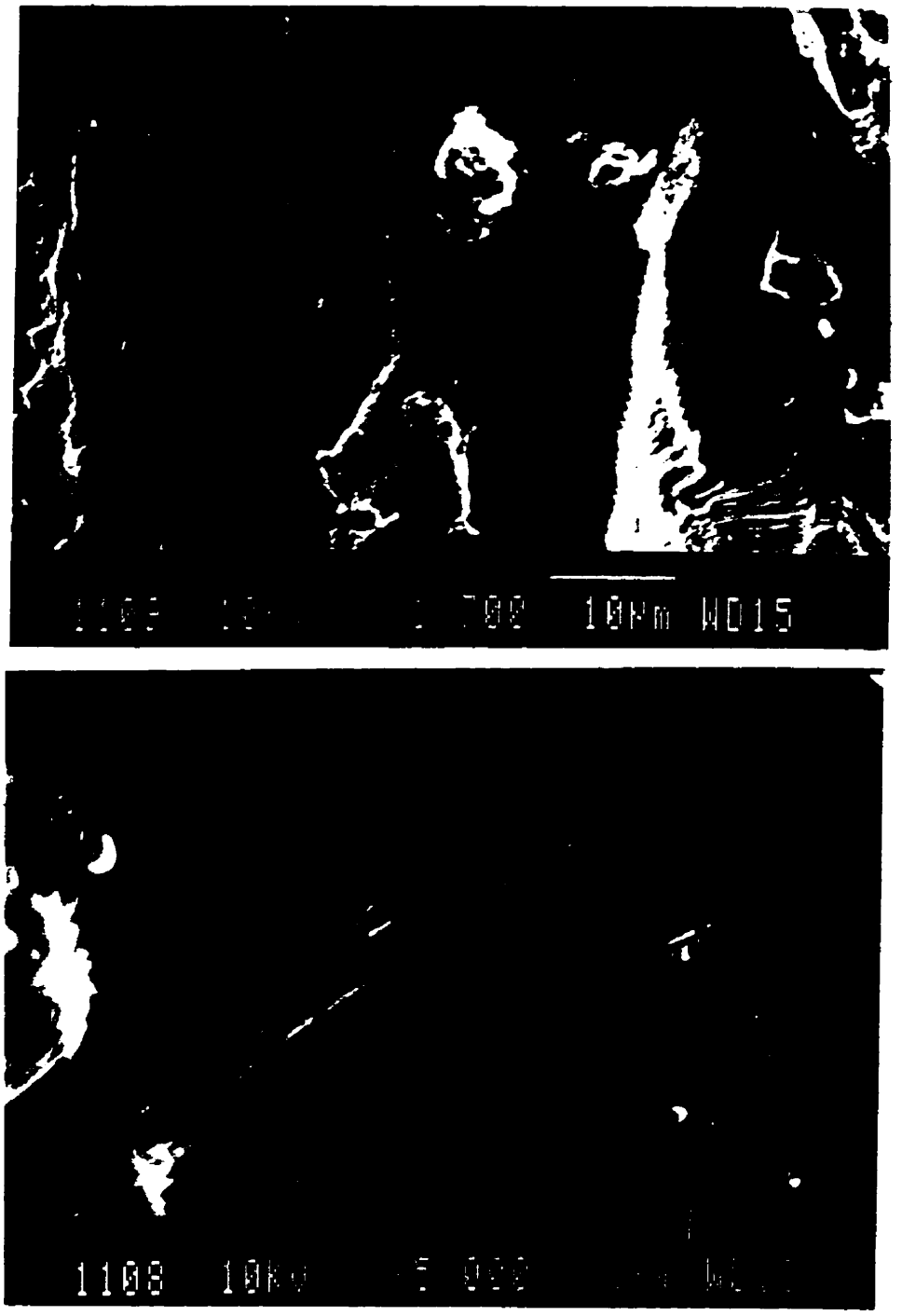

Figure 5.30 (a) Fractographs showing striations in T651 material having 70^{o} grain orientation and fatigue tested at 517 MPa. (b) zoom on striations at 1 mm away from the notch root surface.

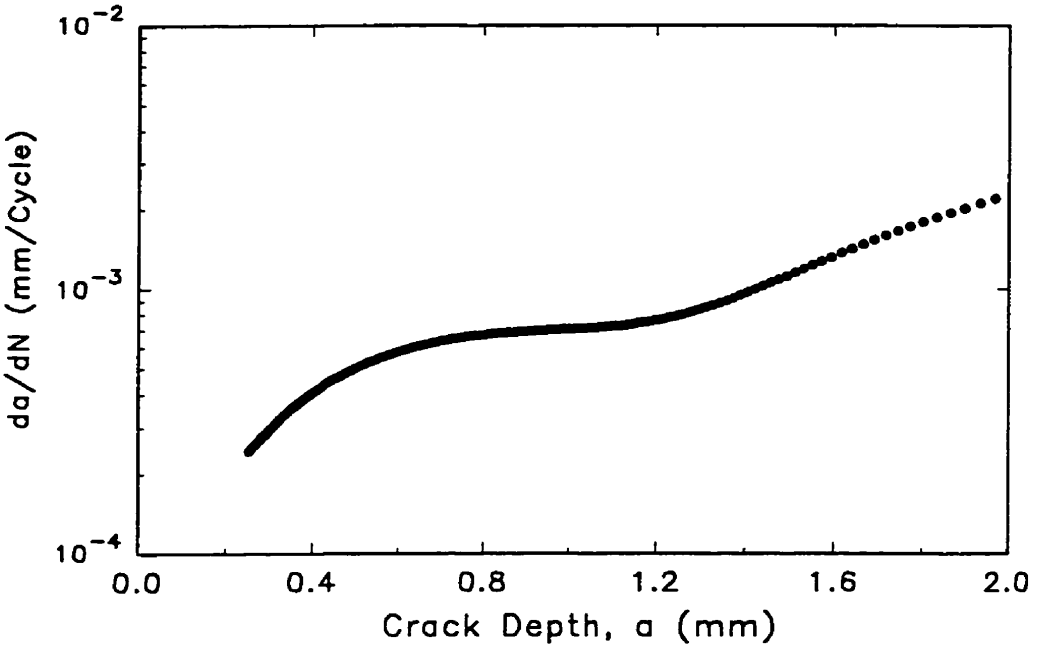

Figure 5.31 A plot of da/dN versus crack depth for the same specimen as shown in fig. 5.30a. Note that at a = 1mm the growth rate is similar to the growth rate calculated by striations counting, fig 5.30b.

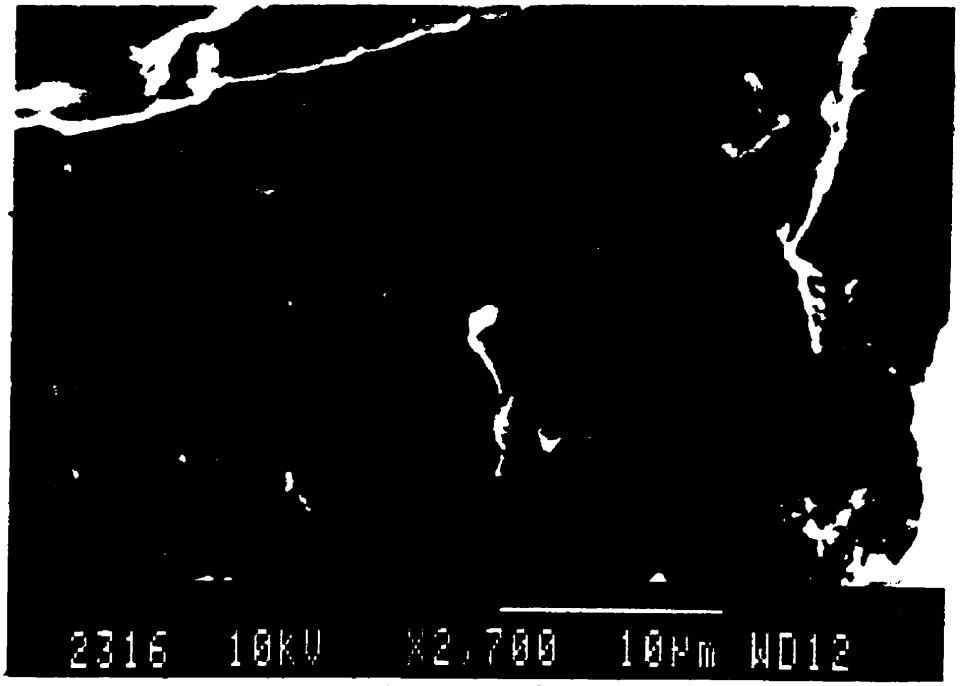

Figure 5.32 Fractograph showing striations in a T651 specimen with grain orientation of 18^{O} fatigue tested at 795 MPa.

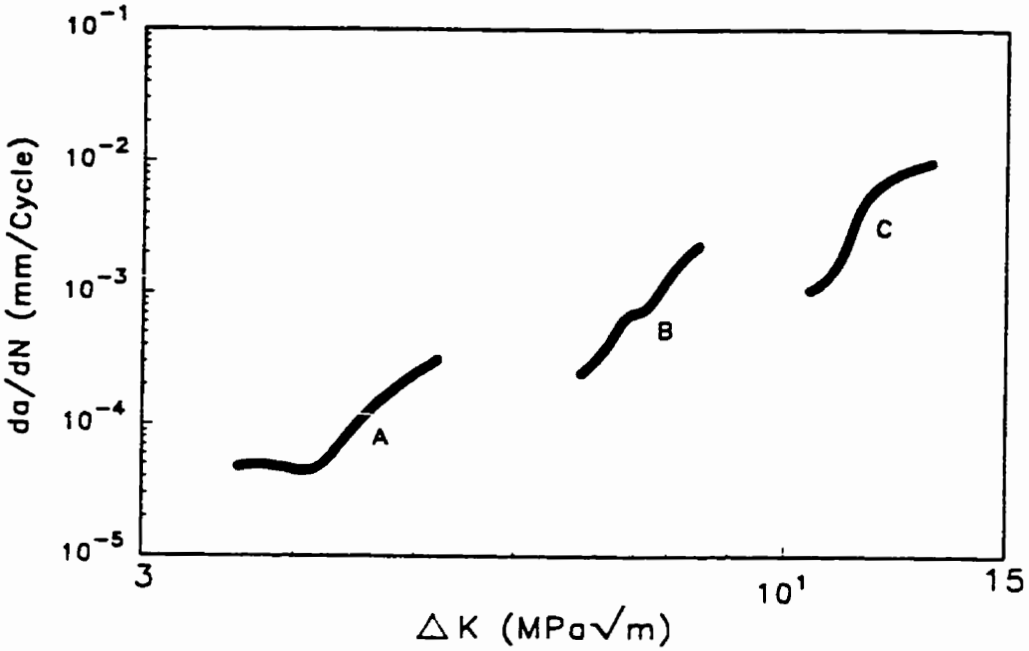

Figure 5.33a Variation of da/dN with ΔK in T651 material possessing 70^{O} grain orientation. Symbols A, B and C denote stress levels of 475 MPa, 517 MPa and 795 MPa respectively.

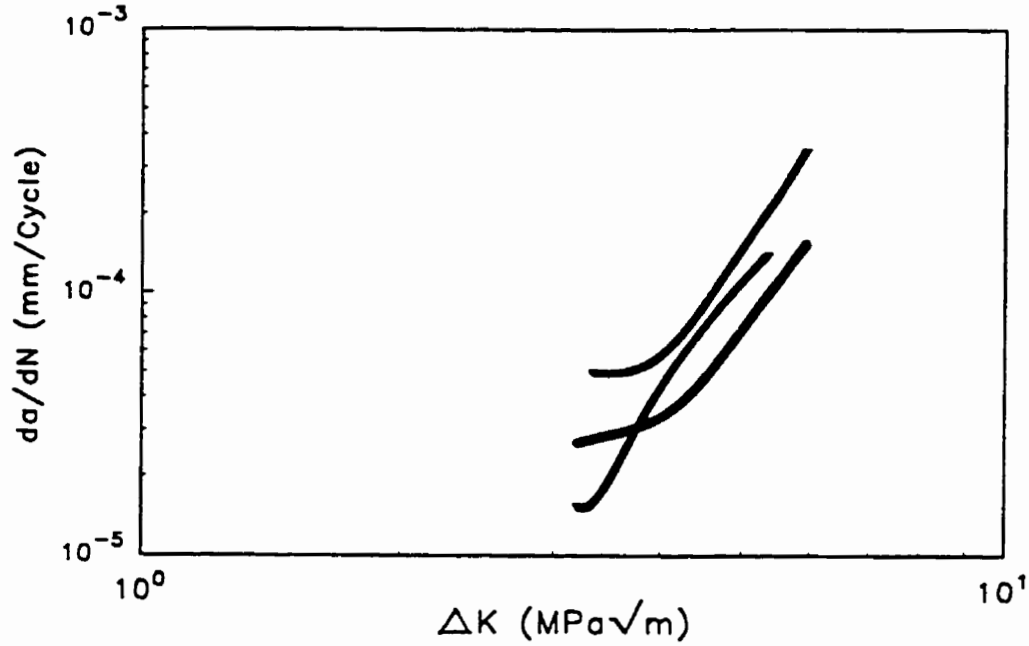

Figure 5.33b Variation of da/dN with ΔK in T651 material possessing 55^{O} grain orientation and stress level of 467 MPa and 475 MPa.

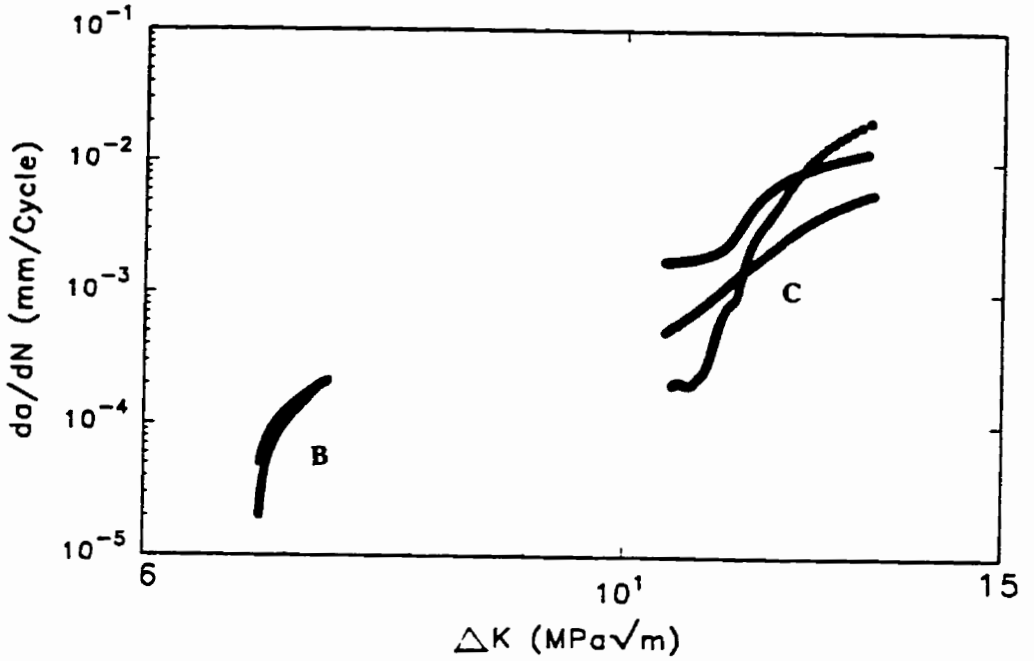

Figure 5.33c Variation of da/dN with ΔK in T651 material possessing18° grain orientation. Symbols B and C denote stress levels of 517 MPa and 795 MPa respectively.

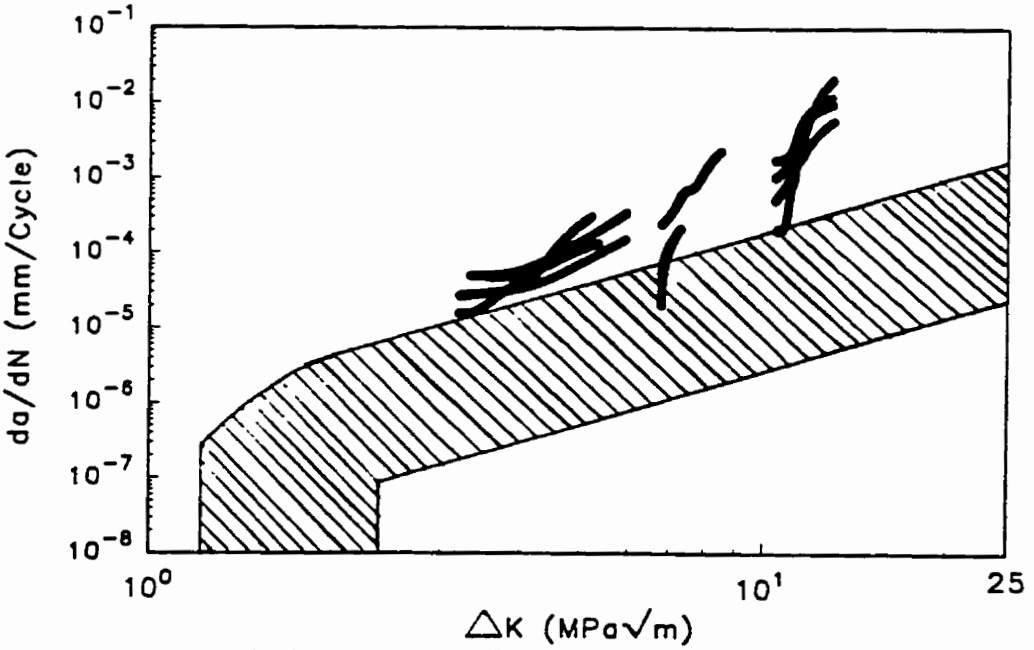

Figure 5.34 A plot of da/dN versus ΔK for all three grain orientations tested in T651 material. Also plotted is the scatter band pertaining to short crack data generated by Newman et al on Al 7075 T6 material fatigue tested at notch root peak stress of 378 MPa.

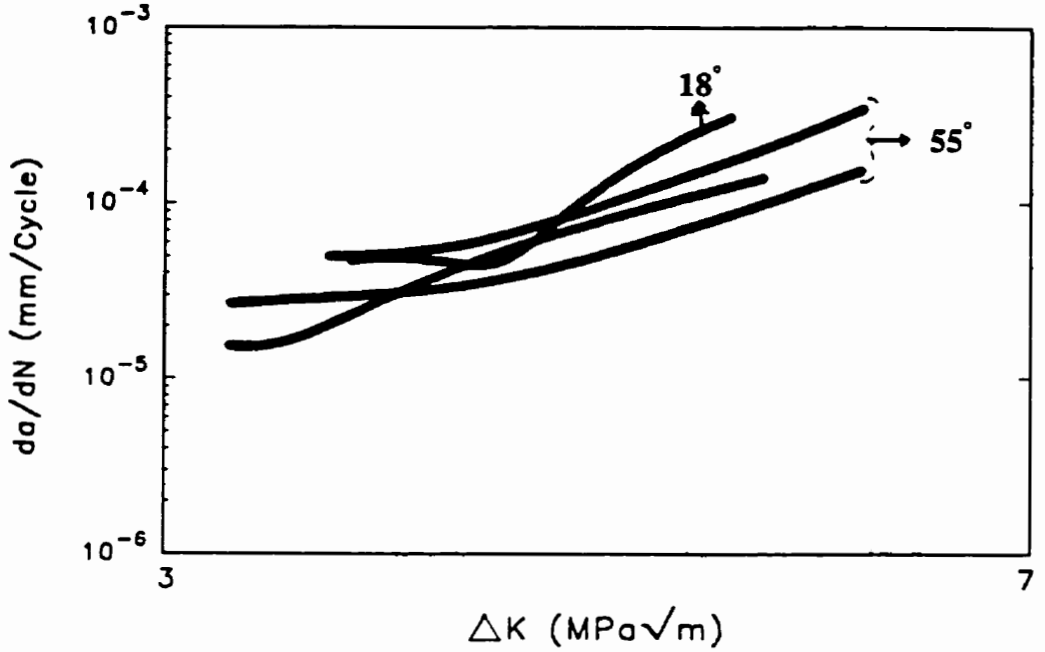

Figure 5.35a Variations of da/dN versus ΔK in T651 material fatigue tested at 475 MPa.

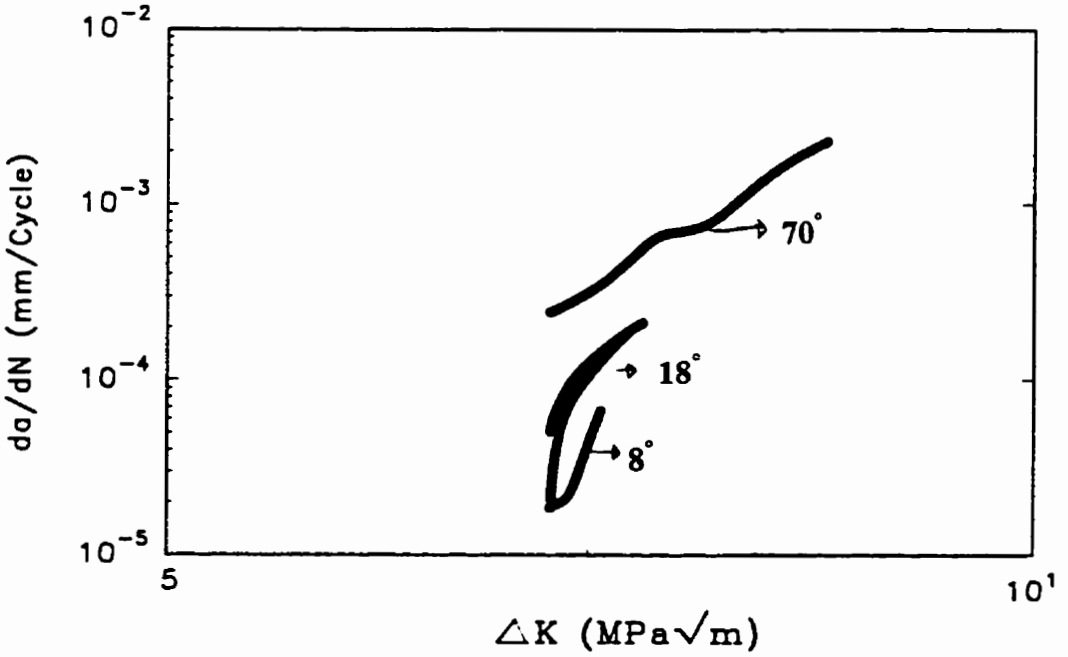

Figure 5.35b Variations of da/dN versus ΔK in T651 material fatigue tested at 517 MPa.

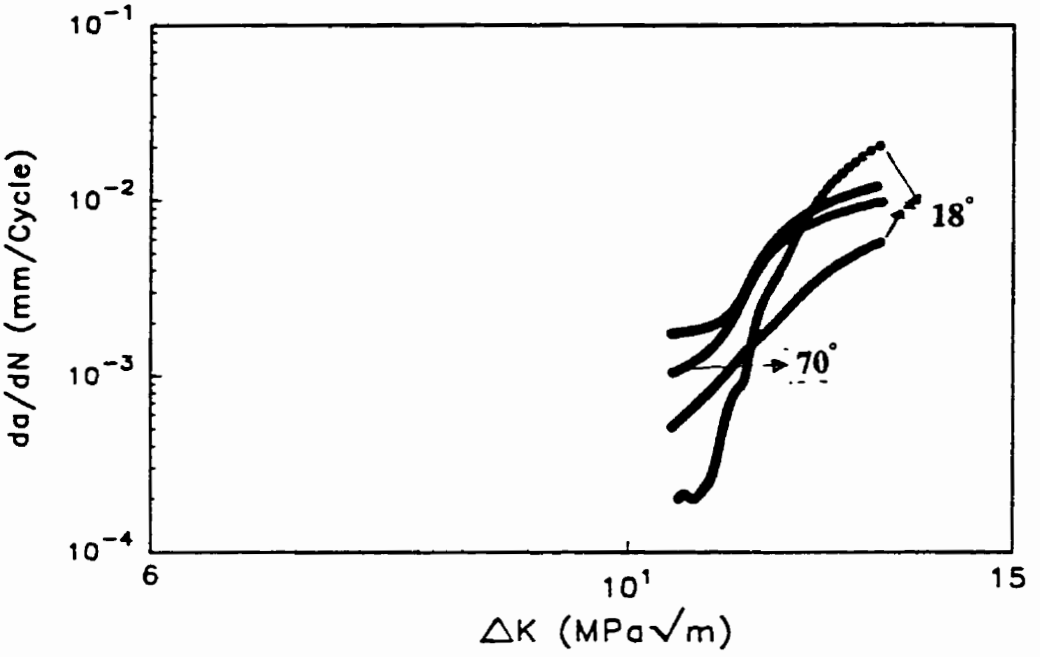

Figure 5.35c Variations of da/dN versus ΔK in T651 material fatigue tested at 795MPa.

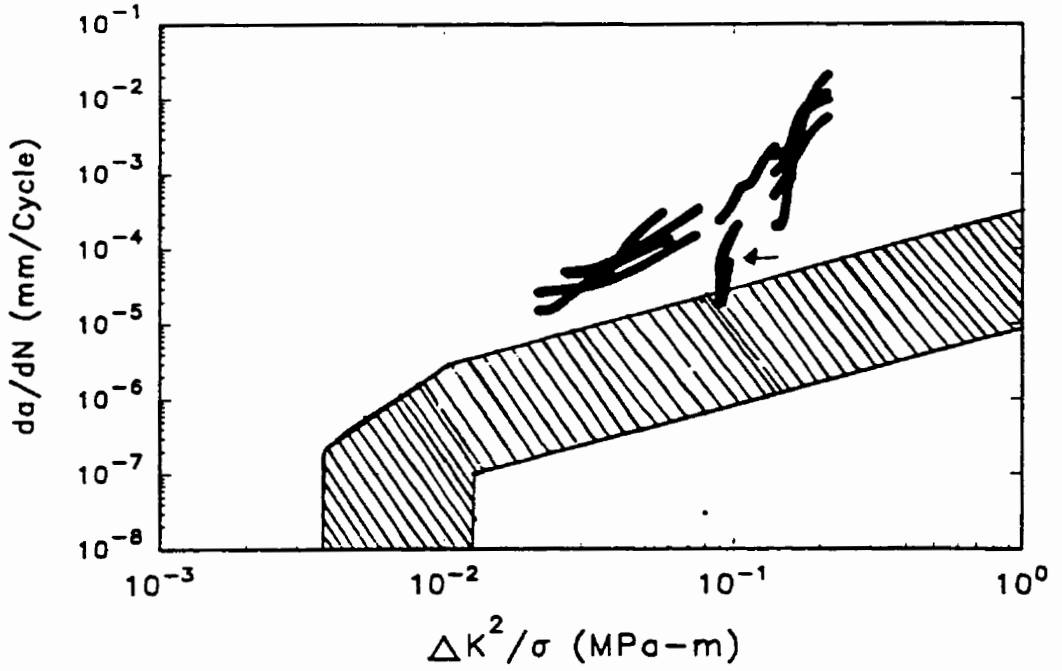

Figure 5.36 A plot of da/dN versus $\Delta K^2/\sigma$ in T651 temper. The scatter band of the data obtained by Newman et al is also shown.

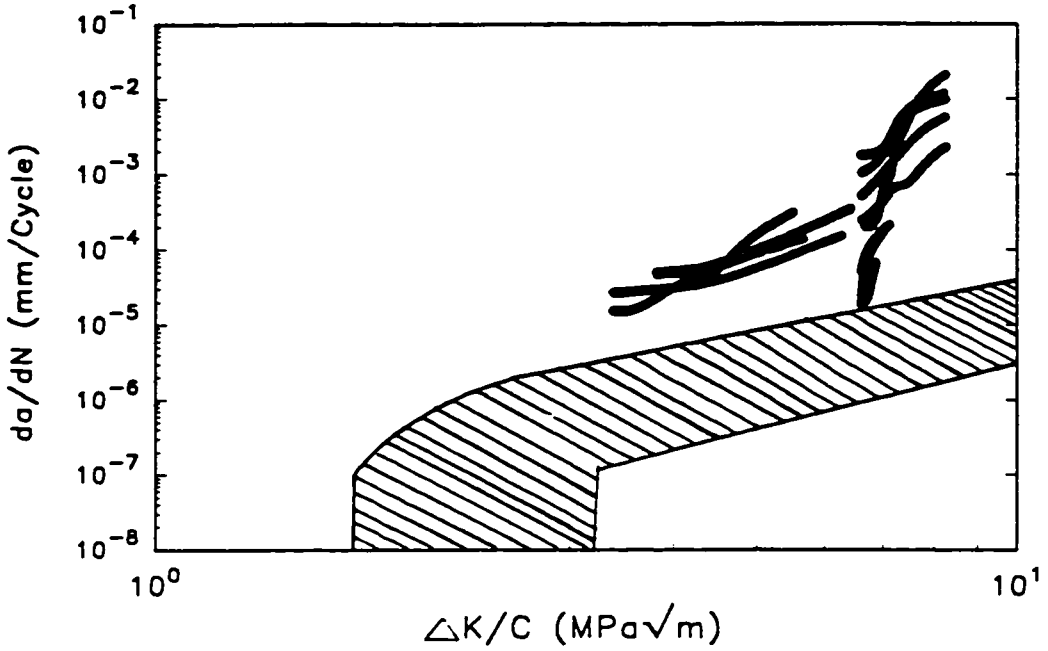

Figure 5.37 A plot of da/dN versus ΔK/C for T651 temper. The scatter band of the data obtained by Newman et al is also shown.

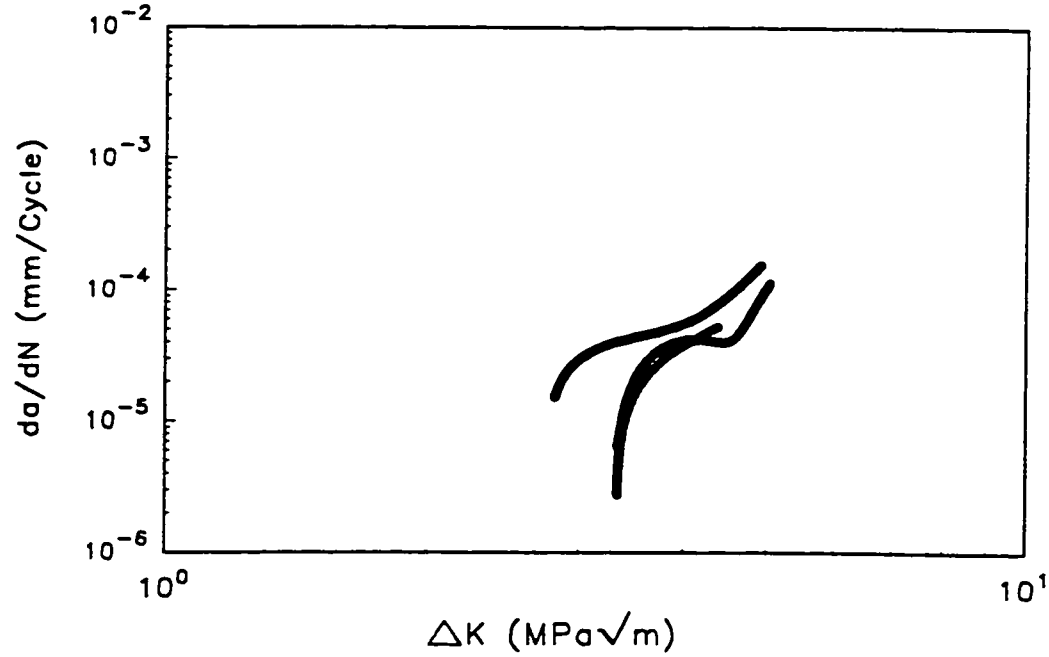

Figure 5.38a Variation of da/dN versus ΔK in T7351 temper possessing 80^{0} grain orientation.

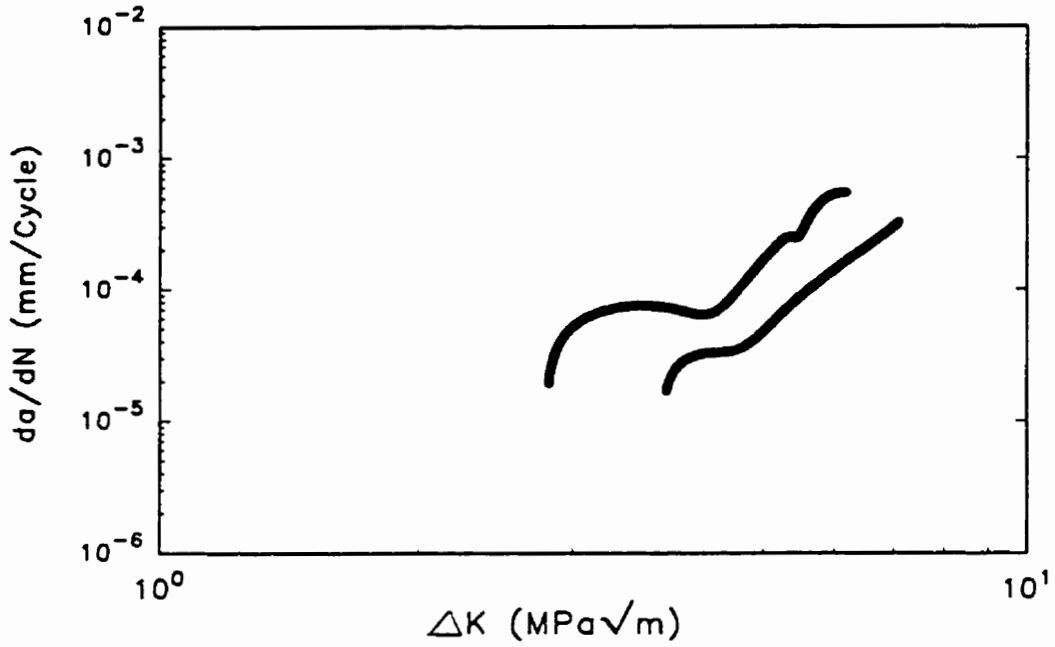

Figure 5.38b Variation of da/dN versus ΔK in T7351 temper possessing 90^{0} grain orientation.

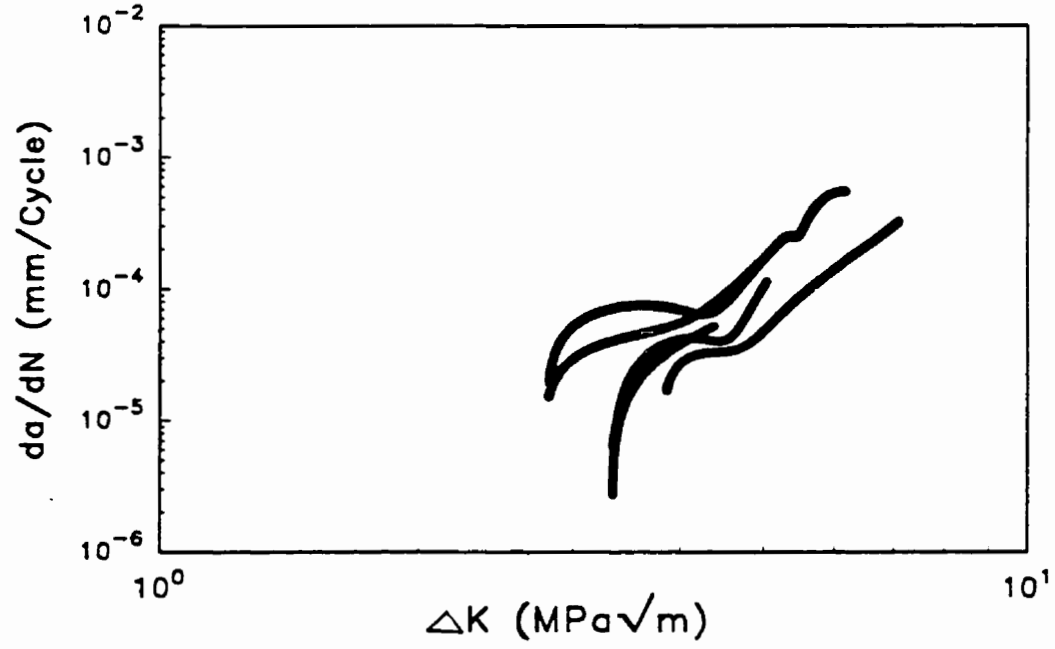

Figure 5.39 Variation of da/dN with ΔK in T7351 material for the two grain orientations.

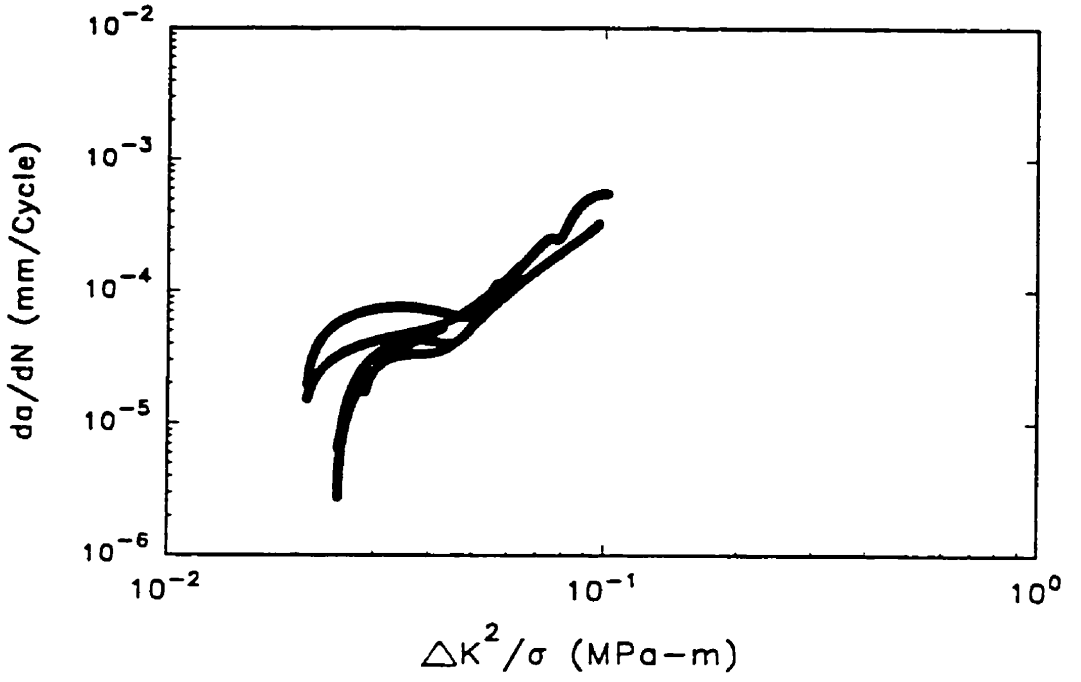

Figure 5.40a A plot of da/dN versus $\Delta K^2/\sigma$ in T7351 material.

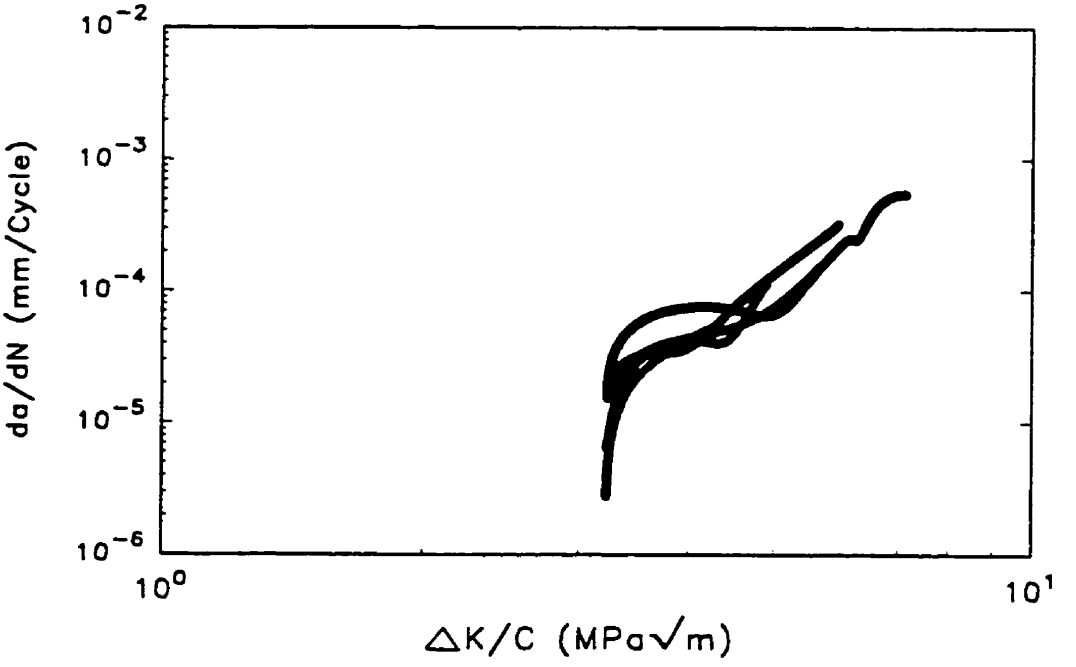

Figure 5.40b A plot of da/dN versus $\Delta K/C$ in T7351 material.

APPENDICES

APPENDIX I

Description of the finite element analysis used to determine the crack depth versus change in ACPD

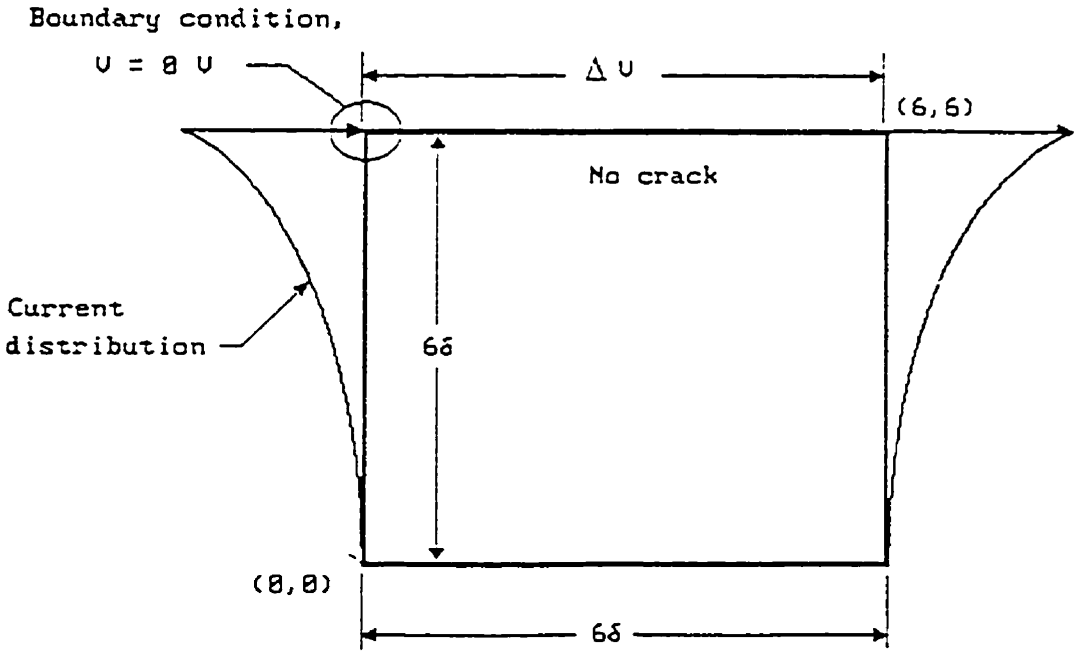

Figure I.1 Schematic of the model with crack depth = 0δ.

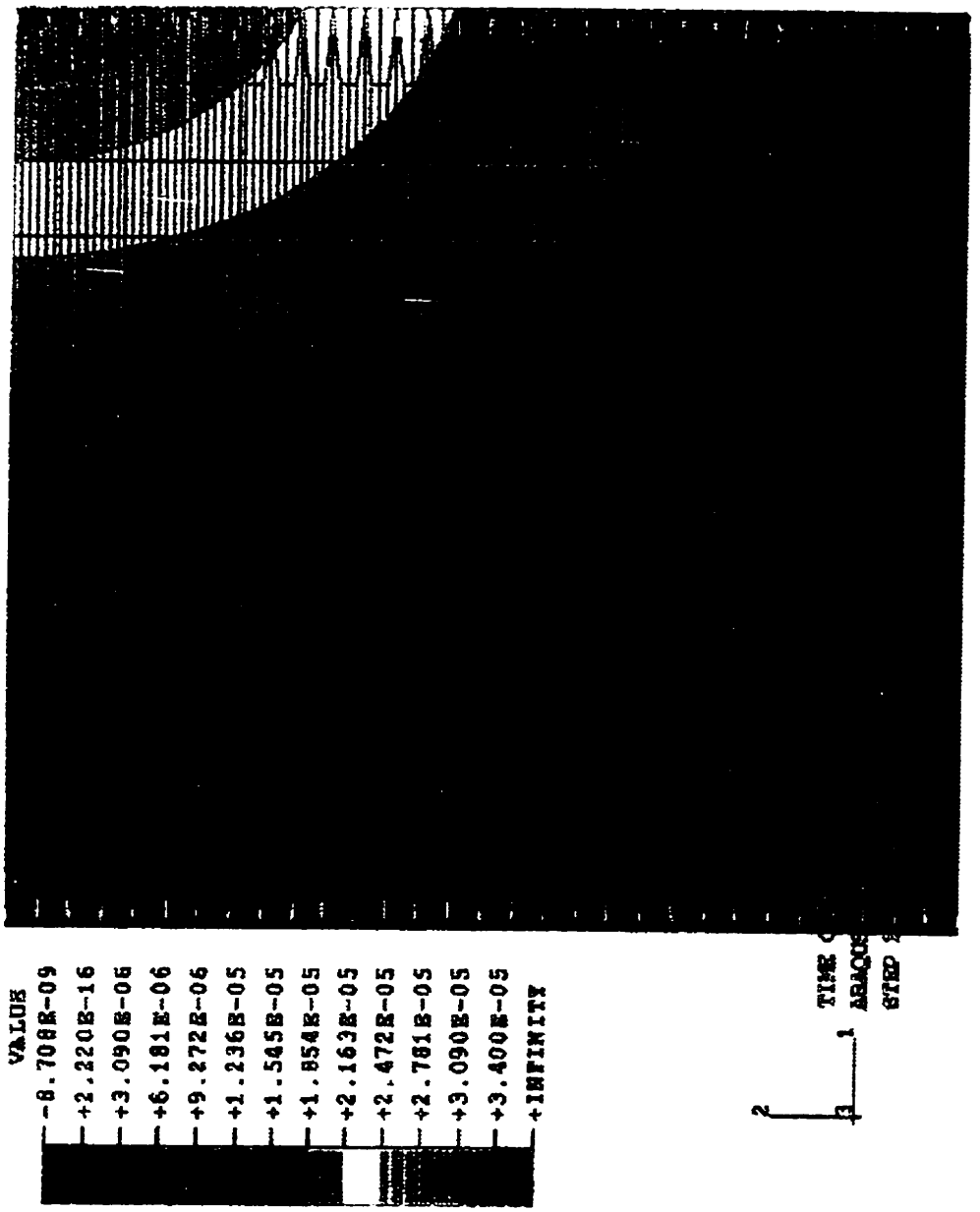

Figure I.2 AC potential distribution when crack depth = 0δ.

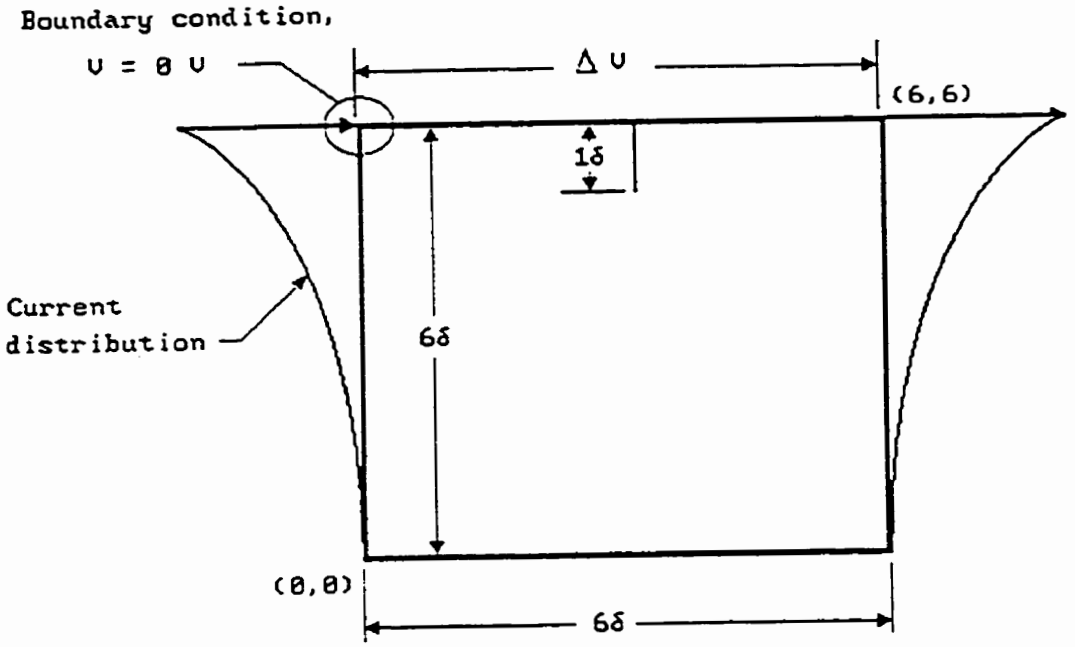

Figure I.3 Schematic of the model with crack depth = 1δ.

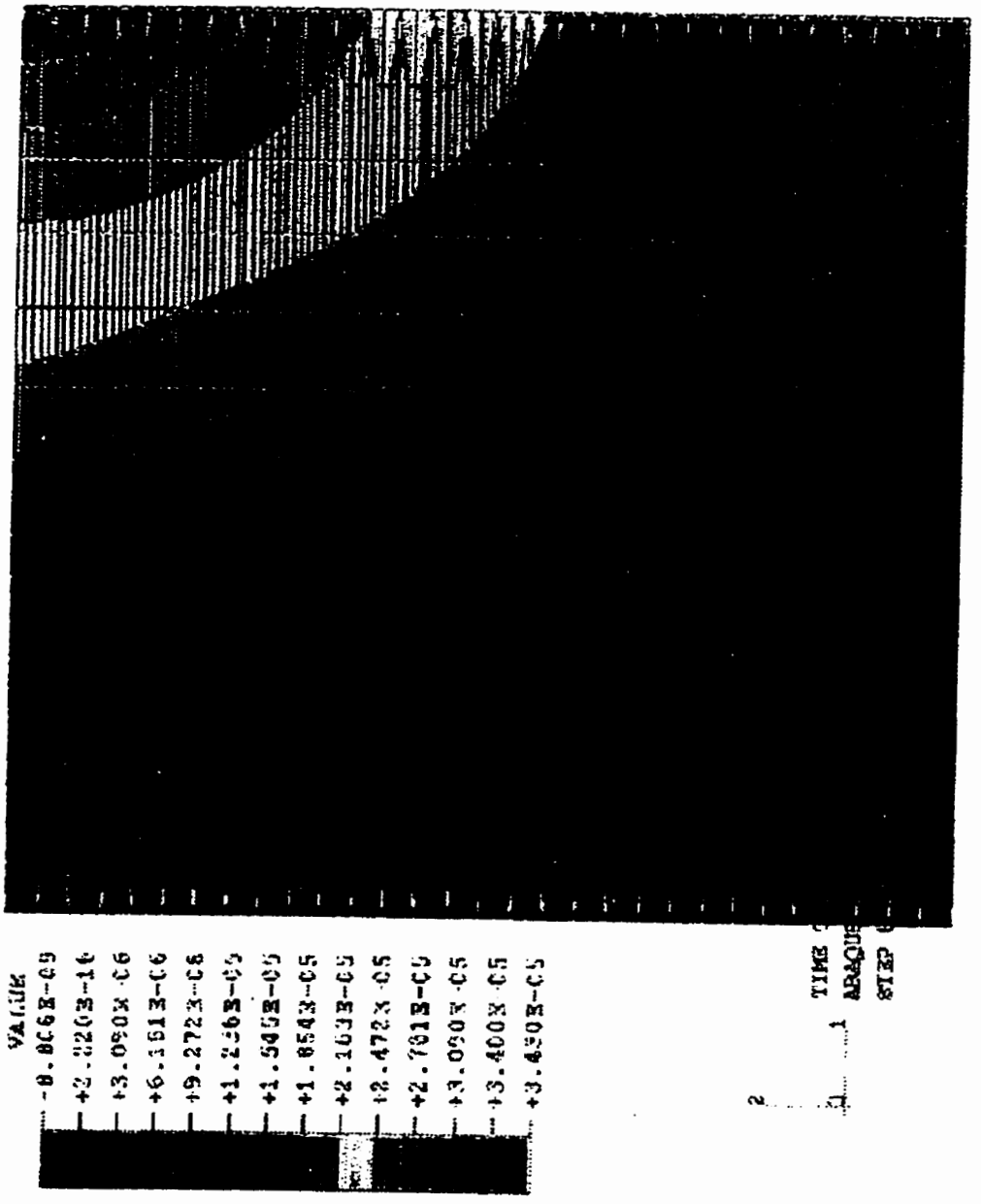

Figure I.4 AC potential distribution when crack depth = 1δ.

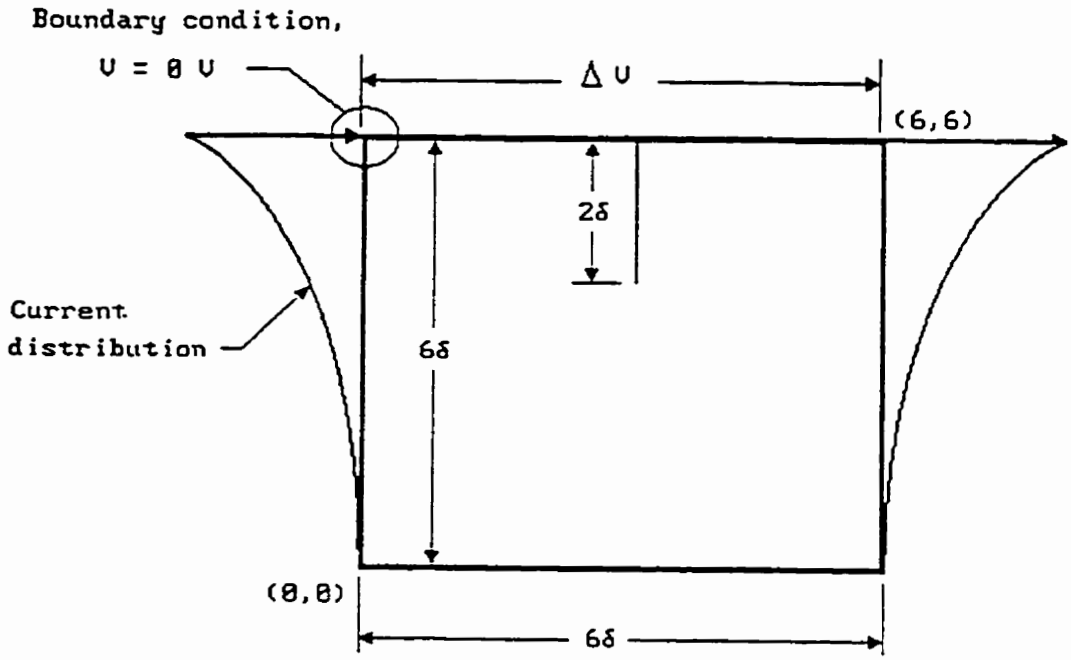

Figure I.5 Schematic of the model when crack depth = 2δ

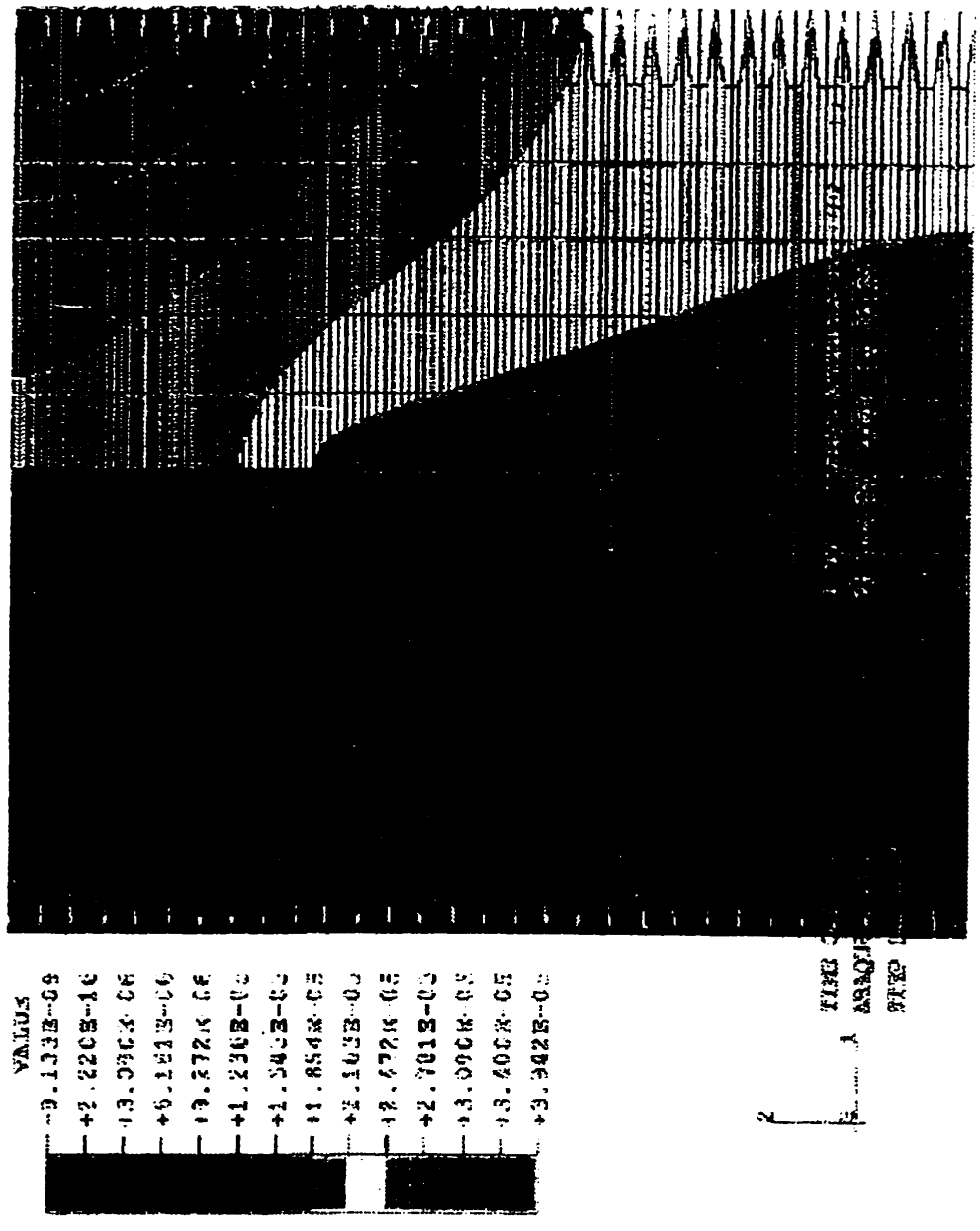

Figure I.6 AC potential distribution when crack depth = 2δ.

APPENDIX II

Description of stress intensity factor for a semi-elliptical crack growing from the centre of a semi-circular notch

$$K = s\sqrt{\pi.a/Q}F_{jn}\left(\frac{c}{a},\frac{c}{t},\frac{a}{r},\frac{a}{w},\frac{r}{t},\frac{r}{w},\Phi\right) \qquad (1)$$

where F_{jn} is the boundary-correction factor.

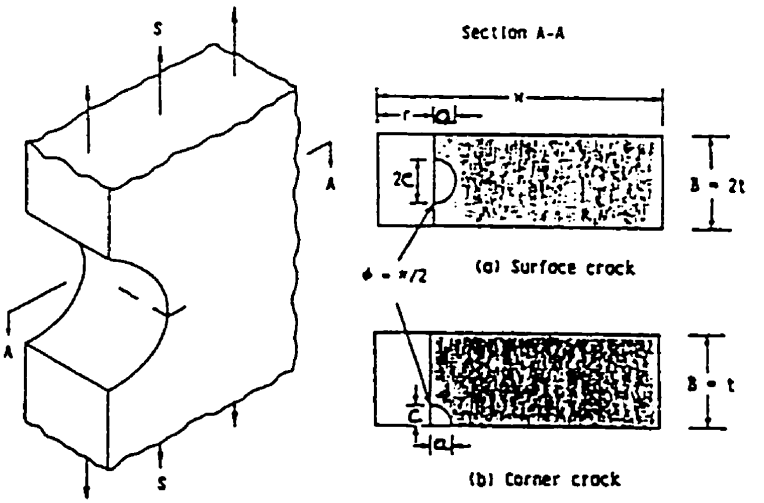

Figure II.1 Definition of dimensions for specimen, surface-crack, and corner crack configurations.

The shape factor Q is given by

$$Q = 1 + 1.464\left(\frac{c}{a}\right)^{1.65} \text{ for } c/a \le 1 \tag{2}$$

$$Q = 1 + 1.464\left(\frac{a}{c}\right)^{1.65} \text{ for } c/a > 1 \tag{3}$$

$$F_{sn} = \left[M_1 + M_2\left(\frac{c}{t}\right)^2 + M_3\left(\frac{c}{t}\right)^4\right] g_1 g_2 g_3 g_4 g_5 f_\phi f_w \tag{4}$$

for $0.2 < c/a < 2$, $c/t < 1$, $1 < r/t < 3.5$, $(r + a)/w < 0.5$, $r/w = 1/16$, and $-\pi/2 < \phi < \pi/2$. (Note that here t is defined as one-half of the full sheet thickness.)

For $c/a \le 1$

$$M_1 = 1 \tag{5}$$

$$M_2 = 0.05 / [0.11 + (c/a)^{3/2}] \tag{6}$$

$$M_3 = 0.29/[0.23 + (c/a)^{3/2}] \tag{7}$$

$$g_1 = 1 - [(c/t)^4 (2.6 - 2c/t)^{1/2}(1 + 4c/a)]\cos\phi \tag{8}$$

$$g_2 = [1 + 0.358\lambda + 1.425\,\lambda^2 - 1.578\lambda^3 + 2.156\lambda^4]/(1 + 0.08\lambda^2) \tag{9}$$

$$\lambda = 1 / [1 + (a/r)\cos(0.9\phi)] \tag{10}$$

$$g_3 = 1 + 0.1(1 - \cos\phi)^2(1-c/t)^{10} \tag{11}$$

$$g_4 = K_T[0.36 - 0.032/(1+a/r)^{1/2}] \tag{12}$$

Where K_T is the elastic stress-concentration factor ($K_T = 3.17$ for uniform stress, $K_T = 3.15$ for uniform displacement) at the semi-circular notch, and

$$g_5 = 1 + (c/a)^{1/2}[0.003(r/t)^2 + 0.035(r/t)(1 - \cos\phi)^3] - 0.35(c/t)^2(1 - 0.5c/a)^3\cos\phi \tag{13}$$

The finite width correction factor f_w was

$$f_w = 1 - 0.2\,\gamma + 9.4\gamma^2 - 19.4\,\gamma^3 + 27.1\,\gamma^4 \qquad (14\text{-a})$$

for uniform stress and

$$f_w = 1 + 2.17\gamma^2 - 3.4\,\gamma^4 + 3.7\,\gamma^6 \qquad (14\text{-b})$$

for uniform displacement width a specimen-Length-To-Width (L/W) ratio of 1.5 (L is measured from the crack plane to the grip line on the specimen) where

$$\gamma = (c/t)^{1/2}(a + r)/w \qquad (15)$$

The function f_ϕ is given by

$$f_\phi = [(c/a)^2\cos^2\phi + \sin^2\phi]^{1/4} \qquad (16)$$

For $c/a > 1$

$$M_1 = (a/c)^{1/2}(1.04 - 0.04\,a/c) \qquad (17)$$

The functions M_2, M_3, g_1, g_2, γ, g_3, g_4, g_5, and f_w are given by equation 6 through 14, respectively, and f_ϕ is given by

$$f_\phi = [(a/c)^2\sin^2\phi + \cos^2\phi]^{1/4} \qquad (18).$$

IMAGE EVALUATION
TEST TARGET (QA-3)

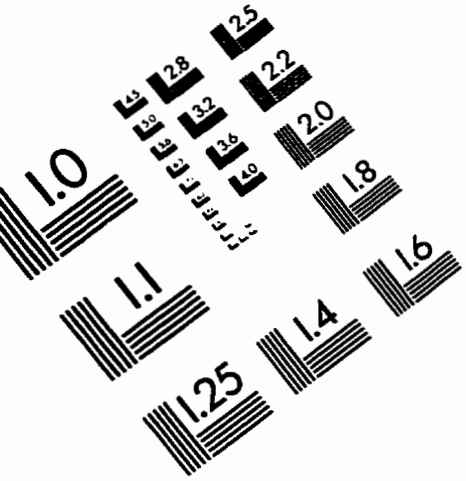

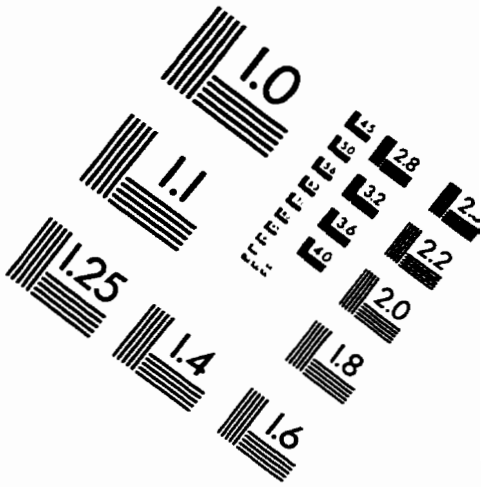

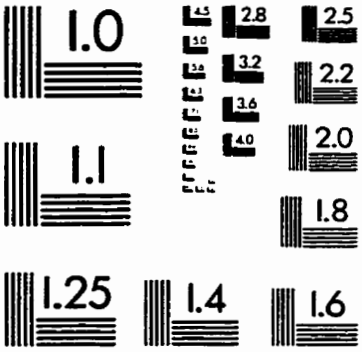

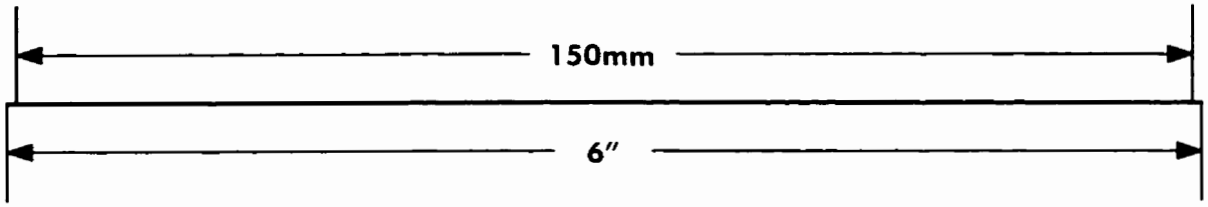

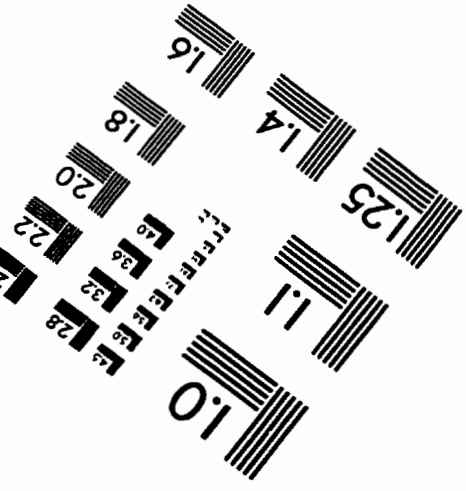

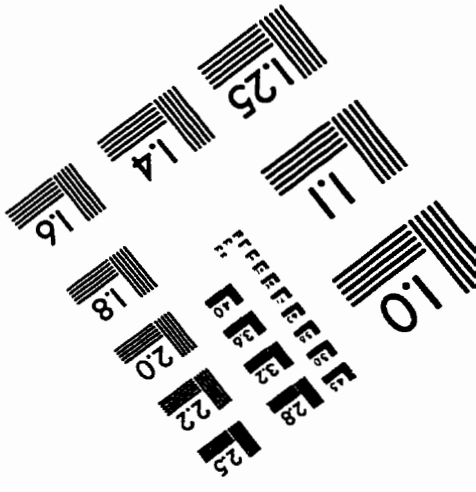

APPLIED IMAGE, Inc
1653 East Main Street
Rochester, NY 14609 USA
Phone: 716/482-0300
Fax: 716/288-5989